



---

# **Uncertainty Quantification and State Estimation for Complex Nonlinear Problems in Space Flight Mechanics**

---

Massimo Vetrivano

Submitted in fulfilment of the requirements for

the Degree of Doctor of Philosophy

Department of Mechanical & Aerospace Engineering

Faculty of Engineering

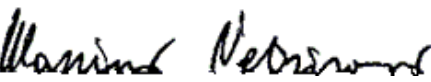
University of Strathclyde

© Massimo Vetrivano, 2016

This thesis is the result of the author's original research. It has been composed by the author and has not been previously submitted for examination which has led to the award of a degree.

The copyright of this thesis belongs to the author under the terms of the United Kingdom Copyright Acts as qualified by University of Strathclyde Regulation 3.50.

Due acknowledgement must always be made of the use of any material contained in, or derived from, this thesis.

Signed: 

Date: 21 May 2017

## **Abstract**

The complex dynamics which describe the motion of a spacecraft far from a massive planetary body or in a highly perturbed environment close to minor celestial objects raises two fundamental but related problems. The first is represented by the difficulty to accurately predict the evolution of its orbit even over short period when its initial conditions are known with a small degree of confidence. The second is given by the need for precise real time estimation of the trajectory when the spacecraft orbits near the asteroid's surface to avoid impacting on it.

The main example of the first problem is the perturbed four body problem for the Earth-Sun-Moon system. Earth-Sun Lagrangian Point Orbits (LPOs) are often selected for astrophysics and solar terrestrial missions while low cost missions aim at exploiting the so called Weak Stability Boundaries (WSB) to move at low propellant expense within the Earth sphere of influence. As current and future missions are planned to be placed on LPOs, it is a critical aspect to clear these regions at the end of operations to avoid damages to other spacecraft.

For the second problem, we have a great number of asteroids and comets orbiting the inner solar system; they represent the so-called minor celestial objects which are very interesting for science since they preserve the remnants of the early formation of the planets and could shed light on the origins of life. At the same time they are very appealing for future commercial applications for the high content of precious ore. Among these celestial objects, the family of Near Earth Objects (NEOs) follows trajectories which lie close to, and sometimes cross, the Earth's orbit. The impact hazard with the Earth has started to become considered as serious threat.

Over the last three decades a number of missions have flown to and explored asteroids and comets, relying heavily on ground support with limited autonomy. In order to perform either asteroid's exploration or collision hazard protection, autonomous navigation is needed, also to deal with the uncertain environment. Then the manipulation of asteroids' orbit and attitude for deflection purposes is therefore required and an interesting problem to be studied.

The aim of the research presented in this dissertation is to identify and develop methodologies for uncertainty propagation for spacecraft orbit and the application to orbit determination for complex nonlinear space mechanics problems, with particular care paid to the case of close proximity operations which are required when performing missions to minor celestial objects. The results are not limited only to this kind of problem but can be applied also to different scenarios.

A first set of results focuses on the prediction of the trajectory evolution under initial condition uncertainties. The accuracy of the propagation of uncertainties is intimately related to the process of trajectory estimation, which relies on the use of the covariance matrix. The covariance matrix gives an idea of the dispersion of the spacecraft in terms of position and velocity. Different techniques to propagate the covariance matrix are used to predict the evolution of the trajectory when the initial conditions are known only to a certain degree of accuracy. They are compared under a highly nonlinear scenario where a spacecraft is injected into a disposal orbit towards an impacting trajectory with the Moon from a Lagrangian Point Orbit.

A second set of results focuses on the identification of the estimation techniques applied to a single spacecraft. The estimation process performs well depending on the capability to propagate the covariance matrix and to incorporate the new information. A number of filtering techniques based

on the Kalman and  $H_\infty$  filters, employing different methods to handle the propagation of the covariance matrix, are presented and tested in typical nonlinear environments, i.e. a WSB transfer an asteroid proximity, to draw precious information on their performance. The analyses demonstrate that only a hybrid Kalman-  $H_\infty$  filter can enable the spacecraft to estimate its trajectory with a good balance between accuracy and computational costs. Then this method is applied to the navigation of spacecraft formation about a NEO showing that the navigation performance is significantly improved by sharing relative information among the spacecraft and the overall system is shown to be fault-tolerant.

Finally the orbit's and attitude manipulation of a small asteroid using a laser ablation system is analysed. An on-board state estimation and control algorithm is presented that simultaneously provides an optimal proximity control and control of the rotational motion of the asteroid. During the deflection, the proximity motion of the spacecraft is coupled with the orbital and rotational motion of the asteroid. The combination of the deflection acceleration, solar radiation pressure, and gravity field and plume impingement will force the spacecraft to drift away from the asteroid. In turn, a variation of the motion of the spacecraft produces a change in the modulus and direction of the deflection action which modifies the rotational and orbital motion of the asteroid.

## Acknowledgments

I would like to acknowledge my supervisor Professor Massimiliano Vasile. This research would not have been possible without Professor Vasile's insight, advice and guidance throughout the project. He gave me the great opportunity to take part to many diverse projects where my research was applied. For many reasons, my experience during the PhD in Glasgow has been one of the most challenging and strongest in my life, it gave me the chance to visit many place during conferences and to meet people I would have never met otherwise. At the same time, big thanks go also to all my friends and colleagues of the Advanced Space Concept Laboratory, with whom I shared many hard and nice periods. Federico, I really enjoyed our time as flatmates and friends discussing about everything, organizing our proper Italian dinners, cooking delicacies and drinking your wine from Friuli. Together with Luca, Simone, Daniele, and Fabrizio we formed a Little Italy in Glasgow. We had great times forgetting the lack of sun and the homesickness. Thank you Willem, we shared travels and projects together and I learnt a lot from working with you; Luca, for listening to my thoughts and sharing yours during our existential discussion. A thank goes to Thomas, my former office mate before the James Weir fire and indefatigable world traveller for projects and conferences. Thank you, Alison, for your help and advice as the only English native speaker of the office, without forgetting of the 2012 Christmas song. Eirini, you are a good friend and it was really nice to talk never endingly with you.

A heartfelt thank goes to my family, my brother Domenico, my aunt Emanuela and my uncle Ugo, my grandmother and my grandfather, the latter worked abroad for many years when Skype, internet

and cheap flights could not make life 'easy' as nowadays. A special thank and hug to my mother, who always unconditionally encouraged me to pursue my dreams. Dad, you are always with me.

A final and special thank goes to Valentina, who pushed me to do always my best in any situation and supported me from 2,000 km away. Thank you for our son Leonardo, who gave me the final push to finalize and conclude this work.

## Contents

Acknowledgments.....	iv
Contents .....	vi
List of Figures .....	xi
List of Tables .....	xvi
Nomenclature .....	xviii
List of symbols .....	xviii
List of constants .....	xxx
List of acronyms .....	xxxii
1 Introduction .....	1
1.1 Research Motivation and Objectives.....	2
1.2 Background.....	4
1.2.1 LPO End of Life Disposal Problem.....	4
1.2.2 Uncertainty Propagation .....	6
1.2.3 Near Earth Objects Problem.....	10
1.2.4 Missions to Minor Celestial Objects.....	12
1.2.5 NEOs Deflection Strategies.....	18
1.3 Methodologies Developed and Implemented .....	20



1.4	Dissertation Organisation .....	23
1.5	Contributions.....	24
2	Uncertainty Propagation.....	30
2.1	Dynamic Equations for Spacecraft Disposal towards the Moon.....	31
2.1.1	Problem Definition.....	32
2.2	Uncertainty Propagation Techniques .....	35
2.2.1	MC Sampling - Calculation of Mean and Covariance .....	36
2.2.2	High-order Taylor Expansions.....	37
2.2.3	Unscented Transformation .....	41
2.2.4	Polynomial Chaos Expansions.....	42
2.3	Results.....	48
2.3.1	Comparisons.....	48
2.3.2	Impact Analysis .....	59
2.4	Summary .....	65
3	Filtering Techniques .....	68
3.1	Kalman Filtering.....	68
3.2	The Extended Kalman Filter .....	71
3.3	The Unscented Kalman Filter.....	73
3.4	High Order Semi-Analytic Extended Kalman Filter .....	76

3.5	Case Study - Weak Stability Boundaries .....	80
3.5.1	Orbit Determination .....	82
3.6	Filter Comparison .....	85
3.6.1	Manoeuvre Design .....	88
3.7	Unscented Particle Filter.....	92
3.8	Polynomial Chaos Based Ensemble Kalman Filter .....	96
3.9	H-infinity Filter .....	100
3.10	Extended H-Infinity Filter.....	107
3.11	The Unscented H-infinity Filter.....	109
3.12	Case Study - Proximity Motion .....	110
3.12.1	Camera Model .....	115
3.12.2	LIDAR Model .....	117
3.12.3	Comparison.....	118
3.13	Summary .....	121
4	Collaborative Formation at NEOs .....	123
4.1	Dynamic Models .....	124
4.1.1	Formation Dynamics .....	124
4.1.2	Dynamic Equations of Asteroid and Spacecraft in the Heliocentric Frame .....	127
4.1.3	Control Strategy.....	128

4.2	Measurements Model.....	130
4.2.1	Camera and LIDAR Model.....	132
4.2.2	Inter-spacecraft Measurements.....	136
4.2.3	Ground Station Measurements.....	137
4.2.4	Sun Doppler Shift Sensor Model.....	137
4.3	Navigation Strategy.....	138
4.4	Data Fusion Process.....	145
4.5	Results.....	146
4.5.1	Non-collaborative vs. Collaborative case.....	148
4.5.2	Failures.....	152
4.6	Asteroid Ephemerides Refinement.....	156
4.7	Summary.....	162
5	Deflecting Small Asteroids.....	164
5.1	Ablation Model.....	165
5.1.1	Optimal distance from the asteroid and force due to the sublimation.....	168
5.2	Proximity Motion Dynamics and Control.....	172
5.3	Proximity Control Strategy.....	175
5.4	Asteroid Rotational Dynamics and Control.....	178
5.5	Proximity and Rotational Motion Reconstruction.....	185

5.5.1	Measurement Model.....	185
5.5.2	Proximity Motion Reconstruction.....	186
5.5.3	Asteroid Rotational Motion Reconstruction.....	192
5.6	Results.....	197
5.6.1	Spacecraft Proximity Control.....	200
5.6.2	Estimated Perturbations during Proximity Operations.....	202
5.6.3	Asteroid Rotational Velocity Control.....	203
5.6.4	Effect of the Asteroid's Rotation on its Deflection.....	207
5.7	Summary.....	211
6	Conclusions.....	213
6.1	Summary and Conclusions.....	213
6.1.1	Key Contributions.....	216
6.2	Limitations of This Work.....	218
6.3	Remarks for Future Work.....	219
	Bibliography.....	223

## List of Figures

Figure 1. Disposal trajectory towards the Moon for Herschel. ....	35
Figure 2. Position (left) and velocity (right) with local STTs. ....	39
Figure 3. Smoliak grid for Hermite polynomials with different level of accuracy .....	47
Figure 4. Statistical distribution for Monte Carlo Simulation and 10,000 samples: x-y position distribution (a), x-z velocity distribution (b).....	50
Figure 5. Statistical distribution for Monte Carlo Simulation and 100,000 samples: x-y position distribution (a), x-z velocity distribution (b).....	50
Figure 6. Statistical distribution for Monte Carlo Simulation and 1,000,000 samples: x-y position distribution (a), x-z velocity distribution (b).....	51
Figure 8. Maximum position (left) and velocity (right) error for STTs and UT with respect to the MC simulation. ....	53
Figure 9. Statistical distribution with 1st order STTs x-y position distribution (a), x-z velocity distribution (b). ....	55
Figure 10. Statistical distribution with 2nd order STTs: x-y position distribution (a), x-z velocity distribution (b). ....	55
Figure 11. Statistical distribution with 3rd order STTs: x-y position distribution (a), x-z velocity distribution (b). ....	56
Figure 12. Statistical distribution with 4st order STTs: x-y position distribution (a), x-z velocity distribution (b). ....	56
Figure 13. Statistical distribution with 2nd order PCE: x-y position distribution (a), x-z velocity distribution (b). ....	57
Figure 14. Statistical distribution with 3rd order PCE: x-y position distribution (a), x-z velocity distribution (b). ....	57

Figure 15. Statistical distribution with 4th order PCE: x-y position distribution (a), x-z velocity distribution (b). .....	58
Figure 16. Statistical distribution with 5th order PCE: x-y position distribution (a), x-z velocity distribution (b). .....	58
Figure 17. Statistical distribution with 6th order PCE: x-y position distribution (a), x-z velocity distribution (b). .....	59
Figure 18. Particles dispersion and density at impact for 1% manoeuvre error and 5 km dispersion error (per component): MC (left) and PCE order 2 (right). .....	61
Figure 19. Particles dispersion and density at impact for 1% manoeuvre error and 5 km dispersion error (per component): PCE order 3 (left) and PCE order 4 (right). .....	62
Figure 20. Particles dispersion and density at impact for 1% manoeuvre error and 5 km dispersion error (per component): PCE order 5 (left) and PCE order 6 (right). .....	62
Figure 21. Particles dispersion and density at impact for 1% manoeuvre error and 5 km dispersion error (per component): PCE order 6 with 200,000 samples. ....	63
Figure 22. Particles dispersion and density at impact for 0.1% manoeuvre error and 1 km dispersion error (per component): MC (left) and PCE order 2 (right). .....	64
Figure 23. Particles dispersion and density at impact for 0.1% manoeuvre error and 1 km dispersion error (per component): PCE order 3 (left) and PCE order 4 (right). .....	65
Figure 24. Particles dispersion and density at impact for 0.1% manoeuvre error and 1 km dispersion error (per component): PCE order 5 (left) and PCE order 6 (right). .....	65
Figure 25. Position a) and velocity b) errors using global STTs, integrated local STTs and local STTs obtained via series reversion. ....	78
Figure 27. Reference frames (Vallado, 2000). .....	84
Figure 28. Comparison of the absolute errors for 100 km position uncertainties and 0.1 km/s velocity uncertainties. ....	86

Figure 29. Comparison of the absolute errors for uncertainties on position and velocity equal to 1% of the nominal unperturbed trajectory.....	87
Figure 30. Definition of the reference coordinate systems. ....	111
Figure 31. Asteroid body frame with respect to the Hill frame.....	112
Figure 32. Measurements models for relative navigation geometry. ....	115
Figure 33. Centroid identification. ....	116
Figure 34. RMSE for a) position and b) velocity. ....	120
Figure 35. Nominal trajectories. ....	127
Figure 36. Relative distance under all perturbations.....	128
Figure 37. Measurements models for (a) relative navigation geometry (b) absolute navigation geometry. ....	131
Figure 38. Pin-Hole camera model.....	133
Figure 41. Estimated a) position and b) velocity RMSE (continuous line) and dispersion (1-sigma, dashed line) for UHF and EHF. ....	142
Figure 42. Controlled a) position and b) velocity average RMSE for UKF, EKF, UHF and EHF. ....	143
Figure 43. Non-Collaborative case: RMSE for estimated a) position, b) velocity, c) controlled position and d) controlled velocity. ....	149
Figure 44. Collaborative case: RMSE for estimated a) position, b) velocity, c) controlled position and d) controlled velocity.....	150
Figure 45. SC-3 failures: RMSE for estimated a) position, b) velocity, c) controlled position and d) controlled velocity.....	153
Figure 46. SC-4 failures: RMSE for estimated a) position, b) velocity, c) controlled position and d) controlled velocity.....	154
Figure 47. Approach and acquisition phase configuration. ....	157

Figure 48. Asteroid estimate a) position and b) velocity error in 14 days using only on-board optical observation from a single spacecraft with ground station tracking. ....	158
Figure 49. Asteroid estimate a) position and b) velocity error in 7 days combined on-board optical observation measurements with ground station tracking. ....	161
Figure 50. Asteroid estimate a) position and b) velocity error in 7 days combined on-board optical observation measurements with ground station observation and sun Doppler. ....	161
Figure 51. Thrusting time required to achieve 1 m/s velocity change with a shooting distance of 50 m. ....	169
Figure 52. a) Force due to the sublimation process with respect to the laser distance from the spot and the velocity of the surface under the spot light; b) cross section showing the force trend with respect to the distance at increasing tangential velocity.....	171
Figure 53. (a) Definition of the inertial and Hill's reference frames; (b) definition of the asteroid's body fixed reference frame.....	173
Figure 54. a) Difference between range to a surface point and the focusing length with Rayleigh length b) Maximum difference as a function of the asteroid rotation around $b_l$ (spacecraft positioned at 50 m from the asteroid's CoM and focusing length of 49.3 m). ....	176
Figure 55. Angular velocity control scheme (a); control arm representation in body frame (b).....	181
Figure 56. Maximum achievable torque: a) optimizing maximum torque $M_\omega$ , c) optimizing $r_{eq}$ . Angle between control torque and the angular velocity: b) optimizing maximum torque $M_\omega$ d) optimizing $r_{eq}$ . ....	183
Figure 57. Equivalent control arm a) with respect to azimuth and polar angles, b) on the ellipsoid surface.....	184
Figure 58. Angular velocity estimation error.....	196
Figure 59. Comparison between different methods of optical flow.....	197
Figure 60. Spacecraft Control: estimated position (a) and velocity error (b).....	200



Figure 61. Discrete Control: actual controlled position (a) and velocity error (b).....	201
Figure 62. Discrete Control: actual defocusing due to spacecraft and asteroid rotation control.....	202
Figure 63. Estimated acceleration from the laser and plume force vs. the actual acceleration.....	203
Figure 64. Asteroid rotation control with spacecraft fixed at 50 m. a) Absolute magnitude and b) z, c) x and d) y axes of the body fixed frame. ....	204
Figure 65. Rotational velocity of the asteroid considering the actual incidence of the laser. a) Absolute magnitude and b) z, c) x and d) y axes of the body fixed frame.....	205
Figure 66. Rotational velocity of the asteroid with angular velocity directed as the orbit tangent and aligned to the maximum axis of inertia. Spacecraft is also placed along the tangent. ....	207
Figure 67. a) Thrust time to achieve the target delta-velocity change as function of the initial rotational velocity of the asteroid. b) Actual acceleration onto the asteroid as function of time with different initial rotational velocities of the asteroid (colour bar). The black portion of the lines represents the time needed to achieve the target change in velocity of 1 m/s.....	208
Figure 68. Asteroid's proximal motion. ....	209
Figure 69. Deviation of the asteroid at the check point as function of the initial rotational velocity of the asteroid. ....	211

## List of Tables

Table 1. Propagation error using STTs. ....	39
Table 2. One-dimensional Hermite polynomials up to the 6 <sup>th</sup> order. ....	45
Table 3. Minimum number of points required for calculating Gaussian integrals of a certain order. ....	47
Table 4. Impact rate convergence for increasing number of MC samples. ....	51
Table 5. Comparison between STTs, PCE and MC simulation for 56 days propagation from LPO to Moon disposal manoeuvre. A 64-bit Linux CentOS 5.4 2.93GHz Intel(R) Xeon(TM) X5570 was used. ....	54
Table 6. Impact rate comparison between MC and PCE: 1% manoeuvre error and 5 km dispersion error (per component). ....	61
Table 7. Impact rate comparison between MC and PCE: 0.1% manoeuvre error and 1 km dispersion error (per component). ....	64
Table 8. Raisting ground station location. ....	82
Table 9. Elapsed CPU time for the filtering processes, using a 64-bit Linux CentOS 5.4 2.93GHz Intel(R) Xeon(TM) X5570 , and absolute error for the estimated state. ....	88
Table 10. OD impacts on Navigation using optimized and nonlinear statistical targeting correction methods. A 64-bit Linux CentOS 5.4 2.93GHz Intel(R) Xeon(TM) X5570 was used. ....	91
Table 11. Orbital and physical properties of 99942 Apophis ....	119
Table 13. Initial spacecraft trajectory parameters. ....	126
Table 14. Average RMSE comparison for different filters - SC1 ....	144
Table 15. Sensors error for close proximity navigation. ....	147
Table 16. Measurements error for asteroid refinement (1-sigma). ....	147

Table 17. Average RMSE in estimated and controlled trajectory for the collaborative and uncollaborative case.....	151
Table 18. Sensors set on spacecraft formation.....	152
Table 19. Average RMSE of the estimated and controlled trajectory in case of failures. ....	155
Table 20. Analysed configurations and final estimated error without and with Doppler shift. ....	159
Table 21. Laser system coefficients. ....	168
Table 22. Orbital elements of 2006 RH120 at Epoch MJD2000 2456200.5 (12 September 2012) ( <a href="http://ssd.jpl.nasa.gov/sbdb.cgi?sstr=2006%20RH120">http://ssd.jpl.nasa.gov/sbdb.cgi?sstr=2006%20RH120</a> ).....	198
Table 23. Spacecraft characteristics. ....	199
Table 24. Errors in the measurements model.....	199

## Nomenclature

### List of symbols

#### Greek Symbols

$\alpha$  coefficients of the multivariate polynomials

$\alpha$  azimuth of the point  $\mathbf{s}$  in the body fixed frame [*rad*]

$\alpha_\infty$  scaling parameter for  $H_\infty$  filter

$\beta$  polar angle of the point  $\mathbf{s}$  in the body fixed frame [*rad*]

$\beta_{ukf}$  coefficient to incorporate prior knowledge of the distribution in the UT

$\chi_0$  is the centre of a sparse grid

$\chi_i^c$  correlated samples points

$\chi_i$  random input

$\chi$  spacecraft longitude in the body fixed reference frame [*rad*]

$\gamma$  spacecraft latitude in the body fixed reference frame [*rad*]

$\zeta_k$  white, zero-mean, uncorrelated measurements noise

$\xi$  elevation angle from the surface normal at the spot location [*rad*]

$\delta\mathbf{a}_p$  vector of the orbit element difference at the check point between the perturbed and the nominal orbit

$\delta v_l$  velocity variation imparted by the ablation process [*km/s*]

$\delta \mathbf{r}$  spacecraft relative position with respect to the asteroid in the inertial frame [ $km$ ]

$\delta \dot{\mathbf{r}}$  spacecraft relative velocity with respect to the asteroid in the inertial frame [ $km/s$ ]

$[\delta \mathbf{r}^h, \delta \dot{\mathbf{r}}^h] = [x_h, y_h, z_h, v_{x_h}, v_{y_h}, v_{z_h}]$  SC relative position and velocity with respect to the asteroid in Hill frame [ $km km/s$ ]

$[\delta \tilde{\mathbf{r}}^h, \delta \tilde{\dot{\mathbf{r}}}^h] = [\tilde{x}_h, \tilde{y}_h, \tilde{z}_h, \tilde{v}_{x_h}, \tilde{v}_{y_h}, \tilde{v}_{z_h}]$  estimated relative position and velocity with respect to the asteroid in the Hill frame with corresponding components [ $km km/s$ ]

$\delta \mathbf{r}_{SC}$  spacecraft position in the inertial frame [ $km$ ]

$\delta \mathbf{r}_{SC}^h$  spacecraft position in the Hill frame [ $km$ ]

$\delta r_{SC}$  distance from the origin of the Hill frame [ $km$ ]

$\delta \mathbf{x}_0$  initial deviation with respect to the reference trajectory

$\delta \mathbf{r}_a$  asteroid's trajectory deviation with respect to the nominal orbit [ $km$ ]

$\delta r_a$  modulus of  $\delta \mathbf{r}_a$  [ $km$ ]

$\Delta t_c$  time interval for the spacecraft to reach the other side of the control box [ $s$ ]

$\Delta \mathbf{v}_{corr}$  correction manoeuvre calculate on per base component  $\Delta v_{corr}^i$  in Hill frame [ $m/s$ ]

$\Delta t_{halt}$  time to completely stop the asteroid rotation [ $s$ ]

$\phi$  solution flow

$\Phi$  state transition matrix

$\varphi_A$  longitude angle for the asteroid body frame

$\varphi_c$  local azimuth of the centroid [ $rad$ ]

$\mathbf{v}_k$  innovation process

$\upsilon$  longitude [ $rad$ ]

$\lambda$  latitude [ $rad$ ]

$\lambda_s$  scattering factor

$v_{laser}$  and  $v_{plume}$  are system noises relative to the laser and the plume [ $km/s^2$ ]

$\eta$  absorbance per unit length of the accumulated ejecta [ $m^{-1}$ ]

$\eta_p$  efficiency of the power system

$\eta_{sys}$  overall efficiency of the power system

$\dot{\mu}$  ejecta mass flow per unit area [ $kg/s/m^2$ ]

$\mu_A, \mu_{Sun}$  gravity constants of the asteroid and the sun respectively [ $m^2/s^3$ ]

$\boldsymbol{\mu}_R$  mean of the response function evaluations

$\mathbf{\Pi}$  matrix used for dynamics evolution of quaternions

$\boldsymbol{\Psi}$  inverse state transition tensors

$\Psi$  are multivariate polynomials

$\rho$  range [ $km$ ]

$\dot{\rho}$  range rate [ $km/s$ ]

$\rho(\boldsymbol{\chi})$  weighting function

$\rho_{H_\infty}$  is a performance bound for  $H_\infty$  filter

$\rho_{plume}$  plume density at a given location [ $kg/m^2$ ]

$\dot{\rho}_{sc}^{Sun}$  range rate due to the Sun Doppler effect [ $km/s$ ]

$\omega_p$  orbit anomaly of the pericentre [ $rad$ ]

$\boldsymbol{\omega} = [\omega_x \quad \omega_y \quad \omega_z]^T$  angular velocity vector in the body reference frame [ $rad/s$ ]

$\boldsymbol{\omega}_I$  angular velocity vector in the inertial frame [ $rad/s$ ]

$\tilde{\boldsymbol{\omega}}_I$  estimated angular velocity in the inertial frame [ $rad/s$ ]

$\boldsymbol{\omega}_{B/C}$  angular velocities of the asteroid relative to the camera [ $rad/s$ ]

$\tilde{\boldsymbol{\omega}}_{B/C}$  estimated angular velocities of the asteroid relative to the camera [ $rad/s$ ]

$\Omega$  orbit anomaly of the ascending node [ $rad$ ]

$\Upsilon$  sigma points

$\Upsilon^a$  augmented sigma points

$\tau_g$  fraction of laser light absorbed by the ejected gas

$\tau$  degradation factor due to contamination

$\mathcal{G}$  true anomaly [ $rad$ ]

$\theta_A$  latitude angle for the asteroid body frame

$\theta_c$  elevation angles of the centroid [ $rad$ ]

$\dot{\boldsymbol{\theta}}$  angular velocity in the inertial frame with which the reference frame rotates [ $rad/s$ ]

$\theta_{check}^*$  argument of latitude at a generic check point [ $rad$ ]

$\dot{\boldsymbol{\theta}}^h$  angular velocity in the Hill frame [ $rad/s$ ]

### Roman Symbols

$a$  orbit semi-major axis [ $km$ ]

$A$  azimuth angle [ $rad$ ]

$\mathbf{A}_{check}$  matrix to transform the orbit element difference into trajectory displacements  $\delta \mathbf{r}_a$

$A_{SA}$  area of the solar arrays [ $m^2$ ]

$A_{S/C-attitude}$  cross section of the spacecraft with respect to the ejection velocity [ $m^2$ ]

$A_{spot}$  area of the laser spot [ $m^2$ ]

$A_M$  area of the solar arrays plus the area of spacecraft bus [ $m^2$ ]

$A_{eq}$  spacecraft cross section area facing the incoming plume of gas [ $m^2$ ]

$\mathbf{a}_p$  perturbative acceleration acting on the spacecraft including second order gravity field [ $km/s^2$ ]

$\mathbf{a}_L$  acceleration due to the laser ablation in the inertial reference frame [ $km/s^2$ ]

$\mathbf{a}_{laser}^h$  acceleration due to the laser ablation in the Hill frame [ $km/s^2$ ]

$\tilde{\mathbf{a}}_L$  estimated acceleration due to the laser ablation in the inertial reference frame [ $km/s^2$ ]

$a_{laser}$  modulus of  $\mathbf{a}_{laser}$  [ $km/s^2$ ]

$\tilde{\mathbf{a}}_L^h$  estimated acceleration due to the laser ablation in the Hill frame [ $km/s^2$ ]

$\tilde{\mathbf{a}}_{plume}$  estimated acceleration produced by the plume [ $km/s^2$ ]

$\tilde{a}_{plume}$  estimated modulus of  $\tilde{\mathbf{a}}_{plume}$  [ $km/s^2$ ]



$a_1, b_1, c_1$  ellipsoid semi-axes [ $km$ ]

$B_i$  is a generic multi-variable polynomial

$c_x, c_y, c_z$  cosine directors of the angular velocity

$C_{nm}$  zonal harmonics coefficients

$C_{20}, C_{22}$  harmonic coefficients for 2 order gravity field

$C_v$  heat capacity of vapour phase [ $J/kg/K$ ]

$C_p$  heat capacity of solid phase and phase [ $J/kg/K$ ]

$C_R$  reflectivity coefficient

$C_{nm}$  higher order zonal harmonics coefficients

$\mathbf{d}_{in}$  estimated position with respect to the target trajectory in Hill frame [ $km$ ]

$e$  orbit eccentricity

$E$  elevation angle [rad]

$E_v^*$  augmented sublimation enthalpy [ $J/kg$ ]

$f$  focal length [ $m$ ]

$\tilde{F}_{plume}$  estimated plume force [ $N$ ]

$\mathbf{F}$  linear state dynamics matrix

$\mathbf{F}_{recoil}$  force produced by the laser recoil in Hill frame [ $N$ ]

$\mathbf{F}_{plume}$  force produced by the plume impingement in Hill frame [ $N$ ]

$\mathbf{F}_{Solar}$  force due to SRP in Hill frame [ $N$ ]

$\mathbf{F}_{sc}$  perturbative force acting on the spacecraft - not including sun and asteroid gravity [ $N$ ]

$[x_h^t, y_h^t, z_h^t]$  target position [ $km$ ]

$\mathbf{F}_L$  force acting on the asteroid due to the ablation in the inertial frame [ $N$ ]

$\mathbf{F}_L^h$  force acting on the asteroid due to the ablation in the Hill frame [ $N$ ]

$F_L$  norm of  $\mathbf{F}_L$  [ $N$ ]

$\mathbf{F}_L^b = [F_y^b, F_y^b, F_z^b]$  force acting on the asteroid due to the ablation in the body frame and components in the body frame [ $N$ ]

$\mathbf{G}^u$  linear input dynamics matrix

$\mathbf{G}$  generic response

$\mathbf{H}$  linear measurements matrix.

$h$  ejecta thickness on exposed surface [ $m$ ]

$\mathbf{I} - \mathbf{J} - \mathbf{K}$  inertial reference frame axes

$\bar{\mathbf{i}} - \bar{\mathbf{j}} - \bar{\mathbf{k}}$  principal axes of inertia of the asteroid (body fixed)

$\mathbf{K}$  filter gain

$i$  orbit inclination [ $rad$ ]

$\mathbf{I}_a$  matrix of inertia of the asteroid [ $kg \cdot m^2$ ]

$I_{zz}$  asteroid inertia along z direction of the body frame [ $kg \cdot m^2$ ]

$l$  distance between the spacecraft and the spot the camera is pointing to [ $km$ ]

$\mathbf{L}_{k+1}$  user-defined observation matrix

$J$  cost function for Kalman filter derivation

$J_{H_\infty}$  cost function for  $H_\infty$  filter derivation

$\mathbf{m}$  propagated mean

$M$  mean anomaly [ $rad$ ]

$m_{sc}$  spacecraft mass [ $kg$ ]

$\dot{m}_{laser}$  measured mean mass flow per unit area [ $kg/m^2$ ]

$\mathbf{M}(f, \mathbf{r}_c)$  feature point matrix

$\mathbf{M}_c = [M_{c-x}, M_{c-y}, M_{c-z}]$  control torque in the Hill reference frame [ $N \cdot m$ ]

$M_\omega$  projection of  $\mathbf{M}_c$  on  $\boldsymbol{\omega}_l$  [ $N \cdot m$ ]

$n_i$  nominal angular velocity at the beginning of the deflection [ $rad/s$ ]

$n_e$  nominal angular velocity at the end of the deflection [ $rad/s$ ]

$\mathbf{n}$  normal to the surface at  $\mathbf{s}$

$\mathbf{P}_k^a$  augmented covariance matrix

$\mathbf{P}_k^{xy}$  cross-correlation between  $\tilde{\mathbf{x}}_k^-$  and  $\tilde{\mathbf{y}}_k^-$

$\mathbf{P}_k^{xw}$  correlation between the state error and process noise

$\mathbf{P}_k^{xy}$  correlation between the state error and measurement noise

$\mathbf{P}_k^{ww}$  correlation between the process noise and measurement noise

$\hat{p}(\mathbf{x}_{0:k} | \mathbf{y}_{1:k})$  posterior distribution

$\mathbf{P}_{x,k}^-$  predicted covariance matrix

$\mathbf{P}_R$  covariance matrix of the response function evaluation

$\mathbf{P}_\chi$  correlation matrix for the grid

$p_{width}$  pixel width [ $m$ ]

$\mathbf{q} = [q_1 \ q_2 \ q_3 \ q_4]^T$  quaternions vector

$\tilde{\mathbf{q}}$  estimated attitude

$\mathbf{Q}$  system noise covariance matrix

$\mathbf{R}$  measurements noise covariance matrix

$r_{eq}$  equivalent control arm [ $km$ ]

$r_{check}$  nominal asteroid position radius at the check point [ $km$ ]

$R_M$  Moon mean radius [ $km$ ]

$\mathbf{R}_{HC}$  rotation matrix from the Hill frame to the camera frame

$\mathbf{r}_c = [x_c \ y_c \ z_c]$  position of surface points with respect to the spacecraft in Hill reference frame [ $km$ ]

$\mathbf{r}_a$  position of the asteroid in the inertial frame [ $km$ ]

$\mathbf{r}_a^h$  position of the asteroid in the Hill reference frame [ $km$ ]

$r_a$  distance of the asteroid from the Sun [ $km$ ]

$\mathbf{s}$  control arm corresponding to the point on the surface where the laser is pointing [ $km$ ]

$[s_x^b, s_y^b, s_z^b]$  components of  $\mathbf{s}$  in the body frame [ $km$ ]

$S_{srp}$  solar flux constant at 1 AU [ $W/m^2$ ]

$S_{nm}$  higher order tesseral harmonics coefficients

$S_{nm}$  tesseral harmonics coefficients

$T_0$  initial surface temperature [ $K$ ]

$T_s$  sublimation temperature [ $K$ ]

$t_{check}$  check point instant, [ $s$ ]

$t_i, t_e$  initial and final time of the deflection [ $s$ ]

$t_{in}$  and  $t_{out}$  entry and exit times from the spot light of a point hit by the laser [ $s$ ]

$\mathbf{u}$  generic system input (known)

$U$  gravity potential [ $km^2/s^2$ ]

$U_{20+22}$  second order gravitational potential [ $km^2/s^2$ ]

$(u^i, v^i)$  position of points on the screen of the camera [ $m$ ]

$(\dot{u}, \dot{v})$  time derivative of position of points on the screen of the camera [ $m/s$ ]

$\bar{v}_s$  measured mean plume velocity at the spacecraft [ $m/s$ ]

$\bar{v}$  ejection velocity [ $km/s$ ]

$\bar{v}_{plume}$  plume's velocity at the spacecraft [ $km/s$ ]

$V_{rot}$  rotational velocity at the sublimation point [ $m/s$ ]

$\mathbf{V}_{B/C}$  linear velocities of the asteroid relative to the camera [ $km/s$ ]

$\tilde{\mathbf{V}}_{B/C}$  estimated linear velocities of the asteroid relative to the camera [ $km/s$ ]

$V_{nm}$  higher order tesseral harmonics coefficients

$w_0$  radius at the focal point [ $m$ ]

$\mathbf{w}_k$  white, zero-mean, uncorrelated process noise

$W_{nm}$  higher order zonal harmonics coefficients

$W_i^{(m)}$  and  $W_i^{(c)}$  weighted sample mean and covariance coefficients

$x_c^a$  distance vector of the feature point to the centre along the boresight direction [ $km$ ]

$\tilde{\mathbf{x}}_k^-$  predicted mean of the state vector

$\tilde{\mathbf{x}}$  estimated variable in the filtering process

$({}^c x_c, {}^c y_c)$  centroid coordinates obtained by the mean position of the all points on the screen of the camera

$(x_{screen}^i, y_{screen}^i)$  pixel position of points on the screen of the camera

$\hat{\mathbf{x}}_h - \hat{\mathbf{y}}_h - \hat{\mathbf{z}}_h$  Hill reference frame axes

$[x_b, y_b, z_b]$  components of the spacecraft relative position in the body frame [ $km$ ]

$\mathbf{x}_{surface}$  vector position of the point with respect to the centre of the asteroid in Hill reference frame [ $km$ ]

$\mathbf{x}_{Surf-SC}$  position of surface points with respect to the spacecraft in Hill reference frame [km]

$\mathbf{y}$  measurements in the filtering process

$y_{\max}$  maximum width of the spot [m]

$\mathbf{z}$  observation variables

### Mathematical notation

$\square$  arbitrary variable

$|\square|$  absolute value of  $\square$

$\|\square\|$  2-norm of  $\square$

$\|\square\|_{\infty}$  norm infinity of  $\square$

$\|\square\|_{\mathbf{M}_k}^2 = (\square)^T \mathbf{M}_k (\square)$   $\mathbf{M}_k$  weighted norm of  $\square$

$\tilde{\square}$  expected value

$\hat{\square}$  versor

$\dot{\square}$  time derivative

$f(\square)$  function of  $\square$

$f^{i,\gamma_1 \dots \gamma_p}$  function partials of the component  $i$  with respect to  $\gamma_1 \dots \gamma_p$

$E(\square)$  expected value of  $\square$

$\Delta(\square)$  finite difference

$\frac{\partial f(\square)}{\partial \square}$  partial derivatives

$\delta \square$  variation of  $\square$

$\square^T$  transpose of  $\square$

$\square^{-1}$  inverse of  $\square$

$\square^\diamond$  pseudo inverse of  $\square$

$\times$  cross product

$\cdot$  scalar product

*min* minimisation problem

*max* maximisation problem.

$\det(\square)$  determinant of  $\square$

$\nabla(\square)$  gradient of  $\square$ .

## List of constants

Astronomical Unit distance 1 AU  $r_{AU} = 1.495978707 \times 10^8 \text{ km}$

Universal gravity constant  $G = 6.67259 \times 10^{-20} \text{ km}^3/(\text{kg}\cdot\text{s}^2)$

Radius of the Earth  $R_{Earth} = 6378.16 \text{ km}$

Radius of the Moon  $R_{Moon} = 1738 \text{ km}$

Earth gravitational constant  $\mu_{Earth} = 3.986004461921757 \times 10^5 \text{ km}^3/\text{s}^2$

Sun gravitational constant  $\mu_{Sun} = 1.3272448769 \times 10^{11} \text{ km}^3/\text{s}^2$



Moon gravitational constant  $\mu_{Moon} = 4.9027801374 \times 10^3 \text{ km}^3/\text{s}^2$

Sun gravitational constant  $\mu_{Sun} = 1.327244876900 \times 10^{11} \text{ km}^3/\text{s}^2$

Speed of light  $c = 299792.458 \text{ km/s}$

Solar flux at 1 AU  $P_{1AU}$  is  $1367 \text{ W}$

Solar Radiation Pressure at 1 AU  $S_{srp} = 4.55982118136 \times 10^{-6} \text{ m/s}^2$ .

### **List of acronyms**

**AU** Astronomical Unit

**CoM** Centre of Mass

**CPU** Central Processing Unit

**DDOR** Delta Differential One-way Ranging

**KF** Kalman Filter

**EKF** Extended Kalman Filter

**ECI** Earth Centred Inertial

**ECEF** Earth Centred Equatorial Frame

**EnKF** Ensemble Kalman Filter

**ESA** European Space Agency

**ESMO** European Student Moon Orbiter

**FOV** Field of view

**GTO** Geostationary Transfer Orbit

**HAEKF** High order semi-Analytical Extended Kalman Filter

**IS** Importance Sampling

**JAXA** Japan Aerospace Exploration Agency

**JD** Julian Date

**LPO** Lagrangian Point Orbit

**LRF** Laser Range Finder

**MC** Monte Carlo

**MCS** Monte Carlo Sampling

**MJD2000** Modified Julian Day since 2000 (counted since 1st of January 2000 at 12:00 pm)

**MOID** Minimum Orbit Intersection Distance

**NASA** National Aeronautics and Space Administration

**NEA** Near Earth Asteroid

**NEO** Near Earth Object

**PHA** Potentially Hazardous Asteroid

**PCE** Polynomial Chaos Expansion

**RMSE** Root Mean Square Error

**SC** spacecraft

**SRP** Solar Radiation Pressure

**SEZ** South East Zenith

**STM** State Transition Matrix

**STTs** State Transition Tensors

**UKF** Unscented Kalman Filter

**UT** Unscented Transformation

**TCM** Trajectory Correction Manoeuvre

**TLI** Trans-Lunar Injection

**WSB** Weak Stability Boundary

# 1 Introduction

The motion of a spacecraft far from a massive planetary body or in a highly perturbed environment close to minor bodies cannot be considered Keplerian. For instance Lagrangian Point Orbits (LPOs) within the sphere of influence of the Earth exploit the effects of the Sun and the Moon, and small perturbation can lead the spacecraft to leave its position. LPOs are often selected for astrophysics and solar terrestrial missions. As current and future missions are planned to be placed on these orbits, it is a critical aspect to clear these regions at the end of operations to avoid damages to other spacecraft. Nonetheless the disposal conditions are uncertain and an efficient disposal strategy must take into account this aspect. Also the motion at minor celestial bodies, whose rotating gravity field is strongly inhomogeneous, can be quite complicated. Missions to minor celestial objects, mostly asteroids and comets, either for asteroid hazard mitigation or science exploration in particular to study the origin of the solar system and the life on Earth, require one or more spacecraft to operate relatively close to the surface where the effects are magnified. Imprecise knowledge of the spacecraft trajectory can lead to impart incorrect orbit maintenance and, as a consequence, to impact on the asteroid's surface.

For these reasons this thesis will develop methodologies for uncertainty propagation of spacecraft orbit disposal and the application to the orbit determination to allow a spacecraft formation to navigate about an asteroid, and methods for a single spacecraft to estimate required information while deflecting a small asteroid and controlling its rotational state. For our analysis, we will mainly consider methods to estimate the spacecraft trajectory in real time using onboard instruments, but we will test some cases in the four body problem with measurements coming from ground tracking.

In this chapter we will introduce the motivations and objectives of the study. We will contextualize the need for disposal analysis and describe Monte Carlo methods for uncertainty propagation of the initial orbit dispersion. Then we will give an updated summary of missions to minor celestial bodies. In this context, we will focus on the degree of autonomy, the presence of ground support and difficulties of proximal phase's operations. We will also present a small overview of asteroid's threat mitigation methods.

Eventually, a summary of the methodologies developed and implemented in this thesis is provided.

## **1.1 Research Motivation and Objectives**

The aim of this research is to investigate methodologies for uncertainty propagation and optimal state estimation for complex nonlinear problems in space flight mechanics. In particular two interesting problems targeted in this thesis are the motion of a spacecraft in the sphere of influence of the Earth and the motion of spacecraft in the proximity of asteroids.

In the first case, the trajectory disposal and transfer to the Moon in the perturbed four body problem are highly unstable and affected by the infinitesimal variation of the initial conditions. In turn the highly nonlinear dynamics can lead to huge deviations at the end of the transfer and to large errors in the estimation of its state if its propagation is not tackled properly.

In the second case, missions to minor celestial objects comprise a wide variety of purposes and can be carried out with different technologies and approaches. There are two kinds of missions which are currently envisaged. The first one regards the scientific exploration of minor celestial objects, the second one foresees the use of a deflection technique to deflect or modify asteroid's trajectory

for hazard mitigation or capture. It is paramount that the two scopes are not mutually exclusive and tend to overlap. In any case, the navigation in close proximity of asteroids can be complicated due to the fact that the environment is uncertain especially if the asteroid presents irregular shape and is rotating. The motion of the spacecraft close to the asteroid is unstable and the perturbations acting on it are sufficient to strip a spacecraft out of its orbit (Hu et al., 2004; Bellei et al., 2009). The common problems, which are required to be addressed, allow studying scientific exploration cases and extending the results to a deflection mission.

Several estimation techniques have been proposed and are currently in use in a variety of applications. Not all these techniques can be used or adapted to this kind of mission, for different criteria, such as flexibility, computational time and accuracy.

Therefore, the first research objective is to consider the uncertainty prediction problem to implement and exploit tools to predict spacecraft trajectory evolution under uncertainty. In order to obtain general analysis, the methods will be tested in the perturbed four body problem (i.e. considering the non-uniform gravity field and the contribution of the solar radiation pressure). The second objective is to identify which estimation techniques are more promising and could be employed for real time operations. For this purpose we considered the navigation of a spacecraft in the chaotic dynamics of a Weak Stability Boundary (WBS) transfer (Belbruno, 1987) and in the proximity motion of the irregular (433) Aphophis asteroid to identify the best solution using available technology. In this respect, we considered a more complicated problem where the best solution is applied to the analysis of a fault-tolerant spacecraft control near Aphophis, because future missions will require cooperation from multiple spacecraft to achieve the mission's goals.

The last objective is to study a methodology to deal with the deflection of an asteroid employing only on-board instruments. Under such kind of mission, the spacecraft needs to control its own trajectory with respect to the asteroid, while applying the deflection strategy. This means that the spacecraft will be subjected to an unknown environment and to the interaction with the asteroid by the deflection, whose effects are not fully predictable. In order to assess the effectiveness and efficiency of the deflection, the complete interaction, through an integrated simulation, has to be modelled. The integrated simulation is required to take into account as many variables as possible to describe the deflection with high fidelity. For instance, the deflection method could need to rely on the knowledge of the asteroid's rotational velocity and attitude. In order to derive these variables, it would be necessary to know the position and velocity of the spacecraft, which depend also on the deflection strategy.

## **1.2 Background**

### **1.2.1 LPO End of Life Disposal Problem**

As explained in Colombo et al. (2014), Libration Point Orbits (LPOs) are often selected for astrophysics and solar terrestrial missions as they offer vantage points for the observation of the Earth, the Sun and the Universe. The neighbourhood of the Lagrangian collinear libration points  $L_1$  and  $L_2$  of the Sun – Earth system has been recognised as a vantage location for astrophysics and solar missions since the end of the 70's, with the NASA ISEE-3 mission (Perozzi and Ferraz-Mello, 2010). Indeed, orbits around  $L_1$  and  $L_2$  are relatively inexpensive to be reached from the Earth and ensure a nearly constant geometry for observation and communication geometry, because the  $L_1$  and  $L_2$  libration orbits always remain close to the Earth at a distance of roughly 1.5 million km.

Moreover,  $L_2$  is situated on the Sun – Earth line beyond the Earth and thus it is suitable for highly precise telescopes requiring great thermal stability. Also, since the Sun, the Earth and the Moon are always behind the spacecraft,  $L_2$  LPO ensures a constant geometry for observation with half of the entire celestial sphere available at all times. Therefore, long periods of uninterrupted scientific observation are possible with nearly no background noise from radiations (Eismont et al., 2003).

No guidelines currently exist for LPO missions' end-of-life; however, as current and future missions are planned to be placed on these orbits, it is a critical aspect to clear these regions at the end of operations (Armellin et al., 2014). In fact, orbits about the Libration points lie in a highly perturbed environment due to the chaotic behaviour of the multi-body dynamics (Canalias et al., 2004); moreover, due to their challenging mission requirements, they are characterised by large-size spacecraft. Therefore, the uncontrolled spacecraft on manifold trajectories could re-enter to Earth or cross the low Earth orbit and geostationary Earth orbit protected regions. Finally, the end-of-life phase can enhance the science return of the mission and the operational knowledge base.

The chaotic nature of the interaction between the spacecraft and the surrounding environment during orbital transfers and the low confidence level in key spacecraft components (such as propulsion and attitude control) imposes expensive and time consuming ground support campaign to ascertain whether the spacecraft will follow the designed trajectory. In the case of disposal manoeuvres this is undesired also considering that this could be the last manoeuvre available. For this reason the disposal option must be tested in order to assure high disposal rates and possibly inform the mission planning that a mid-course correction manoeuvre could be required.



### 1.2.2 Uncertainty Propagation

For the disposal problem, orbit uncertainty quantification and propagation play a major role (Vetrisano and Vasile, 2016). For nonlinear orbital dynamics, it is not possible to make simplifying assumptions on the orbit evolution because the probability distribution may not remain Gaussian, in particular during long disposal periods. In this work we investigate the use of different methods applied to the propagation of the uncertainty with respect to the knowledge of the initial spacecraft position and velocity prior at the disposal manoeuvre. In particular this work focuses on a new application of Polynomial Chaos (PC) methods (Ghanem and Spanos, 1991; Ghanem and Dham, 1998; Xiu and Karniadakis, 2002; Le Matre et al., 2004; Ghanem and Doostan, 2006) for the quantification of disposal rate success from LPO to the Moon.

The objective of the uncertainty analysis on the initial conditions is to predict the evolution of the disposal orbit under system performance and environmental perturbations, as well as to allocate possible correction manoeuvres. Extensive efforts have been devoted to the development of accurate numerical algorithms so that simulation predictions are reliable in the sense that numerical errors are well under control and understood. In 2006, Park and Scheeres derived analytical expressions of a nonlinear trajectory solution using a higher order Taylor series approach and applied the results to spacecraft orbit determination by integrating the so called State Transition Tensors (STTs). The STTs map analytically the local nonlinear motion of the spacecraft at the current epoch to the initial deviated conditions from the nominal trajectory. The main characteristic and advantage of using the higher order STTs reside in that they can be used to propagate many samples and the covariance matrix using only algebraic formulas. The problem with this approach

is that the number of equations to be solved to have a representation of the solutions around the nominal trajectory grows dramatically with the order of the representation and therefore simplification could be required to treat the equations analytically.

One of the most commonly used methods is Monte Carlo Sampling (MCS). In MCS, one generates independent realizations of random inputs based on their prescribed probability distribution. For each realization the data is fixed and the problem becomes deterministic. Upon solving the deterministic realisations of the problem, one collects an ensemble of solutions, i.e. realisations of the random solutions. From this ensemble, statistical information can be extracted, e.g. expected mean value, variance, etc. Although MCS is straightforward to apply as it only requires repetitive executions of deterministic simulations, typically a large number of executions are needed, for the solution statistics converge relatively slowly.

A PC expansion, or PCE, provides a means for approximating the solution to a large set of stochastic ordinary differential equations. PCE have been applied to a number of fields, among them nuclear reactor design (Gilli et al., 2012), structural mechanics (Shi and Ghanem, 2004; Ghanem and Doostan, 2006), fluid dynamics (Knio and Le Maître, 2006; Hosder et al., 2006; Najm 2009), estimation (Blanchard et al., 2010) etc. For some applications in statistics see Evans and Swartz (1992). In the space field the method was used in Jones and Alireza (2013) to estimate the collision probability for two satellites, while it was applied to the 2-body uncertainty propagation problem in Cheng et al. (2011).

The PCE approach of computing disposal probability requires no fundamental simplifying assumptions, and reduces the computation time compared to Monte Carlo sampling. The attractive

attributes of this method are its strong mathematical rigor and ability to produce functional representations of any stochastic quantities (Eldred et al., 2011).

One method to reconstruct a PCE is the stochastic Galerkin approach, which seeks to directly construct an approximation for the unknown stochastic solution based on complete orthogonal polynomials (Ghanem and Spanos, 1991). The stochastic Galerkin method exploits an assumption of smoothness of the stochastic solution in the random domain and returns high accuracy and faster convergence rate. Nonetheless, as the number of uncertain parameters of the problem increases, the efficiency of the problem results affected because the number of polynomial bases needed to obtain accurate reconstructions increases dramatically.

For this purpose, the alternative method of stochastic collocation has been studied by Xiu and Hesthaven (2005), Babuska et al. (2007) and Ganapathysubramanian and Zabarar (2007). The idea beneath the stochastic collocation approach is to approximate the unknown stochastic response by a polynomial interpolation function in the multi-dimensional random domain. The interpolant is constructed by samples taken from the deterministic problem at a pre-determined set of nodes. This approach offers high accuracy as the stochastic Galerkin method as well as easy implementation as the sampling-based methods.

The computational effort required for the collocation approach is directly proportional to the number of support nodes used for reconstructing the response function. As a result, the key issue for this approach represented by the selection of the support nodes, such that using the minimal number of nodes to achieve good approximations. One such possible choice for constructing the multi-dimensional interpolation is to use tensor product of appropriate one-dimensional interpolation

functions. Babuska et al. (2007) proposed a methodology which employs a collocation scheme based on tensor product of one-dimensional interpolation functions using Gauss quadrature nodes. Although, the tensor product approach can easily extend the one-dimensional interpolation formula to the multi-dimensional case, it suffers from the curse of dimensionality, as also in this case the number of realizations required constructing the PCE response increases exponentially with the number of random dimensions. As proposed in Xiu and Hesthaven (2005), a more attractive choice, is based on sparse grids generated using the Smolyak algorithm (Smolyak, 1963). Smolyak's construction, often called sparse grid, provides a general tool for constructing efficient algorithms able to solve multivariate problems with orders of magnitude reduction in the number of support nodes while giving the same level of approximation as the usual tensor product. In this framework, the work of Genz and Keister (1996) introduced fully symmetric interpolatory integration rules for Smolyak sparse grid of Gauss-Hermite nodes.

In this thesis we will exploit the sparse-grids of Genz and Keister (1996), because they proved to be accurate and efficient at lower number of support nodes. Moreover these grids are suited for employing the orthogonality properties of Hermite polynomials, reducing the complexity of the integrations required to calculate PCE interpolants. In this way the PCE can conveniently generate the complete probabilistic distribution (e.g. probability density function PDF) of the output response at a certain instant of time. Consequently, the lower order statistic moments, such as mean and standard deviation as well as the impact rate in this case, can be derived directly from the approximated PDF.

### 1.2.3 Near Earth Objects Problem

Near Earth Objects (NEO), the majority of which are asteroids, are defined as any minor celestial object with a perihelion less than 1.3 AU and an aphelion greater than 0.983 AU. A subclass of these, deemed Potentially Hazardous Asteroids (PHA), are defined as those with a Minimum Orbital Intersection Distance (MOID) from the Earth's orbit less than or equal to 0.05 AU and a diameter larger than 150 m. As of 28th of April 2016, 14331 NEOs have been detected; of those, about 3600 have a diameter between 0.3 and 1 km, and 1690 are listed as PHA<sup>1</sup>. Impacts from asteroids of about 1 km or more in diameter are considered to be capable of causing global climate change and the destruction of ozone, with a land destruction area equivalent to a large state or country. Those with an average diameter of 100 m can cause significant tsunamis and/or the land destruction of a large city. It is estimated that there are between 30000–300000 NEOs with diameters around 100 m, meaning a large number of NEOs are still undetected. NEOs have been generating a growing scientific interest because, as primordial remnants of our solar system, they preserve precious information on its formation, composition and evolution. Besides, their collision with the early Earth would have influenced the shape and composition of our planet. Some NEOs are especially attractive targets for low-cost missions, because of their orbital accessibility with current technologies. This easy accessibility suggests the possibility to use them as source of raw materials and for the settlement of future human outposts (Seboldt et al., 2000). Nevertheless, NEO collision with the Earth represents a possible threat to mankind. In particular, small size asteroids

---

<sup>1</sup> [http:// neo.jpl.nasa.gov/stats](http://neo.jpl.nasa.gov/stats)

pose a concrete threat on the short term, with significant expected damages at regional level. Advances in orbit determination and theoretical studies on hazard characterisation have increased the capability of predicting potential impacts (Chapman et al., 1994). In April 2013, the American administration approved the NASA budget for 2014, and it included \$ 105 million for the first year of funding for a mission to retrieve a small asteroid of roughly 7 to 10 meters diameter, using propulsion, to move it into a high Earth orbit, possibly a high lunar orbit. The origin of this mission was a study by the private Keck Institute titled ‘Asteroid Retrieval Feasibility Study’ which was published in April 2012.

One of the main goals of this thesis is to study navigation techniques applied to the deflection of an asteroid's orbit, in case we detect one headed on a collision course with Earth (Vetrisano et al., 2014). The manipulation of asteroids, in fact, still remains an open problem. Increasing our capabilities in asteroid orbit and attitude manipulation is therefore required, both for protection of collision hazard and for future asteroid exploitation.

In the last three decades a number of probes have explored asteroids and comets, relying on a strong support from ground. Such an approach is advantageous when the communication time is reduced and allows performing computationally expensive planning which could not be done with the current on-board computers. In practice it means that the spacecraft needs to be visible during critical phases, limiting the tasks the mission could accomplish. On the contrary when distances or visibility constraints do not permit to heavily rely on ground support, the spacecraft necessarily has to use its own on-board system to pursue mission's goals and navigation. On-board systems allow increasing scientific returns but are intrinsically less reliable because of the sensors failures that could occur when intervention from ground is not possible.

#### 1.2.4 Missions to Minor Celestial Objects

A number of missions have flown to asteroids and comets. Some of them encountered asteroids on their way to outer planets, but they can reasonably be deemed among this small group. The following list contains a brief description of the most relevant missions, relatively to this study:

- The Halley Armada, as the probes which visited the Halley's comets in 1986, was composed of the Soviet Vega 1 and Vega 2, the Japanese probes Suisei and Sakigake, the NASA Explorer the ESA Giotto. The Japanese and American spacecraft are less interesting because they approached or observed the comet from noticeable distance; the one which flew the closest was Suisei at 151,000 km. Vega 1 and Vega 2 were directed towards the comet after performing a fly-by of Venus and having released their respective descent module to the atmosphere of that planet. These spacecraft made their closest encounter with the comet at 8,890 and 8,080 km respectively on the 4<sup>th</sup> and 6<sup>th</sup> March 1986. The information collected from the on-board cameras was used to help pinpoint Giotto's close fly-by of the comet. Because of the dust, Vega 1 was affected by 80% power loss, while the available power was reduced to 40% on Vega 2. The objectives of the mission were to obtain the first images of a nucleus of a comet and study the composition of the volatile components. Giotto was the first spacecraft to make close up observations of the comet at 596 km on March 13 and returned both images and scientific data back to Earth, surprisingly surviving despite being hit by some small particles. One impact sent it spinning off its stabilized spin axis so that its antenna no longer always pointed at the Earth, and importantly, its dust shield no longer protected its instruments.

Nonetheless Giotto was able to re-stabilize itself and continued gathering science data. After a hibernation period, the spacecraft was retargeted for a flyby with the comet 26P Grigg-Skjellerup on July 10, 1992, which it approached to a distance of about 200 km.

- Deep Impact was launched to the comet 9P Tempel 1 on the 12<sup>th</sup> January 2005. The main goal of the mission was to hit the comet with an impactor spacecraft and to observe the nucleus during the impact, collecting images and performing analysis of the internal structure. The spacecraft reached out the comet on July 4, 2005 and released the impactor. Using spacecraft optical observations of the comet and conventional ground-based navigation techniques, the joined spacecraft were manoeuvred at 880,000 km to a collision trajectory with the nucleus of Tempel 1, and the impactor was released 24 h before impact. Then the flyby spacecraft was manoeuvred to a path with a closest approach of 500 km from the comet where it could observe the impact.
- Deep Space 1 was the first to test new technologies like a new propulsion system (ion drive) and an autonomous navigation through the interplanetary space. The spacecraft made a flyby with the asteroid (9969) Braille on July 28, 1999. Deep Space 1 was intended to perform the flyby at 56,000 km/h at only 240 m from the asteroid. Due to technical difficulties, including a software crash shortly before approach, the craft instead passed Braille at a distance of 26 km. Then the spacecraft made a close encounter with the periodic comet 19P/Borrelly on September 22, 2001 capturing many images of its nucleus from a distance of about 2.200 km. The spacecraft carried an experiment for artificial intelligence system being given primary command of a spacecraft. Known as Remote Agent, the software ran on the on-board computer of Deep Space 1, more than



96,500,000 km from Earth. The tests were a step toward robotic explorers that are less costly and more independent from ground control.<sup>2</sup>

- Galileo had as scientific objectives Jupiter and its moons, but on its way it came within 1,600 km of the 6.1 km asteroid 951 Gaspra on October 29, 1991. On August 28, 1993 the spacecraft had a second encounter with the 32 km asteroid 243 Ida at a distance of 2,400 km and discovered for the first time the presence of a satellite orbiting around it, called Dactyl. Both the asteroids are in the main belt.
- NEAR Shoemaker was the first probe orbiting around a NEA, the 17 km (433) Eros down to 35 km altitude. The spacecraft, during its voyage to Eros, made a flyby of a 61 km main belt asteroid (253) Mathilde on June 27, 1997 from a distance of 2,400 km. After a first attempt of an orbital insertion failed owing to a problem at the propulsion system, finally on February 14, 2000 NEAR Shoemaker entered in orbit around Eros and began to map its surface. The mission was concluded on February 12, 2001. Before exhausting the fuel supply, the spacecraft attempted a controlled descent on (433) Eros (not really a landing because it was not provided of legs for this purpose). In this way NEAR Shoemaker became also the first probe to land on an asteroid.
- MUSES-C Hayabusa was the first spacecraft designed to deliberately land on an asteroid and then take off. Hayabusa was not designed to land but only to touch down the surface with its sample capturing device. However, it was the first craft designed from the outset to make physical contact with the surface of an asteroid. The scientific objective of

---

<sup>2</sup> <http://ti.arc.nasa.gov/tech/asr/planning-and-scheduling/remote-agent/>

MUSES-C was the analysis of the surface of a Near Earth Asteroid and returning a sample to the Earth. The target of the mission was the asteroid (25143) Itokawa. The spacecraft arrived in the middle of September 2005, orbiting for about five months around Itokawa. Hayabusa surveyed the asteroid surface from a distance of about 20 km. After this the spacecraft moved closer to the surface at 70 m, and then approached the asteroid for a series of soft landings and for the collection of samples at a safe site. Autonomous optical navigation was employed extensively during this period because the long communication delay prohibited Earth-based real-time commanding. Artificial target markers were released in order to cancel the surface relative velocity during descent. While flying in deep space, the spacecraft suffered from many hardware failures (i.e. ion thrusters and reaction wheels), which would have compromised the mission without the intervention and support from ground.

- Stardust was the first spacecraft directed to a comet after the mission Giotto in 1986. It was launched in the year 1999 and made a close encounter with the 5 km radius periodic comet 81P Wild 2 in January 2004. The original encounter distance was planned to be 150 km, but this was changed to minimize the risk of catastrophic dust collisions. Stardust flew within 240 km of the comet 81P Wild 2, catching samples of comet particles and scoring detailed pictures of the nucleus. The capsule carrying cometary particles (the first sample return mission for this kind of missions) successfully touched down on January 15, 2006 at the U.S. Air Force Utah Test and Training Range. On November 2, 2002 the spacecraft passed within about 3,079 km of the asteroid (5535) Annefrank and images of it were taken on January 2, 2004. After the completion of this mission, NASA planned to

revisit Tempel 1 on February 14, 2011 to finish the investigation begun in 2005 when the Deep Impact mission blasted a crater into the comet. In January 2009 Stardust-NExT (New Exploration of Tempel 1 as the extension of the mission was called) used the Earth's gravity to change trajectory and increase speed. Stardust-NExT encountered Tempel 1 at about at the same point in the comet's orbit a couple of weeks after the comet's perihelion. The spacecraft made its closest approach to the comet at a distance of approximately 178 km.

- Rosetta was a robotic spacecraft built and launched by the European Space Agency to perform a detailed study of the 4 km comet 67P/Churyumov–Gerasimenko. The spacecraft was launched in 2004, and performed two successful asteroid flyby missions on its way to the comet. The craft completed its fly-by of asteroid 2867 Šteins at 800 km distance in September 2008 and of 21 Lutetia at 3162 km in July 2010. The spacecraft rendez-voused with the comet 67P/Churyumov–Gerasimenko in August 2014 and was able to release the lander Philae which landed on the comet surface after touching down three times.

Among this numerous family of spacecraft, only few flew or orbited around a minor celestial object. Only the mission MUSES-C performed proximity operations at distances below 1 km for an extended period of 5 months. The probe Philae did not land on the predicted spot due to a combination of technical and environmental factors (Garnier et al., 2015).

From these examples one can see that the risk of failures of one sensor or the whole spacecraft is quite high for different reasons. The presence of dust and particles is the first cause of failure, and

then the missions could require the instruments to work continuously or to face a long period in hibernation before starting operations.

What complicates proximity operations the most is that the shape of the asteroid and its rotational motion can be quite unknown before acquiring final orbit. Moreover the perturbations acting on the spacecraft, mainly the rotating non-uniform gravity field and solar radiation pressure can drive the spacecraft out of its orbit. Generally the gravitational harmonics of the minor celestial bodies are estimated from onboard data collected during a close fly-by (Morley et al., 2009) or during approach phases (Scheeres et al., 2004a) or by ground based radar imaging data (Scheeres et al., 2004b). Then flying and maintaining a spacecraft around or close to the asteroid could be complicated by the fact the knowledge of these figures is affected by uncertainties due to the relatively low information available.

The majority of missions which have flown to minor celestial objects received vital support from ground, either to detect the asteroid or to perform their mission. Determining the relative position and velocity with high accuracy from ground requires the use of the so-called delta differential one-way ranging (DDOR). The DDOR technique is very expensive because it needs the simultaneous use of at least two largely separated ground stations, receiving the signal transmitted from the probe and for calibration from a radio source, e.g. quasar. The main drawback of ground support is that it requires the collection for a long time of big batch of data to be processed through a suitable recursive method, e.g. recursive weighted-least squares.

For instance combining DDOR measurements from ground with images from one single camera, the Hayabusa mission performed a suitable set of dogleg manoeuvres to observe the asteroid from

different phase angles, while refining asteroid trajectory and acquire the object. The dogleg approach required performing small manoeuvres and, as a consequence, the approach lasted more than 1 month, considerably longer than a direct rendezvous with the asteroid. Reducing the time to approach the asteroid is important when responsiveness is critical to start, for instance, a deflection mission.

When real-time operations are required, recursive methods cannot be employed because they would require storing a large amount of data on the onboard memory. For this reason, sequential methods based on the nonlinear Kalman filter (KF) family have been widely used in space since the mission Apollo. Nonetheless, also including the Philae lander on Rosetta, only two cases successfully employed a fully autonomous system to guide the spacecraft. Hayabusa used an Extended Kalman Filter (EKF) to process optical and on-board ranging measurements during the very last phases of the descent and landing onto the asteroid Itokawa. The impactor of Deep Impact used its autonomous navigation software based on the so-called Unscented Kalman Filter (UKF) to guide itself for 24 hours to an impact point in a lighted portion of the nucleus using images. Only Hayabusa, though, proved that methods based on optical navigation camera and laser light radar/laser range finder integrated measurements represent feasible options for a single spacecraft to approach, hover and land on the asteroid (Kubota et al., 2003; Li et al., 2006).

### **1.2.5 NEOs Deflection Strategies**

In the past two decades, different techniques for asteroid manipulation have been studied and compared. The majority of them consider a variation in the asteroid's nominal orbit due to a change in linear momentum. The mitigation strategies can be catalogued depending on their interaction

with the asteroid, as with contact or contactless. For completeness sake, a brief description of the solutions, which foresees a spacecraft to accomplish the mission, is given in the following.

For instance contact solutions comprise:

- kinetic impactors or nuclear interceptors (when deflagrated on the surface of the asteroid), which produce an impulsive change in the linear momentum of the asteroid;
- mass drivers or pogo-stick which produces a multi-impulsive change in the linear momentum of the NEO by ejection of material or by a series of hard landing on the asteroid;
- attached propulsion devices which imparts a low-thrust acceleration continuously modifying the linear momentum.

Contactless solutions comprises all the methods which produce a low-thrust accelerations on the asteroid, e.g. gravity tractor, ion-beam-shepherd and surface ablation by a light source.

The gravity tractor consists of a spacecraft hovering above the asteroid; the gravitational attraction between the two bodies is exploited to pull the asteroid and move it. The ion-beam shepherd directs a beam of quasi-neutral plasma impinging against the asteroid's surface to create a small force on it (Bombardelli et al., 2011). The ablation method is achieved by irradiating the asteroid with a light source. This can be either collected and focused solar radiation or a laser light source (Vasile and Maddock, 2012). Within the illuminated focal point, the absorbed energy increases the temperature of the asteroid, enabling it to sublimate. The ablated material then expands to form an ejecta plume. The resulting thrust induced by the ejecta plume pushes the asteroid away from its original trajectory.

Unlike contact solutions, contactless solutions have the advantage of not being affected by the uncertainties on the asteroid surface and composition, because they do not need physical contact with the NEO.

Amongst the many possibilities to deflect NEOs, Sanchez et al. (2009) demonstrated that surface ablation is one of the most promising methods for asteroid deflection. Moreover, in a study supported by the European Space Agency (ESA), the ion-beam-shepherd and the ablation concepts were also considered appealing for a technology demonstrator intended to deflect a small rocky asteroid (Vasile et al., 2013).

### **1.3 Methodologies Developed and Implemented**

The present research focuses on the uncertainty propagation for the four body problem and optimal estimation techniques mainly applied to the proximal motion of an asteroid for both scientific and hazard mitigation purposes.

The first scope of this research is to investigate valid techniques alternative to full Monte Carlo simulations which allows predicting the evolution of uncertainty region in the case of disposal trajectory impacting on the Moon.

The second scope is to identify these methods which allow performing fast and reliable on-board estimation. Nonetheless, part of the work is also applied to particular cases of deep space navigation, during flight along the so called Weak Stability Boundaries regions, in which ground estimate are the only state of the art available solution. This case permits us to briefly explore the design of the manoeuvre under uncertainty. Given the fact that the motion along these regions is

highly nonlinear and chaotic one can derive precious information, and then use the outcomes for the asteroid case.

The results are applied to the case of a single spacecraft performing formation flying with a relatively big asteroid. The motion in formation with the asteroid requires, then, to implement also a suitable navigation strategy to prevent the spacecraft from colliding onto the asteroid. The concept is extended to the investigation of the state estimation technique to data fuse the measurements coming from multiple heterogeneous sensors mounted on a disaggregated spacecraft flying in formation with a minor body. Each satellite employs and processes the measurements coming from its own on board measurements combined with the information available from the other members of the formation. Various sets of sensors are mounted on different satellites in the formation. It is shown that the decentralised processing allows the formation to be single point failure tolerant, since the failure of one spacecraft marginally affects spacecraft operations. When failure on a single spacecraft occurs, other members of the formation can supply for the necessary information which still allows the spacecraft to determine its orbit. A particular strategy applicable to a number of spacecraft is developed and results are applied to a four spacecraft formation. The use of a disaggregated spacecraft, or swarm, endows each of the members of the formation with a higher degree of autonomy allowing for accurate autonomous orbit determination with limited intervention from ground. This capability goes into the direction of reducing mission management costs and increasing real time operations which allows extending mission objectives.

Since the actual asteroid trajectory could be uncertain prior to the beginning of the operations, we propose to employ on-board optical observations from the formation flying towards the asteroid along with ground station tracking to improve the asteroid's trajectory estimate prior to starting the



orbit acquisition. On board optical measurements from navigation cameras have been widely used in recent years during deep space navigation and approach (Konimoto et al., 2006). For instance, as mentioned previously, relying only on one single camera, the Hayabusa mission performed a suitable set of dogleg manoeuvres to observe the asteroid from different phase angles, refine asteroid trajectory and acquire the object. As a consequence of repetitive small manoeuvres and subsequent ground observations, this kind of approach lasts longer than a direct rendezvous at the asteroid.

The final scope is to apply the identified estimate solution to the case of the deflection and manipulation of a small asteroid using laser ablation for a technology demonstration, considering one single spacecraft. During the deflection, the proximity motion of the spacecraft is coupled with the orbital and rotational motion of the asteroid. In fact, a change in the angular velocity of the asteroid induces a variation of the sublimation rate that, in turn, affects both the orbital and rotational motion of the asteroid. At the same time a change in the sublimation rate, orbital and rotational motion affects the proximity motion of the spacecraft as it changes the perturbations due to the impingement with the plume of gas, the gravity of the asteroid and the relative acceleration between asteroid and spacecraft. Given that the spot size of the laser beam needs to be kept below an acceptable limit to guarantee constant sublimation, the spacecraft needs to manoeuvre to maintain its relative distance under the effect of perturbations that are a function of the sublimation process. Kahle et al. (2005) and Colombo et al. (2006) showed that the lower is the angular velocity of the asteroid the higher is the imparted deflection acceleration. In this way the simultaneous control of both the spacecraft relative position and the asteroid angular velocity is strongly needed. The rotational motion of the asteroid is then controlled by off-setting the thrust vector, induced by

the laser, with respect to the centre of mass. The spacecraft proximity motion and the instantaneous rotational velocity of the asteroid are estimated through two filters: an augmented Unscented Kalman Filter to determine the spacecraft trajectory from optical and laser ranging measurements, and a batch filter which processes optical flow measurements from the camera to reconstruct the rotational velocity of the asteroid.

## **1.4 Dissertation Organisation**

This dissertation is divided into 6 chapters, which introduce different aspects of the research on the optimal estimation techniques and uncertainty analysis. In general, the first part of each chapter explains the theoretical development and the method adopted, subsequently some results are presented as the application of the theory. The thesis is organised as follows.

Chapter 2 explains the different and commonly used techniques which can be used for orbit uncertainty propagation. These are applied to the case of the disposal of a spacecraft towards an impacting trajectory with the Moon. In particular it proposes the use of polynomial chaos expansion to perform fast and accurate Monte Carlo simulations.

Chapter 0 introduces the reader to the state of the art estimation techniques. The different formulations are tested in different environments to draw necessary information and select the most suitable filter to be employed in the next chapters. In particular we tested part of these techniques in the four body problem for the case of the European Student Moon Orbiter (ESMO) and in the case of close proximity operations around the asteroid (433) Apophis.

Chapter 4 presents the application of the identified most suitable estimation technique to the case of a single spacecraft and a formation in the proximity of the asteroid Aphophis. In Section 4.6 we exploit the concept of the formation to propose an asteroid's trajectory refinement without the use of dogleg manoeuvre.

Chapter 5 presents an approach to control the rotational motion of an asteroid while a spacecraft is deflecting its trajectory through laser ablation.

Finally Chapter 6 summarises the finding of this research and gives an insight into possible further developments of this study that will be subject of future work.

## **1.5 Contributions**

The contents of this dissertation have been published or are being published in five stand-alone but highly related journal papers where I am the first author. I also contributed with my work to other three journal papers.

The analyses and comparisons for the propagation of trajectory uncertainties were used to assess the disposal strategy for the spacecraft Herschel in the ESA/GSP study "End-Of-Life Disposal Concepts for Lagrange-Point and Highly Elliptical Orbit Missions" during 2013 and 2014. The rigorous comparison has been submitted for revision to *Advances in Space Research*.

The outcomes of the different navigation strategies applied to the deep space navigation of the European Student Moon Orbiter are comprised in three different papers published in 2012. The journals were *Acta Astronautica*, *Celestial Mechanics and Dynamical Astronomy* and the *Journal of Astrodynamics*.

The results on the comparative assessment of different navigation strategies for the spacecraft formation were presented at the 63<sup>rd</sup> International Astronautical Congress, Naples, Italy, 2012. A more exhaustive version of this study was published on the journal of Advances in Space Research.

Finally the algorithm which simulates the integrated spacecraft navigation and asteroid manipulation was presented at The Sixth International Meeting on Celestial Mechanics in Viterbo, Italy in September 2013. This study was published on the journal Celestial Mechanics and Dynamical Astronomy.

External Presentation:

- 1 Vetrisano, M and Vasile, M.: Navigation to the Moon along Low-Energy Transfers: the Case of the European Student Moon Orbiter. New Trends in Astrodynamics and Application VI, New York, June 2011.
- 2 Vetrisano, M: Flight Dynamics - Preliminary Design Review of ESMO, ESTEC, Noordwijk, The Netherlands, May 2011.
- 3 Vetrisano, M.: 'Integrated Flight Dynamics and Contingency Analyses for the European Student Moon Orbiter. Presented at the International Student Board zone, 63<sup>rd</sup> International Astronautical Congress, Naples, Italy. October 2012.
- 4 Vetrisano, M.: Light-Touch2 - Navigation strategy, ASTRIUM, Stevenage, UK. November 2012.
- 5 Vetrisano, M.: Final Design Review of Light-Touch2 - Navigation strategy, ESTEC, Noordwijk, The Netherlands, January 2013.

- 6 Vetrisano, M., Colombo, C., Vasile, M.: Proximity autonomous GNC for asteroid's attitude control and deflection using laser ablation. The Sixth International Meeting on Celestial Mechanics. San Martino al Cimino, Viterbo, Italy, 1-7 September 2013.

Reports:

- 1 Van der Weeg, W., Vetrisano, M.: ESMO Mission Analysis & Flight Dynamics Preliminary Design Review Report, Glasgow, University of Strathclyde, 2011.
- 2 Van der Weeg, W., Vetrisano, M.: ESMO MIAS Design and Developments Programme, Glasgow, University of Strathclyde, 2011.
- 3 Vasile, M., Gibbings, A., Vetrisano, M., Garcia Yarnoz, D., Sanchez Cuartielles, J.P., Burns, D., Hopkins, J.M., Colombo, C., Branco, J., Wayman, A., Eckersley, S.: Light Touch2, Effective Solutions to Asteroid Manipulation, February 2013.
- 4 Colombo, C., Letizia, F., Soldini, S., Vasile, M., Vetrisano, M., van der Weg, W., Alessi, E. M., Rossi A.: End-Of-Life Disposal Concepts for Lagrange-Point and Highly Elliptical Orbit Missions. Final Report, 2013, ESA/ESOC contract No. 4000107624/13/F/MOS.

Conference Papers:

- 1 Vetrisano, M., Vasile, M.: 'Navigation Strategies and Contingency Analysis for the European Student Moon Orbiter'. 62<sup>nd</sup> International Astronautical Congress, Cape Town, SA. October 2011.
- 2 Van der Weeg, W., Vetrisano, M., Prioroc, C.L., Stefanescu, M.R., Beghella Bartoli, S.: 'Advance Transfer Options and Integrated Flight Dynamics Analyses for the European Student Moon Orbiter'. 63<sup>rd</sup> International Astronautical Congress, Naples, Italy. October 2012.

- 3 Vetrisano, M., Vasile, M.: ‘Collaborative Guidance Navigation and Control of Disaggregated Spacecraft in the Proximity of Minor Celestial Bodies’. 63rd International Astronautical Congress, Naples, Italy. October 2012.
- 4 Vetrisano, M., Yang, H., Vasile, M. and Zhang, W.: ‘Autonomous Navigation of Spacecraft Formations for Asteroid Exploration’. 23rd Symposium on Space Flight Dynamics, Pasadena, CA, USA. November 2012.
- 5 Vasile, M., Gibbings, A., Vetrisano, M., Garcia Yarnoz, D., Sanchez Cuartielles, J.P., McInnes, C., Burns, D., Hopkins, J.M., Colombo, C., Joao Branco, Wayman, A. , Eckersley, S.: ‘Light-Touch2: A Laser-Based Solution for the Deflection, Manipulation and Exploitation of Small Asteroids’. Planetary Defense Conference 2013, Flagstaff, USA.
- 6 Vetrisano, M., Colombo, C. Vasile, M., 2013: ‘Autonomous GNC for asteroid’s deflection and attitude control via laser ablation’. 64th International Astronautical Congress, Beijing, China. October 2013.
- 7 Vetrisano, M., Branco, J., Garcia-Yarnoz, D., 2013: ‘Effective approach navigation prior to small body deflection’. The Sixth Space Generation Congress (SGC) 2013, 64th International Astronautical Congress, Beijing, China. September-October 2013.
- 8 Colombo C., Lewis H., Letizia F., Soldini S., Gössnitzer L., Alessi E. M., Rossi A., Dimare L., Vasile M., Vetrisano M., van der Weg W., McInnes C., Macdonald M., Landgraf M.: ‘End-of-life disposal trajectories for libration point and highly elliptical orbit missions’. The 64th International Astronautical Congress, 2013, Beijing, China, IAC-13.A6.P.24.

#### Journal Articles

- 1 Zuiani, F., Gibbings, A., Vetrivano, M., Rizzi, F., Martinez, C., Vasile, M.: 'Orbit Determination and Control for the European Student Moon Orbiter'. *Acta Astronautica*, Elsevier, 2012, doi:10.1016/j.actaastro.2012.03.031
- 2 Vetrivano, M., Vasile, M.: Navigating to the Moon along low-energy transfers: 'The case of the European Student Moon Orbiter'. *Celestial Mechanics and Dynamical Astronomy*, Springer 2012. DOI 10.1007/s10569-012-9436-9
- 3 Vetrivano, M., Van der Weg, W., Vasile, M.: 'Navigation Strategy for a Low-Cost Micro Satellite to the Moon'. *Journal of Astrodynamics* Vol.2 No.1, Mar. 2012.
- 4 Yang, H. X., Vetrivano, M. and Vasile, M., Zhang, W.: 'Autonomous navigation of spacecraft formation in the proximity of minor bodies'. *Proceedings of the Institution of Mechanical Engineers Part G Journal of Aerospace Engineering* 06/2015; DOI:10.1177/0954410015590465
- 5 Vetrivano, M. and Vasile, M.: 'Autonomous navigation of a spacecraft formation in the proximity of an asteroid'. *Advances in Space Research*. Volume 56, Issue 8, Pages 1547-1804 (15 October 2015). doi:10.1016/j.asr.2015.07.024
- 6 Vetrivano, M., Colombo, C., Vasile, M.: 'Asteroid rotation and orbit control via laser ablation'. *Advances in Space Research*. Volume 56, Issue 8, Pages 1547-1804 (15 October 2015). doi:10.1016/j.asr.2015.06.035
- 7 Colombo, C., Alessi, E.M., van der Weg, W., Soldini, S., Letizia, F., Vetrivano, M., Vasile, M., Rossi, A. and Landgraf, M.: 'End-of-life disposal concepts for Libration point orbit and highly elliptical orbit missions'. *Acta Astronautica*, Volume 110, May–June 2015, Pages 298–312. doi:10.1016/j.actaastro.2014.11.002

- 8 Vetrivano, M., Vasile, M.: 'Analysis of Spacecraft Disposal Solutions from LPO to the Moon with High Order Polynomial Expansions'. *Advances in Space Research*, April 2017.  
<https://doi.org/10.1016/j.asr.2017.04.005>



## 2 Uncertainty Propagation

In this Chapter we consider different techniques that can be applied to the analysis and study of the evolution of trajectory uncertainties. In particular we consider the use of high order State Transition Tensors (STTs), Unscented Transformations (UT) and Polynomial Chaos Expansion (PCE) applied to the analysis of the disposal of a spacecraft from a Libration point in the Earth-Sun system to the Moon under the effects of initial orbit uncertainties. The problem of the perturbed four body problem is particularly interesting because it is highly nonlinear when the orbit approaches the Moon and it allows us to introduce the techniques which will be used in Chapter 0 for the estimation of the orbit evolution.

This Chapter presents the use of PCEs as a non-intrusive approach to propagate uncertainty in dynamical systems. The Chapter will compare the use of PCEs against high order Taylor expansions and the use of standard covariance matrix propagations. It will be shown that the use of the ellipsoid of uncertainty that corresponds to the propagation of the covariance matrix with a first order Taylor expansions is not enough to correctly capture the dispersion of the trajectories that result in a crash on the Moon. Furthermore, it will be shown that the use of low order PCEs outperforms high orders Taylor expansions of similar order and it is competitive against a full scale Monte Carlo sampling.

This Chapter is organised as follows. Section 2.1 describes the disposal trajectory dynamics for Herschel. Then, Section 2.2 presents the methods that were used for uncertainty propagation of the initial disposal conditions. Section 2.3 compares the different techniques and applies the most

suitable one to the study of the impact conditions. In particular in Section 2.3.1 we consider a numerical and topological comparison to select the PCE method. Eventually Section 2.3.2 analyses the impact rate and dispersion shape on the Moon at impact for two different levels of initial uncertain distributions.

## **2.1 Dynamic Equations for Spacecraft Disposal towards the Moon**

We first introduce the perturbed equations of motion for a spacecraft moving in the Earth-Moon system. In fact we are interesting in predicting statistical quantities such as the rate of impact on the Moon for a Lagrangian Point Orbit (LPO) mission. Herschel, launched on 14 May 2009 towards a Lissajous orbit around the outer collinear Lagrange point ( $L_2$ ) of the Sun-Earth System, is a multi-user observatory mission, dedicated to perform astronomical observations in the far-infrared and sub-millimetre wavelength range. Given the limited amount of propellant and the relatively short flight time, the envisaged end-of-life strategy foresees a disposal manoeuvre into a lunar impacting trajectory (Colombo et al., 2013; Colombo et al., 2015). At the end of life the spacecraft can rely on a limited ground support, thus the actual disposal trajectory will only be known with a low degree of confidence. As current and future missions are planned to be placed on LPO it is a critical aspect to clear these regions when the mission is not active anymore. It is fundamental to assess the influence of uncertainties in the initial trajectory in the evolution of the trajectory towards the re-entry or impact on a celestial body. In particular, the following sections and experiments considered the disposal toward the Moon of the Herschel spacecraft through an impact trajectory.

### 2.1.1 Problem Definition

The dynamics of this problem is the perturbed four body problem with the contribution of SRP and the higher order gravity harmonics of the Moon in the Earth Centred Ecliptic reference Frame (ECEF):

$$\begin{aligned} \dot{\mathbf{r}} &= \mathbf{v} \\ \dot{\mathbf{v}} &= -\frac{\mu_E}{r^3} \mathbf{r} - \mu_S \left( \frac{\mathbf{r}_{Ssc}}{r_{Ssc}^3} - \frac{\mathbf{r}_{SE}}{r_{SE}^3} \right) - \mu_M \left( \frac{\mathbf{r}_{Msc}}{r_{Msc}^3} - \frac{\mathbf{r}_{ME}}{r_{ME}^3} \right) + \mathbf{a}_{Solar} + \mathbf{a}_{nm} \end{aligned} \quad (1)$$

where the trajectory of the spacecraft is given in terms of position and velocity  $[\mathbf{r} \quad \mathbf{v}]$ . The sum of Eq.(1) contains the gravity accelerations exerted by the Sun and the Moon;  $\mathbf{r}_{Ssc}$  and  $\mathbf{r}_{Msc}$  are the their respective distances from the spacecraft, while their positions with respect to the Earth are given  $\mathbf{r}_{SE}$  and  $\mathbf{r}_{ME}$  respectively;  $\mu_E$ ,  $\mu_S$ ,  $\mu_M$  are constants of Earth, Sun and Moon.  $\mathbf{a}_{Solar}$  is the solar pressure modelled as follows (Kubo-aka and Sengoku, 1999):

$$\mathbf{a}_{Solar} = C_R \frac{P_{1AU}}{c_{light}} \left( \frac{r_{AU}}{r_{Ssc}} \right)^2 \frac{(\mathbf{r}_{Ssc})}{r_{Ssc}} \frac{A}{m_{sc}} = C_R S_{SRP} \left( \frac{r_{AU}}{r_{Ssc}} \right)^2 \frac{(\mathbf{r}_{Ssc})}{r_{Ssc}} \frac{A}{m_{sc}} \quad (2)$$

where  $A$ ,  $m_{sc}$  are the satellite cross section area and mass respectively,  $C_R$  the radiation pressure coefficient and  $S_{srp}$  is the solar radiation pressure at 1 AU equal to the ratio between the solar constant  $P_{1AU}$  and the speed of light  $c_{light}$ .  $\mathbf{a}_{nm}$  includes only the higher order terms (with  $n, m > 0$  since the zero order is already included in the nominal dynamics).

In fact, due to the non-uniform density distribution and its rotation, the Moon cannot be regarded as a perfect sphere. The asphericity of this body gives rise to perturbations that affect all orbital

elements, especially at low altitude. The model that has been considered to describe these effects is based on the standard Legendre polynomials of the gravity field potential as defined by Cunningham (1970). This allows an efficient computation of the potentials and resulting perturbation as a function of the Cartesian coordinates in the body fixed reference frame. The gravity potential  $U$  can be written as:

$$U = \frac{\mu_M}{R_M} \sum_{n=0}^{\infty} \sum_{m=0}^n (C_{nm} V_{nm} + S_{nm} W_{nm}) \quad (3)$$

where  $R_M$  the Moon mean radius,  $C_{nm}$ ,  $S_{nm}$  are the potential coefficients that describe the distribution of the mass within the body. For the Moon the potential coefficients are the ones from 100th-degree gravity model ‘LP100K’.  $V_{nm}$  and  $W_{nm}$  satisfy the recurrence relations:

$$\begin{aligned} V_{mm} &= (2m-1) \frac{R_B}{r^2} \{xV_{m-1,m-1} - yW_{m-1,m-1}\} \\ W_{mm} &= (2m-1) \frac{R_B}{r^2} \{xW_{m-1,m-1} + yV_{m-1,m-1}\} \end{aligned} \quad (4)$$

and

$$\begin{aligned} V_{nm} &= \frac{R_B}{r^2} \left\{ \frac{2n-1}{n-m} zV_{n-1,m} - \frac{n+m-1}{n-m} R_B V_{m-2,m} \right\} \\ W_{nm} &= \frac{R_B}{r^2} \left\{ \frac{2n-1}{n-m} zW_{m-2,m} - \frac{n+m-1}{n-m} R_B W_{m-2,m} \right\} \end{aligned} \quad (5)$$

where  $r$  is the distance of the spacecraft from the centre of mass of the body. The set of equations hold for  $n = m+1$  if  $V_{n-1,m}$  and  $W_{n-1,m}$  are set to zero. Furthermore, the initial values  $V_{00} = R_B/r$  and  $W_{00} = 0$  are known. The recursions used here are stable, which means that small numerical errors in the computation of the low-order terms do not affect results for high orders. The overall

acceleration  $\mathbf{a}_{nm}^M = [\ddot{x}_M \quad \ddot{y}_M \quad \ddot{z}_M]^T$  ( $M$  is used to indicate that is expressed in the Moon fixed equatorial frame) due to the gravity field is equal to the gradient  $U$  and can be directly calculated from  $V_{nm}$  and  $W_{nm}$  as

$$\ddot{x}_M = \sum_{nm} \ddot{x}_{nm}, \quad \ddot{y}_M = \sum_{nm} \ddot{y}_{nm}, \quad \ddot{z}_M = \sum_{nm} \ddot{z}_{nm}$$

with partial accelerations

$$\begin{aligned}
m=0 &\rightarrow \begin{cases} \ddot{x}_{nm} = \frac{\mu_M}{R_M^2} (-C_{n0} V_{n+1,1}) \\ \ddot{y}_{nm} = \frac{\mu_M}{R_M^2} (-C_{n0} W_{n+1,1}) \end{cases} \\
m>0 &\rightarrow \begin{cases} \ddot{x}_{nm} = \frac{1}{2} \frac{\mu_M}{R_M^2} \left[ (-C_{nm} V_{n+1,m+1} - S_{nm} W_{n+1,m+1}) + \frac{(n-m+2)!}{(n-m)!} (C_{nm} V_{n+1,m-1} + S_{nm} W_{n+1,m-1}) \right] \\ \ddot{y}_{nm} = \frac{\mu_M}{R_B^2} \left[ (-C_{nm} W_{n+1,m+1} + S_{nm} V_{n+1,m+1}) + \frac{(n-m+2)!}{(n-m)!} (-C_{nm} W_{n+1,m-1} + S_{nm} V_{n+1,m-1}) \right] \end{cases} \quad (5) \\
\ddot{z}_{nm} &= \frac{\mu_M}{R_B^2} \left[ (n-m+1) (-C_{nm} V_{n+1,m} + S_{nm} W_{n+1,m}) \right]
\end{aligned}$$

Being the acceleration defined in the Moon fixed reference frame a rotation to the inertial frame is necessary. Given that the equations of motion for the complete model have been defined in the ECEF, the results from Seidelmann et al. (2006) have been considered for the Moon. The nonlinear process in Eq.(1) can be discretized in time and written as:

$$\mathbf{x}_{k+1} = f(t, \mathbf{x}_k) \quad (6)$$

where we explicitly state the dependency of the dynamics from the time given that the actual relative positions of the Sun, Earth and Moon deeply affect this kind of trajectory.

Figure 1 reports the disposal trajectory towards the Moon for the spacecraft Herschel, in November 2011. The initial condition for the propagation was:

$$\mathbf{x}(t_0) = \begin{bmatrix} \mathbf{r}(t_0)^T & \mathbf{v}(t_0)^T \end{bmatrix}^T = \begin{bmatrix} 887698.5km & 1402038.8km & 387608.7km & -0.0963km/s & -0.0485km/s & 0.0744km/s \end{bmatrix}.$$

The propagation of 60 days did include also the solar radiation pressure with

$$C_R \frac{A}{m_{sc}} = 0.0075 \frac{m^2}{kg} \text{ and harmonics terms up to degree } 10^{\text{th}} \text{ for the Moon in this case. Note that this}$$

trajectory will also be used as the reference one in the following analyses.

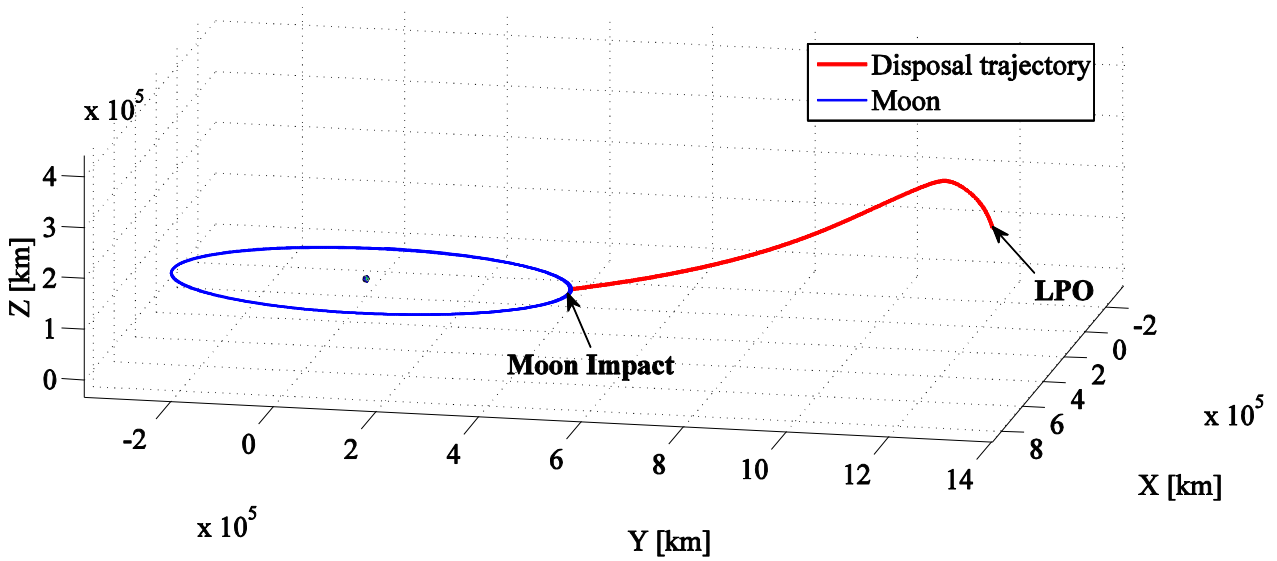


**Figure 1. Disposal trajectory towards the Moon for Herschel.**

## 2.2 Uncertainty Propagation Techniques

We now review a number of techniques for uncertainty propagation which were considered during this work. We start first with Monte Carlo, then we show the semi-analytic method of the high order Taylor expansions, and eventually we move to the quasi-Monte Carlo ones, i.e. the unscented transformation and polynomial chaos method.

### 2.2.1 MC Sampling - Calculation of Mean and Covariance

The MC samples at initial time are generated using a random generator. In order to exploit higher convergence rates, we have to generate the initial ensemble by randomly selecting the initial points in a proper way. In fact it could happen that the generated samples are correlated especially when the number of points is not very high. The mean value of the distribution could be biased by some value with respect to the nominal one and the covariance matrix could be full instead of being diagonal, as reported in the following equations:

$$\begin{aligned}\boldsymbol{\chi}_0 &= \frac{1}{N} \sum_{i=1}^N \boldsymbol{\chi}_i^c \\ \mathbf{P}_\chi &= \frac{1}{N-1} \sum_{i=1}^N (\boldsymbol{\chi}_i^c - \boldsymbol{\chi}_0)(\boldsymbol{\chi}_i^c - \boldsymbol{\chi}_0)^T\end{aligned}\tag{7}$$

where  $\boldsymbol{\chi}_0$  is the centre of the grid, and  $\mathbf{P}_\chi$  is the correlation matrix. We used the superscript  $c$  for the generated samples  $\boldsymbol{\chi}_i^c$  to indicate that they are correlated. One way to circumvent this problem is to apply the Mahalanobis decorrelation transformation (Mardia et al., 1979), which allows transforming correlated points of the grid  $\boldsymbol{\chi}_i^c$  into uncorrelated ones  $\boldsymbol{\chi}_i$ :

$$\boldsymbol{\chi}_i = \mathbf{P}_\chi^{-1/2} (\boldsymbol{\chi}_i^c - \boldsymbol{\chi}_0)\tag{8}$$

This is a convenient procedure, which we will exploit when generating the sample population for STTs and PCE techniques.

## 2.2.2 High-order Taylor Expansions

In this section we review the use of high order Taylor expansions in the spatial dimension to propagate uncertainty in dynamical systems.

This section describes the fundamental aspects which this method is based on. The local spacecraft dynamics can be described by applying a Taylor series expansion about the reference nominal trajectory  $\mathbf{x}_0$  for some initial deviation  $\delta\mathbf{x}_0$ :

$$\delta\mathbf{x}(t) = \phi(t, \mathbf{x}_0 + \delta\mathbf{x}_0; t_0) - \phi(t, \mathbf{x}_0; t_0) \quad (9)$$

$\phi$  is the solution flow which maps the initial state at  $t_0$  to  $t$ . The  $s$ -th order solution can be expressed using the Einstein summation convention:

$$\delta x^i(t) = \sum_p^s \frac{1}{p!} \phi_{(t,t_0)}^{i,\gamma_1 \dots \gamma_p} \delta x_0^{\gamma_1} \dots \delta x_0^{\gamma_p} \quad (10)$$

where  $\gamma_1 \dots \gamma_p \in \{1, \dots, n\}$  denotes the  $\gamma_i$  component of the state vector corresponding to the  $s$ -th derivative,  $n$  is the number of components of the state vector and:

$$\phi_{(t,t_0)}^{i,\gamma_1 \dots \gamma_p}(t; \mathbf{x}_0; t_0) = \left. \frac{\partial^p \phi_{(t,t_0)}^i(t; \boldsymbol{\xi}_0; t_0)}{\partial \xi_0^{\gamma_1} \dots \partial \xi_0^{\gamma_p}} \right|_{\xi_0^{\gamma_j} = x_0^{\gamma_j}} \quad (11)$$

The higher-order partials of the solution define the global state transition tensors, which map the initial deviations at time  $t_0$  to the deviation at time  $t$ . The higher order effects are included in the STTs. Note that for  $s=1$ , the STTs reduces to the simple state transition matrix. The differential equations up to the third order are given by the following equations (Park and Scheeres, 2006a):



$$\begin{aligned}
\dot{\phi}^{i,a} &= f^{i,\alpha} \phi^{\alpha,a} \\
\dot{\phi}^{i,ab} &= f^{i,\alpha} \phi^{\alpha,ab} + f^{i,\alpha\beta} \phi^{\alpha,a} \phi^{\beta,b} \\
\dot{\phi}^{i,abc} &= f^{i,\alpha} \phi^{\alpha,abc} + f^{i,\alpha\beta} \left( \phi^{\alpha,a} \phi^{\beta,bc} + \phi^{\alpha,ab} \phi^{\beta,c} + \phi^{\alpha,ac} \phi^{\beta,b} \right) + f^{i,\alpha\beta\delta} \phi^{\alpha,a} \phi^{\beta,b} \phi^{\delta,c}
\end{aligned} \tag{12}$$

where  $\alpha, \beta, \in \delta \{1, \dots, n\}$  and  $a, b, c = \{1, \dots, n\}$  are the indexes for the first, second and third order derivative.  $f^{i,\gamma_1 \dots \gamma_p}$  are the partials of the dynamics and are computed as follows:

$$f^{i,\gamma_1 \dots \gamma_p} = \left. \frac{\partial^p f^i(t; \xi_0; t_0)}{\partial \xi_0^{\gamma_1} \dots \partial \xi_0^{\gamma_p}} \right|_{\xi_0^{\gamma_j} = x_0^{\gamma_j}} \tag{13}$$

Note that the partial derivatives in Eqs.(11) and (13) are calculated with respect to the nominal trajectory. The calculation of the STTs requires the forward integration of  $\sum_{q=1}^{s+1} 6^q$  differential equations starting with initial values  $\phi_{(t_0, t_0)}^{i,a} = 1$ , if  $i = a$ , and zero otherwise. When the order is  $s = 3$ , the 1554 equations need to be integrated simultaneously.

Moreover the computational time and complexity are increased by the numerical evaluations of the analytical partials of the dynamics. In this work, the partials were computed analytically using the symbolic manipulator in the MATLAB<sup>RM</sup> Symbolic Toolbox. As an example, the third order STTs integration along a 5 day period required approximately 8 hours using a Windows 7 OS 3.16Ghz Intel<sup>(R)</sup> Core<sup>(TM)</sup>2 Duo CPU.

The coupled integration of thousands equations could introduce numerical errors when integrated over a long period of time. For this reason a good practice is to consider the nominal trajectory and to integrate the STTs over a short period time, say 1 day. The intermediate STTs are called local

STTs. While the global STTs map the deviation at the initial time  $t_0$  to the deviation at time  $t_{k+1}$ , the local STTs map the deviation at time  $t_k$  to the deviation at time  $t_{k+1}$ .

Figure 2 shows the result of the propagation for 5 days of the variation vector, with respect to the actual trajectory, by using up to the fourth order local STTs.

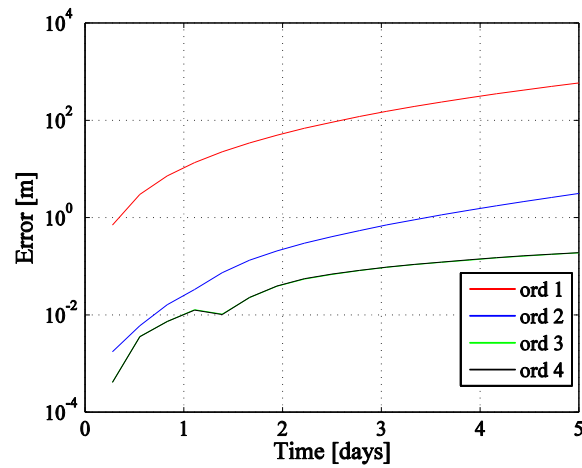


**Figure 2. Position (left) and velocity (right) with local STTs.**

A value of  $\delta \mathbf{x}_0 = [2500km \ 2500km \ 2500km \ 0.01km/s \ 0.01km/s \ 0.01km/s]^T$  was used to magnify the error over this short period. The third and fourth orders prove to be the most accurate.

The corresponding errors at the end of 5 days are reported in Table 1.

**Table 1. Propagation error using STTs.**

Order	1	2	3	4
Position error [m]	585.111	3.133	0.189	0.190
Velocity error [m/s]	$3.5 \cdot 10^{-3}$	$2.4 \cdot 10^{-5}$	$9.6 \cdot 10^{-7}$	$8.8 \cdot 10^{-7}$

It is clear that the linear approach is not sufficiently accurate. A second order approach keeps the error relatively small. Nonetheless the third and fourth orders show higher precision, especially for what concerns the velocity errors which is about two orders of magnitude smaller than the second order one.

Once the state transition tensors are available for some time interval  $[t_k, t_{k+1}]$ , the mean and covariance matrix of the relative dynamics at  $t_k$  can be mapped analytically to  $t_{k+1}$  as a function of the probability distribution at  $t_k$ . From  $t_k$  to  $t_{k+1}$  the propagated mean and covariance can be stated as:

$$\begin{aligned} \mathbf{m}_{k+1}^i &= \phi^i(t_{k+1}; \mathbf{m}_k^+) + \delta \mathbf{m}_{k+1}^i = \phi^i(t_{k+1}; \mathbf{m}_k^+) + \sum_{p=1}^s \frac{1}{p!} \phi_{(t_{k+1}, t_k)}^{i, \gamma_1 \dots \gamma_p} E[\delta x_k^{\gamma_1} \dots \delta x_k^{\gamma_p}] \\ P_{k+1}^{ij} &= E[(\delta x_{k+1}^i - \delta m_{k+1}^i)(\delta x_{k+1}^j - \delta m_{k+1}^j)] = \\ & \sum_{p=1}^s \sum_{q=1}^s \frac{1}{p!q!} \phi_{(t_{k+1}, t_k)}^{i, \gamma_1 \dots \gamma_p} \phi_{(t_{k+1}, t_k)}^{j, \varsigma_1 \dots \varsigma_q} E[\delta x_k^{\gamma_1} \dots \delta x_k^{\gamma_p} \delta x_k^{\varsigma_1} \dots \delta x_k^{\varsigma_q}] - \delta m_{k+1}^i \delta m_{k+1}^j \end{aligned} \quad (14)$$

where  $\{\gamma_i, \varsigma_j\} \in \{1, \dots, n\}$  are the indexes for the different order derivative. If one sticks to the hypothesis of an initial Gaussian distribution, the joint characteristic function for a Gaussian random vector can be computed as (see Park and Scheeres, 2006b and Park, 2007)

$$\mathcal{G}(\mathbf{u}) = E[e^{j\mathbf{u}^T \mathbf{x}}] = \exp(j\mathbf{u}^T \mathbf{m} - \frac{1}{2} \mathbf{u}^T \mathbf{P} \mathbf{u}) \quad (15)$$

where  $j = \sqrt{-1}$  and the expected higher moments can be computed using:

$$E[\mathbf{x}^{\gamma_1} \mathbf{x}^{\gamma_2} \dots \mathbf{x}^{\gamma_p}] = j^{-p} \left. \frac{\partial^p \mathcal{G}(\mathbf{u})}{\partial \mathbf{u}^{\gamma_1} \partial \mathbf{u}^{\gamma_2} \dots \partial \mathbf{u}^{\gamma_p}} \right|_{\mathbf{u}=0} \quad (16)$$

When generating a number of discrete samples, the mean and covariance matrix are mapped between each step  $k$  using the STTs as

$$\mathbf{m}_i(t) = \frac{1}{N} \sum_{k=1}^N \phi_i(t; x_k^0, t^0) \quad (17)$$

$$\mathbf{P}_{ij}(t) = \frac{1}{N-1} \sum_{k=1}^N [\mathbf{m}_i(t) - \phi_i(t; x_k^0, t^0)] [\sum_{k=1}^N [\mathbf{m}_j(t) - \phi_j(t; x_k^0, t^0)]] \quad (18)$$

where equal weights were given to all the samples.

### 2.2.3 Unscented Transformation

This technique, which is based on MC sampling, works on the premises that one can well approximate the posteriori covariance by propagating a limited set of optimally chosen samples (Julier et al., 1995). The set of sigma points  $\chi_i$  are then given as:

$$\mathbf{Y}_i = \begin{cases} \tilde{\mathbf{x}}_k & i = 0 \\ \tilde{\mathbf{x}}_k + \left( \sqrt{(n + \kappa_{ukf}) \mathbf{P}_k} \right)_i & i = 1, 2, \dots, n \\ \tilde{\mathbf{x}}_k - \left( \sqrt{(n + \kappa_{ukf}) \mathbf{P}_k} \right)_i & i = n + 1, \dots, 2n \end{cases} \quad (19)$$

where  $\mathbf{Y}$  is a matrix consisting of  $(2n - 1)$  vectors, with  $\kappa_{ukf} = \alpha_{ukf}^2 (n + \lambda_{ukf}) - n$ ,  $\kappa_{ukf}$  is a scaling parameter, constant  $\alpha_{ukf}$  determines the extension of these vectors around  $\tilde{\mathbf{x}}_k$ . We set  $\alpha_{ukf}$  equal to  $10^{-3}$  and  $\lambda_{ukf}$  is set equal to  $3 - n$ .

The sigma points are transformed or propagated through the nonlinear function, the so-called unscented transformation, to give:

$$\mathbf{Y}_{i,k+1} = f(t, \mathbf{Y}_{i,k}), i=0, 1, \dots, 2n \quad (20)$$

The predicted mean of the state vector  $\tilde{\mathbf{x}}_k^-$ , the covariance matrix  $\mathbf{P}_{x,k}^-$  can be approximated using the weighted mean and covariance of the transformed vectors:

$$\begin{aligned} \mathbf{Y}_{i,k|k-1} &= f(t, \mathbf{Y}_{i,k-1}) \\ \tilde{\mathbf{x}}_k^- &= \sum_{i=0}^{2n} W_i^{(m)} \mathbf{Y}_{i,k|k-1} \\ \mathbf{P}_k^- &= \sum_{i=0}^{2n} W_i^{(c)} \left[ \mathbf{Y}_{i,k|k-1} - \tilde{\mathbf{x}}_k^- \right] \left[ \mathbf{Y}_{i,k|k-1} - \tilde{\mathbf{x}}_k^- \right]^T \end{aligned} \quad (21)$$

where  $W_i^{(m)}$  and  $W_i^{(c)}$  are the weighted sample mean and covariance given by:

$$\begin{aligned} W_0^{(m)} &= \kappa / (n + \kappa) \\ W_0^{(c)} &= \kappa_{ukf} / (n + \kappa_{ukf}) + (1 - \alpha_{ukf}^2 + \beta_{ukf}) \\ W_i^{(m)} &= W_i^{(c)} = \kappa_{ukf} / \left[ 2(n + \kappa_{ukf}) \right], \quad i = 1, 2, \dots, 2n \end{aligned} \quad (22)$$

and  $\beta_{ukf}$  is used to incorporate prior knowledge of the distribution with  $\beta_{ukf} = 2$  (Crassidis and Junkins, 2004).

#### 2.2.4 Polynomial Chaos Expansions

The use of Taylor expansions requires having access to the dynamic model and to calculate high order derivatives. The number of partial to be propagated grows significantly with the size of the problem and the order of the expansion, therefore one can see the propagation of each partial as a sample to be evaluated. Advanced software packages like COSYinfinity (Valli et al., 2013) can perform this evaluation very efficiently; on the other hand one may still want to use the idea of sampling but to obtain a polynomial representation of the propagated region of uncertainty using a

limited number of samples. One way to do it is to use stochastic collocation or stochastic expansions. In both cases an access to the model and its derivatives is not required. In this section, the use of PCE to propagate uncertainties in dynamic models is introduced.

The main aspects of this method involve (1) solving the system of stochastic state equations via the PCE methodology to gain efficiency; and (2) sampling the PCE approximation of the stochastic solution with an arbitrarily large number of samples, at virtually no additional computational cost, to drastically reduce the sampling errors.

The PCE method employs a set of polynomial functions, used as orthogonal basis, to approximate the function form between the stochastic response output and each of its random inputs. The chaos expansion for a component  $l$  of a generic response  $\mathbf{G}$  takes the form:

$$G_l = a_0 B_0 + \sum_{i_1=1}^{\infty} a_{i_1} B_1(\chi_{i_1}) + \sum_{i_1=1}^{\infty} \sum_{i_2=1}^{i_1} a_{i_1 i_2} B_2(\chi_{i_1}, \chi_{i_2}) + \sum_{i_1=1}^{\infty} \sum_{i_2=1}^{i_1} \sum_{i_3=1}^{i_2} a_{i_1 i_2 i_3} B_3(\chi_{i_1}, \chi_{i_2}, \chi_{i_3}) + \dots \quad (23)$$

where  $\chi_i$  are random inputs and  $B_i$  is a generic multi-variable polynomial. This expression can be simplified by replacing the order-based indexing with a term-based indexing:

$$G_l = \sum_{j=0}^{\infty} \alpha_{lj} \Psi_j(\boldsymbol{\chi}) \quad (24)$$

where there is a one-to-one correspondence between  $a_{i_1 i_2 i_3}$  and  $\alpha_{lj}$ , and between  $B_n(\chi_{i_1}, \chi_{i_2}, \dots, \chi_{i_n})$  and  $\Psi_j(\boldsymbol{\chi})$ . Each of the  $\Psi_j(\boldsymbol{\xi})$  is a multivariate polynomials which involve products of the one-dimensional polynomials. In practice, one truncates the infinite expansion at a finite number of random variables and a finite expansion order,  $p$ :

$$G_l \cong \sum_{j=0}^p \alpha_{lj} \Psi_j(\boldsymbol{\chi}) \quad (25)$$

Using Hermite polynomials, a multivariate polynomial  $B(\boldsymbol{\xi})$  of order  $n$  is defined from:

$$B_n(\chi_{i_1}, \chi_{i_2}, \dots, \chi_{i_v}) = e^{\frac{1}{2}\boldsymbol{\chi}^T \boldsymbol{\chi}} (-1)^n \frac{\partial^n}{\chi_{i_1}, \dots, \chi_{i_v}} e^{-\frac{1}{2}\boldsymbol{\chi}^T \boldsymbol{\chi}} \quad (26)$$

which can be shown to be a product of one-dimensional Hermite polynomials involving a multi-index  $m_i^j$ :

$$B_n(\chi_{i_1}, \chi_{i_2}, \dots, \chi_{i_v}) = \Psi_j(\boldsymbol{\chi}) = \prod_{i=1}^n \psi_{m_i^j}(\chi_{i_i}) \quad (27)$$

As an example Table 2 reports the one-dimensional Hermite polynomials up to the 6<sup>th</sup> order. For a Hermite multivariate polynomial the number of coefficients of the expansions for each uncertain variable is given by  $\frac{(i_v + n)!}{i_v! n!}$  which shows that the expansions tend to increase quite rapidly with the number of variables and order. In the PCE approach, simulations are used as black boxes and the calculation of chaos expansion coefficients for response metrics of interest is based on a set of simulation response evaluations. To calculate these responses, PCE coefficients have been evaluated using spectral projection (Eldred et al., 2011). The spectral projection approach projects the response  $\mathbf{G}$  against each basis function using inner products and employs the polynomial orthogonality properties to extract each coefficient. Each coefficient of the Eq.(25) can be calculated as:

$$\alpha_{lj} = \frac{\langle G_l, \Psi_j \rangle}{\langle \Psi_j^2 \rangle} = \frac{1}{\langle \Psi_j^2 \rangle} \int_{\Omega} G \Psi_j \rho(\boldsymbol{\chi}) d\boldsymbol{\chi} \quad (28)$$

where the inner product involves a multi-dimensional integral over the support range of the weighting function  $\rho(\chi)$ .

**Table 2. One-dimensional Hermite polynomials up to the 6<sup>th</sup> order.**

$n$	$\psi_n(\chi)$
1	$\chi$
2	$\chi^2 - 1$
3	$\chi^3 - 3\chi$
4	$\chi^4 - 6\chi^2 + 3$
5	$\chi^5 - 10\chi^3 + 15\chi$
6	$\chi^6 - 15\chi^4 + 45\chi^2 - 15$

#### 2.2.4.1 Gauss-Hermite Cubature Rules

The multi-dimensional integral of Eq.(24) has been evaluated using Smoliak sparse grid (Agarwal et al., 2003). At each point of the grid is associated a suitable weight which depends on the choice of the basis, the order of the polynomial and the accuracy one wants to achieve, such that the integral in Eq.(28) can be written as the sum of discrete number of terms:

$$\int_{\Omega} G_l \Psi_j \rho(\chi) d\chi \cong \sum_{i=1}^{ngrid} G_l(\chi_i) \Psi_j(\chi_i) w(\chi_i) \quad (29)$$

In this way using a limited number of points over the Smolyak grid one can propagate the uncertain parameters at a certain instant of time and project the response to obtain the PCE representations. Analytical expressions of the mean and covariance matrix are then available as:



$$\begin{aligned}
\boldsymbol{\mu}_R &= E[\mathbf{G}] \cong \sum_{j=0}^p \boldsymbol{\alpha}_j E[\Psi_j] = \boldsymbol{\alpha}_0 \\
\mathbf{P}_R &= E[(\mathbf{G} - \boldsymbol{\mu}_R)(\mathbf{G} - \boldsymbol{\mu}_R)^T] \cong \sum_{j=0}^p \boldsymbol{\alpha}_j (\boldsymbol{\alpha}_j)^T E[\Psi_j^2]
\end{aligned} \tag{30}$$

$\boldsymbol{\mu}_R$  and  $\mathbf{P}_R$  are the exact moments of the expansion, which converge to moments of the true response function. It is possible to construct the initial polynomial expansion description by choosing a suitable cubature rule. We used Gauss-Hermite cubature rules, which have to be used in the case of Hermite polynomials. The interested reader can refer to the work of Genz and Keister (1996), where the sparse grids are discussed and efficiently calculated for this class of polynomials, by exploiting symmetric interpolatory integration rules for multidimensional integrals over infinite regions with a Gaussian weight function. In the work of Genz and Keister (1996) it is shown that a Gaussian integral for a polynomial of order  $n$  can be calculated perfectly using a grid of level  $l = 2n + 1$ .

In Figure 3 we show the normalised Smoliak grid for 3 uncertain parameters  $\chi_1$ ,  $\chi_2$  and  $\chi_3$  using Hermite polynomials as bases using grids with different level of accuracy.

As one can see when the level of accuracy is increased the grid is populated by a higher number of samples, which cover also a broader uncertain space. For example the maximum uncertain parameter reaches  $1.7 \sigma$  for a level 2 grid, while it is  $4 \sigma$  for a level 6 grid. This gives the chance to better describe the evolution of the uncertain space exploring regions with very low probability.

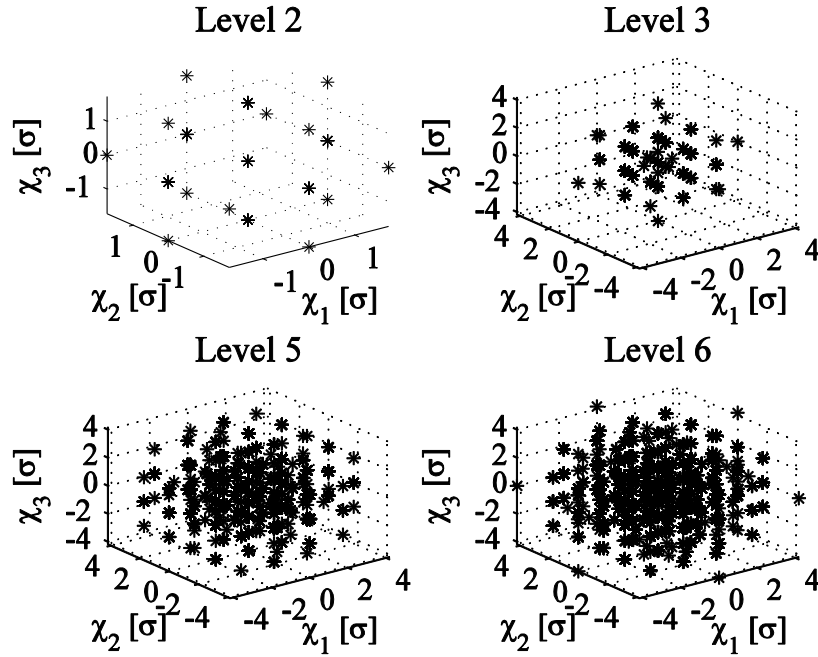


**Figure 3. Smoliak grid for Hermite polynomials with different level of accuracy**

Table 3 shows the minimum number of points needed to calculate the discrete integrals of Eq.(29) for 6 uncertain variables as a function of the order of the polynomials. As a reference for classic sparse grid cubature rules, the nodes for numerical integration were obtained from Heiss and Winschel (2007) where the polynomial exactness for a Gaussian distribution is given for  $n = 2l - 1$ .

**Table 3. Minimum number of points required for calculating Gaussian integrals of a certain order.**

Order	1	3	5	7	9	11
Genz-Keister sparse grid	1	13	73	257	749	2021
Classic Sparse grid	1	13	85	389	1433	4541

As one can see Genz-Keister grids allows decreasing the number of sampling points as the order of the polynomial increases while maintaining the same accuracy level (see the work of Genz and

Keister, 1996 where a detailed comparison was carried out). In this way a further computational speed gain can be achieved.

## 2.3 Results

We will first show the comparison between the presented methods of Section 2.2 and select the most suitable alternative to MC technique. Then we will apply this to the study of the impact on the surface of the Moon for the disposal trajectory of Section 2.1.1 by considering initial uncertain disposal conditions.

### 2.3.1 Comparisons

Given that the uncertainty analysis of disposal trajectories from LPO to the Moon is a new application of PCE in astrodynamics, we first compare the methods presented in Section 2.2 to evaluate their accuracy and computational cost and establish which one provides the best representation of the dispersion of the final states. Section 2.3.1.1 derives the reference distribution using a Monte Carlo Simulation. Section 2.3.1.2 compares the ability of each method to correctly predict mean and covariance versus their computational cost while Section 2.3.1.3 tests the ability of STT and PCEs to represent the full distribution. The dynamical model used in all the tests in this section includes only Earth, Sun and Moon and light pressure and does not consider the full harmonic expansion of the gravity field of the Moon or the n-body perturbation  $\mathbf{a}_{pb}$ . The dynamic equations were numerically integrated with an explicit, variable step size, Runge-Kutta integration method with respectively a  $10^{-9}$  and  $10^{-9}$  relative and absolute accuracies.

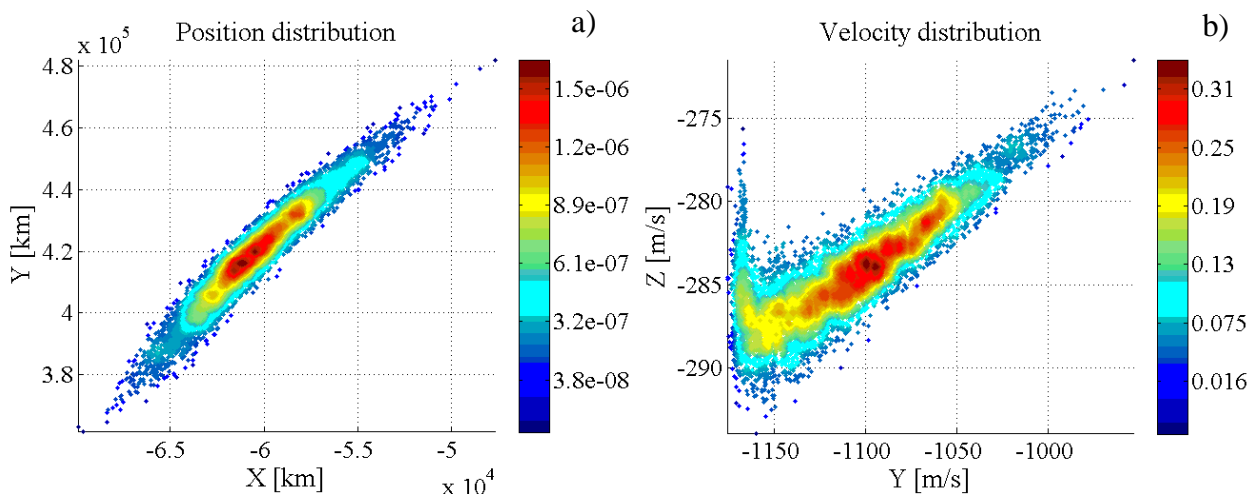
### 2.3.1.1 Reference Distribution

In this section we derive the reference distribution used in the following comparisons. The distribution is derived from a full MC simulation using the complete model. The simulation was run for an increasing number samples, from  $10^4$  to  $10^6$ , to verify the correctness of the predicted distribution.

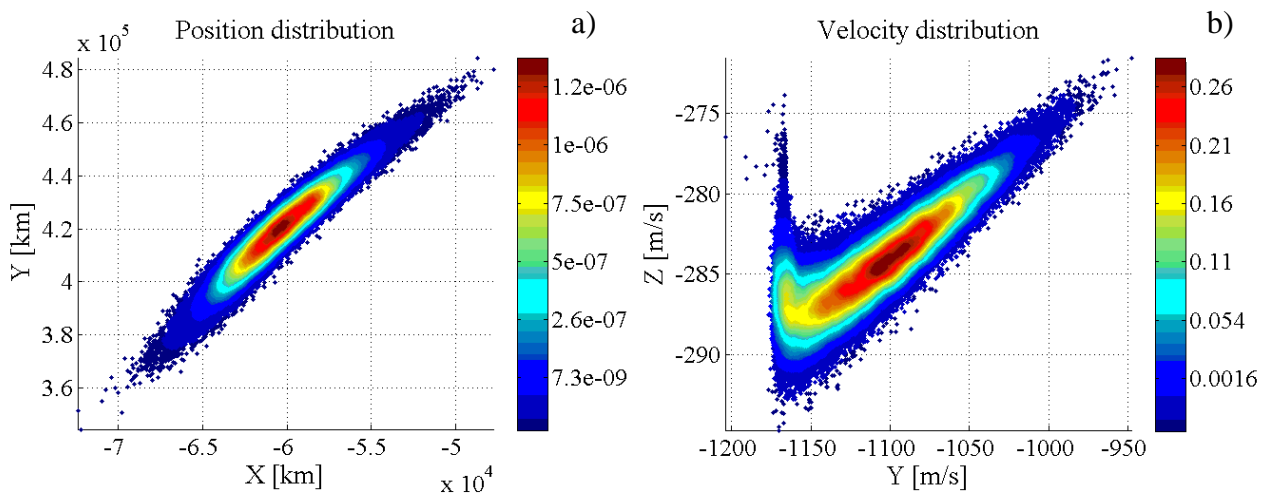
The uncertain quantities are assumed to be uncorrelated and normally distributed with standard deviation  $\sigma = [5\text{km} \ 5\text{km} \ 5\text{km/s} \ 3.89 \cdot 10^4 \text{ km/s} \ 7.68 \cdot 10^4 \text{ km/s} \ 2.59 \cdot 10^4 \text{ km/s}^T]$  and zero mean. These values are typical position errors for this kind of mission (see Godard et al. 2009) and will be used for the analysis in the remainder of this paper. The variation in velocity represents 1% ( $1\sigma$ ) of the disposal manoeuvre. Note that trajectories are propagated up to 12 hours before the nominal impact because the numerical integration of the STTs beyond that point resulted very difficult due to the proximity to the singularity (represented by the Moon centre) of the equations of motion.

Figure 4 to Figure 6 show the contour plots of the resulting distributions in the final position projected on the plane x-y and the final velocity projected on the plane x-z. These projections show the most significant nonlinearities and asymmetries in the final distributions. The probability density was computed as the ratio between fraction of particles within a circle centred in each MC sample and the corresponding area. Radii of 100 km for the position and of 20 cm/s for the velocity were used. To be noted that final distributions are not Gaussian, although the initial samples were drawn from a Gaussian distribution.

Figure 4 to Figure 6 show the shape can be described fairly well even with 10,000 samples, although the tails fail to cover all the range which only more samples are able to describe. More samples define low probability density more accurately such that the transition between the different density levels becomes smoother, as in Figure 6.



**Figure 4. Statistical distribution for Monte Carlo Simulation and 10,000 samples: x-y position distribution (a), x-z velocity distribution (b).**



**Figure 5. Statistical distribution for Monte Carlo Simulation and 100,000 samples: x-y position distribution (a), x-z velocity distribution (b).**

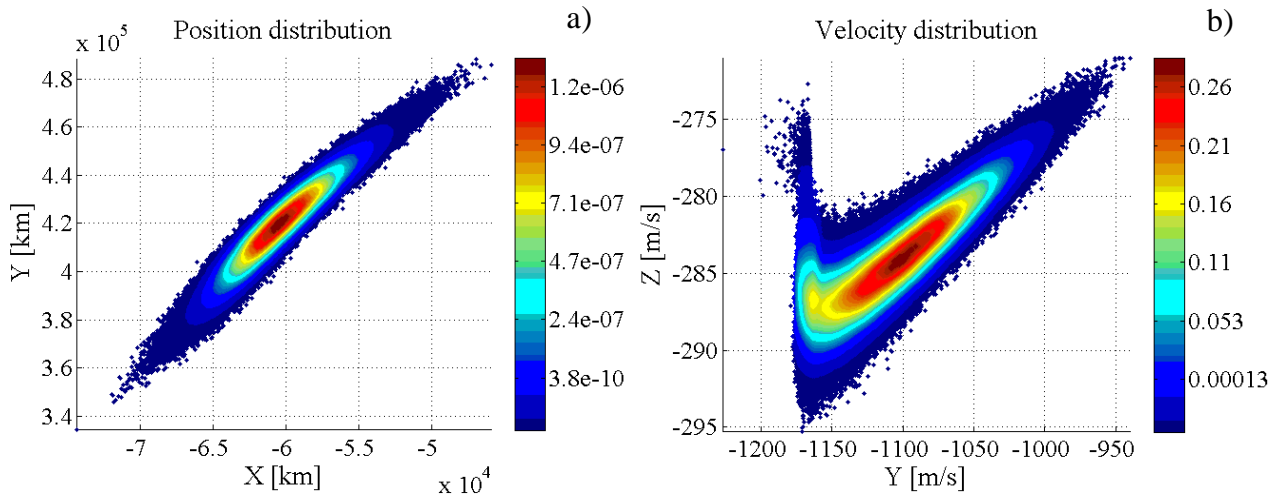


**Figure 6. Statistical distribution for Monte Carlo Simulation and 1,000,000 samples: x-y position distribution (a), x-z velocity distribution (b).**

If we then evaluate the impact rate for these cases as reported in Table 4, we see that the relative difference is below 0.3 per mille between  $10^5$  and  $10^6$  samples. We can conclude that  $10^5$  is a sufficient sample size to describe the distribution of the final states in the case under investigation.

**Table 4. Impact rate convergence for increasing number of MC samples.**

Number of samples	10,000	100,000	1,000,000
Impact rate %	19,740	19.951	20.007
Difference %	-1.335	-0.029	/

### 2.3.1.2 Estimation of Mean and Covariance

The first comparative analysis considers the evolution of the maximum error on the estimation of mean and covariance calculated with the methods in Section 2.2. The maximum error was defined as the absolute value of the difference between the mean calculated with UT, PCE, SSTs and the one calculated with MCS plus the maximum norm of the difference between the covariance matrix calculated with UT, PCE, SSTs and the one calculated with MCS. Figure 7 reports the results for

the STTs, with order up to 4, and the UT, while Figure 8 shows the same analysis for PCE, with order up to 6. PCE were generated using grids with  $l = n$  because we noticed that the best results are achieved when the number of samples is higher than the number of coefficients in the expansion.

Figure 7 shows that the error remains negligible for 40 days till the contribution of the gravity of the Moon becomes significant. At that point the first order STTs depart from the MCS reference solution. At the end of the simulation when the trajectories get closer to the moon and the distribution gets stretched, the order of the STTs needs to be increased to recover the nonlinearities. The accuracy of the results depends on the order for the STTs for both the position (Figure 7a) and velocity (Figure 7b). Remarkably, the UT is equivalent to second order STTs at representing the dispersion of the position but is better than the 4<sup>th</sup> order STTs at representing the dispersion of the velocities. Although the UT is not modelling the full shape of the distribution, it is still able to pick a set of points that provides a good approximation of the covariance. The STTs of order 4, instead, do not capture with sufficient accuracy the deformation of the uncertainty region and, as a consequence, the subsequent calculation of the covariance results less accurate. The result in Figure 8 shows that, in this test case, a PCE of order 2 achieves a better approximation of mean and variance of STTs of order 4 for both position and velocity. In particular, the error in velocity, at the final time, is about one order of magnitude lower than the 4<sup>th</sup> order STTs and the UT.

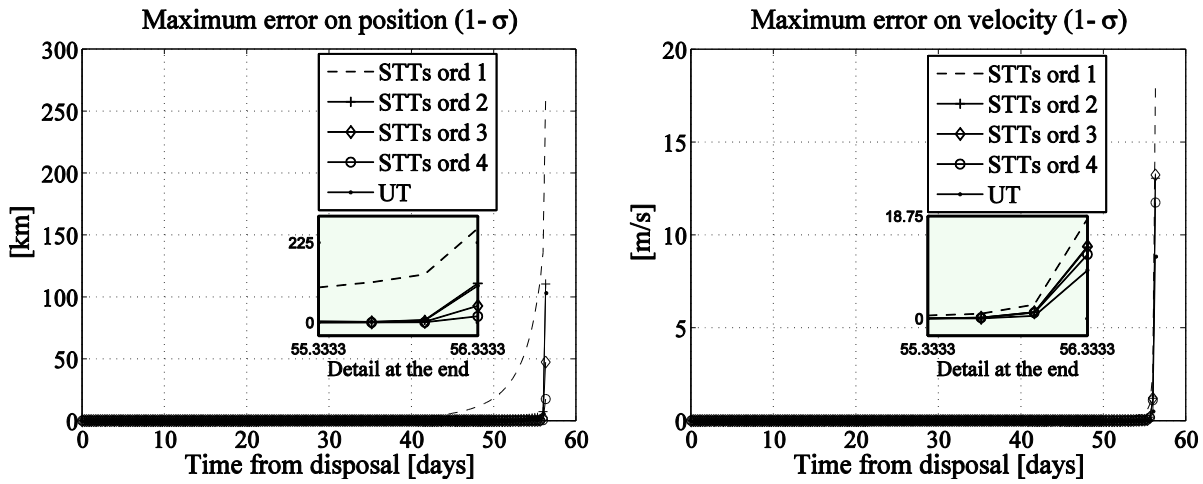


Figure 7. Maximum position (left) and velocity (right) error for STTs and UT with respect to the MC simulation.

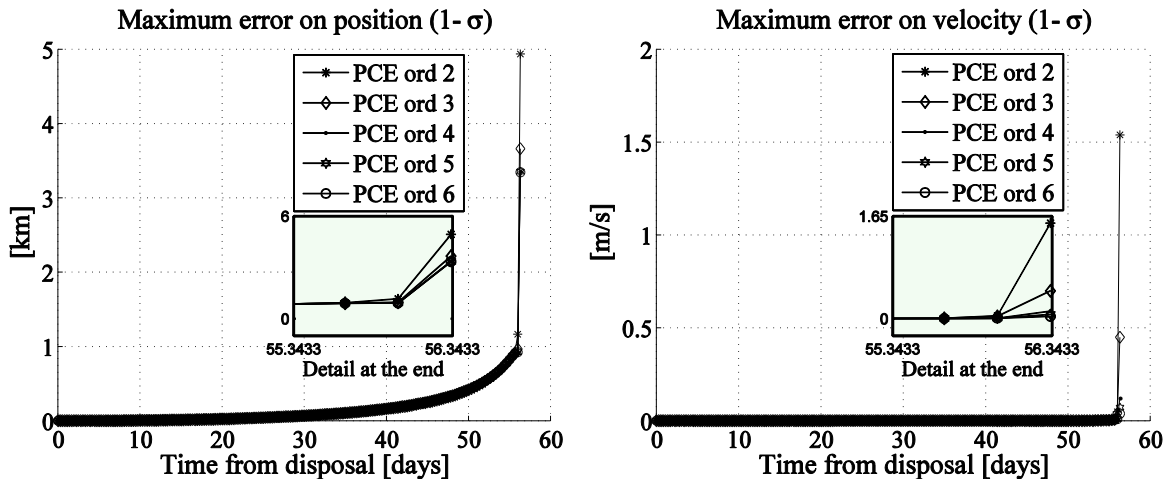


Figure 8. Maximum position (left) and velocity (right) error for PCE and UT with respect to the MC simulation.

Table 5 reports the maximum error in position and velocity at the end of the simulation, and for convenience the computational time to the end of simulation. As the order of the expansion increases it goes down to less than 2 cm/s (order 6). This accuracy was obtained with less than one twelfth of the Monte Carlo simulations. The most expensive methods are the ones that need to integrate a great number of coupled differential equations for the STTs. In fact the computational



cost for a 4<sup>th</sup> order STTs has the same order of magnitude as the propagation of  $10^5$  samples of the full MC simulation. A 6<sup>th</sup> order PCE is as computationally expensive as 3<sup>rd</sup> order STTs. It is also true that we did not fully exploit the symmetry of the tensors, which can potentially lead to halve the CPU time to compute them. Nonetheless the overall computational cost would favour other methods over the STTs.

**Table 5. Comparison between STTs, PCE and MC simulation for 56 days propagation from LPO to Moon disposal manoeuvre. A 64-bit Linux CentOS 5.4 2.93GHz Intel(R) Xeon(TM) X5570 was used.**

Method	Maximum position error (1- $\sigma$ ) [km]	Maximum velocity error (1- $\sigma$ ) [m/s]	Number of integrations /points (p)	(i)	CPU time [s]
UT	107.59	8.869	13 (p)		63.53
STTs $n=1$	265.20	18.282	42 (i)		221
STTs $n=2$	110.32	13.061	258 (i)		1269
STTs	47.30	13.222	1554 (i)		9,683
STTs $n=4$	17.47	11.743	9330 (i)		154,931
PCE $n=2$	3.13	1.06	73 (p)		222
PCE $n=3$	2.76	0.258	257 (p)		773
PCE $n=4$	2.19	0.101	749 (p)		2,244
PCE $n=5$	2.25	0.048	2021 (p)		6,050
PCE $n=6$	2.24	0.017	4725 (p)		14,139
MC	0	0	$10^5$ (p)		299,093

### 2.3.1.3 Approximation of the Full Distribution

The second comparative analysis computes the maximum absolute difference (maximum absolute error) in the distributions of position and velocity at the final time between the STTs, the PCE and

the full MCS predictions with  $10^5$  samples. With the STTs the distribution is derived by integrating all the partials only once and then running a MCS on expansion (10).

Figure 9 to Figure 12 show the resulting distributions for different levels of expansion. Note that the distribution returned by the UT would look like the one in Figure 10.

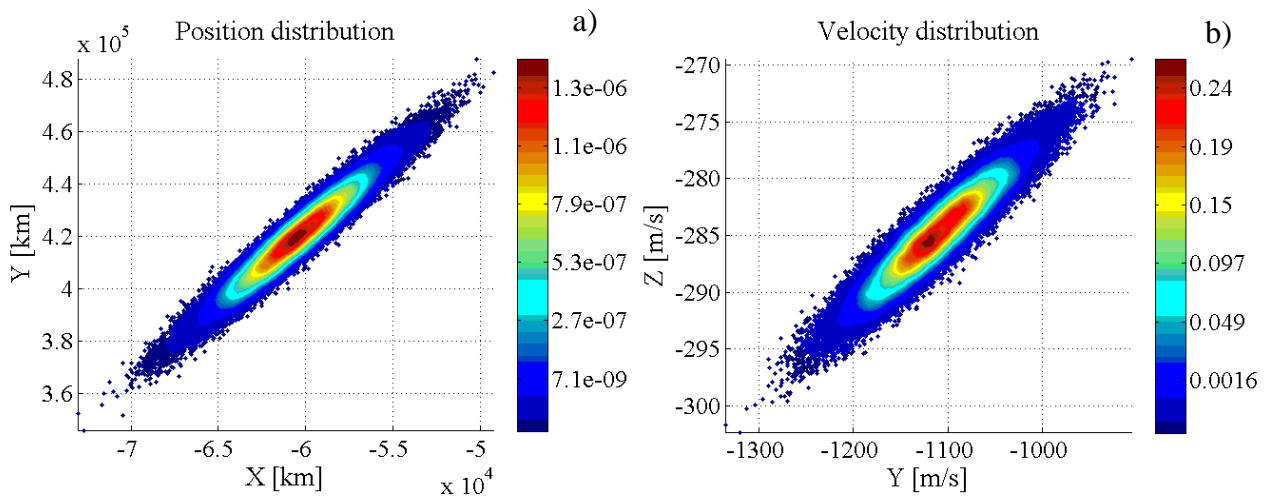


**Figure 9. Statistical distribution with 1st order STTs x-y position distribution (a), x-z velocity distribution (b).**

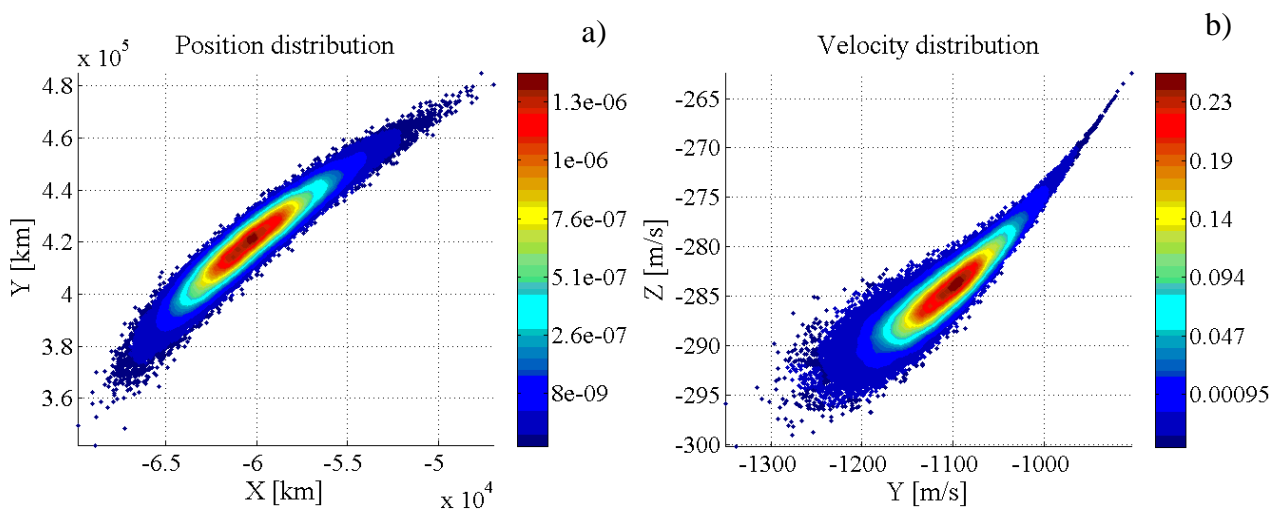


**Figure 10. Statistical distribution with 2nd order STTs: x-y position distribution (a), x-z velocity distribution (b).**

While the position distribution can be approximated quite well with low order STTs (Figure 9a) to Figure 12a)), the same is not possible for the velocity (Figure 9b) to Figure 12b)). The distribution obtained from STTs of order 1, for both position and velocity, are simply ellipsoids (see Figure 9). This first order approximation partially captures the shape of the distribution in position but fails to represent the velocities.

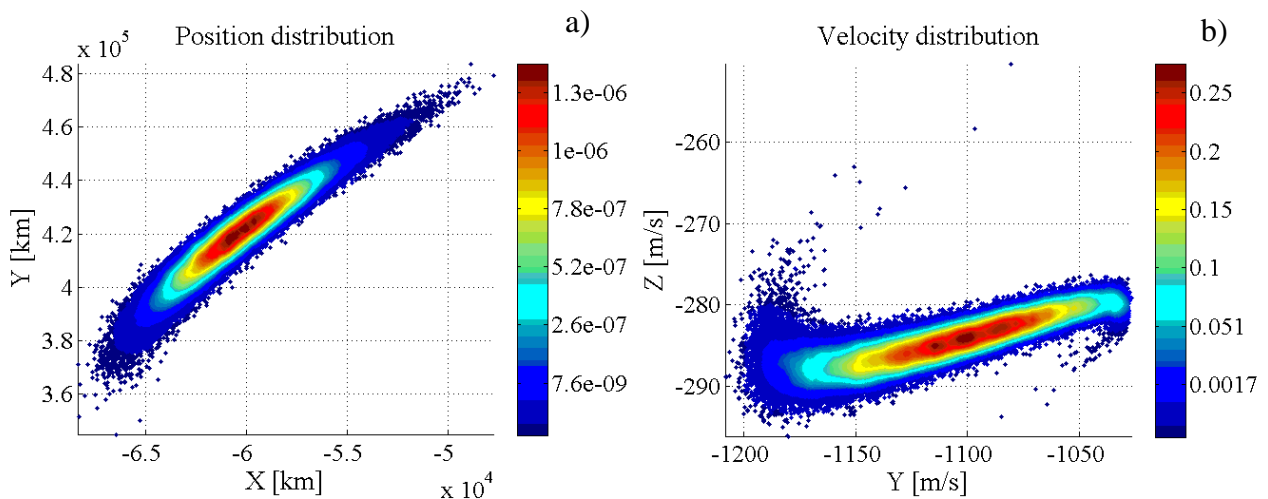


**Figure 11. Statistical distribution with 3rd order STTs: x-y position distribution (a), x-z velocity distribution (b).**

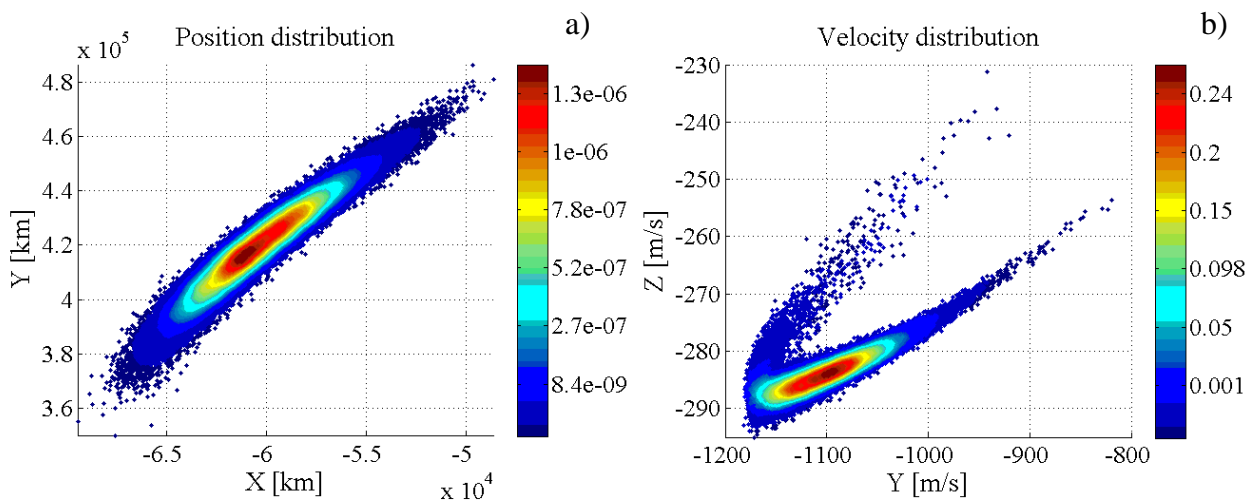


**Figure 12. Statistical distribution with 4th order STTs: x-y position distribution (a), x-z velocity distribution (b).**

From Figure 10 one can see that the 2<sup>nd</sup> order STTs distribution of velocity has a teardrop shape which is still far from the result in Figure 6. The third order STT approximation performs slightly better (Figure 11b)) and only the fourth order STTs approximation resembles the uncertain region obtained with the full MCS, although with many samples scattered far from the actual uncertain region (see Figure 12b)).

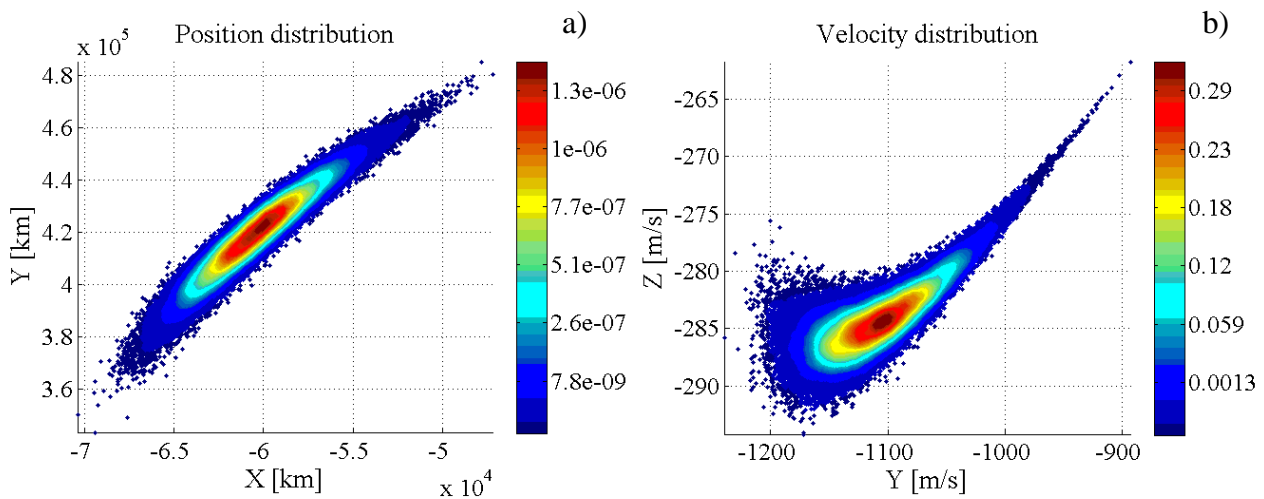


**Figure 13. Statistical distribution with 2nd order PCE: x-y position distribution (a), x-z velocity distribution (b).**

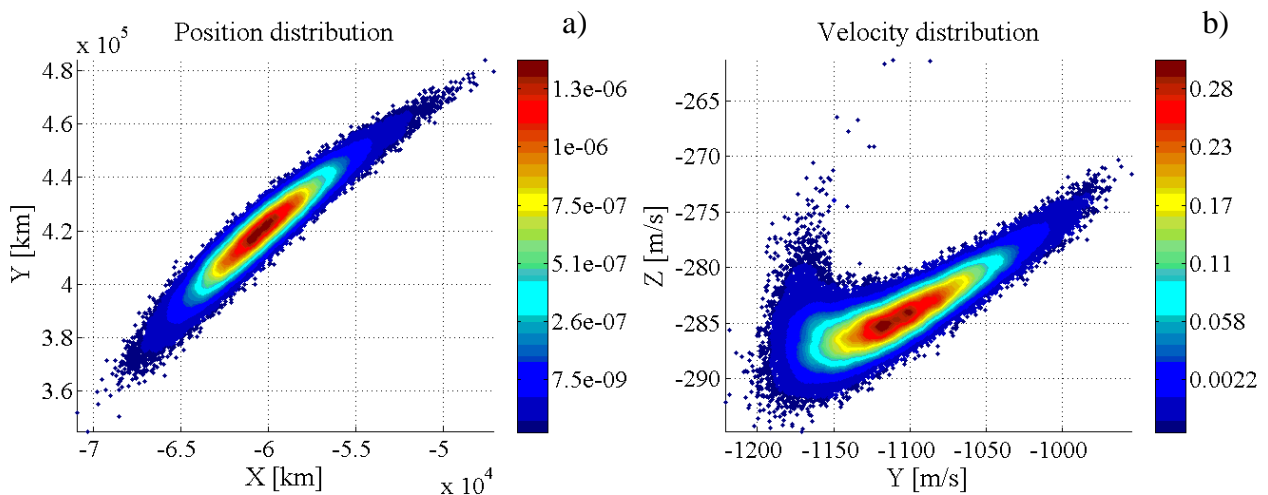


**Figure 14. Statistical distribution with 3rd order PCE: x-y position distribution (a), x-z velocity distribution (b).**

PCEs show better accuracy in the description of the distribution (see Figure 13 to Figure 17). A 2<sup>nd</sup> order PCE provides a better representation than 2<sup>nd</sup> and 3<sup>rd</sup> order STTs, as can be seen in Figure 13. The representation improves as the order increases from 3<sup>rd</sup> to 6<sup>th</sup> (see Figure 14b) to Figure 17b)).

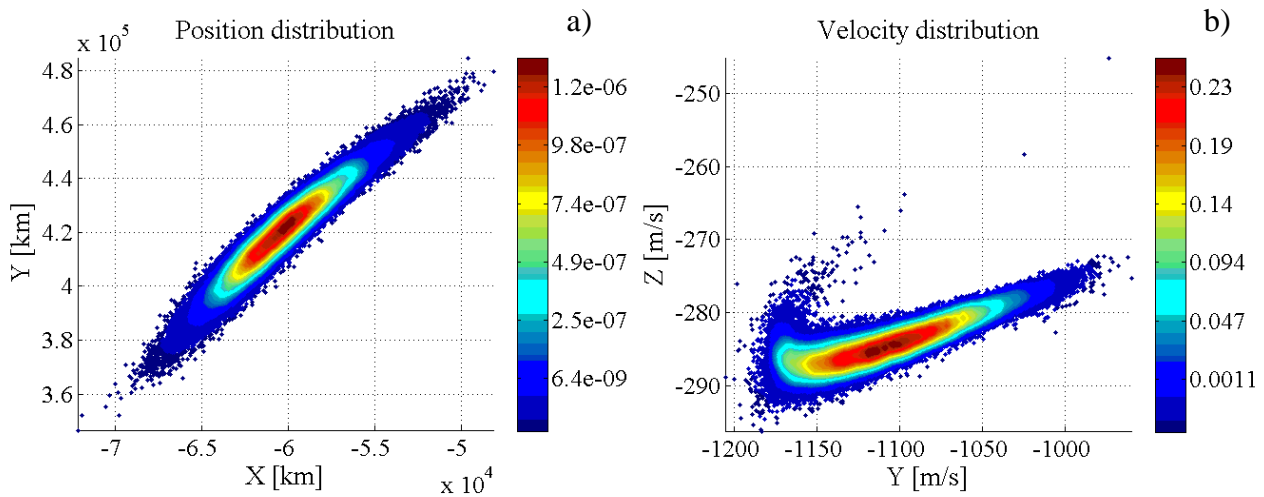


**Figure 15. Statistical distribution with 4th order PCE: x-y position distribution (a), x-z velocity distribution (b).**

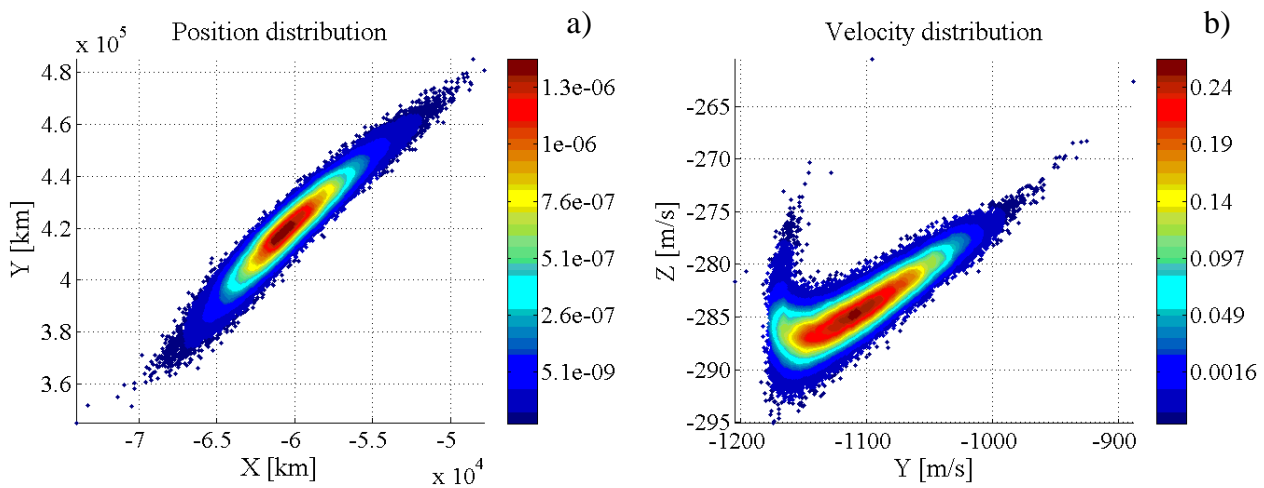


**Figure 16. Statistical distribution with 5th order PCE: x-y position distribution (a), x-z velocity distribution (b).**

The 6<sup>th</sup> order PCE distributions, in Figure 17, are almost coincident with the full the ones derived from the full MCS. The PCE displayed the remarkable ability to globally represent the distribution

better than the SSTs. As to be expected the STTs representation is more accurate nearer the nominal solution and loses accuracy as the sampled points move away from it. The PCE instead is computed by sampling globally over the uncertain space and, thus, achieves a better global representation.

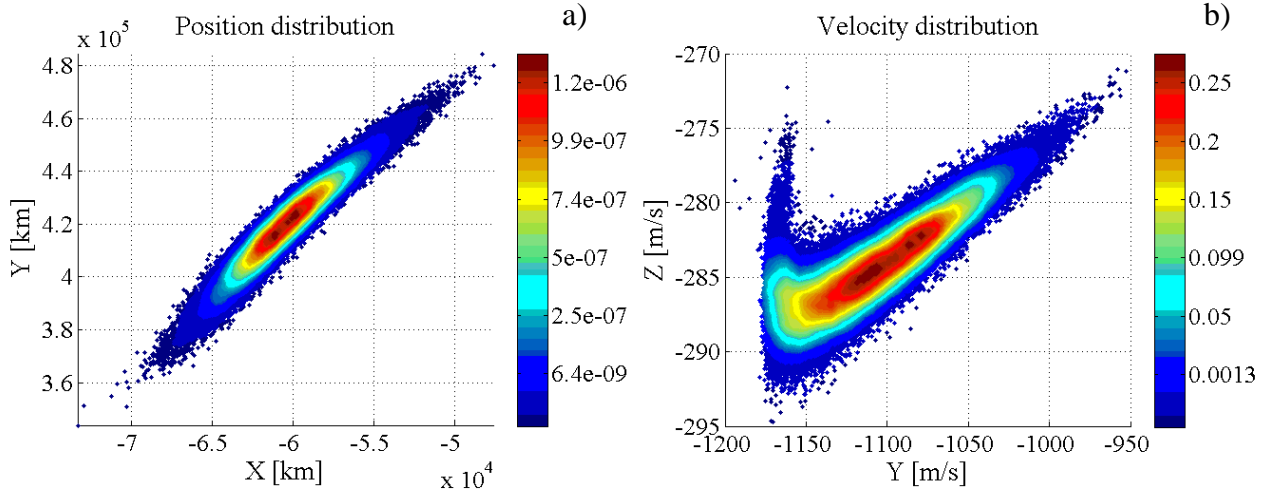


**Figure 17. Statistical distribution with 6th order PCE: x-y position distribution (a), x-z velocity distribution (b).**

### 2.3.2 Impact Analysis

Through the numerical comparison of Section 2.3.1.1 as well with the topological comparisons in Section 2.3.1.3, we have seen that the PCEs outperform the UT and STTs methods. Given the numerical accuracy and capability to describe the distribution of position and velocity components, we want to see if we can use the PCE expansion to estimate the impact rate of the proposed disposal trajectory. The impact rate  $r_{impact}$  is calculated by finding the number of sampled trajectories  $N_{impacts}$  intersecting the Moon surface:

$$r_{impact} = 100 \frac{N_{impacts}}{N_{samples}} \% \quad (31)$$

The impact is identified when the periselene is below the radius of the Moon:

$$r_{perigee}(\chi_i) \leq R_{Moon} \quad (32)$$

where  $r_{perigee}$  is the response function representation of the periapsis in terms of initial uncertain parameters;  $R_{Moon}$  is the Moon mean radius. The response function has been sampled  $10^5$  times with the samples generated through the Mahalanobis decorrelation transformation (see Section 2.2.1). The approximation that we used here is to reconstruct the distribution few hours before the nominal impact time and then consider the orbital parameters to derive the distribution of the impacting particles following the criteria of Eq.(31). The orbital anomaly  $\theta_{impact}$  corresponding to the intersection with the Moon surface is given by the following:

$$\theta_{impact} : r(\theta, \chi_i) = R_{Moon} \quad (33)$$

In this way it is then possible to convert the intersection point back to Cartesian coordinates and represent the distribution of the impacting particles on the Moon. This is due to the fact that the description of the distribution cannot be performed using a low degree polynomial as the particle will impact at different instants of time while some of them will miss the surface.

We first compare the impact rate for MC and PCE in Table 6. We can deduce that as the order of the PCE increases, the error relatively to MC simulations reduces, at least starting from order 3. The increase in order 3 can be adducted to the samples distribution itself. We see that a 6<sup>th</sup> order

We want to see then if this accuracy reflects in the distribution on the Moon surface. Figure 18 to Figure 20 report the samples density and distribution on the south hemisphere of the Moon where

all the impacting samples end up. PCE produces an impact rate which is just a 1% higher than the true value from MC.

**Table 6. Impact rate comparison between MC and PCE: 1% manoeuvre error and 5 km dispersion error (per component).**

	MC	PCE ord 2	PCE ord 3	PCE ord 4	PCE ord 5	PCE ord 6
Impact rate %	19.951	20.858	21.007	20.515	20.430	20.180
Relative error %	/	4.55	5.41	2.83	2.40	1.14

The density distribution was defined as the ratio between the particles hitting a circle of 30 km radius centred on each impacting particle and the total number of particles and the corresponding area. As one can see the distribution and particle density are very similar.

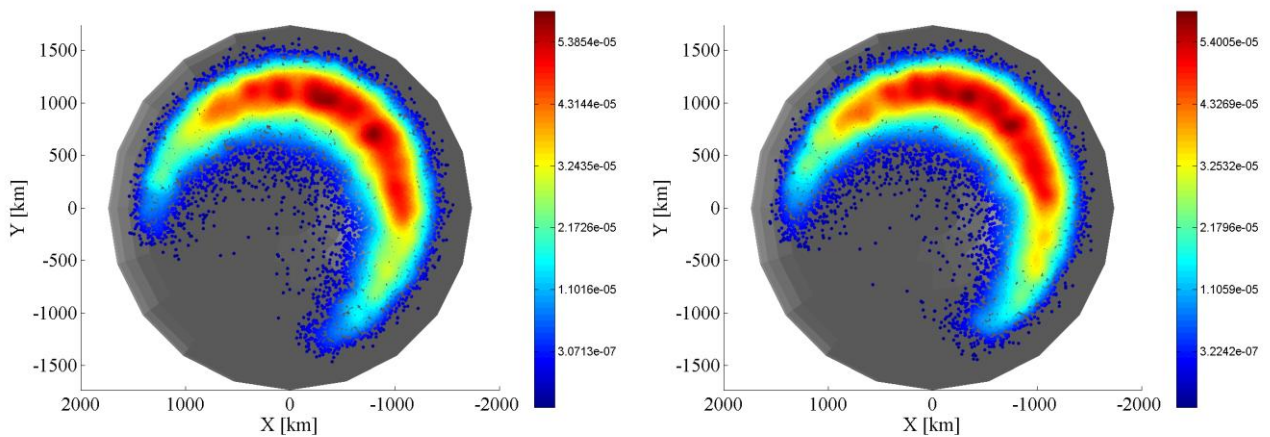


**Figure 18. Particles dispersion and density at impact for 1% manoeuvre error and 5 km dispersion error (per component): MC (left) and PCE order 2 (right).**

Apparently the low order distributions spread over the south hemisphere similarly to the MC, although the error in impact rate is quite high. Indeed the areas with higher probability density of MC in the left picture of Figure 18 are better represented by the higher order.



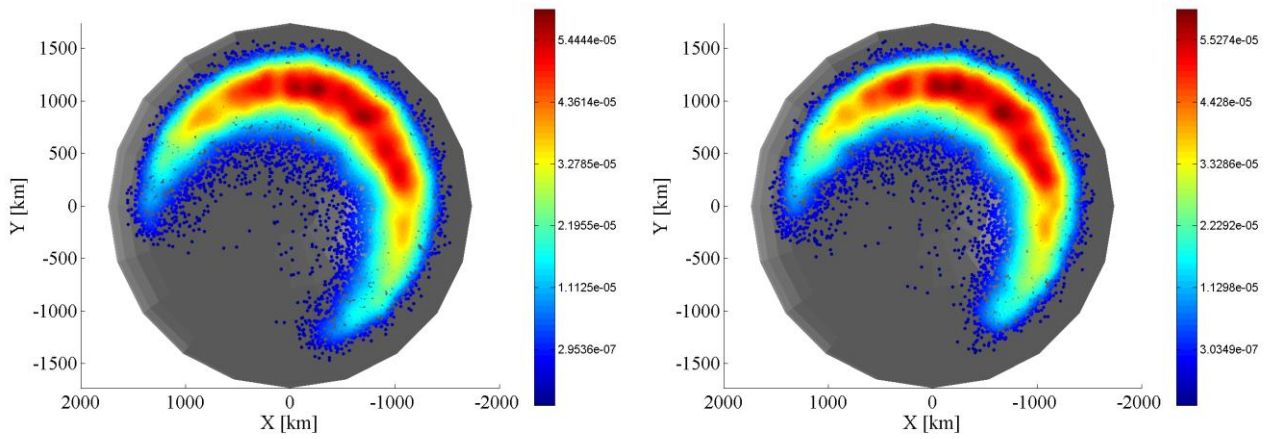


**Figure 19. Particles dispersion and density at impact for 1% manoeuvre error and 5 km dispersion error (per component): PCE order 3 (left) and PCE order 4 (right).**

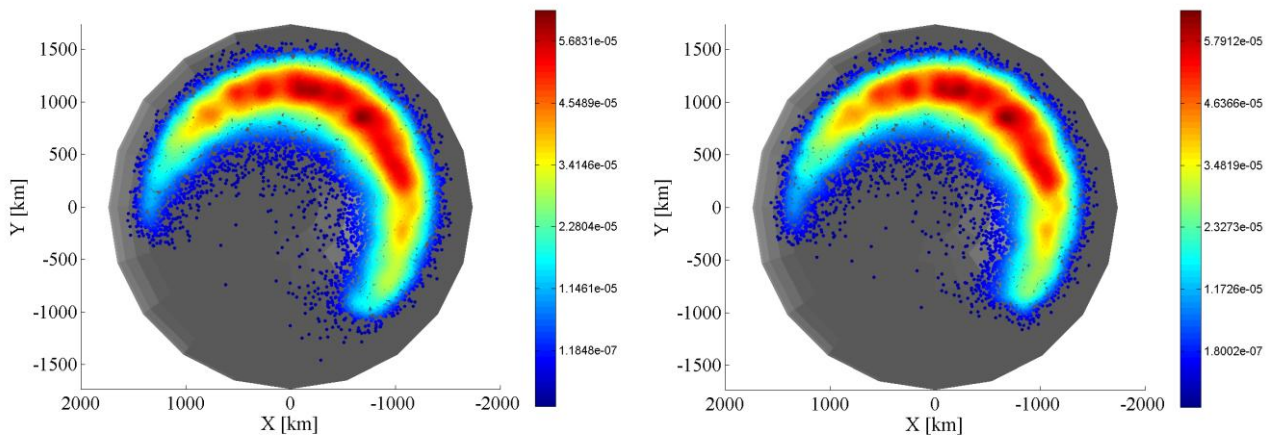


**Figure 20. Particles dispersion and density at impact for 1% manoeuvre error and 5 km dispersion error (per component): PCE order 5 (left) and PCE order 6 (right).**

The reason is due to the fact that the PCE representation of low order is particularly effective at reconstructing the area closer to the mean, given the shape of the grid shown in Figure 3 of Section 2.2.4.1. At the same time all the impacting particles are concentrated in the area closer to the nominal trajectory. If we want to obtain a distribution more similar to the MC one, we might need

to use more samples for the higher order. In fact if we employ 200,000 samples as in Figure 20, the distribution for order 6 becomes more similar to the MC one. Remind that we do not need additional integration, thus no additional integration time is required.

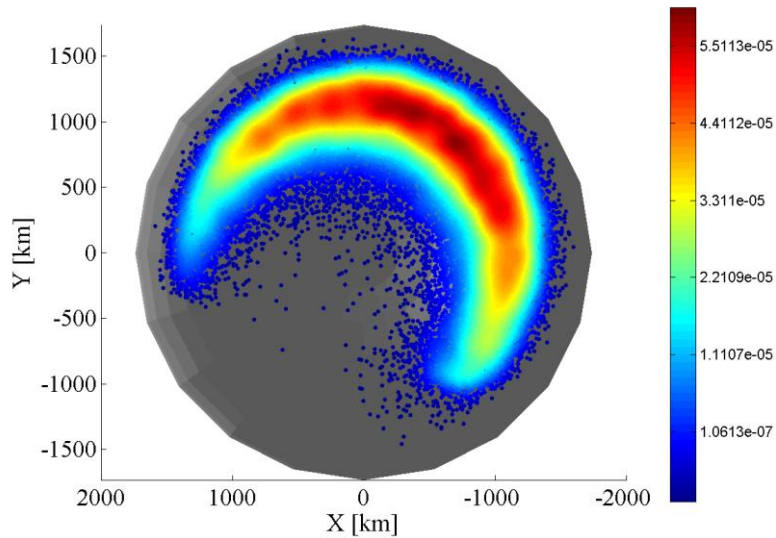


**Figure 21. Particles dispersion and density at impact for 1% manoeuvre error and 5 km dispersion error (per component): PCE order 6 with 200,000 samples.**

As a confirmation of this, we consider another case where the dispersion in position is limited to 1 km per component, while the one for the velocity is just 0.1% of the disposal manoeuvre. In this way almost all the samples will impact the Moon, as shown in Table 7. As in the previous case we see that the higher order PCE are more accurate in the description of the overall impact statistics. In general there is a very good agreement between MC simulation and PCE expansions.

The difference is less than 0.05 % with the actual number calculated with MC. The error for a 6<sup>th</sup> order is even lower than 0.005%, thanks to the less deformation extent of this distribution. Nonetheless it is possible to use a lower order to capture the whole statistics.

**Table 7. Impact rate comparison between MC and PCE: 0.1% manoeuvre error and 1 km dispersion error (per component).**

	MC	PCE ord 2	PCE ord 3	PCE ord 4	PCE ord 5	PCE ord 6
Impact rate %	92.326	92.354	92.337	92.331	92.331	92.329
Relative error %	/	0.03	0.012	0.005	0.005	0.004

In fact one can see from Figure 22 to Figure 24 that the particles are less scattered with respect to the previous case. The actual shape of the MC distribution of Figure 22 left is similar to the one reported in Figure 18 left, although it is less extended over the surface.

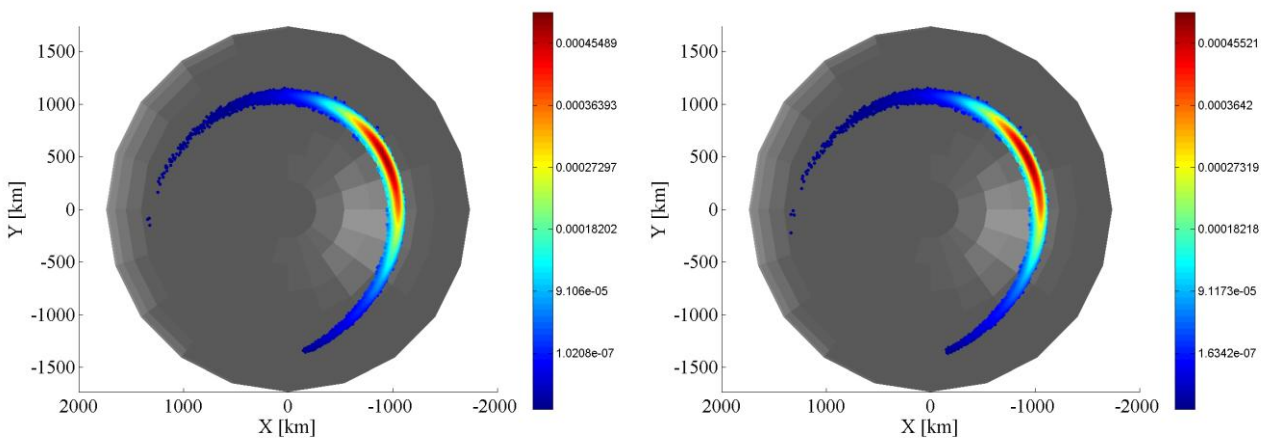


**Figure 22. Particles dispersion and density at impact for 0.1% manoeuvre error and 1 km dispersion error (per component): MC (left) and PCE order 2 (right).**

It is also clear from this figure that the effect of non-linearities in Figure 18 is to spread and move the area where the density is relatively higher. In fact the maximum density is approximately one order of magnitude higher than the previous case ( $4.5 \cdot 10^{-4}$  against  $5.4 \cdot 10^{-5}$ ). For what concerns the PCE representation, any order can describe the distribution fairly well, as direct consequence of the lower level of dispersion.

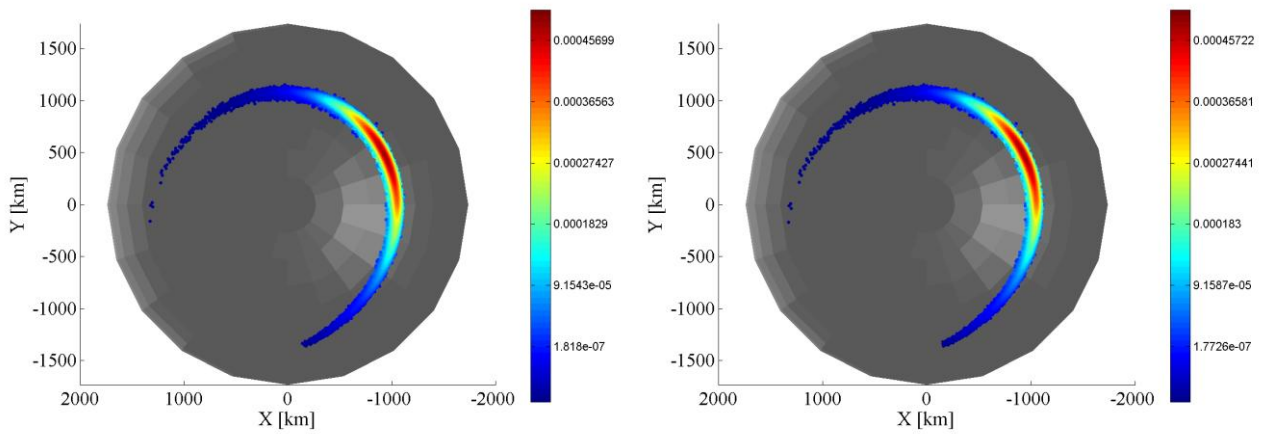


**Figure 23. Particles dispersion and density at impact for 0.1% manoeuvre error and 1 km dispersion error (per component): PCE order 3 (left) and PCE order 4 (right).**

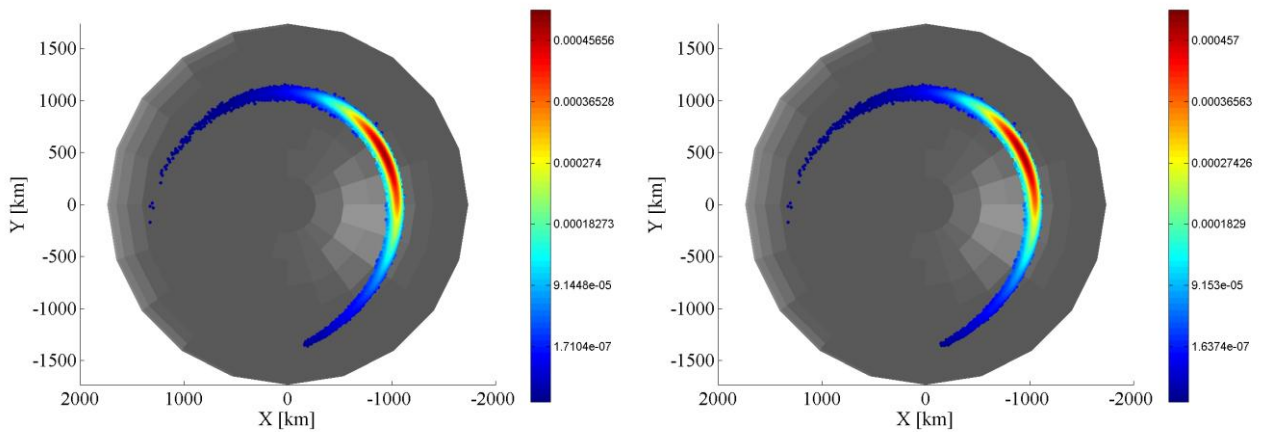


**Figure 24. Particles dispersion and density at impact for 0.1% manoeuvre error and 1 km dispersion error (per component): PCE order 5 (left) and PCE order 6 (right).**

## 2.4 Summary

In this Chapter we have applied the STTs and PCE expansions to the study of the propagation of uncertainties in the initial conditions for the disposal from LPO to the Moon. We studied in particular the disposal of Herschel from the Lagrangian Point  $L_2$  where the initial disposal

conditions are affected by uncertainties due to both orbit determination and system performance. Multivariate Hermite polynomials were employed, because they have infinite support range and they can easily be applied to the propagation of the initial conditions uncertainty.

It emerged that PCE are an appropriate tool for this type of analyses and provide accurate predictions at low computational cost. The particular PCE proposed in this Chapter is based on multivariate Hermite polynomials with integration over Genz and Keister sparse-grids. Multivariate Hermite polynomials are chosen because they have infinite support and can well represent mixtures of Gaussian distributions. Two key features of PCE are exploited: the ability to produce functional representations of any generic stochastic distribution and the direct derivation of the statistical moments from the coefficients of the PCE expansion. The latter is used when comparing the lower order statistic moments, i.e. the mean and covariance, against UT and low order SSTs while the former is exploited when computing the impact rate.

The MC method has been used to validate the procedures. The main drawback of MC is represented by the slow convergence rate which requires running a great number of simulations. Unless more efficient method to deal with the propagation of higher order terms of the SSTs, also the SSTs have proved to be not that efficient in terms of computational time. This is a problem when several reference trajectories have to be tested. On the contrary, the PCE expansion proves to be a valid alternative for dealing with such a problem with considerable less computational effort and the capability to include nonlinear effects with no approximation. In fact we have seen that first order Taylor expansions cannot properly handle the propagation of the covariance matrix especially when the trajectory comes closer to the Moon where the nonlinear effects are also magnified by the non-

uniform gravity field of this body. The resulting distribution would be completely wrong with respect to the actual one.

The results show that, for such a complex nonlinear problem, one can efficiently and accurately approximate the response function using a statistical polynomial approximation. Once the coefficients of the expansions have been obtained, one can generate many samples and apply any criteria to draw figures of interests. In our case we obtained the number of impacts on the Moon surface. The only care that must be used regards the minimum order required to obtain a satisfactory approximation. In principle one can test the PCE methods for the disposal problem, and identify the order of polynomials which can describe the disposal statistic with the required accuracy. Then one can stick to this order for similar disposal trajectories. We have seen that when the initial dispersion is quite small, the error between PCEs and MC is not meaningful. In fact we have noticed that the critical part of the transfer is represented by the last few hours before the nominal impact, because the deformation and stretch of the distribution become untreatable with a low order expansion if the initial dispersion is relatively big. For this reason we have had to simplify the final phase considering the Keplerian elements of the PCE samples. When considering the final distribution on the Moon, we have seen that the PCE solution resembles the MC, keeping in mind that a perfect superimposition is not possible unless the order of the polynomials is dramatically increased.

### 3 Filtering Techniques

This Chapter presents an overview of the main state of the art estimation techniques commonly applied to nonlinear dynamics problems. Two main families of filters were considered in the following of this chapter. The first family is the one of Kalman filters and the second one is the one of  $H_\infty$  filters, also called minmax filters. These works on different premises but both share a common structure, in which the variables object of the estimation process are first propagated between the instants of time, in which the measurements are received, to obtain a time update estimate at the subsequent time the new measurements are available. At this stage the measurements are included via a suitable gain to obtain a measurement update. Examples of the application of these techniques are provided in the Sun-Earth-Moon four-body problem framework and in the Sun-Asteroid three-body problem during proximal motion, for a number of filters which inherits the method seen for uncertainty propagation of Chapter 2.

#### 3.1 Kalman Filtering

Before introducing the following nonlinear filter based on the extension of the Kalman Filter, it seems opportune to briefly describe how the Kalman filter (KF) was derived. There are different versions of Kalman filter, based on continuous or discrete dynamics. Given the fact that all the work of this thesis is based on discrete set of measurements, we decided to deal this topic using the discrete system.

First of all consider a generic linear discrete-time system between two subsequent instant of time  $t_k$  and  $t_{k+1}$  as

$$\begin{aligned}\mathbf{x}_{k+1} &= \mathbf{F}_k \mathbf{x}_k + \mathbf{G}_k^u \mathbf{u}_k + \mathbf{w}_{k+1} \\ \mathbf{y}_{k+1} &= \mathbf{H}_{k+1} \mathbf{x}_{k+1} + \boldsymbol{\zeta}_{k+1}\end{aligned}\quad (34)$$

$\mathbf{x}_k$  is the state variable, whose dynamics depends on the matrix  $\mathbf{F}_k$  which rules the evolution of the system between two subsequent instant of time, if no known input  $\mathbf{u}_k$  is applied through the matrix  $\mathbf{G}_k^u$ ;  $\mathbf{y}_{k+1}$  is the set of available measurements of the variable  $\mathbf{x}_k$  through the measurement matrix  $\mathbf{H}_{k+1}$ .  $\mathbf{w}_k$  and  $\boldsymbol{\zeta}_k$  are white, zero-mean, uncorrelated process, or system, and measurement noise respectively. Statistical properties of these noises are known:

$$\begin{aligned}\mathbf{w}_k &\sim N(0, \mathbf{Q}_k) \\ \boldsymbol{\zeta}_k &\sim N(0, \mathbf{R}_k) \\ E[\mathbf{w}_k \mathbf{w}_j^T] &= \mathbf{Q}_k \delta_{k-j} \\ E[\boldsymbol{\zeta}_k \boldsymbol{\zeta}_j^T] &= \mathbf{R}_k \delta_{k-j} \\ E[\boldsymbol{\zeta}_k \mathbf{w}_j^T] &= 0\end{aligned}\quad (35)$$

where  $E[\dots]$  is used to indicate the expected value of the quantity between brackets,  $\delta_{k-j}$  is the Kronecker delta function ( $\delta_{k-j} = 1$  if  $k = j$ ,  $\delta_{k-j} = 0$  otherwise). The goal is to estimate the state  $\mathbf{x}_k$  based on the knowledge of  $\mathbf{F}_k - \mathbf{G}_k$  and the availability of noisy measurements  $\mathbf{y}_{k+1}$ . Using all the measurements up to the time  $k$ , it is possible to form an a posteriori estimate  $\tilde{\mathbf{x}}_k^+$ . The "+" superscript indicates that the estimate is a posteriori. If all of the measurements are available up to



time  $k-1$ , one can look for an a priori estimate  $\tilde{\mathbf{x}}_k^-$ . The "-" superscript denotes that the estimate is a priori.

In order to derive the Kalman filter structure, we want to find an estimator of Eq.(34) as

$$\tilde{\mathbf{x}}_{k+1}^+ = \tilde{\mathbf{x}}_{k+1}^- + \mathbf{K}_{k+1}(\mathbf{y}_{k+1} - \mathbf{H}_{k+1}\tilde{\mathbf{x}}_{k+1}^-) \quad (36)$$

$\tilde{\mathbf{x}}_{k+1}^-$  is obtained by Eq.(34) without considering the noise;  $\mathbf{K}_{k+1}$  is the Kalman gain which has to be found through an optimality criterion. The optimality criterion is to minimize the sum of the variances of the estimation errors at time  $k+1$ , which is given by the following:

$$J_{k+1} = E[(\boldsymbol{\varepsilon}_{k+1}^+)^T \boldsymbol{\varepsilon}_{k+1}^+] = E[(\mathbf{x}_{k+1} - \tilde{\mathbf{x}}_{k+1}^+)^T (\mathbf{x}_{k+1} - \tilde{\mathbf{x}}_{k+1}^+)] = Tr(\mathbf{P}_{k+1}^+) \quad (37)$$

where  $\mathbf{P}_{k+1}$  is the covariance matrix of the state, and  $Tr$  indicates the trace of the matrix. Before minimising the function, let us have a look at  $\mathbf{P}_{k+1}$  by substituting  $\hat{\mathbf{x}}_{k+1}^+$  from Eq.(36)

$$\begin{aligned} \boldsymbol{\varepsilon}_{k+1}^+ &= (\mathbf{I} - \mathbf{K}_{k+1}\mathbf{H}_{k+1})(\mathbf{x}_{k+1} - \tilde{\mathbf{x}}_{k+1}^-) - \mathbf{K}_{k+1}\boldsymbol{\varsigma}_{k+1} = (\mathbf{I} - \mathbf{K}_{k+1}\mathbf{H}_{k+1})\boldsymbol{\varepsilon}_{k+1}^- - \mathbf{K}_{k+1}\boldsymbol{\varsigma}_{k+1} \\ \mathbf{P}_{k+1}^+ &= E[(\mathbf{x}_{k+1} - \tilde{\mathbf{x}}_{k+1}^+)(\mathbf{x}_{k+1} - \tilde{\mathbf{x}}_{k+1}^+)^T] \\ &= E[(\mathbf{I} - \mathbf{K}_{k+1}\mathbf{H}_{k+1})\boldsymbol{\varepsilon}_{k+1}^- - \mathbf{K}_{k+1}\boldsymbol{\varsigma}_{k+1}]^T [(\mathbf{I} - \mathbf{K}_{k+1}\mathbf{H}_{k+1})\boldsymbol{\varepsilon}_{k+1}^- - \mathbf{K}_{k+1}\boldsymbol{\varsigma}_{k+1}] \\ &= \mathbf{K}_{k+1}E[\mathbf{v}_{k+1}(\boldsymbol{\varepsilon}_{k+1}^-)^T](\mathbf{I} - \mathbf{K}_{k+1}\mathbf{H}_{k+1})^T - (\mathbf{I} - \mathbf{K}_{k+1}\mathbf{H}_{k+1})E[\boldsymbol{\varepsilon}_{k+1}^-\boldsymbol{\varsigma}_{k+1}^T] + \mathbf{K}_{k+1}E[\boldsymbol{\varsigma}_{k+1}\boldsymbol{\varsigma}_{k+1}^T]\mathbf{K}_{k+1} \\ &= (\mathbf{I} - \mathbf{K}_{k+1}\mathbf{H}_{k+1})\mathbf{P}_{k+1}^-(\mathbf{I} - \mathbf{K}_{k+1}\mathbf{H}_{k+1}) + \mathbf{K}_{k+1}\mathbf{R}_{k+1}\mathbf{K}_{k+1} \end{aligned} \quad (38)$$

where we have exploited that the measurements noise and the state are not correlated and  $E[\boldsymbol{\varepsilon}_{k+1}^-\boldsymbol{\varsigma}_{k+1}^T] = 0$ . Before calculating the Kalman gain, we need to calculate the covariance matrix  $\mathbf{P}_{k+1}^-$  as a function of the posteriori covariance matrix at the previous time step. This is simply given by the definition of covariance matrix and of the dynamics equations in Eq.(34):

$$\begin{aligned}
\mathbf{P}_{k+1}^- &= E[(\mathbf{x}_{k+1} - \tilde{\mathbf{x}}_{k+1}^-)(\mathbf{x}_{k+1} - \tilde{\mathbf{x}}_{k+1}^-)^T] = E[(\mathbf{F}_k(\mathbf{x}_k - \tilde{\mathbf{x}}_k^+) + \mathbf{w}_k)(\mathbf{F}_k(\mathbf{x}_k - \tilde{\mathbf{x}}_k^+) + \mathbf{w}_k)^T] \\
&= \mathbf{F}_k E[(\mathbf{x}_k - \tilde{\mathbf{x}}_k^+)(\mathbf{x}_k - \tilde{\mathbf{x}}_k^+)^T] \mathbf{F}_k^T + E[\mathbf{w}_k \mathbf{w}_k^T] = \\
&= \mathbf{F}_k \mathbf{P}_k^+ \mathbf{F}_k^T + \mathbf{Q}_k
\end{aligned} \tag{39}$$

Now the Kalman gain is obtained by deriving the function  $J_{k+1}$  with respect to  $\mathbf{K}_{k+1}$  and setting it equal to zero:

$$\frac{\partial J_{k+1}}{\partial \mathbf{K}_{k+1}} = 2(\mathbf{I} - \mathbf{K}_{k+1} \mathbf{H}_{k+1}) \mathbf{P}_{k+1}^- \mathbf{H}_{k+1}^T + 2\mathbf{K}_{k+1} \mathbf{R}_{k+1} \tag{40}$$

In this way the Kalman gain is given as:

$$\mathbf{K}_{k+1} = \mathbf{P}_{k+1}^- \mathbf{H}_{k+1}^T (\mathbf{H}_{k+1} \mathbf{P}_{k+1}^- \mathbf{H}_{k+1}^T + \mathbf{R}_{k+1})^{-1} \tag{41}$$

The set of equations Eqs.(41), (39) and (36) represents the general form of the linear discrete-time Kalman filter, which is a starting point for the following nonlinear methods based on the Kalman filter.

### 3.2 The Extended Kalman Filter

The EKF is a well-known dynamic optimal filter which was first employed in the Apollo program (Battin and Levine, 1970). The EKF linearizes the equations of motion about the estimated state.

The dynamics and measurements model used in the filtering are as follows:

$$\begin{aligned}
\dot{\mathbf{x}}(t) &= \mathbf{f}(\mathbf{x}(t), t, \mathbf{w}) \\
\mathbf{y}_k &= \mathbf{h}(\mathbf{x}_k, t, \boldsymbol{\zeta}_k)
\end{aligned} \tag{42}$$

where  $\mathbf{f}(\mathbf{x}(t), t, \mathbf{w})$  is a vector field of the dynamical system. The function  $\mathbf{h}(\mathbf{x}_k, t, \boldsymbol{\zeta}_k)$  is the measurements model,  $\mathbf{x}_k$  is the  $k^{\text{th}}$  state vector at the measurement time  $t_k$ .

The EKF is composed of two conceptually distinct phases: the time update and the measurements update. The time update phase consists of the propagation of the latest estimate  $\tilde{\mathbf{x}}_k^+$  to obtain an a-priori estimate at current epoch  $\tilde{\mathbf{x}}_{k+1}^-$  with the corresponding covariance matrix  $\mathbf{P}_{k+1}^-$  (Montenbruck and Gill, 2000):

$$\begin{aligned}\tilde{\mathbf{x}}_{k+1}^- &= \mathbf{x}(t_{k+1}; \mathbf{x}(t_k)) = \tilde{\mathbf{x}}_k^+ \\ \mathbf{P}_{k+1}^- &= \mathbf{F}_k \mathbf{P}_k^+ \mathbf{F}_k^T\end{aligned}\quad (43)$$

where the predicted state  $\tilde{\mathbf{x}}_{k+1}^-$  is obtained by integrating forward Eq.(42) starting from the latest state estimate  $\tilde{\mathbf{x}}_k^+$ ;  $\mathbf{F}_{k+1}$  represents the state transition matrix (STM), commonly indicated as  $\boldsymbol{\Phi}_{k+1}$ , coming from the linearization of the dynamic equations about the updated state:

$$\begin{aligned}\mathbf{F}_k &= \boldsymbol{\Phi}_{k+1}(t_{k+1}, t_k) = \boldsymbol{\Phi}_k(t_k, t_k) + \int_{t_k}^{t_{k+1}} \mathbf{f}(\mathbf{x}, t) \boldsymbol{\Phi}_{k+1}(t, t_k) dt \approx \mathbf{I} + \mathbf{A}_k \Delta t \\ \mathbf{A}_k &= \frac{\partial \mathbf{f}(\mathbf{x}_k^+)}{\partial \mathbf{x}_k^+}\end{aligned}\quad (44)$$

being  $\boldsymbol{\Phi}_k(t_k, t_k)$  equal to the identity matrix. The measurement update phase consists of the computation of the Kalman gain  $\mathbf{K}_{k+1}$  and the state estimate  $\tilde{\mathbf{x}}_{k+1}^+$  and covariance matrix,  $\mathbf{P}_{k+1}^+$  updates:

$$\begin{aligned}
\mathbf{K}_{k+1} &= \mathbf{P}_{k+1}^- \mathbf{H}_{k+1}^T \left[ \mathbf{H}_{k+1} \mathbf{P}_{k+1}^- \mathbf{H}_{k+1}^T + \mathbf{R} \right]^{-1} \\
\tilde{\mathbf{x}}_{k+1}^+ &= \tilde{\mathbf{x}}_{k+1}^- + \mathbf{K}_{k+1} (\mathbf{y}_{k+1} - \mathbf{h}(\tilde{\mathbf{x}}_{k+1}^-)) \\
\mathbf{H}_{k+1} &= \frac{\partial \mathbf{h}(\tilde{\mathbf{x}}_{k+1}^-)}{\partial \tilde{\mathbf{x}}_{k+1}^-} \\
\mathbf{P}_{k+1}^+ &= (\mathbf{I} - \mathbf{K}_{k+1} \mathbf{H}_{k+1}) \mathbf{P}_{k+1}^-
\end{aligned} \tag{45}$$

where  $\mathbf{H}_{k+1}$  is the Jacobian matrix of the measurement function. The Kalman gain as reported in Eq.(45) minimizes the a posteriori error covariance matrix. It represents a function of the relative certainty of the measurements and current state. As the gain increases the measurements are trusted more and the estimates rely less on the prediction model. On the contrary as the gain decreases, measurements tend to be ignored and the estimate relies more heavily on the prediction model.

### 3.3 The Unscented Kalman Filter

The unscented Kalman filter (Julier et al., 1995) works on the premises that by using a limited set of optimally chosen sample, it should be easier to approximate a Gaussian distribution than to approximate a nonlinear function. The UKF was shown to be preferable to the Extended Kalman filter (EKF) in the case of nonlinear systems as the expected error in terms of mean and covariance matrix is lower, and it does not require the derivation of the Jacobian matrix (Crassidis and Junkins, 2001).

Once the dynamics and measurement models have been defined as in Eq.(42), one can briefly describe the Unscented Kalman filter. The filter state vector and covariance matrix updates are represented as follows:

$$\begin{aligned}\tilde{\mathbf{x}}_k^+ &= \tilde{\mathbf{x}}_k^- + \mathbf{K}_k \mathbf{v}_k \\ \mathbf{P}_k^+ &= \mathbf{P}_k^- - \mathbf{K}_k \mathbf{P}_k^{\omega\nu} \mathbf{K}_k^T\end{aligned}\quad (46)$$

where the innovation process  $\mathbf{v}_k$  and the gain  $\mathbf{K}_k$  are:

$$\begin{aligned}\mathbf{v}_k &\equiv \mathbf{y}_k - \tilde{\mathbf{y}}_k^- = \mathbf{y}_k - \mathbf{h}(\tilde{\mathbf{x}}_k^-, k) \\ \mathbf{K}_k &= \mathbf{P}_k^{xy} (\mathbf{P}_k^{\omega\nu})^{-1}\end{aligned}\quad (47)$$

The matrix  $\mathbf{P}_k^{xy}$  is the cross-correlation between  $\tilde{\mathbf{x}}_k^-$  and  $\tilde{\mathbf{y}}_k^-$ . The approach used in the filter design requires augmenting the covariance matrix with:

$$\mathbf{P}_k^a = \begin{bmatrix} \mathbf{P}_k^+ & \mathbf{P}_k^{x\omega} & \mathbf{P}_k^{x\nu} \\ (\mathbf{P}_k^{x\omega})^T & \mathbf{Q}_k & \mathbf{P}_k^{\omega\nu} \\ (\mathbf{P}_k^{x\nu})^T & (\mathbf{P}_k^{\omega\nu})^T & \mathbf{R}_k \end{bmatrix}\quad (48)$$

where  $\mathbf{P}_k^{xw}$  is the correlation between the state error and process noise,  $\mathbf{P}_k^{xv}$  is the correlation between the state error and measurement noise, and  $\mathbf{P}_k^{wv}$  is the correlation between the process noise and measurement noise, which is zero in this case. If  $L$  is the number of elements per column of the augmented covariance matrix  $\mathbf{P}_k^a$ , then a set of  $2L$  samples  $\mathbf{Y}_k^a(i)$ , with  $i = 1, \dots, 2L$  called sigma points, are generated such that:

$$\begin{aligned}\mathbf{Y}_k^a(i) &= \boldsymbol{\sigma}_k(i) + \tilde{\mathbf{x}}_k^a \\ \boldsymbol{\sigma}_k &= \pm \eta \sqrt{\mathbf{P}_k^a} \\ \mathbf{Y}_k^a(0) &= \tilde{\mathbf{x}}_k^a\end{aligned}\quad (49)$$

where  $\eta$  is a suitable scaling factor,  $\tilde{\mathbf{x}}_k^a$  is the augmented state,

$$\tilde{\mathbf{x}}_k^a = \begin{bmatrix} \tilde{\mathbf{x}}_k \\ \mathbf{0}_{q \times 1} \\ \mathbf{0}_{z \times 1} \end{bmatrix} \quad (50)$$

$q$  is the dimension of  $\mathbf{w}$ , and  $z$  is the dimension of  $\mathbf{y}_k$ . The sampled sigma points are then:

$$\mathbf{Y}_k^a(i) = \begin{bmatrix} \mathbf{Y}_k^x(i) \\ \mathbf{Y}_k^w(i) \\ \mathbf{Y}_k^c(i) \end{bmatrix} \quad (51)$$

$\mathbf{Y}_k^x$  is the vector of the first  $n$  (size of  $\mathbf{x}_k$ ) elements of  $\mathbf{Y}_k^a$ ,  $\mathbf{Y}_k^w$  is a vector of the next  $q$  elements of  $\mathbf{Y}_k^a$  and  $\mathbf{Y}_k^c$  is the vector of the last  $z$  components of  $\mathbf{Y}_k^a$ . The sigma points are transformed or propagated using the UT of Eq.(20), here specialised for the state and measurements calculation:

$$\begin{aligned} \mathbf{Y}_{i,k+1}^a(i) &= \mathbf{f}(\mathbf{Y}_{i,k}^x, \mathbf{Y}_{i,k}^w, \mathbf{u}_k, t_k) \\ \mathbf{Y}_{i,k+1}^c(i) &= \mathbf{h}(\mathbf{Y}_{i,k+1}^x, \mathbf{u}_{k+1}, \mathbf{Y}_{i,k+1}^c, t_{k+1}) \end{aligned} \quad (52)$$

The predicted mean of the state vector, the covariance matrix and the mean observation can be approximated using the weighted mean and covariance of the transformed vectors similarly to Eq.(21):

$$\begin{aligned} \tilde{\mathbf{x}}_{k+1}^- &= \sum_{i=0}^{2L} W_i^m \mathbf{Y}_{i,k+1}^x \\ \mathbf{P}_{k+1}^- &= \sum_{i=0}^{2L} W_i^c [\mathbf{Y}_{i,k+1}^x(i) - \tilde{\mathbf{x}}_{k+1}^-] [\mathbf{Y}_{i,k+1}^x(i) - \tilde{\mathbf{x}}_{k+1}^-]^T \\ \tilde{\mathbf{y}}_{k+1}^- &= \sum_{i=0}^{2L} W_i^m \mathbf{Y}_{i,k+1}^c \end{aligned} \quad (53)$$

where  $W_i^m$ ,  $W_i^c$  are suitable weighting factors calculated exactly as in Eq.(22). Finally the updated covariance and the cross correlation matrix are:

$$\begin{aligned}
\mathbf{P}_{k+1}^{yy} &= \mathbf{P}_{k+1}^{DD} = \sum_{i=0}^{2L} W_i^{\text{cov}} [\boldsymbol{\gamma}_{i,k+1} - \tilde{\mathbf{y}}_{k+1}^-][\boldsymbol{\gamma}_{i,k+1} - \tilde{\mathbf{y}}_{k+1}^-]^T \\
\mathbf{P}_{k+1}^{xy} &= \sum_{i=0}^{2L} W_i^{\text{cov}} [\boldsymbol{\Upsilon}_{i,k+1}^x - \tilde{\mathbf{x}}_{k+1}^-][\boldsymbol{\gamma}_{i,k+1} - \tilde{\mathbf{y}}_{k+1}^-]^T
\end{aligned} \tag{54}$$

In this way it is possible to update the filter to the next observation and prediction at time  $t_{k+1}$  using the equations reported in Eq.(46).

### 3.4 High Order Semi-Analytic Extended Kalman Filter

Park and Scheeres (2006a, 2006b) derived analytical expressions of a nonlinear trajectory solution using higher order Taylor series approach and applied the results to spacecraft trajectory calculation, in particular navigation and manoeuvre design. In their work they presented a semi-analytic filtering method by exploiting the STTs to sequentially update the state vector with contributions from each measurement. They called this nonlinear filter High-order semi-Analytic Extended Kalman filter (HAEKF), since the implementation follows the same steps of the conventional Kalman filter. When applied to spacecraft navigation the advantage of using the higher order semi-analytic extended Kalman filter is that the STTs can be calculated offline prior to their usage in the filter itself. This section describes the fundamental aspects which this method is based on. We use here the results of Section 2.2.2, where we introduced the STTs for uncertainty propagation.

When implementing the filter it is necessary to calculate the STTs at each intermediate time, in between  $t_0$  and  $t$ , at which a new measurement is available. The intermediate STTs are called local

STTs. Whereas the global STTs map the deviation at the initial time  $t_0$  to the deviation at time  $t_{k+1}$ , the local STTs map the deviation at time  $t_k$  to the deviation at time  $t_{k+1}$ .

There are two methods to compute the local STTs. The first method integrates all the partials from  $t_k$  to  $t_{k+1}$  without using the information from the global STTs. The second method, indeed, calculates the local STTs from  $t_k$  to  $t_{k+1}$ , having previously integrated the global STTs over the time spans  $t_0 - t_k$  and  $t_0 - t_{k+1}$ . The local STTs can be calculated by computing the Inverse State Transition Tensors (ISTTs) via series reversion, as follows:

$$\begin{aligned}
\psi^{i,a} &= [\Phi^{-1}(t, t_0)]^{i,a} \\
\psi^{i,ab} &= -\psi^{i,\alpha} \phi^{\alpha, j_1, j_2} \psi^{j_1, a} \psi^{j_2, b} \\
\psi^{i,abc} &= -[\psi^{i,\alpha} \phi^{\alpha, j_1, j_2, j_3} + \psi^{i,\alpha} (\phi^{\alpha, j_1} \phi^{\beta, j_2, j_3} + \phi^{\alpha, j_1, j_2} \phi^{\beta, j_3} + \phi^{\alpha, j_1, j_3} \phi^{\beta, j_2})] \psi^{j_1, a} \psi^{j_2, b} \psi^{j_3, c}
\end{aligned} \tag{55}$$

where  $j_1, j_2, j_3 = \{1, \dots, n\}$  are the indexes for the first, second and third order derivative. Note that the series reversion requires the calculation of the inverse of the state transition matrix. The inverse matrix needs to be calculated with high precision otherwise the terms in the expansion result can be affected by a considerable error.

The solution calculated using the STTs obtained by series reversion produces oscillations towards the end of the integration period. Figure 25 shows the result from Vetrivano et al., 2012 for the propagation during 2.5 days of the variation vector, with respect to an Earth departing trajectory,  $\delta \mathbf{x}_0 = [2500km \ 2500km \ 2500km \ 0.01km/s \ 0.01km/s \ 0.01km/s]^T$  by using third order global STTs, third order integrated local STTs and third order local STTs calculated via series reversion.



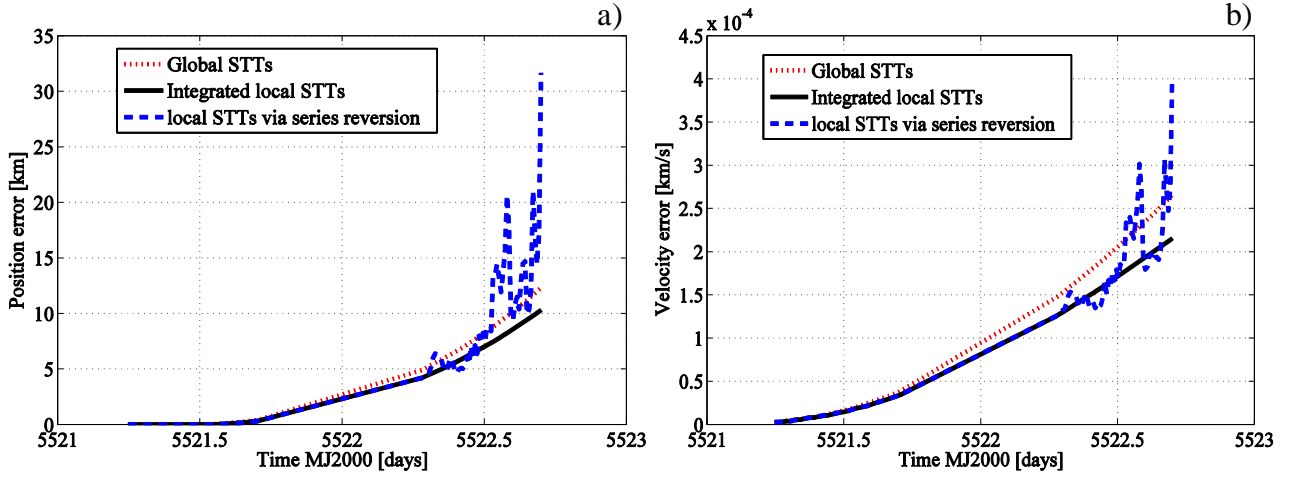


**Figure 25. Position a) and velocity b) errors using global STTs, integrated local STTs and local STTs obtained via series reversion.**

The solution calculated using the STTs obtained by series reversion produces oscillations towards the end of the integration period. In order to avoid this problem, in the remainder of this work, the integrated local STTs are used. In order to avoid this problem, in the remainder of this work, the integrated local STTs are used. Once the state transition tensors are available for some time interval  $[t_k \ t_{k+1}]$ , the mean and covariance matrix of the relative dynamics at  $t_k$  can be mapped analytically to  $t_{k+1}$  as a function of the probability distribution at  $t_k$ . Similarly to Eq.(14), the propagated mean and covariance from  $t_k$  to  $t_{k+1}$  can be stated as:

$$\begin{aligned}
\delta m_{k+1}^i(\delta \mathbf{x}_k) &= \sum_{p=1}^s \frac{1}{p!} \phi_{(t_{k+1}, t_k)}^{i, \gamma_1 \dots \gamma_p} E[\delta x_k^{\gamma_1} \dots \delta x_k^{\gamma_p}] \\
P_{k+1}^{ij} &= E[(\delta x_{k+1}^i - \delta m_{k+1}^i)(\delta x_{k+1}^j - \delta m_{k+1}^j)] \\
&= \sum_{p=1}^s \sum_{q=1}^s \frac{1}{p!q!} \phi_{(t_{k+1}, t_k)}^{i, \gamma_1 \dots \gamma_p} \phi_{(t_{k+1}, t_k)}^{j, \zeta_1 \dots \zeta_q} E[\delta x_k^{\gamma_1} \dots \delta x_k^{\gamma_p} \delta x_k^{\zeta_1} \dots \delta x_k^{\zeta_q}] - \delta m_{k+1}^i \delta m_{k+1}^j
\end{aligned} \tag{56}$$

where  $\{\gamma_i, \zeta_j\} \in \{1, \dots, n\}$  are the indexes for the first, second and third order derivative. The assumption in the construction of the filter is, however, that the statistical distribution remains close to Gaussian. This assumption was proved to provide a sufficiently accurate state estimation (Park and Scheeres, 2006a; Park, 2007). If one sticks to the hypothesis of a Gaussian distribution, the joint characteristic function for a Gaussian random vector can be computed as in Eq.(16) and the state prediction and associated covariance can be calculated as follows:

$$\begin{aligned} \mathbf{m}_{k+1}^i &= \phi^i(t_{k+1}; \mathbf{m}_k^+) + \delta \mathbf{m}_{k+1}^i = \phi^i(t_{k+1}; \mathbf{m}_k^+) + \sum_{p=1}^s \frac{1}{p!} \phi_{(t_{k+1}, t_k)}^{i, \gamma_1 \dots \gamma_p} E[\delta x_k^{\gamma_1} \dots \delta x_k^{\gamma_p}] \\ (\mathbf{P}_{k+1}^-)^{ij} &= \sum_{p=1}^s \sum_{q=1}^s \frac{1}{p!q!} \phi_{(t_{k+1}, t_k)}^{i, \gamma_1 \dots \gamma_p} \phi_{(t_{k+1}, t_k)}^{j, \zeta_1 \dots \zeta_q} E[\delta x_k^{\gamma_1} \dots \delta x_k^{\gamma_p} \delta x_k^{\zeta_1} \dots \delta x_k^{\zeta_q}] - \delta m_{k+1}^i \delta m_{k+1}^j + Q_k^{ij} \end{aligned} \quad (57)$$

For the measurements update phase it is assumed that the linearization of the measurements function provides a sufficient approximation. In this way the Kalman gain  $\mathbf{K}_{k+1}$ , the state estimate  $\mathbf{m}_{k+1}^+$  and the covariance matrix  $\mathbf{P}_{k+1}^+$  can be computed as follows:

$$\begin{aligned} \mathbf{K}_{k+1} &= \mathbf{P}_{k+1}^- \mathbf{H}_{k+1}^T [\mathbf{H}_{k+1} \mathbf{P}_{k+1}^- \mathbf{H}_{k+1}^T + \mathbf{R}]^{-1} \\ \mathbf{m}_{k+1}^+ &= \mathbf{m}_{k+1}^- + \mathbf{K}_{k+1} (\mathbf{y}_{k+1} - \mathbf{h}(\mathbf{m}_{k+1}^-)) \\ \mathbf{P}_{k+1}^+ &= (\mathbf{I} - \mathbf{K}_{k+1} \mathbf{H}_{k+1}) \mathbf{P}_{k+1}^- \end{aligned} \quad (58)$$

where  $\mathbf{m}_{k+1}^+$  substitutes  $\hat{\mathbf{x}}_{k+1}^+$ . The linear assumption simplifies the problem a great deal since the updated phase does not require the computation of the higher order partials of the measurements equations. In this way the filter velocity is increased, but at the same time the precision is not affected considerably. Note that when  $s = 1$ , the HAEKF becomes the linear Kalman filter, whose performance is inferior to the EKF, as demonstrated by Maybank (1982). Since the STTs are integrated offline with respect to the nominal trajectory, the idea is to use second and third order

expansions in order to incorporate the nonlinear effects exploiting the advantages given by the pre-integration.

### 3.5 Case Study - Weak Stability Boundaries

In this section we provide the application of the EKF, UKF and HAEKF to the case of the European Student Moon Orbiter (ESMO). ESMO was the fourth small satellite mission within ESA's Education Satellite Program. As shown in Figure 26 the spacecraft would use its chemical propulsion system (Croisard et al., 2009) to transfer itself from GTO to its lunar operational orbit at the Moon using a Weak Stability Boundaries (WSB) transfer (Belbruno, 1987).

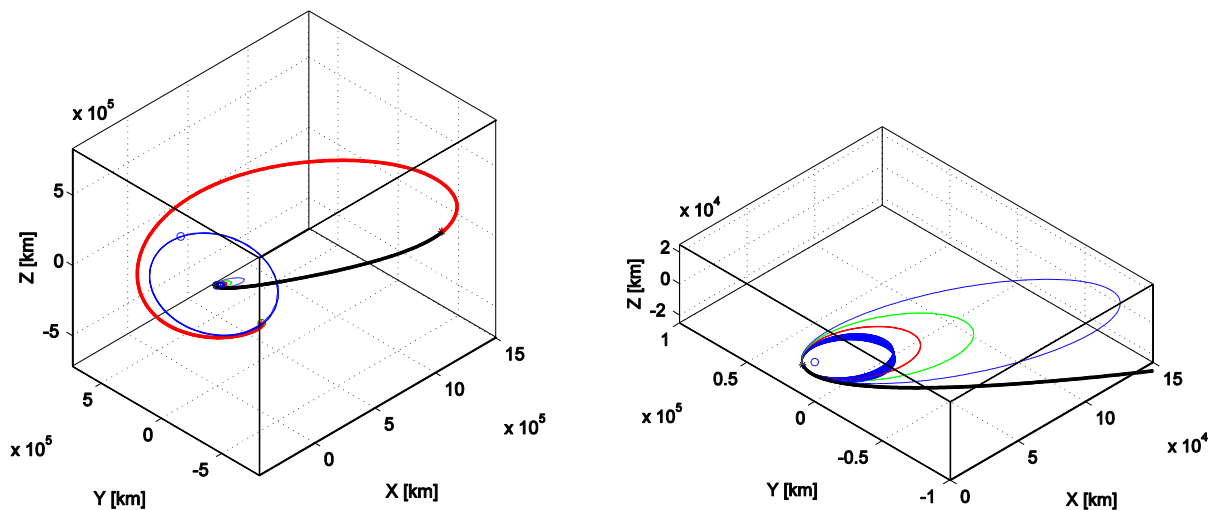


**Figure 26. Typical trajectory for WSB transfers in the Earth Centred Inertial frame. The blue line represents the Moon's orbit around the Earth, the black-red line is the WSB transfer from Earth to Moon, which is preceded by the apogee raising strategy (shown in more detail in the right plot) close to the Earth.**

This type of transfer was selected due to its associated propellant saving, and to cope consistently with a variety of injection conditions resulting from the fact ESMO would have been a secondary

payload with no control on the launch date. The WSB transfer employs the 3-body dynamics of the Sun, Earth, and Moon advantageously in order to change the orbit plane, and to raise the perigee of the orbit from the Earth up to the Moon. The equations of motion used for propagation are based on the n-body formulation where in this case the motion of the mass-less spacecraft is influenced by the Sun, Earth, and Moon point masses are the same as Eq.(1) (Bate et al., 1971), recalled here for convenience:

$$\dot{\mathbf{r}} = \mathbf{v}$$

$$\dot{\mathbf{v}} = -\frac{\mu_E}{r^3}\mathbf{r} - \mu_S \left( \frac{\mathbf{r}_{Ssc}}{r_{Ssc}^3} - \frac{\mathbf{r}_{SE}}{r_{SE}^3} \right) - \mu_M \left( \frac{\mathbf{r}_{Msc}}{r_{Msc}^3} - \frac{\mathbf{r}_{ME}}{r_{ME}^3} \right) \quad (59)$$

where  $\mathbf{r}$  and  $\mathbf{v}$  are respectively the position and velocity vectors of the spacecraft with respect to the Earth in the J2000 inertial reference frame,  $\mathbf{r}_{Ssc}$  and  $\mathbf{r}_{Msc}$  are the Sun-spacecraft and Sun-Earth vectors,  $\mathbf{r}_{ME}$  and  $\mathbf{r}_{SE}$  are the Moon-spacecraft and Moon-Earth vectors,  $\mu_E$ ,  $\mu_S$ ,  $\mu_M$  are the planetary constants of Earth, Sun and Moon respectively. The position of Sun and Moon with respect to the Earth and the spacecraft are calculated using analytical ephemeris (Vallado, 2000), accounting for secular variations in the orbital elements of both the Earth and the Moon. An analytical model was used to describe the secular variation of the angles between the Earth-equatorial and the Moon-equatorial reference frame.

When considering the perturbed equations of motion, one needs to consider also the contribution of the solar radiation pressure. The dynamics model used in the filtering takes the following form (Montenbruck and Gill, 2000):

$$\dot{\mathbf{x}}(t) = \begin{bmatrix} \dot{\mathbf{r}} \\ \dot{\mathbf{v}} \end{bmatrix} = \begin{bmatrix} \mathbf{v} \\ \mathbf{f}(\mathbf{x}(t), t) \end{bmatrix} + \begin{bmatrix} \mathbf{0} \\ \mathbf{a}_{Solar} + \mathbf{a}_w \end{bmatrix} \quad (60)$$

where  $\mathbf{f}(\mathbf{x}(t), t)$  is the set of nonlinear continuous-time equations in the second of Eq.,  $\mathbf{a}_w$  is the random noise acceleration produced by the attitude system,  $\mathbf{a}_{Solar}$  was calculated using Eq.(2)

In this case we considered a spacecraft mass of about 500 kg and a cross section area of 1.4 m<sup>2</sup>. A value of 1.2 for  $C_R$  was also assumed.

### 3.5.1 Orbit Determination

The Orbit Determination, OD, is performed by processing raw measurements coming from the only available ground station of Raisting, located in Germany, whose coordinates are listed in Table 8. The set of measurements includes range and range rate  $\rho$  and  $\dot{\rho}$ , from the ground station, plus the pointing angles  $A, E$  (respectively azimuth and elevation).

**Table 8. Raisting ground station location.**

Latitude $\lambda$ [deg]	Longitude $\upsilon$ [deg]	Altitude above mean sea level [m]	Minimum Elevation angle [deg]
47.90221	11.11579	553	1

Since the actual position of the spacecraft is given in the Earth Centred Inertial (ECI) reference frame, it is necessary to write the state of ESMO as it was seen in the local South East Zenith (SEZ) reference frame of the ground station as shown in Figure 27.

The range in the ECI reference frame is given by the difference in position of the spacecraft and ground station location (Montenbruck and Gill, 2000):

$$\boldsymbol{\rho}_{ECI} = \mathbf{r}_{ECI} - \mathbf{r}_{site-ECI} \quad (61)$$

where  $\mathbf{r}_{site-ECI}$  is the ECI position of the ground station. The range and velocity vectors in the SEZ frame are given by the following transformations:

$$\begin{aligned} \boldsymbol{\rho}_{SEZ} &= \mathbf{A}_{SEZ-ECEF} \mathbf{A}_{ECI-ECEF}^T \boldsymbol{\rho}_{ECI} \\ \dot{\boldsymbol{\rho}}_{SEZ} &= \mathbf{A}_{SEZ-ECEF} \mathbf{A}_{ECI-ECEF}^T \mathbf{v}_{ECI} \end{aligned} \quad (62)$$

where  $\mathbf{A}_{SEZ-ECEF}$  and  $\mathbf{A}_{ECI-ECEF}$  are respectively the transformation matrix from the Earth Centred Earth fixed (ECEF) reference frame to SEZ and the transformation matrix from ECEF to ECI:

$$\begin{aligned} \mathbf{A}_{ECI-ECEF} &= \begin{pmatrix} \cos \theta_g & -\sin \theta_g & 0 \\ \sin \theta_g & \cos \theta_g & 0 \\ 0 & 0 & 1 \end{pmatrix} \\ \mathbf{A}_{SEZ-ECEF} &= \begin{pmatrix} \sin \nu_g \cos \lambda_g & -\sin \nu_g \sin \lambda_g & -\cos \lambda_g \\ -\sin \lambda_g & \cos \lambda_g & 0 \\ \cos \nu_g \cos \lambda_g & \cos \nu_g \sin \lambda_g & \sin \nu_g \end{pmatrix} \end{aligned} \quad (63)$$

$\lambda_g$  and  $\nu_g$  are the latitude and longitude of the ground station;  $\theta_g = 280.4606 + \Omega t$  is the rotation angle between the ECI and ECEF reference frame about the z-axis;  $\Omega$  is the Earth's angular speed expressed in deg/day and  $t$  is the time expressed in MJD2000.

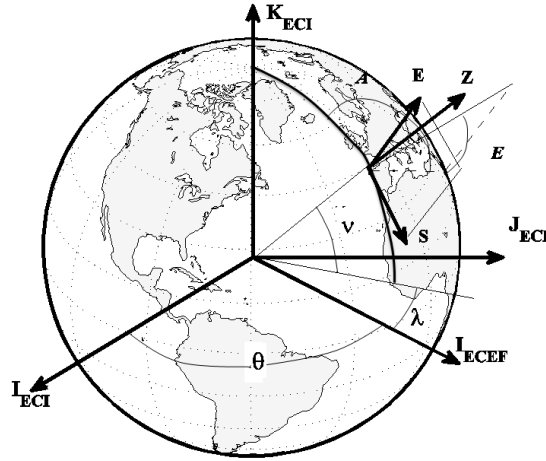


**Figure 27. Reference frames (Vallado, 2000)**

Finally the set of simulated measurements is obtained from the SEZ position and velocity:

$$\begin{aligned}
 \rho &= |\mathbf{p}_{SEZ}| \\
 E &= \sin^{-1} \frac{\rho_Z}{\rho} \\
 A &= \sin^{-1} \frac{\rho_E}{\sqrt{\rho_S^2 + \rho_E^2}} \\
 \dot{\rho} &= \frac{\dot{\mathbf{p}}_{SEZ} \cdot \mathbf{p}_{SEZ}}{\rho}
 \end{aligned} \tag{64}$$

being  $\rho_S$ ,  $\rho_E$ , and  $\rho_Z$  the components of the range in the SEZ frame.

The actual measurements were simulated by perturbing the nominal ones defined in Eq.(64) with a random noise with normal distribution. In this way the observation equations become

$$\mathbf{z} = h(\mathbf{r}, t, \boldsymbol{\zeta}_k) = [\rho \quad E \quad A \quad \dot{\rho}]' + [\zeta_\rho \quad \zeta_E \quad \zeta_A \quad \zeta_{\dot{\rho}}]' \tag{65}$$

We considered OD measurement errors ( $1\sigma$ ) of 15 m on range ( $\zeta_\rho$ ), of 0.5 mm/s on range-rate ( $\zeta_{\dot{\rho}}$ ), and 20 mdeg on angles ( $\zeta_E$  and  $\zeta_A$ ).

### 3.6 Filter Comparison

This section presents a comparison among the three filters described in Section 3.1 in order to define the most suitable filtering technique. The results in this section will be used in the next Chapter to show the impact of the different methods on the navigation.

As a representative example, this section reports the results for the first orbit determination campaign, which is allocated soon after the final translunar injection manoeuvre. The initial state vector in the Earth Centred Inertial (ECI) frame at the beginning of the Earth-WSB leg with  $t_0 = 5497.31\text{MJD}2000$  is:

$$\mathbf{x} = [5681.1\text{km} \quad -3862.8\text{km} \quad -336.3\text{km} \quad 5.948\text{km/s} \quad 8.852\text{km/s} \quad -1.198\text{km/s}]^T.$$

It is considered that a 2.5 days orbit determination campaign is then performed. The set of pseudo-measurements is taken every 10 minutes, when the spacecraft is visible from the ground station. The time step between measurement samples is higher than the one used in the following sections to emphasize the effects of dynamics non-linearities. In fact, a desirable benefit of high order nonlinear filters would be to reduce the number of steps to obtain the same order accuracy. It is therefore important that the reduction of the number of steps compensates for the higher cost of each step.



In the evaluation of the three filters, many different sets of pseudo measurements were simulated but the results showed negligible difference in the filter performance given the state and measurement uncertainties considered in the comparison. During the filtering process comparison, then, the same measurements have been used and it is assumed that the system dynamics is known completely.

Figure 28 shows the comparison when the dispersion of the initial states of the spacecraft is assumed to follow a Gaussian distribution with zero mean and standard deviation equal to 100 km in position and 0.1 km/s in velocity. The initial position guess is randomly generated with initial error of 100 km and 0.1 km/s in position and velocity.

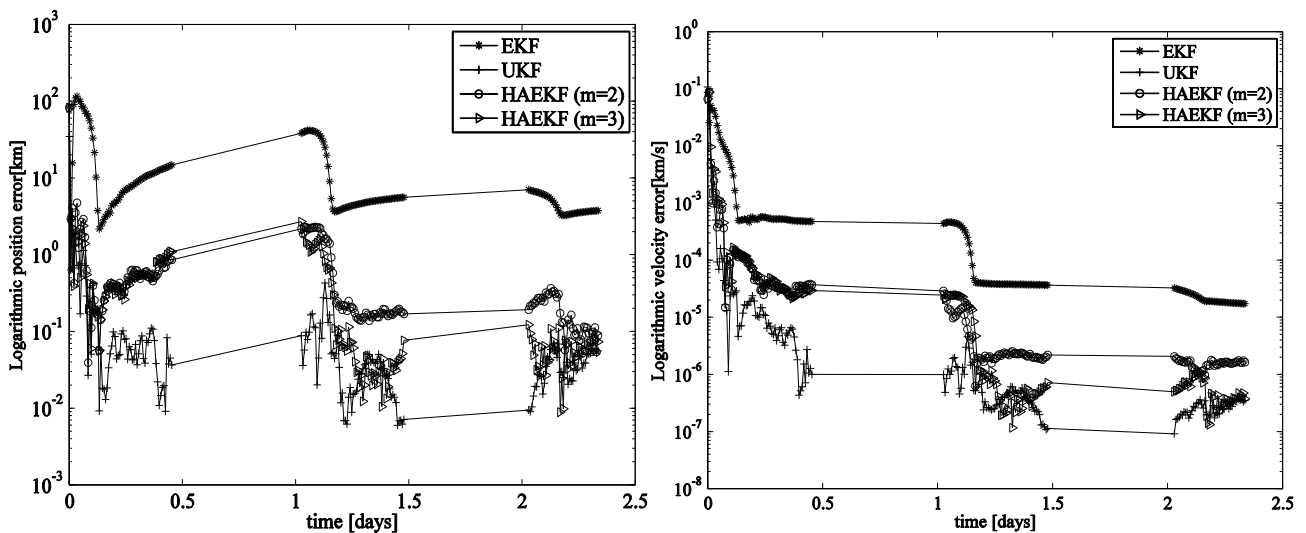


**Figure 28. Comparison of the absolute errors for 100 km position uncertainties and 0.1 km/s velocity uncertainties.**

From Figure 28, we can see that the second and third order HAEKF and UKF present better convergence results and produce a more accurate estimate than the EKF. The increments in velocity and position error (straight line in Figure 28) are due to the propagation of the last estimate since the

spacecraft is not visible during that period and measurements are not available. If an initial uncertainty in position and velocity equal to 1% of the nominal state vector is considered, the UKF shows superior performance over the other filter methods, as shown in Figure 29.

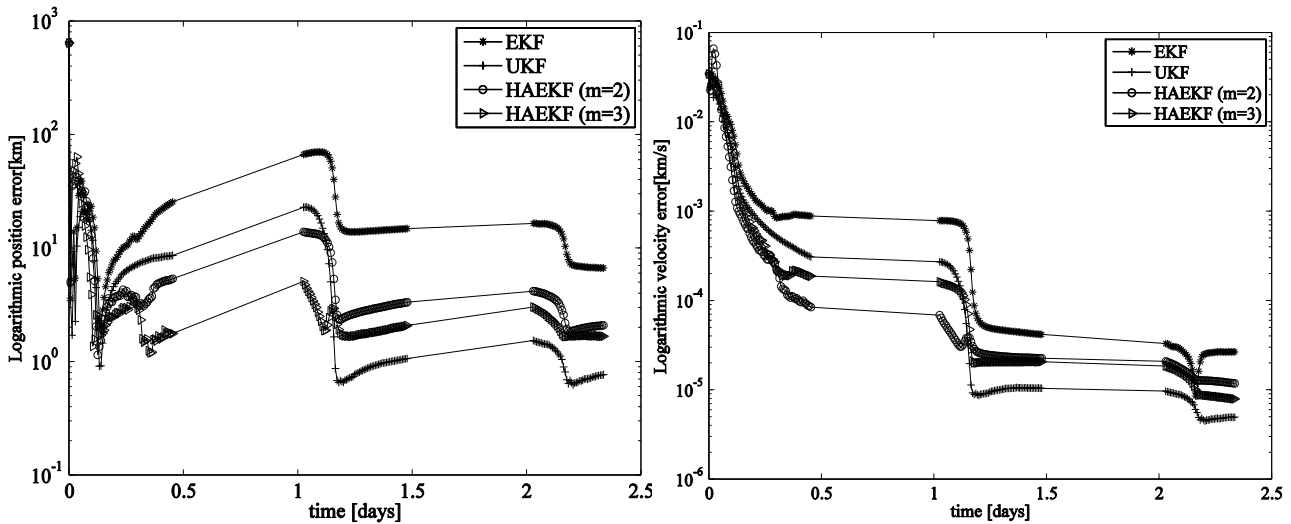


**Figure 29. Comparison of the absolute errors for uncertainties on position and velocity equal to 1% of the nominal unperturbed trajectory.**

The absolute errors are computed more accurately by the UKF, with a final position error lower than 1 km and velocity error lower than  $10^{-5}$  km/s. The higher precision is due to the fact that the measurements models are used without introducing any linearization assumption. Even if the third order HAEKF provides a solution essentially equivalent to the UKF when the initial guess is relatively close to the actual position and good results in the other case, it yields a much slower filter process.

Table 9 reports the elapsed CPU time necessary to process all the measurements by the different filters during the 2.5 days observational period. The most computational intensive filter is represented by the third order HAEKF itself, while the elapsed CPU time for the second order

HAEKF and UKF is about 50 seconds. The EKF is the fastest method but it is still the least precise when compared to the other methods.

**Table 9. Elapsed CPU time for the filtering processes, using a 64-bit Linux CentOS 5.4 2.93GHz Intel(R) Xeon(TM) X5570 , and absolute error for the estimated state.**

	EKF	UKF	HAEKF s=2	HAEKF s=3
Elapsed CPU time [s]	20.52	47.02	45.06	1737.22
Absolute position error [km]	6.657	0.765	2.081	1.602
Absolute velocity error [km/s]	$2.648 \cdot 10^{-5}$	$4.939 \cdot 10^{-6}$	$1.117 \cdot 10^{-5}$	$7.905 \cdot 10^{-6}$

The EKF required the integration of  $n + n^2 = 42$  equations (necessary for the update of the estimated state and the integration of the STM), being  $n = 6$ , and the UKF required the integration of  $(2n + 1)n = 78$  equations (for the updated estimated state and the propagation of the sigma points) between each measurement update. Moreover, the higher cost of the UKF with respect to the EKF is also given by the definition of the innovation process in Eq.(51) and Eq.(53). Although the HAEKF required only 6 integrations between each measurement update in Eq.(57), less than the UKF and EKF, the number of joint functions evaluations and summations required computing the mean value and covariance matrix in Eq.(56)-(57) between each measurement update is

$$\sum_{q=1}^s 6^q + \left( \sum_{p=1}^{s+1} 6^{p+1} \right)^2, \text{ which is equal to } 66822 \text{ and } 2397854 \text{ for } s = 2 \text{ and } s = 3 \text{ respectively.}$$

### 3.6.1 Manoeuvre Design

We make a step back to the propagation analysis to consider how the statistical information from the filtering can be used in the design of manoeuvre correction. The major impact of the estimation process is on the control of the spacecraft trajectory. A poor estimate could lead to an incorrect implementation of trajectory correction manoeuvres (TCMs) when deviations between the nominal

trajectory and the estimated one occur. We wanted to compare the effects on the navigation for UKF and HAEKF filters in exam in Section 3.6. We showed that the EKF present the worse performance for the studied problem.

Intermingled along the transfer and in between the orbit determination some TCMs are optimally timed and executed to reduce the error with respect to the nominal trajectory. Thus, the goal of each TCM is to minimise the deviation from the nominal trajectory at certain points, called waypoints, along the transfer. During the observation period the measurements are assumed to be received every 60 seconds (Thornton and Border, 2003).

Following each TCM, an orbit determination campaign estimates both position and velocity. Two TCMs are allocated after each OD to correct the trajectory up to the next waypoint  $t_{wp}$ . At each waypoint, the nominal state of the spacecraft is  $\mathbf{x}_{\text{nominal}}(t_{wp})$  and the state provided by the implementation of the TCMs is  $\mathbf{x}(t_{wp}, \mathbf{u})$ . Each TCM is defined by its time of execution  $t_{TCM}$  and the components of the velocity variation with respect to the local velocity vector.

Given the different nature of the two filters, one can compare a classical approach to navigation, using a deterministic approach for the UKF and a statistical approach for the HAEKF.

In the first case, the following constrained optimisation problem is then solved to optimally allocate and size each pair of TCMs:

$$\begin{aligned}
 & \min_{\mathbf{u} \in U} \Delta v_{TCM_1} + \Delta v_{TCM_2} \\
 & s.t. \\
 & \mathbf{x}(t_{wp}, \mathbf{u}) - \mathbf{x}_{\text{nominal}}(t_{wp}) = 0
 \end{aligned} \tag{66}$$

where the control vector  $\mathbf{u}$  contains the TCM's time of execution and  $\Delta\mathbf{v}$  components. Thus, the scheduling (time and date), direction and magnitude of the TCM must be optimised.

Conversely, in the second case the following problem proposed by Park and Scheeres (2006b) was solved:

$$\min_{\Delta\mathbf{v}_1^{TCM}} \left( \delta\mathbf{m}_r^{waypoint} \right)^2 = \left( E[\phi_r(t^{waypoint}; \delta\mathbf{m}_r^{TCM}, \delta\mathbf{m}_v^{TCM} + \Delta\mathbf{v}_1^{TCM}; t^{TCM})] \right)^2 \quad (67)$$

with:

$$\Delta\mathbf{v}_2^{TCM} = -\delta\mathbf{m}_v^{waypoint} \quad (68)$$

This method represents the so called nonlinear statistical targeting correction method introduced by Park and Scheeres (2006b) for the high-order expansion semi-analytical method. The statistical information contained in the covariance matrix at the end of the OD is included in the propagation of the mean trajectory using Eq.(57). Thus the correction manoeuvre is based on the mean of the propagation of all the possible trajectories from the OD and not on the only mean estimate propagation. In this way the TCMs are setting to zero the mean of all trajectory deviations at the waypoint.

It has to be pointed out that if the manoeuvres are performed, the actual state error at the waypoint will be not zero, but the statistical mean error will be zero, if the STTs order is sufficiently accurate to take into account all the nonlinear effects. In this comparison, the time and location of the TCM and waypoint was fixed for all the filters and to be consistent with problem of Eq.(67), the problem of Eq.(66) was modified by imposing a condition on the final velocity equivalent to Eq.(68).

Table 10 reports the results for both the optimized manoeuvre and statistical targeting correction applied to the first waypoint. Since the orbit determination estimate for the UKF proved to be the most accurate, optimised manoeuvres were calculated on the basis of 100 runs, while the nonlinear-statistical targeting corrections were calculated for the HAEKF ( $s = 2,3$ ) results. The actual trajectory is the one corresponding to the propagation of 1% perturbed trajectory whose estimated state is reported in Figure 29. The waypoint was placed at six days after the end of the orbit determination. It is assumed that the correction manoeuvres are not affected by errors. As it can be seen, the results are almost the same in terms of total correction for all filters. This is achieved due to the fact the effects of the non-linearity are included in both methods. The best actual state is achieved by optimising the TCMs on the basis of the estimated state by UKF. The optimized manoeuvre method allows us to consider the actual nonlinear dynamics, while higher orders introduce an approximation.

**Table 10. OD impacts on Navigation using optimized and nonlinear statistical targeting correction methods. A 64-bit Linux CentOS 5.4 2.93GHz Intel(R) Xeon(TM) X5570 was used.**

	Optimised manoeuvre correction	Statistical targeting correction	
	UKF	HAEKF $s=2$	HAEKF $s=3$
CPU time [s]	2452.721	0.599	27.974
Total correction $\Delta v$ [m/s]	77.104	77.083	77.101
Actual position error [km]	2.89	12.10	10.56
Actual velocity error [m/s]	0.003	0.032	0.025

The CPU time difference is considerable for the optimised manoeuvre. In this case the STTs approach results faster because the trajectory is not integrated, and the computational cost is due to the *fminsearch* operations.

As pointed out by Park and Scheeres (2006b) when the navigation data are accurate, both the correction manoeuvres are essentially the same. The nonlinear-statistical targeting correction depends on the statistical knowledge about the state vector (given by the covariance matrix), whereas the optimised manoeuvre relies only on the mean value.

The statistical targeting correction method results to be a flexible method since the evaluation of the manoeuvre can be done in one minimisation, while the optimised method need to be assessed by a Monte Carlo simulation. Anyway in the case of the statistical targeting correction method the effects of nonlinearities are significant and it would be necessary to increase the STTs order since the final actual state is less precise than the one obtained using the optimised method.

### 3.7 Unscented Particle Filter

A popular solution strategy for the general filtering problem is to use sequential Monte Carlo methods, also known as particle filters. These methods allow for a complete representation of the posterior distribution of the states, so that any statistical estimates, such as the mean and variance, can be easily computed. They can therefore, deal with any nonlinearities or distributions.

The particle filter belongs to the family of Monte Carlo sequential filter, in which a set of weighted particles, drawn from the simulations, are used to map integrals to weighted sums. In this way the posterior distribution  $\hat{p}(\mathbf{x}_{0:k} | \mathbf{y}_{1:k})$  can be approximated by:

$$\hat{p}(\mathbf{x}_{0:k} | \mathbf{y}_{1:k}) = \frac{1}{N_p} \sum_{i=1}^{N_p} \delta_{\mathbf{x}_{0k}^{(i)}}(dx_{0:k}) \quad (69)$$

where the random samples  $\{\mathbf{x}_{0:k}^{(i)} : i=1:N\}$ , are drawn from the posterior distribution and  $\delta(d)$  denotes the Dirac delta function. Consequently, any expectations of the form

$$E[g_t(\mathbf{x}_{0:k})] = \int g_t(\mathbf{x}_{0:k}) p(\mathbf{x}_{0:k} | \mathbf{y}_{1:k}) d\mathbf{x}_{0:k} \quad (70)$$

can be approximated by the following estimate

$$E[g_t(\mathbf{x}_{0:k})] \approx \frac{1}{N_p} \sum_{i=1}^{N_p} g_t(\mathbf{x}_{0:k}^{(i)}) \quad (71)$$

where the particle  $\mathbf{x}_{0:k}^{(i)}$  is assumed to be independent and identically distributed. Since sampling from the posterior distribution  $p(\mathbf{x}_{0:k} | \mathbf{y}_{1:k})$  is not always possible, it is common practice to sample from a proposal distribution  $q(\mathbf{x}_{0:k} | \mathbf{y}_{1:k})$ . By sampling from this distribution, the expectation of interest in Eq.(70) can be approximated by the following estimate:

$$E[g_t(\mathbf{x}_{0:k})] \approx \sum_{i=1}^{N_p} g_t(\mathbf{x}_{0:k}^{(i)}) \tilde{w}_k^{(i)} \quad (72)$$

where  $\tilde{w}_k^{(i)}$  are the normalized importance weights given by

$$\tilde{w}_k^{(i)} = \frac{w_k^{(i)}}{\sum_j^{N_p} w_k^{(j)}} \quad (73)$$

and  $w_t^{(i)}$  is obtained from

$$w_t^{(i)} = w_t^{(i)} \frac{p(\mathbf{y}_t | \mathbf{x}_t) p(\mathbf{x}_t | \mathbf{x}_{t-1})}{q(\mathbf{x}_t | \mathbf{x}_{0:t-1}, \mathbf{y}_{1:t})} \quad (74)$$

The proposal distribution must be similar to the actual distribution, which is unknown. For this reason the most popular choice (van der Merwe et al., 2000; Gordon et al., 1993) is to use



$$q(\mathbf{x}_k | \mathbf{x}_{0:k-1}, \mathbf{y}_{1:k}) = p(\mathbf{x}_k | \mathbf{x}_{k-1}) \quad (75)$$

which simplifies Eq.(74), but at the same time can lead to degeneracy. This problem consists in the fact that only a few particles will have significant importance weights when their likelihood is evaluated.

To avoid the degeneracy, a resampling stage may be used to eliminate samples with low importance weights and multiply samples with high importance weights.

Since we can sample from the proposal distribution and evaluate the likelihood and transition probabilities, all we need to do is generate a prior set of samples and iteratively compute the importance weights. This procedure, known as sequential importance sampling (SIS) (van der Merwe et al., 2000), allows us to obtain the type of estimates described by Eq.(72).

The implemented particle filter descends from the one described in van der Merwe et al. (2000) and exploits unscented Kalman filter to generate the importance proposal distribution. For this reason it was named Unscented Particle Filter, UPF. The use of UKF allows the particle filter to incorporate the latest observations into a prior updating routine.

The unscented Kalman Filter is able to more accurately propagate the mean and covariance of the Gaussian approximation to the state distribution, than the EKF. In comparison to the EKF, the UKF tends to generate more accurate estimates of the true covariance of the state. Distributions generated by the UKF generally have a bigger support overlap with the true posterior distribution than the overlap achieved by the EKF estimates. This is in part related to the fact that the UKF calculates the posterior covariance accurately to the 3<sup>rd</sup> order, whereas the EKF relies on a first order biased approximation. For this reason the UKF was chosen to generate the proposal distribution generation

within the particle filter framework. The UKF also has the ability to scale the approximation errors in the higher order moments of the posterior distribution allowing for heavier tailed distributions.

The implemented UPF is composed of three basic steps:

- 1) *Initialization*:  $N_p$  particles within the a priori distribution are generated
- 2) *Importance sampling step*: the UKF as described in Section 3.3 is performed on each particle, and the importance sampling weights are calculated from Eq.(74). Note that the Gaussian assumption implies that the posterior distribution after the update is given by a normal distribution:

$$p(\mathbf{y}_k, \mathbf{x}_k) = \frac{1}{\sqrt{(2\pi)^z \det \mathbf{R}}} \exp\left(-\frac{1}{2}(\mathbf{y}_k - \mathbf{h}(\mathbf{x}_k))^T \mathbf{R}(\mathbf{y}_k - \mathbf{h}(\mathbf{x}_k))\right) \quad (76)$$

- 3) *Resampling*: all the particles whose weight is below  $1/(4N_p)$  are discarded and replace by particles drawn from the higher values of weight at step 2. In this way the resampling operations is reduced while avoiding the degeneracy issue.

At each iteration, it is possible to estimate the posterior distribution as in Eq.(69) and to calculate mean and covariance matrix from Eq.(72):

$$\begin{aligned} \tilde{\mathbf{x}}_k &= \sum_{i=1}^{N_p} \tilde{\mathbf{x}}_k^{(i)} \tilde{w}_k(\tilde{\mathbf{x}}_k^{(i)}) \\ P_k^{nm} &= \sum_{i=1}^{N_p} (\tilde{\mathbf{x}}_k^{n(i)} - \tilde{\mathbf{x}}_k^n) \tilde{w}_k(\tilde{\mathbf{x}}_k^{(i)}) (\tilde{\mathbf{x}}_k^{m(i)} - \tilde{\mathbf{x}}_k^m) \end{aligned} \quad (77)$$

Because the sigma points set used in the UKF are deterministically designed to capture certain characteristic of the prior distribution, one can explicitly optimize the algorithm to work with

distributions that have heavier tails than Gaussian distributions, i.e. Cauchy or Student-t distributions. This characteristic makes the UKF very attractive for the generation of proposal distributions.

### **3.8 Polynomial Chaos Based Ensemble Kalman Filter**

As for the particle filter, the ensemble Kalman filter (EnKF) has been under extensive investigation regarding its properties and efficiency (Li and Xiu, 2009). Compared to other variants of the Kalman filter, EnKF is straightforward to implement, as it employs random ensembles to represent solution states. This, however, introduces sampling errors as for the PF that affect the accuracy of EnKF in a negative manner. Though sampling errors can be easily reduced by using a large number of samples, in practice this is undesirable as each ensemble member is a solution of the system. An efficient EnKF implementation is to employ polynomial chaos expansion, PCE. The main aspects of this method involve (1) solving the system of stochastic state equations via the PCE methodology to gain efficiency; and (2) sampling the PCE approximation of the stochastic solution with an arbitrarily large number of samples, at virtually no additional computational cost, to drastically reduce the sampling errors.

The basics of PCE technique for covariance and mean state propagation were already introduced in Section 2.2.4 where we saw that these statistical quantities can be drawn directly from the coefficients of the polynomial expansion through Eq.(30). So it is possible to describe in details the so called Ensemble Kalman filter based on polynomial chaos expansion. We did not use the approach of Li and Xiu (2009), because the way they proposed to update the ensemble is not as robust as the one usually employed in the EnK filter. Moreover their work focuses on linear

systems, so our approach does include the full dynamics without any further approximation. The only approximation introduced here descends from the expansion and the number of samples used to describe statistical properties.

An initial ensemble is required at time  $t_0$ . Assuming we have an initial best-guess estimate and some idea of the error in this estimate expressed through a covariance matrix, we may generate an initial ensemble by taking the best-guess estimate and adding random perturbations from a distribution determined by the covariance matrix. It is possible to construct the initial polynomial expansion description by choosing a suitable cubature rule. We used the Gaussian-Hermite cubature rule, which has to be used in the case of Hermite polynomials (Eldred et al., 2011).

Let

$$\tilde{\mathbf{x}}^-(t_k, \boldsymbol{\chi}) = \sum_{j=0}^p \boldsymbol{\alpha}_j^-(t_k) \Psi_j(\boldsymbol{\chi}) \quad (78)$$

be the solution of the forecast equations at each time step, where  $\boldsymbol{\alpha}_j^-$ , the expansion coefficient of degree up to  $p$ , are obtained through the spectral projection.

Once a description of the update step is available through the projection, one can generate a large number of forecast state realizations on randomly chosen coordinates of the grid  $\boldsymbol{\chi}_i^c$ , denoted with  $\tilde{\mathbf{x}}_i^-$ . We chose to generate the ensemble by randomly selecting points  $\boldsymbol{\chi}_i^c$  on the grid. The reason for the superscript  $c$  is due to a problem which arises in this way: the grid is biased, i.e. it will be centred on a point which is not zero, and also the points could result in being correlated.

$$\begin{aligned}\boldsymbol{\chi}_0 &= \frac{1}{N} \sum_{i=1}^N \boldsymbol{\chi}_i^c \\ \mathbf{P}_\chi &= \frac{1}{N-1} \sum_{i=1}^N (\boldsymbol{\chi}_i^c - \boldsymbol{\chi}_0)(\boldsymbol{\chi}_i^c - \boldsymbol{\chi}_0)^T\end{aligned}\quad (79)$$

where  $\boldsymbol{\chi}_0$  is the centre of the grid, and  $\mathbf{P}_\chi$  is the correlation matrix. I circumvented this problem by applying the Mahalanobis decorrelation transformation to transform correlated points of the grid  $\boldsymbol{\chi}_i^c$  into uncorrelated ones  $\boldsymbol{\chi}_i$  using Eq.(8).

The mean and the covariance matrix of the forecast ensemble  $\hat{\mathbf{x}}_i^-$  are denoted as  $\hat{\mathbf{x}}_e^-$  and  $\mathbf{P}_e^-$ . This value could be calculated directly from Eq.(30), but since the number of samples affects the actual procedure, it is convenient to redefine these values as:

$$\begin{aligned}\tilde{\mathbf{x}}_e^- &= \frac{1}{N} \sum_{i=1}^N \tilde{\mathbf{x}}_i^- \\ \mathbf{P}_e^- &= \frac{1}{N-1} \sum_{i=1}^N (\tilde{\mathbf{x}}_i^- - \tilde{\mathbf{x}}_e^-)(\tilde{\mathbf{x}}_i^- - \tilde{\mathbf{x}}_e^-)^T\end{aligned}\quad (80)$$

It is convenient to introduce the forecast ensemble matrix

$$\tilde{\mathbf{X}}^- = \frac{1}{\sqrt{N-1}} (\tilde{\mathbf{x}}_1^- \quad \tilde{\mathbf{x}}_2^- \quad \dots \quad \tilde{\mathbf{x}}_N^-) \quad (81)$$

and the ensemble perturbation matrix:

$$\mathbf{P}_x^- = \frac{1}{\sqrt{N-1}} (\tilde{\mathbf{x}}_1^- - \tilde{\mathbf{x}}_e^- \quad \tilde{\mathbf{x}}_2^- - \tilde{\mathbf{x}}_e^- \quad \dots \quad \tilde{\mathbf{x}}_N^- - \tilde{\mathbf{x}}_e^-) \quad (82)$$

Then the ensemble covariance matrix may be expressed as:

$$\mathbf{P}_e^- = \mathbf{P}_x^- (\mathbf{P}_x^-)^T \quad (83)$$

Using each sample one may obtain the corresponding forecast measurement ensemble  $\tilde{\mathbf{y}}_i = h(t_k, \tilde{\mathbf{x}}_i^-)$ , which does not include the noise. Similarly to the ensemble matrix and covariance matrix, it is possible to draw the same quantities referred to the measurements:

$$\begin{aligned} \tilde{\mathbf{Y}} &= \frac{1}{\sqrt{N-1}} (\tilde{\mathbf{y}}_1 \quad \tilde{\mathbf{y}}_2 \quad \dots \quad \tilde{\mathbf{y}}_N) \\ \mathbf{P}_y &= \frac{1}{\sqrt{N-1}} (\hat{\mathbf{y}}_1 - \tilde{\mathbf{y}}_e \quad \tilde{\mathbf{y}}_2 - \tilde{\mathbf{y}}_e \quad \dots \quad \tilde{\mathbf{y}}_N - \tilde{\mathbf{y}}_e) \end{aligned} \quad (84)$$

where  $\tilde{\mathbf{y}}_e = \frac{1}{N} \sum_{i=1}^N \tilde{\mathbf{y}}_i$ . To obtain the desired statistics from the analysis ensemble an observation ensemble has to be define as:

$$\mathbf{y}_i = \mathbf{y} + (h(t_k, \hat{\mathbf{x}}_i^-, 0) - h(t_k, \hat{\mathbf{x}}_i^-, \boldsymbol{\zeta})) \quad (85)$$

which leads to an observation matrix and an observation perturbation matrix:

$$\begin{aligned} \mathbf{Y} &= \frac{1}{\sqrt{N-1}} (\mathbf{y}_1 \quad \mathbf{y}_2 \quad \dots \quad \mathbf{y}_N) \\ \mathbf{R}_y &= \frac{1}{\sqrt{N-1}} (\mathbf{y}_1 - \mathbf{y} \quad \mathbf{y}_2 - \mathbf{y} \quad \dots \quad \mathbf{y}_N - \mathbf{y}) \end{aligned} \quad (86)$$

In this way, one defines an observation ensemble covariance matrix  $\mathbf{R}_e$  which, in the linear case, is coincident with the measurement noise covariance matrix  $\mathbf{R}$ :

$$\mathbf{R}_e = \mathbf{R}_y \mathbf{R}_y^T \quad (87)$$

An ensemble version of the update step results:

$$\tilde{\mathbf{X}}^+ = \tilde{\mathbf{X}}^- + \mathbf{K}_e (\mathbf{Y} - \tilde{\mathbf{Y}}) \quad (88)$$

$\tilde{\mathbf{X}}^+$  is the update ensemble matrix.  $\mathbf{K}_e$  is the ensemble Kalman gain, which would be equal to  $\mathbf{P}_e^- \mathbf{H}^T (\mathbf{H} \mathbf{P}_e^- \mathbf{H}^T + \mathbf{R}_e)^{-1}$  if the problem was linear. For the ensemble nonlinear case, the Kalman gain becomes:

$$\mathbf{K}_e = \mathbf{P}_x^- \mathbf{P}_y^T (\mathbf{P}_y \mathbf{P}_y^T + \mathbf{R}_y \mathbf{R}_y^T)^{-1} \quad (89)$$

So one obtains a large number of update state samples from the columns of the  $\tilde{\mathbf{x}}_i^+ = \sqrt{N+1} \tilde{\mathbf{X}}_i^+$ . The update step can be described using the PCE technique as:

$$\tilde{\mathbf{x}}^+(t_k, \boldsymbol{\chi}) = \sum_{j=0}^P \mathbf{a}_j^+(t_k) \Psi_j(\boldsymbol{\chi}) \quad (90)$$

where in this case the coefficients of the expansion are calculated using equal weights:

$$\mathbf{a}_j^+ = \frac{1}{\langle \Psi_j^2 \rangle} \left( \frac{1}{N} \sum_{i=1}^N \tilde{\mathbf{x}}_i^+ \Psi_j(\boldsymbol{\chi}_i) \right) \quad (91)$$

Using the PCE approach, at each step one can obtain a large number of forecasts, simply by sampling the polynomial chaos expansion at almost no additional computational cost (required in the case of integration of many other samples).

### 3.9 H-infinity Filter

The Kalman filter is the best estimator to minimize the variance of the state covariance matrix when certain conditions are met (Mayback, 1982). In fact the Kalman filter is the minimum variance

estimator if the noise is Gaussian, and it is the linear minimum variance estimator if the noise is not Gaussian. Nonetheless, one needs to know the mean and correlation of the noise  $\mathbf{w}_k$  and  $\boldsymbol{\zeta}_k$  at each time instant. Secondly, we need to know the covariance matrices  $\mathbf{Q}_k$  and  $\mathbf{R}_k$  of the noise processes. Finally, the system model matrices  $\mathbf{F}_k$  and  $\mathbf{H}_k$  are also required. The Kalman filter uses  $\mathbf{Q}_k$  and  $\mathbf{R}_k$ , along with  $\mathbf{F}_k$  and  $\mathbf{H}_k$ , as design parameters, so if these matrices are not known, it may be difficult to successfully use a Kalman filter.

If one desires to minimize a different cost function, such as the worst-case estimation error, then the Kalman filter may not accomplish these objectives.

Even though the Kalman filter has proved to work reasonably well when the Kalman filter hypotheses are not satisfied, another alternative which was explored here is the  $H_\infty$  filter, also called the min-max filter. The  $H_\infty$  filter does not assume to precisely know the noise statistics, and it minimizes the worst-case estimation error.

A common way to derive the  $H_\infty$  filter is to use a game theory approach. A full procedure for the  $H_\infty$  filter can be found in (Simon, 2006), so in the following only the main results will be shown. For simplicity we recall the standard linear discrete-time equations similarly to Eq.(34) between two subsequent instant of time  $t_k$  and  $t_{k+1}$  as

$$\begin{aligned}\mathbf{x}_{k+1} &= \mathbf{F}_k \mathbf{x}_k + \mathbf{w}_k \\ \mathbf{y}_k &= \mathbf{H}_k \mathbf{x}_k + \boldsymbol{\zeta}_k\end{aligned}\tag{92}$$



where the input variables were not included.  $\mathbf{w}_k$  and  $\mathbf{v}_k$  may be random variables with unknown statistics, or they may be deterministic and nonzero mean. The scope is to estimate  $\mathbf{z}_{k+1}$ , a linear combination of the state to estimate, as

$$\mathbf{z}_k = \mathbf{L}_k \mathbf{x}_k \quad (93)$$

where  $\mathbf{L}_{k+1}$  is a user-defined matrix, which could be equal to the identity matrix if one wants to directly estimate  $\mathbf{x}_{k+1}$ . The estimate of  $\mathbf{z}_k$  is denoted  $\tilde{\mathbf{z}}_k$ , while the estimate of the state at time zero is  $\tilde{\mathbf{x}}_0$ . The estimate of  $\mathbf{z}_k$  is based on the measurements up to a certain time  $(N-1)$ . Using the game theory approach to  $H_\infty$  filtering, the objective function to minimize while finding the estimate  $\tilde{\mathbf{z}}_k$  is given as:

$$J_1 = \frac{\sum_{k=0}^{N-1} \|\mathbf{z}_k - \tilde{\mathbf{z}}_k\|_{\mathbf{S}_k}^2}{\|\mathbf{x}_0 - \tilde{\mathbf{x}}_0\|_{\mathbf{P}_0^{-1}}^2 + \sum_{k=0}^{N-1} \left( \|\mathbf{w}_k\|_{\mathbf{Q}_k^{-1}}^2 + \|\boldsymbol{\zeta}_k\|_{\mathbf{R}_k^{-1}}^2 \right)} \quad (94)$$

where  $\mathbf{S}_k$  is a suitable matrix;  $\|(\dots)\|_{\mathbf{M}_k}^2 = (\dots)^T \mathbf{M}_k (\dots)$  represents the norm of a vector weighted on the generic matrix  $\mathbf{M}_k$ . The natural system dynamics, the adversary nature, will provide the system with disturbances  $\mathbf{w}_k$  and  $\boldsymbol{\zeta}_k$ , and initial condition  $\mathbf{x}_0$  such that to maximise the function  $J_1$ . In other words the nature's goal is to maximise the estimation error  $(\mathbf{z}_k - \tilde{\mathbf{z}}_k)$ . The terms at the dominator of  $J_1$  prevent the nature to achieve very large value by using very high value for  $\mathbf{w}_k$  and  $\boldsymbol{\zeta}_k$ , and initial condition  $\mathbf{x}_0$ .

In this way, one can see the fundamental difference with the Kalman filter. In Kalman filtering, nature is assumed to be indifferent. Thanks to the fact that the statistics of noise is given, one can use that knowledge to obtain a statistically optimal state estimate.

Nature cannot change this statistical knowledge to degrade our state estimate. Conversely, in the case of  $H_\infty$  filtering, nature actively seeks to degrade the state estimate as much as possible.  $\mathbf{P}_0$ ,  $\mathbf{Q}_k$ ,  $\mathbf{R}_k$ , and  $\mathbf{S}_k$  in Eq.(94) are symmetric positive definite matrices chosen by the design process based on the specific problem. In this way, one can deduce that  $\mathbf{P}_0$ ,  $\mathbf{Q}_k$ ,  $\mathbf{R}_k$  are analogous to those same quantities in the Kalman filter, if those quantities are known. Thus, if one knows that the initial estimation error, the process noise, and the measurement noise statistics, then one should use those quantities for  $\mathbf{P}_0$ ,  $\mathbf{Q}_k$ ,  $\mathbf{R}_k$  in the  $H_\infty$  estimation problem. In the Kalman filter, there is nothing analogous to the  $\mathbf{S}_k$  matrix given in Eq.(94). The Kalman filter minimizes the weighted sum of estimation error variances for all positive definite  $\mathbf{S}_k$  matrices. But in the  $H_\infty$  the choice of  $\mathbf{S}_k$  affects the filter gain as will be shown later. The direct minimisation of the function is not tractable, so one can define a threshold to find an estimate  $\tilde{\mathbf{z}}_k$  that gives

$$J_{H_\infty}^1 < \frac{1}{\rho_{H_\infty}} \quad (95)$$

where  $\rho_{H_\infty}$  is a performance bound. In this way one obtains a new function  $J_{H_\infty}$  :

$$J_{H_\infty} < -\frac{1}{\rho_{H_\infty}} \|\mathbf{x}_0 - \tilde{\mathbf{x}}_0\|_{\mathbf{P}_0^{-1}}^2 + \sum_{k=0}^{N-1} \left( \|\mathbf{z}_k - \tilde{\mathbf{z}}_k\|_{\mathbf{S}_k}^2 - \frac{1}{\rho_{H_\infty}} \left( \|\mathbf{w}_k\|_{\mathbf{Q}_k^{-1}}^2 + \|\mathbf{s}_k\|_{\mathbf{R}_k^{-1}}^2 \right) \right) < 1 \quad (96)$$

The minmax problem becomes:

$$J_{H_\infty}^* = \min_{\hat{\mathbf{z}}_k} \max_{\mathbf{w}_k, \mathbf{S}_k, \mathbf{x}_0} J_{H_\infty} \quad (97)$$

Considering that  $\mathbf{z}_k = \mathbf{L}_k \mathbf{x}_k$ , it is equivalent to look for a  $\hat{\mathbf{x}}_k$  that minimizes  $J_{H_\infty}$ , so the problem can be stated as:

$$J_{H_\infty}^* = \min_{\hat{\mathbf{x}}_k} \max_{\mathbf{w}_k, \mathbf{S}_k, \mathbf{x}_0} J_{H_\infty} \quad (98)$$

One can replace  $\mathbf{v}_k$  considering that  $\mathbf{w}_k$  and  $\mathbf{v}_k$ ,  $\mathbf{x}_0$  fully determine the value of  $J_{H_\infty}$ , so the function can be alternatively described as:

$$J_{H_\infty}^* = \min_{\hat{\mathbf{x}}_k} \min_{\mathbf{w}_k, \mathbf{y}_k, \mathbf{x}_0} J_{H_\infty} \quad (99)$$

Considering the second equation in Eq.(92) one can see that

$$\|\mathbf{S}_k\|_{R_k^{-1}}^2 = \|\mathbf{y}_k - \mathbf{H}_k \mathbf{x}_k\|_{R_k^{-1}}^2 \quad (100)$$

In this way, referring to Eq.(93):

$$\|\mathbf{z}_k - \tilde{\mathbf{z}}_k\|_{\mathbf{S}_k}^2 = \|\mathbf{L}_k (\mathbf{x}_k - \tilde{\mathbf{x}}_k)\|_{\mathbf{S}_k}^2 = (\mathbf{x}_k - \tilde{\mathbf{x}}_k)^T \mathbf{L}_k^T \mathbf{S}_k \mathbf{L}_k (\mathbf{x}_k - \tilde{\mathbf{x}}_k) = \|\mathbf{x}_k - \tilde{\mathbf{x}}_k\|_{\bar{\mathbf{S}}_k}^2 \quad (101)$$

where  $\bar{\mathbf{S}}_k = \mathbf{L}_k^T \mathbf{S}_k \mathbf{L}_k$ . By substituting Eqs.(100) and (101) into Eq.(96), a final version of the function is obtained

$$\begin{aligned} J_{H_\infty} &= -\frac{1}{\rho_{H_\infty}} \|\mathbf{x}_0 - \tilde{\mathbf{x}}_0\|_{\mathbf{P}_0^{-1}}^2 + \sum_{k=0}^{N-1} \left( \|\mathbf{x}_k - \tilde{\mathbf{x}}_k\|_{\bar{\mathbf{S}}_k}^2 - \frac{1}{\rho_{H_\infty}} \left( \|\mathbf{w}_k\|_{Q_k^{-1}}^2 + \|\mathbf{y}_k - \mathbf{H}_k \mathbf{x}_k\|_{R_k^{-1}}^2 \right) \right) < 1 \\ &= \psi(\mathbf{x}_0) + \sum_k^{N+1} \Gamma_k \end{aligned} \quad (102)$$

Where  $\psi(\mathbf{x}_0)$  and  $\Gamma_k$  are defined by the above expression. To solve the problem, one needs to find a stationary point of  $J$  with respect to  $\mathbf{x}_0$  and  $\mathbf{w}_k$ , which is also a stationary point with respect to  $\tilde{\mathbf{x}}_k$  and  $\mathbf{y}_k$ .

In order to find a stationary point with respect to  $\mathbf{x}_0$  and  $\mathbf{w}_k$ , one needs to look for the maximum of the  $J_{H_\infty}$  subjected to the constraint  $\mathbf{x}_{k+1} = \mathbf{F}_k \mathbf{x}_k + \mathbf{w}_k$ . Using the technique of Lagrange multipliers, used in constrained optimisation, this means to find constrained maximum of the function in the form:

$$\begin{aligned}
J_a &= \psi(\mathbf{x}_0) + \sum_k^{N+1} \left( \Gamma_k + \frac{2}{\rho_{H_\infty}} \boldsymbol{\lambda}_{k+1}^T (\mathbf{F}_k \mathbf{x}_k + \mathbf{w}_k - \mathbf{x}_{k+1}) \right) \\
&= \psi(\mathbf{x}_0) + \sum_k^{N+1} H_k - \sum_k^N \boldsymbol{\lambda}_k^T \mathbf{x}_k + \boldsymbol{\lambda}_0^T \mathbf{x}_0 \\
&= \psi(\mathbf{x}_0) + \sum_k^{N+1} \left( H_k - \frac{2}{\rho_{H_\infty}} \boldsymbol{\lambda}_k^T \mathbf{x}_k \right) - \frac{2}{\rho_{H_\infty}} \boldsymbol{\lambda}_N^T \mathbf{x}_N + \frac{2}{\rho_{H_\infty}} \boldsymbol{\lambda}_0^T \mathbf{x}_0
\end{aligned} \tag{103}$$

where  $\boldsymbol{\lambda}_k$  are the Lagrange multipliers and  $H_k = \Gamma_k + \boldsymbol{\lambda}_{k+1}^T (\mathbf{F}_k \mathbf{x}_k + \mathbf{w}_k)$  is the Hamiltonian function.

The term  $\frac{2}{\rho_{H_\infty}}$  is introduced to scale the Lagrange multiplier by a constant to make the ensuing the

resolution more straightforward. The conditions that are required for a constrained stationary point

with respect to  $\mathbf{x}_0$  and  $\mathbf{w}_k$  are:

$$\begin{aligned}
\frac{\partial J_a}{\partial \mathbf{x}_k} &= 0 \quad k = 0, \dots, N \\
\frac{\partial J_a}{\partial \mathbf{w}_k} &= 0 \quad k = 0, \dots, N-1 \\
\frac{\partial J_a}{\partial \boldsymbol{\lambda}_k} &= 0 \quad k = 0, \dots, N
\end{aligned} \tag{104}$$

The conditions for the stationary point with respect to  $\tilde{\mathbf{x}}_k$  and  $\mathbf{y}_k$  are given by:

$$\begin{aligned}\frac{\partial J_a}{\partial \hat{\mathbf{x}}_k} &= 0 & k = 0, \dots, N \\ \frac{\partial J_a}{\partial \mathbf{y}_k} &= 0 & k = 0, \dots, N-1\end{aligned}\tag{105}$$

In order for the identified stationary points  $\tilde{\mathbf{x}}_k$  to be a minimum, the second derivative of the function with respect to  $\tilde{\mathbf{x}}_k$  must be positive. It results that this value is as follows:

$$\begin{aligned}\frac{\partial^2 J_a}{\partial^2 \hat{\mathbf{x}}_k} &= 2(\bar{\mathbf{S}}_k + \rho_{H_\infty} \bar{\mathbf{S}}_k \bar{\mathbf{P}}_k \bar{\mathbf{S}}_k) > 0 \\ \bar{\mathbf{P}}_k^{-1} &= \mathbf{P}_k^{-1} (\mathbf{P}_k^{-1} - \rho_{H_\infty} \bar{\mathbf{S}}_k + \mathbf{H}_k^T \mathbf{R}_k^{-1} \mathbf{H}_k) \mathbf{P}_k^{-1}\end{aligned}\tag{106}$$

The value of  $\bar{\mathbf{S}}_k$  in Eq.(101) should always be positive definite, which means that  $\mathbf{S}_k$  will be positive definite. This means that  $\tilde{\mathbf{x}}_k$  will be a minimizing value of  $J_{H_\infty}$  if  $\bar{\mathbf{P}}_k$  is positive definite. So the condition required for to minimize  $J_{H_\infty}$  is that  $(\mathbf{P}_k^{-1} - \rho_{H_\infty} \bar{\mathbf{S}}_k + \mathbf{H}_k^T \mathbf{R}_k^{-1} \mathbf{H}_k)^{-1}$ , or equivalently  $(\mathbf{P}_k^{-1} - \rho_{H_\infty} \bar{\mathbf{S}}_k + \mathbf{H}_k^T \mathbf{R}_k^{-1} \mathbf{H}_k)$ , be positive definite.

The individual terms in this expression are always positive definite, so the condition to minimize  $J_{H_\infty}$  can be obtained if the term  $\rho_{H_\infty} \bar{\mathbf{S}}_k$  is sufficiently small. This can be obtained by considering small value of the performance index  $\rho_{H_\infty}$ , or by the choice of small values in either  $\mathbf{S}_k$  or  $\mathbf{L}_k$ .

Eventually, from the resolution of the set of Eqs.(104) and (105) with the constraints of Eq.(106), one obtains the structure of the  $H_\infty$  filter algorithm similarly to the one of the Kalman filter in Section 3.1:

$$\begin{aligned}
\mathbf{K}_k &= \mathbf{P}_k \left[ \mathbf{I} - \rho_{H_\infty} \bar{\mathbf{S}}_k \mathbf{P}_k + \mathbf{H}_k^T \mathbf{R}_k^{-1} \mathbf{H}_k \mathbf{P}_k \right]^{-1} \mathbf{H}_k^T \mathbf{R}_k^{-1} \\
\tilde{\mathbf{x}}_{k+1} &= \mathbf{F}_k \tilde{\mathbf{x}}_k + \mathbf{F}_k \mathbf{K}_k (\mathbf{y}_k - \mathbf{H}_k \tilde{\mathbf{x}}_k) \\
\mathbf{P}_{k+1} &= \mathbf{F}_k \mathbf{P}_k \left[ \mathbf{I} - \rho_{H_\infty} \bar{\mathbf{S}}_k \mathbf{P}_k + \mathbf{H}_k^T \mathbf{R}_k^{-1} \mathbf{H}_k \mathbf{P}_k \right]^{-1} \mathbf{F}_k^T + \mathbf{Q}_k
\end{aligned} \tag{107}$$

The following condition must hold at each time step  $k$  in order for the above estimator to be a solution to the problem

$$\left( \mathbf{P}_k^{-1} - \rho_{H_\infty} \bar{\mathbf{S}}_k + \mathbf{H}_k^T \mathbf{R}_k^{-1} \mathbf{H}_k \right) > 0 \tag{108}$$

### 3.10 Extended H-Infinity Filter

In the case of nonlinear discrete time system, the  $H_\infty$  filter can be adapted as in the case of the extended Kalman filter of Section 3.2. This means that the structure of the filter in Eqs.(107) and (108) remains the same, but in this case the system dynamics and the measurements matrix are obtained by linearising the equations:

$$\begin{aligned}
\mathbf{F}_k &= \mathbf{\Phi}_{k+1}(t_{k+1}, t_k) = \mathbf{\Phi}_k(t_k, t_k) + \int_{t_k}^{t_{k+1}} \mathbf{f}(\mathbf{x}, t) \mathbf{\Phi}_{k+1}(t, t_k) dt \approx \mathbf{I} + \mathbf{A}_k \Delta t \\
\mathbf{A}_k &= \frac{\partial \mathbf{f}(\hat{\mathbf{x}}_k)}{\partial \hat{\mathbf{x}}_k} \\
\mathbf{H}_k &= \frac{\partial \mathbf{h}(\hat{\mathbf{x}}_k)}{\partial \hat{\mathbf{x}}_k}
\end{aligned} \tag{109}$$

where  $\mathbf{H}_k$  is the Jacobian matrix of the measurements function, calculated around the state estimate at the time  $k$ , differently from the extended Kalman filter, where it was calculated at time  $k+1$ , around the propagated estimate. At each time step the extended  $H_\infty$  filter must satisfy the constraint  $(\mathbf{P}_k^{-1} - \rho_{H_\infty-k} \bar{\mathbf{S}}_k + \mathbf{H}_k^T \mathbf{R}_k^{-1} \mathbf{H}_k) > 0$ , where in this case the performance parameter was tuned at each iteration. An effective way to assure the above constraint is to impose:

$$\rho_{H_\infty-k}^{-1} > \max \left( \text{eig} \left( \bar{\mathbf{S}}_k^{-1} \left( \mathbf{P}_k^{-1} + \mathbf{H}_k^T \mathbf{R}_k^{-1} \mathbf{H}_k \right) \right)^{-1} \right) \quad (110)$$

By introducing a scaling parameter this condition is assured if

$$\rho_{H_\infty-k}^{-1} = \alpha_\infty \max \left( \text{eig} \left( \bar{\mathbf{S}}_k^{-1} \left( \mathbf{P}_k^{-1} + \mathbf{H}_k^T \mathbf{R}_k^{-1} \mathbf{H}_k \right) \right)^{-1} \right) \quad (111)$$

where  $\alpha_\infty$  is obviously greater than one. The structure in Eq.(107) can be arranged in a more convenient way which will be used also in the next Section for the Unscented  $H_\infty$  filter:

$$\begin{aligned} \mathbf{P}_k^- &= \mathbf{F}_{k-1} \mathbf{P}_{k-1}^+ \mathbf{F}_{k-1}^T + \mathbf{Q}_k \\ \mathbf{K}_k &= \mathbf{P}_k^- \mathbf{H}_k^T \left[ \mathbf{H}_k \mathbf{P}_k^- \mathbf{H}_k^T + \mathbf{R} \right]^{-1} \\ \tilde{\mathbf{x}}_k^+ &= \tilde{\mathbf{x}}_k^- + \mathbf{K}_k (\mathbf{y}_k - \mathbf{h}(\tilde{\mathbf{x}}_k^-)) \\ \mathbf{P}_k^+ &= \mathbf{P}_k^- - \mathbf{P}_k^- \begin{bmatrix} \mathbf{H}_k^T & \mathbf{L}_k^T \end{bmatrix} \mathbf{R}_{e,k}^{-1} \begin{bmatrix} \mathbf{H}_k \\ \mathbf{L}_k \end{bmatrix} \mathbf{P}_k^- \end{aligned} \quad (112)$$

where  $\mathbf{R}_{e,k}^{-1}$  is defined as:

$$\mathbf{R}_{e,k} = \begin{bmatrix} \mathbf{R}_k & \emptyset \\ \emptyset & -\rho_{H_\infty-k} \bar{\mathbf{S}}_k \end{bmatrix} + \begin{bmatrix} \mathbf{H}_k \\ \mathbf{L}_k \end{bmatrix} \mathbf{P}_k^- \begin{bmatrix} \mathbf{H}_k^T & \mathbf{L}_k^T \end{bmatrix} \quad (113)$$

The extended  $H_\infty$  filter has an observer structure similar to that of the extended Kalman filter, and  $\mathbf{Q}$  and  $\mathbf{R}$  play a similar role as the covariance matrices of the process noise and the measurement noise in the extended Kalman filter. Moreover, the extended  $H_\infty$  filter reduces to the extended Kalman filter when  $\rho_{H_\infty-k}$  tend to infinity. Thus, the  $\rho_{H_\infty-k}$  may be thought of as a tuning parameter to control the trade-off between  $H_\infty$  filter performance and minimum variance performance. Considering that we are interested in the whole set of state variables, for simplicity we used identity matrices for both  $\mathbf{S}_k$  and  $\mathbf{L}_k$ . The update step becomes:

$$\left(\mathbf{P}_k^+\right)^{-1} = \left(\mathbf{P}_k^-\right)^{-1} + \mathbf{H}_k^T \mathbf{R}_k^{-1} \mathbf{H}_k - \rho_{H_\infty-k} \mathbf{I}_d \quad (114)$$

where  $\mathbf{I}_d$  is the identity matrix.

### 3.11 The Unscented H-infinity Filter

As the extended  $H_\infty$  filter adopts the idea of the extended Kalman filter, the inherent disadvantages associated with the extended Kalman filter, such as the smoothing and lower nonlinearity requirements of the nonlinear functions and the computation errors of Jacobian matrices, remains a challenge to overcome. Analogously to the extended  $H_\infty$  filter, one can exploit other instruments developed in the Kalman filter framework, such as unscented transformation, to overcome the approximation of the Jacobian matrices (Li and Jia, 2010).

Using the unscented transformation and substituting the results from Eqs.(47) and (54)



$$\begin{aligned}
\tilde{\mathbf{x}}_k^+ &= \tilde{\mathbf{x}}_k^- + \mathbf{P}_k^{xy} (\mathbf{P}_k^{\nu\nu})^{-1} (\mathbf{y}_k - \mathbf{h}(\tilde{\mathbf{x}}_k^-)) \\
\mathbf{P}_k^+ &= \mathbf{P}_k^- - \mathbf{P}_k^- \begin{bmatrix} \mathbf{P}_k^{xy} & \mathbf{P}_k^- \end{bmatrix} \mathbf{R}_{e,k}^{-1} \begin{bmatrix} (\mathbf{P}_k^{xy})^T \\ (\mathbf{P}_k^-)^T \end{bmatrix}
\end{aligned} \tag{115}$$

where

$$\mathbf{R}_{e,k} = \begin{bmatrix} \mathbf{P}_k^{\nu\nu} & (\mathbf{P}_k^{xy})^T \\ \mathbf{P}_k^{xy} & -\rho_{H_\infty-k} \mathbf{S}_k + \mathbf{P}_k^- \end{bmatrix} \tag{116}$$

One can see that the parameter  $\rho_{H_\infty-k}$  needs to be chosen such that the determinant of  $\mathbf{P}_k^+$  is positive definite. This is guaranteed if the parameter satisfies the constraint of Eq.(111), which, exploiting the properties of the unscented transformation for  $\mathbf{H}_k = (\mathbf{P}_k^-)^{-1} \mathbf{P}_k^{xy}$ , becomes:

$$\rho_{H_\infty-k}^{-1} = \alpha_\infty \max \left( \text{eig} \left( \bar{\mathbf{S}}_k^{-1} \left( (\mathbf{P}_k^-)^{-1} + (\mathbf{P}_k^-)^{-1} \mathbf{P}_k^{xy} \mathbf{R}_{e,k}^{-1} [(\mathbf{P}_k^-)^{-1} \mathbf{P}_k^{xy}]^T \right) \right)^{-1} \right) \tag{117}$$

Similarly to the extended  $H_\infty$  filter, we used identity matrices for both  $\mathbf{S}_k$  and  $\mathbf{L}_k$  because we are interested in the whole set of state variable. In this way the updated covariance matrix becomes:

$$(\mathbf{P}_k^+)^{-1} = (\mathbf{P}_k^-)^{-1} + (\mathbf{P}_k^-)^{-1} \mathbf{P}_k^{xy} \mathbf{R}_{e,k}^{-1} [(\mathbf{P}_k^-)^{-1} \mathbf{P}_k^{xy}]^T - \rho_{H_\infty-k} \mathbf{I}_d \tag{118}$$

### 3.12 Case Study - Proximity Motion

In this section, we are going to compare the performance of all but the EKF and HAEKF filters. We have already shown that the UKF presents superior performance to these the HAEKF and EKF for the nonlinear WSB transfer problem.

First we describe the problem of proximity motion for a spacecraft in formation with an asteroid. Chapter 4 will deal with the same problem for the case of a formation of 4 spacecraft. It is convenient to describe the dynamic motion of each spacecraft in the rotating Hill reference frame.

In the proximity of the asteroid, the spacecraft is subject to the force due to solar pressure, the gravity of the asteroid, the gravity of the Sun, the centrifugal and Coriolis forces.

With reference to Figure 30, two coordinate systems are defined.

- a) Inertial heliocentric reference frame  $S\{\mathbf{I}, \mathbf{J}, \mathbf{K}\}$  (Cui et al., 2010): the Sun is the centre of the frame, I-axis directs to the Vernal equinox, J-axis is perpendicular to I-axis in the fundamental plane. K-axis points out perpendicular with respect to fundamental plane following the right-handed coordinates system.
- b) Asteroid Hill rotating reference frame  $A\{\hat{\mathbf{x}}_h, \hat{\mathbf{y}}_h, \hat{\mathbf{z}}_h\}$ : the centre A is the barycentre of the asteroid, x-axis is in the orbit radius direction, while y-axis is perpendicular to x-axis in the orbit plane, z-axis completes the right-handed coordinates system which is on the out-of-plane direction. The relative position  $\delta\mathbf{r}^h = [x_h, y_h, z_h]^T$  and velocity  $\delta\dot{\mathbf{r}}^h = [\dot{x}_h, \dot{y}_h, \dot{z}_h]^T$  of spacecraft with respect to the asteroid are described in this coordinate system.

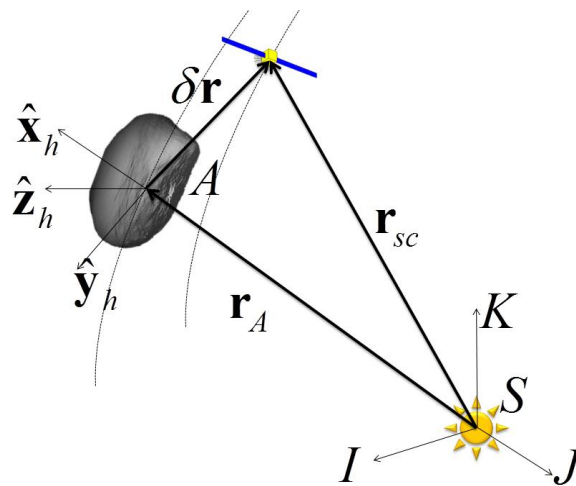


**Figure 30. Definition of the reference coordinate systems.**

It is assumed that the asteroid is an ellipsoid with semi-axes  $a_l$ ,  $b_l$  and  $c_l$  (Scherees, 2012). The asteroid rotates around the  $z$ -axis with angular velocity  $\omega_A$  as in Figure 31.

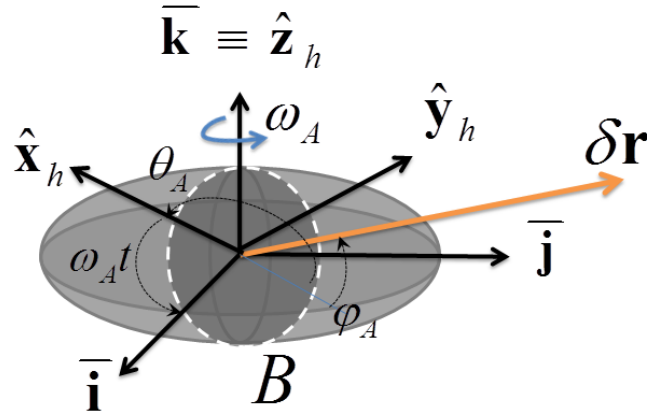


**Figure 31. Asteroid body frame with respect to the Hill frame.**

The geometric shape model of the asteroid is expressed as

$$\left(\frac{x_b}{a_l}\right)^2 + \left(\frac{y_b}{b_l}\right)^2 + \left(\frac{z_b}{c_l}\right)^2 = 1 \quad (119)$$

where  $a_l$ ,  $b_l$  and  $c_l$  are the semi-axes physical dimensions of the asteroid and the subscript  $b$  refers to the body frame  $B\{\bar{\mathbf{i}}, \bar{\mathbf{j}}, \bar{\mathbf{k}}\}$ .

It has been demonstrated that the second-degree and second-order gravity field terms dominated the orbital stability of the spacecraft for close proximity motion to uniformly rotating asteroid (Scherees, 2012). Therefore, the gravity field of the asteroid could be expressed as the sum of a spherical field plus a second-degree and second-order field (Hu, 2002),

$$U_{20+22} = \frac{\mu_A}{\delta r^3} \left( C_{20} \left( 1 - \frac{3}{2} \cos^2 \theta_A \right) + 3C_{22} \cos^2 \theta_A \cos 2\varphi_A \right) \quad (120)$$

where  $\mu_A$  is the asteroid gravitational constant,  $\delta r$  is the relative distance between the spacecraft and the asteroid, and the harmonic coefficients  $C_{20}$  and  $C_{22}$  are a function of the semi-axes

$$\begin{aligned} C_{20} &= -\frac{1}{10} (2c_I^2 - a_I^2 - b_I^2) \\ C_{22} &= \frac{1}{20} (a_I^2 - b_I^2) \end{aligned} \quad (121)$$

$\theta_A$ ,  $\varphi_A$  are the latitude and longitude angles, respectively as shown in Figure 31. They are defined as

$$\begin{aligned} \theta_A &= \arctan \left( \frac{z_h}{\sqrt{x_h^2 + y_h^2}} \right) \\ \varphi_A &= \arctan \left( \frac{y_h}{x_h} \right) + \omega_A t \end{aligned} \quad (122)$$

$t$  is the time. It is assumed that the body frame is coincident with the asteroid Hill frame at the beginning of the simulations. In this analysis, the spacecraft is subject to the force due to the gravity of the Sun, solar pressure and the irregular gravity of the asteroid. Other forces induced by spacecraft operations with mirrors are not considered. The nonlinear relative equations of motion are given by (Vasile and Maddock, 2012):

$$\begin{aligned}
\ddot{x}_h &= 2\dot{\theta} \left( \dot{y}_h - y_h \frac{\dot{r}_A}{r_A} \right) + x_h \dot{\theta}^2 + \mu_{Sun} \left( \frac{1}{r_A^2} - \frac{r_A + x_h}{r_{sc}^3} \right) + a_{Solar} - \mu_A \frac{x_h}{\delta r^3} + \frac{\partial U_{20+22}}{\partial x_h} + a_{w_x} \\
\ddot{y}_h &= -2\dot{\theta} \left( \dot{x}_h - x_h \frac{\dot{r}_A}{r_A} \right) + y_h \dot{\theta}^2 - \mu_{Sun} \frac{y_h}{r_{sc}^3} - \mu_A \frac{y_h}{\delta r^3} + \frac{\partial U_{20+22}}{\partial y_h} + a_{w_y} \\
\ddot{z}_h &= -\mu_{Sun} \frac{z_h}{r_{sc}^3} - \mu_A \frac{z_h}{\delta r^3} + \frac{\partial U_{20+22}}{\partial z_h} + a_{w_z}
\end{aligned} \tag{123}$$

with

$$\begin{aligned}
\ddot{\theta} &= -\frac{2\dot{r}_A}{r_A} \dot{\theta} \\
\dot{r}_A &= \dot{\theta}^2 r_A
\end{aligned} \tag{124}$$

$\theta$  is the true anomaly of the asteroid,  $r_A$  and  $r_{sc}$  are the orbit radius of the asteroid and spacecraft, respectively;  $\dot{r}_A$  is the radial velocity of the asteroid. Note that the perturbations acting on the asteroid trajectory are assumed to be null and no effects such as solar radiation and spacecraft tugging is considered. The only perturbations modelled are the ones acting on the spacecraft. Beyond the gravitational perturbations from the asteroids, the major perturbation is due to the solar radiation  $a_{Solar}$ , acting on the solar mirrors along the  $x_h$ -axis.

Additional noise  $\mathbf{a}_w = [a_{wx}, a_{wy}, a_{wz}]$  is in the order of  $10^{-9} \text{ m/s}^2$ , due to acceleration caused by the unbalanced attitude control manoeuvres. During the analysis a mass of about 500 kg and maximum cross section area of  $20 \text{ m}^2$  were considered. A mean value of 1.2 for  $C_R$  general an uncertainty of 20% solar pressure is introduced as random noise.

### 3.12.1 Camera Model

To reconstruct the navigation measurement, the camera takes the images of the surface features with the position available during the characterization phase to estimate the spacecraft motion. The measurement model is expressed in the camera coordinate system.

First, the geometric relationship is defined in the asteroid Hill rotating reference frame. The position vector of the  $i$ -th feature is  $\mathbf{x}_{surface}^i$ , which is selected randomly on the asteroid surface according to Eq.(119). The spacecraft position vector with respect to the asteroid is defined as  $\delta\mathbf{r}_{SC}$ , while  $\mathbf{x}_{Surf-SC}^i$  refers to the position vector from the estimated spacecraft to the feature. A certain number of points are taken on the asteroid surface. With respect to Figure 32, the position of each point is given as:

$$\mathbf{x}_{Surf-SC}^i = \mathbf{x}_{surface}^i - \delta\mathbf{r}_{SC} \quad (125)$$

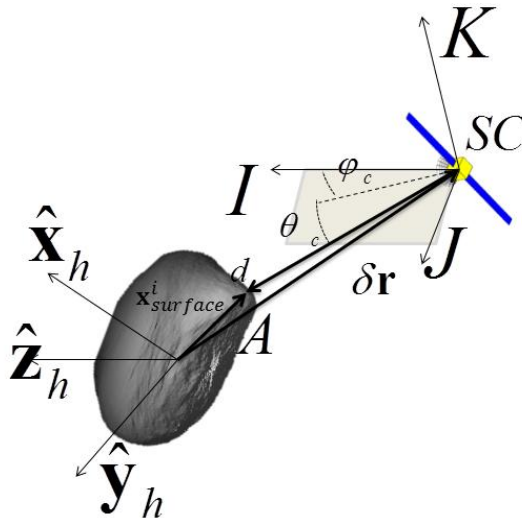


Figure 32. Measurements models for relative navigation geometry.

Then these points are given in the camera reference frame in the components  $(x_{cam}, y_{cam}, z_{cam})^i$  :

$$\begin{aligned} x_c^i &= \mathbf{x}_{Surf-SC}^i \cdot \mathbf{x}_{camera} \\ y_c^i &= \mathbf{x}_{Surf-SC}^i \cdot \mathbf{y}_{camera} \\ z_c^i &= \mathbf{x}_{Surf-SC}^i \cdot \mathbf{z}_{camera} \end{aligned} \quad (126)$$

where  $\mathbf{x}_{camera}$ ,  $\mathbf{y}_{camera}$  and  $\mathbf{z}_{camera}$  represent the axes of the camera coordinate system. If  $\mathbf{v}^i = [v_x^i \ v_y^i \ v_z^i]^T$  is the normalized local vector corresponding to each point, the position of the surface point in terms of pixel can be defined as:

$$\begin{aligned} u^i &= v_x^i t_c / p_{width} \\ v^i &= v_y^i t_c / p_{width} \end{aligned} \quad (127)$$

where  $t_c = f / v_z^i$ ,  $f$  and  $p_{width}$  are the focal length and pixel width of the camera, respectively. The coordinates  $(u^i, v^i)^T$  are obtained by the image of the feature point on the screen of the camera. A representation of this stage of the process is reported in Figure 33.

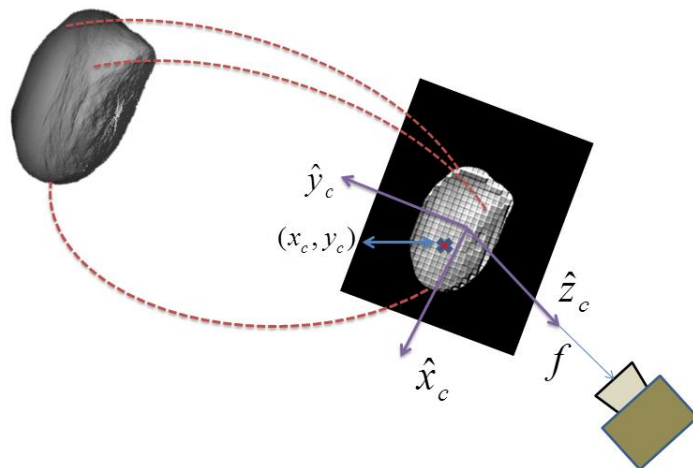


**Figure 33. Centroid identification.**

The centroid coordinates  $(x_c, y_c)$  are obtained by the mean position of all the points on the screen of the camera. From the pixel representation on the screen of the camera, local azimuth and elevation angles can be obtained as:

$$\begin{aligned}\varphi_c &= \tan^{-1} \frac{y_c}{x_c} \\ \theta_c &= \tan^{-1} \frac{f}{\sqrt{(x_c)^2 + (y_c)^2}}\end{aligned}\tag{128}$$

The measurements from the camera are affected by both attitude and pixelization errors. Note that here the illumination conditions are not considered, so it is assumed that each spacecraft sees the whole visible surface from its position. This is sensible if one assumes that a complementary map could be built while starting the orbit acquisition, combining the pictures from the whole formation.

Considering the Gaussian white measurement noise  $\boldsymbol{\zeta}_c$ , the camera observation equation is presented as

$$\mathbf{y}_c = h_c(\mathbf{x}) + \boldsymbol{\zeta}_c = [\varphi_c \ \theta_c]^T + \boldsymbol{\zeta}_c\tag{129}$$

### 3.12.2 LIDAR Model

LIDAR works at a range from 50 km to 50 m which provides range from the spacecraft to the target object. It is assumed that LIDAR illuminates the point on the surface that corresponds to the centroid (Dionne et al., 2009). Then, this distance is simply given by:

$$l = \left| \delta \mathbf{r} - \mathbf{x}_{surface}^c \right|\tag{130}$$



where  $\mathbf{x}_{surface}^c$  is the position of the point on the asteroid's surface along the centroid direction. The observation equation of LIDAR including the measurement noise is described as

$$\mathbf{z}_d = h_d(\mathbf{x}) + \nu_l = l + \varsigma_l \quad (131)$$

Its accuracy depends on the characteristics error of the sensor, along with a bias defined by the mounting error of the instrument,  $\varsigma_l$  is the zero-mean Gauss white measurement noise.

If the range  $l$  is pre-processed in combination with the angular measurements from Eq.(129), a relative position vector from the spacecraft to the surface point can be constructed as

$$\mathbf{y} = \begin{bmatrix} l \\ \varphi_c \\ \theta_c \end{bmatrix} = h(\mathbf{x}) + \varsigma \quad (132)$$

where  $\mathbf{z}$  is the measurement vector obtained from the combination of camera and LIDAR,  $h(\mathbf{x})$  is the vector containing the model measurements,  $\varsigma$  is the Gauss white noise.

### 3.12.3 Comparison

We considered a single spacecraft flying in formation with the asteroid Aphophis, whose characteristics are enlisted in Table 11. The initial condition for spacecraft trajectory is

$$\mathbf{x} = [0.4932km \quad -5.1123km \quad -1.3581km \quad 0km/s \quad 0km/s \quad 0km/s]^T$$

with respect to Hill reference frame.

**Table 11. Orbital and physical properties of 99942 Apophis**

Element	Notation	Value
Semi-major axis	$a_A$	0.9224 AU
Eccentricity	$e_A$	0.1912
Inclination	$i_A$	0.05814 rad
Longitude of ascending node	$\Omega_A$	3.05682 rad
Argument of periapsis	$\varpi_A$	2.2061 rad
Orbital Period	$T_A$	323.5969 d
Gravitational constant	$\mu_A$	$1.801599 \times 10^{-9} \text{ km}^3/\text{s}^2$
Physical dimensions	$a_1, b_1, c_1$	191 m, 135 m, 95 m
Rotational velocity	$\omega_A$	$5.8177 \times 10^{-5} \text{ rad/s}$

Since the spacecraft does not orbit the asteroid, this condition was arbitrarily set in order to avoid the spacecraft impacting onto the asteroid during filtering process of 1 day. We used an accuracy  $\zeta_r = 10 \text{ m}$  (1-sigma) and  $\zeta_c = [10^{-3} \ 10^{-3}] \text{ rad}$  (1-sigma) on the LIDAR and camera's angles respectively. A biased of 1 m on the range and  $0.5 \cdot 10^{-3} \text{ rad}$  on angles was also assumed. The initial position guess was generated with initial error of 20% in position and  $10^{-5} \text{ km/s}$  in velocity. The dispersion of the initial states of the spacecraft was equal to 50% of the initial guess. For this comparison we considered 100 runs for each filter, because given the proximity and reduced initial dispersion the results are very sensitive to the measurements set. Figure 34 shows the root mean square error, RMSE for position and velocity. The trends are very similar, except that the UPF presents a higher peak in the initial transient. This is essentially due to the fact that at the beginning many particles are generated in the low probability regions, and this leads to higher errors which are compensated as the filter starts converging. Also the UKF has a similar peak with a longer transient in the position error. The EnKF and the  $H_\infty$  filters converge towards lower error regions without initial peaks. Nonetheless the UPF has a low RMSE in both the position and velocity components because it shows faster convergence in the initial transient.

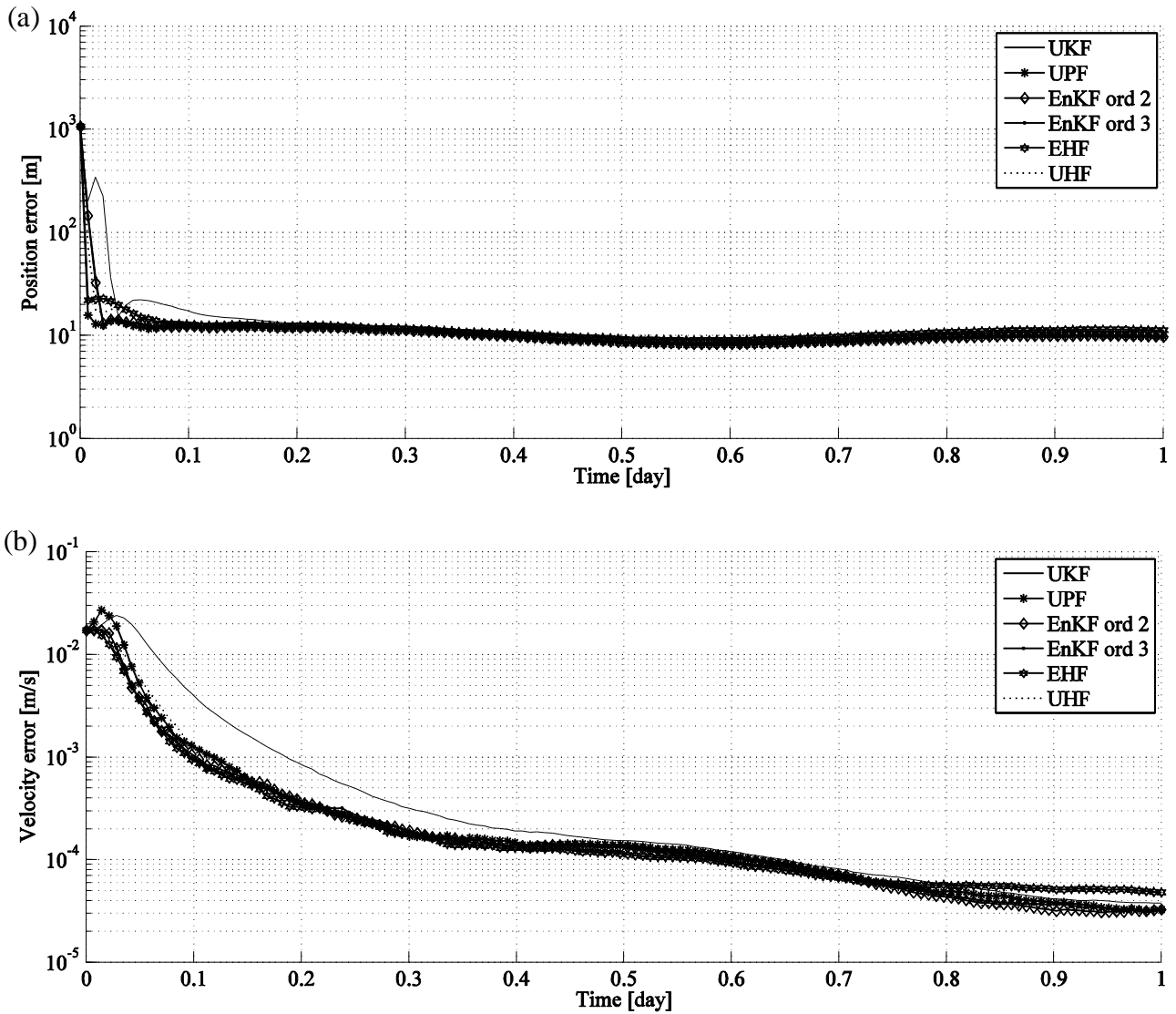


**Figure 34. RMSE for a) position and b) velocity.**

Table 12 reports statistical quantities for this comparison. As one can see, among the Kalman family the PF and EnKF order 3 achieves the best performances, the first in terms of position while the second achieves in terms of velocity error. Moreover increasing the polynomial order slightly improves the convergence towards lower error region, meaning that a second order polynomial is capable to describe with accuracy the statistics quantities. Nevertheless, the computational time

results the highest compare to the EHF, UHF and UKF. The PF requires about 2 orders of magnitude more time than the UKF. This is due to the UT which has been applied at each step to 100 particles, i.e. 7200 integrations plus the resampling process.

**Table 12. Elapsed CPU time per run for the filtering processes of the proximity motion, using a 64-bit Linux CentOS 5.4 2.93GHz Intel<sup>(R)</sup> Xeon<sup>(TM)</sup> X5570 , and absolute error for the estimated state.**

	UKF	PF	EnKF ord. 2	EnKF ord. 3	EHF	UHF
Mean CPU time per simulation [s]	362	38732	8222	12112	302	380
RMS position error [m]	23.49	17.43	18.59	18.55	18.62	18.30
RMS velocity error [mm/s]	1.78	1.19	0.91	0.89	0.99	0.83

The EnKF requires much time because the update step needs repetitive operations on 104 samples, whilst the propagation step needs to propagate 73 and 253 samples respectively against 42 of the EHF and 72 of the UKF and UHF. The UHF results to be the most accurate with an acceptable computational time, even though the gain with respect to the EHF is not very high. This means that by sampling with a relatively small interval, the linear approximation is still valid. The example showed that the measurements noise is moderately non-Gaussian, so the assumption of Gaussian noise is still valid for this kind of problem although the  $H_\infty$  filters showed better convergence properties.

### 3.13 Summary

In this chapter, the main families of Kalman and H-infinity have been introduced and explained in details. We compared different filters applied to the case of the European Student Moon Orbiter for a WSB transfer and to the case of a spacecraft proximal motion close to the asteroid Aphophis. We have seen that the main difference between Kalman filters is represented by the way the statistics

values represented by the covariance matrix and the mean are propagated. For highly nonlinear problems such as the WSB transfer a first order propagation, i.e. the EKF, is not accurate enough to describe the evolution of the statistics under nonlinear dynamics. The results show that the computational cost of the operation is not compatible with on-board systems when one seeks higher accuracy. The higher order terms could be a solution because the STTs could be calculated offline and then used with simple algebraic formulas. Nonetheless STTs can be suitable only for missions in which the dynamics are well known and the spacecraft follows the nominal trajectory with a small deviation. If the spacecraft had to follow a completely different trajectory, STTs should be calculated and would be very demanding for on board systems.

The Unscented Kalman Filter outperforms other Kalman filters, mainly in terms of balance between accuracy and computational cost. UKF is best choice for on-board application, especially when the system and measurements noises are (quasi) Gaussian. Particle filters such as the UPF and EnKF based on polynomial chaos are very precise as well but they are very demanding for the required computational time.

When no precise a priori information relatively to these noises is available, the minmax filters, i.e. Extended and Unscented H-infinity Filter, must be preferred for their capability to minimize the expected error when the system and measurements noises are maxima. From our analysis the best compromise between accuracy and computational time is represented by the Unscented H-infinity filter which has hybrid characteristics between the Kalman and the H-infinity filter, thanks to the use of a tuning parameter and to the UT which allows propagating the mean and the covariance accurately, thanks to the better inclusion of the non-linear effects with respect to the EHF.

The content of this Chapter was published in Vetrisano, M. and Vasile, M., 2015: 'Autonomous navigation of a spacecraft formation in the proximity of an asteroid'. *Advances in Space Research*. Volume 56, Issue 8, Pages 1547-1804 (15 October 2015). doi:10.1016/j.asr.2015.07.024

## 4 Collaborative Formation at NEOs

In this Chapter we want to apply a suitable filter technique to the case of a formation flying in formation with a relatively big asteroid. The asteroid 99942 Apophis was considered, also because is seen as good representative of PHAs with relatively low aphelion. Method based on optical navigation camera and laser light radar/laser range finder integrated measurements has been proved to be a feasible option for a single spacecraft to approach or land on the asteroid. Although a formation would require controlling an increased number of degrees of freedom, one could exploit higher flexibility to achieve the mission's goal and improve system's performance. This Chapter proposes to complement spacecraft to asteroid information from camera and ranging instrument with inter-spacecraft measurements. For multiple spacecraft systems, the inter-spacecraft relative observations can be evaluated to obtain better estimations. A Lyapunov controller is also implemented for each member of the formation to counteract the effect of the perturbations using a low thrust propulsion system. A suitable data fusion process to handle a variable number of spacecraft is presented. We demonstrate that the navigation accuracy is improved by sharing the information within the member of the formation, even in presence of failures and contingencies.

Another aspects treated in this work is the possibility to use 2-spacecraft as in-orbit observatory to improve asteroid's trajectory estimate prior to starting the orbit acquisition. Since actual missions to PHAs would require short warning and the actual asteroid's trajectory could be uncertain, on-board optical observations from the formation could be used along with ground station tracking. On board optical measurements from navigation cameras have been widely used in recent years during deep space navigation and approach Konimato et al. (2006). For instance, relying only on one single

camera, the Hayabusa mission performed a suitable set of dogleg manoeuvres to observe the asteroid from different phase angle, refine asteroid trajectory and acquire the object. A dogleg approach, though, requires performing small manoeuvres and, as a consequence, lasts longer than a direct rendezvous at the asteroid. It is shown for different approach configurations that a 2-spacecraft formation can improve the accuracy of the asteroid ephemeris without performing dogleg manoeuvres. It is also considered to employ the Sun Doppler shift effects to increase the accuracy of the orbit determination following work of Yim et al. (2000) for the deep space navigation of a single spacecraft.

## **4.1 Dynamic Models**

Spacecraft formation dynamics in the proximity of an asteroid is complicated due to the small mass and irregular shape of the target asteroid. The asteroid is considered as the leading member of the spacecraft formation. The following sections provide the dynamic model to illustrate the state variables which will be considered for the navigation later in Section 4.3.

### **4.1.1 Formation Dynamics**

The reference systems and the dynamic equations are the same as the ones introduced in Section 3.12. The nonlinear relative equations of motion are the same of Eq.(123), reported again for simplicity considering the contribution of a possible control action:

$$\begin{aligned}
\ddot{x}_h &= 2\dot{\theta} \left( \dot{y}_h - y_h \frac{\dot{r}_A}{r_A} \right) + x_h \dot{\theta}^2 + \mu_{Sun} \left( \frac{1}{r_A^2} - \frac{r_A + x_h}{r_{sc}^3} \right) + a_{Solar} - \mu_A \frac{x_h}{\delta r^3} + \frac{\partial U_{20+22}}{\partial x_h} + a_{w_x} + u_x \\
\ddot{y}_h &= -2\dot{\theta} \left( \dot{x}_h - x_h \frac{\dot{r}_A}{r_A} \right) + y_h \dot{\theta}^2 - \mu_{Sun} \frac{y_h}{r_{sc}^3} - \mu_A \frac{y_h}{\delta r^3} + \frac{\partial U_{20+22}}{\partial y_h} + a_{w_y} + u_y \\
\ddot{z}_h &= -\mu_{Sun} \frac{z_h}{r_{sc}^3} - \mu_A \frac{z_h}{\delta r^3} + \frac{\partial U_{20+22}}{\partial z_h} + a_{w_z} + u_z
\end{aligned} \tag{133}$$

with  $\mathbf{u} = [u_x \quad u_y \quad u_z]^T$  is a control input which will be defined later in Section 4.1.3.

Beyond the gravitational perturbations from the asteroids, the major perturbation is again the solar radiation pressure  $a_{Solar}$  (see Eq.(2) for its definition). Additional noise  $\mathbf{a}_w = [a_{w_x} \quad a_{w_y} \quad a_{w_z}]^T$  is in the value of  $10^{-9} \text{ m/s}^2$ , due to the acceleration caused by the unbalanced attitude control manoeuvres.

For what concerns the proximal motion, a formation of 4 spacecraft is considered following the work of (Vasile and Maddock, 2012). The estimated state variables are 3 dimensional position and velocity of the 4 spacecrafts, and a total of twenty-four states to characterize the formation. The corresponding state equation of the navigation system is described as

$$\begin{aligned}
\dot{\mathbf{x}}^h &= f(\mathbf{x}^h) + \mathbf{w} = [\dot{x}_1 \quad \dot{y}_1 \quad \dot{z}_1 \quad \ddot{x}_1 \quad \ddot{y}_1 \quad \ddot{z}_1 \quad \dot{x}_2 \quad \dot{y}_2 \quad \dot{z}_2 \quad \ddot{x}_2 \quad \ddot{y}_2 \quad \ddot{z}_2 \\
&\quad \dot{x}_3 \quad \dot{y}_3 \quad \dot{z}_3 \quad \ddot{x}_3 \quad \ddot{y}_3 \quad \ddot{z}_3 \quad \dot{x}_4 \quad \dot{y}_4 \quad \dot{z}_4 \quad \ddot{x}_4 \quad \ddot{y}_4 \quad \ddot{z}_4]^T + \mathbf{w}
\end{aligned} \tag{134}$$

where  $\mathbf{x}^h = [\delta \mathbf{r}_{SC-1}^h, \delta \dot{\mathbf{r}}_{SC-1}^h, \delta \mathbf{r}_{SC-2}^h, \delta \dot{\mathbf{r}}_{SC-2}^h, \delta \mathbf{r}_{SC-3}^h, \delta \dot{\mathbf{r}}_{SC-3}^h, \delta \mathbf{r}_{SC-4}^h, \delta \dot{\mathbf{r}}_{SC-4}^h]^T$  is the state vector containing the relative position and velocity of all spacecrafts. For simplicity we omitted the subscript  $h$ , thus all the components refers to the Hill reference frame.  $[\dot{x}_i, \dot{y}_i, \dot{z}_i]^T$  and  $[\ddot{x}_i, \ddot{y}_i, \ddot{z}_i]^T$  are the relative velocity and acceleration of the  $i$ -th spacecraft with respect to asteroid, respectively,  $\mathbf{w} = \mathbf{a}_w$  is the white Gaussian process noise.



The spacecraft formation is assumed to fly in the proximity of 99942 Apophis. 99942 Apophis is particularly interested due to its high impact probability and a logical choice for a deflection mission. The Keplerian elements along with the physical properties of Apophis were already listed in Table 11.

The initial conditions for spacecraft trajectories are given in terms of coordinate variation with respect to the asteroid's nominal trajectory, as reported in Table 13. These orbits were designed in Vasile and Maddock (2012) to maintain the spacecraft close to the asteroid, reduce the requirements for control and contamination from plumes and allow the spacecraft formation to point the solar beam towards the same spot on the surface. During the analysis, an initial mass of spacecraft is 500 kg with the maximum cross section area is about 20 m<sup>2</sup>. A mean value of 1.2 for the reflectivity coefficient is assumed. In general, an uncertainty of 20% solar pressure is introduced as random noise.

**Table 13. Initial spacecraft trajectory parameters.**

	$x_h$ (km)	$y_h$ (km)	$z_h$ (km)	$\dot{x}_h$ ( $10^{-9}$ km/s)	$\dot{y}_h$ ( $10^{-9}$ km/s)	$\dot{z}_h$ ( $10^{-9}$ km/s)
SC1	0.0323	-0.5000	-0.774	0.193	-4.480	-7.837
SC2	0.046	-1.039	-0.608	0.051	-18.120	-6.350
SC3	0.0323	-0.503	0.307	0.259	-4.533	-3.652
SC4	0.092	-1.104	0.451	0.009	-1.467	-4.942

Without the effects of perturbation the evolution of the formation during one revolution of the asteroid around the Sun would be represented by periodic non-Keplerian orbits as reported in Figure 35.

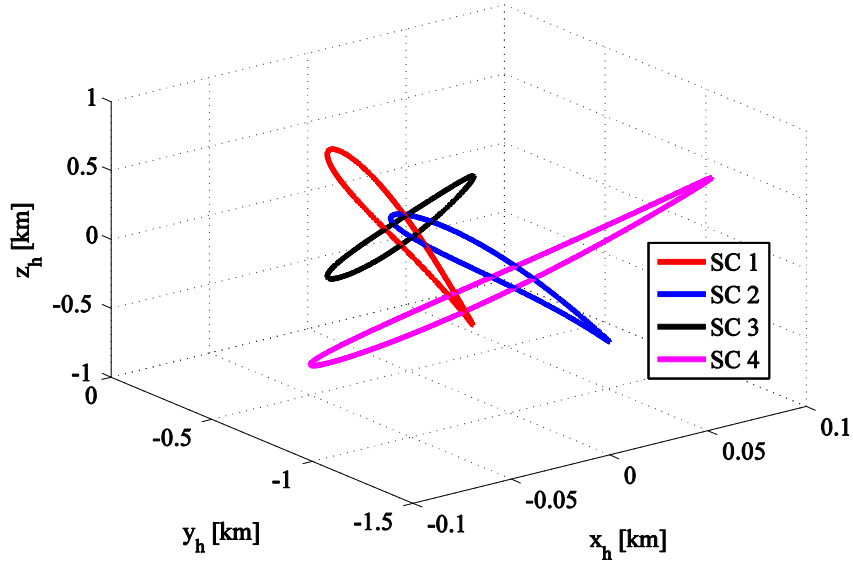


**Figure 35. Nominal trajectories.**

#### 4.1.2 Dynamic Equations of Asteroid and Spacecraft in the Heliocentric Frame

In order to integrate the set of Eq.(133), the dynamics equations of the asteroid can be written as

$$\begin{aligned}\dot{\mathbf{r}}_A &= \mathbf{v}_A \\ \ddot{\mathbf{r}}_A &= -\frac{\mu_{Sun}}{r_A^3} \mathbf{r}_A\end{aligned}\quad (135)$$

where  $\mathbf{v}_A$  is the asteroid velocity in the heliocentric frame. Note that the perturbations acting on the asteroid are assumed to be null and no effects such as solar radiation and spacecraft tugging is considered.

When considering deep space navigation, also the spacecraft dynamics are given in heliocentric frame. In this case for each spacecraft the state equations become

$$\dot{\mathbf{x}}_{SC-i} = f(\mathbf{x}_{SC-i}) = \begin{bmatrix} \dot{\mathbf{r}}_{SC-i} \\ -\frac{\mu_{Sun}}{r_{SC}^3} \mathbf{r}_{sc-i} + C_R S_{srp} \left( \frac{r_{IAU}}{r_{SC}} \right)^2 \frac{(\mathbf{r}_{SC-i})}{r_{SC-i}} \frac{A}{m_{sc}} \end{bmatrix} + \mathbf{w}_{SC-i} \quad (136)$$

where  $\mathbf{x}_{SC-i} = [\mathbf{r}_{SC-i}, \dot{\mathbf{r}}_{SC-i}]^T$  is the spacecraft state in the heliocentric frame,  $\mathbf{w}_{SC-i}$  is a Gaussian white noise similarly to  $\mathbf{w}$  of Eq.(134).

#### 4.1.3 Control Strategy

Given Eq.(133), the resultant of all the disturbing forces acting on the spacecraft is clearly not zero. The combined effect from the perturbations is that the spacecraft will crash on the asteroid, as shown in Figure 36. The impacts occur in less than one day.

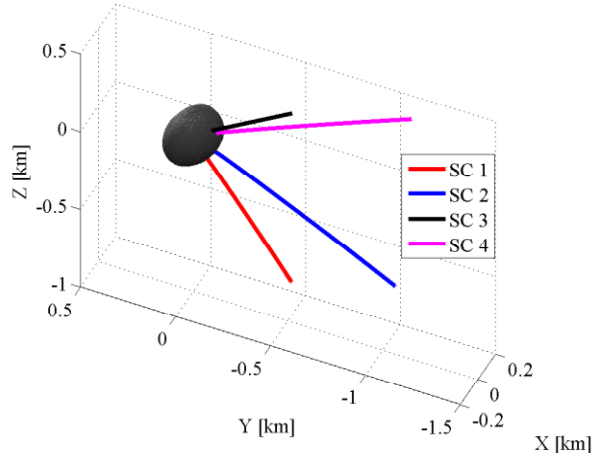


**Figure 36. Relative distance under all perturbations.**

Thus, it is clear that a control force is required to maintain the spacecrafts orbits as close as possible to the nominal ones.

Given the reduced distances from the asteroid, one can assume that centrifugal and Coriolis forces are negligible compared to solar pressure, while the inhomogeneous gravity of the asteroid and any other non-spherical terms in the gravity field expansion result in only a small perturbation, then a simple control law based on the control Lyapunov function can be built up (Vasile and Maddock, 2012):

$$V = \frac{1}{2} \delta v^2 + \frac{1}{2} \kappa \left( (x - x_{ref})^2 + (y - y_{ref})^2 + (z - z_{ref})^2 \right) \quad (137)$$

where  $\delta \mathbf{r}_{ref} = [x_{ref} \ y_{ref} \ z_{ref}]^T$  are the coordinates of a spacecraft along the nominal formation orbit in the Hill reference frame,  $\delta \mathbf{r} = [x \ y \ z]^T$  is the actual position of the spacecraft;  $\kappa$  is the elastic coefficient. It is assumed that the motion along the reference formation orbit is much slower than the control action. The Lyapunov function of Eq.(137) is 0 when the spacecraft is on the reference trajectory, which represents the equilibrium point of the varied system. The necessary condition for the stability of the equilibrium point is that there must be a controller  $\mathbf{u}$  which makes  $dV/dt < 0$ . Thus the temporal variation  $V$  of is a negative definite function, which means that the choice of the control law of Eq.(138) ensures that the equilibrium point of the system is asymptotically stable. A controller which satisfies this condition can be defined as follows:

$$\mathbf{u} = - \left( \mathbf{a}_{Sun}(\delta \mathbf{r}) - \frac{\mu_A}{\delta r^3} \delta \mathbf{r} \right) - \kappa (\delta \mathbf{r} - \delta \mathbf{r}_{ref}) - c_d \delta \mathbf{v} \quad (138)$$

where  $c_d$  is a steady dissipative coefficient. If the actual trajectory of the spacecraft is known, the continuous control in Eq.(138) can now be introduced into the full dynamic model in Eq.(133). Nevertheless, the trajectory is estimated by the navigation system, while the actual position of the

spacecraft is never known exactly. The predicted estimation is then used by the controller to maintain the relative formation (shown later in Section 4.3). Once the controller is inserted in the spacecraft dynamics, one obtains a close loop problem in which control is performed together with estimation, and the filter equations have to consider the action of the controller itself. During the controlled phases, it is assumed that the asteroid trajectory is precisely known, the state variables to be estimated are the only ones related to the spacecraft formation.

## 4.2 Measurements Model

An accurate measurement model plays a key role in the navigation problem in order to obtain precise orbit determination. The main navigation measurements come from on-board high resolution camera and LIDAR. The camera provides image information which is limited by the range ambiguity, while the LIDAR provides the range measurement which complements the navigation system. In Section 4.2.1 and 4.2.2, the models used for relative navigation are described. The absolute navigation measurement models used to refine the asteroid trajectory are built up in Section 4.2.3 and 4.2.4. With reference to Figure 37, the set of information provided by the sensors assembly is given by:

- 1) High resolution camera which provides elevation and azimuth angles of the feature point on the asteroid surface.
- 2) LIDAR which measures the distance from the spacecraft to the asteroid surface.
- 3) Inter-spacecraft measurements which include the relative angular measurements along with the distance between two spacecrafts.
- 4) Range and range rate obtained from ground station.

5) Sun Doppler shift sensor descends from the radial velocity of the spacecraft with respect to the Sun.

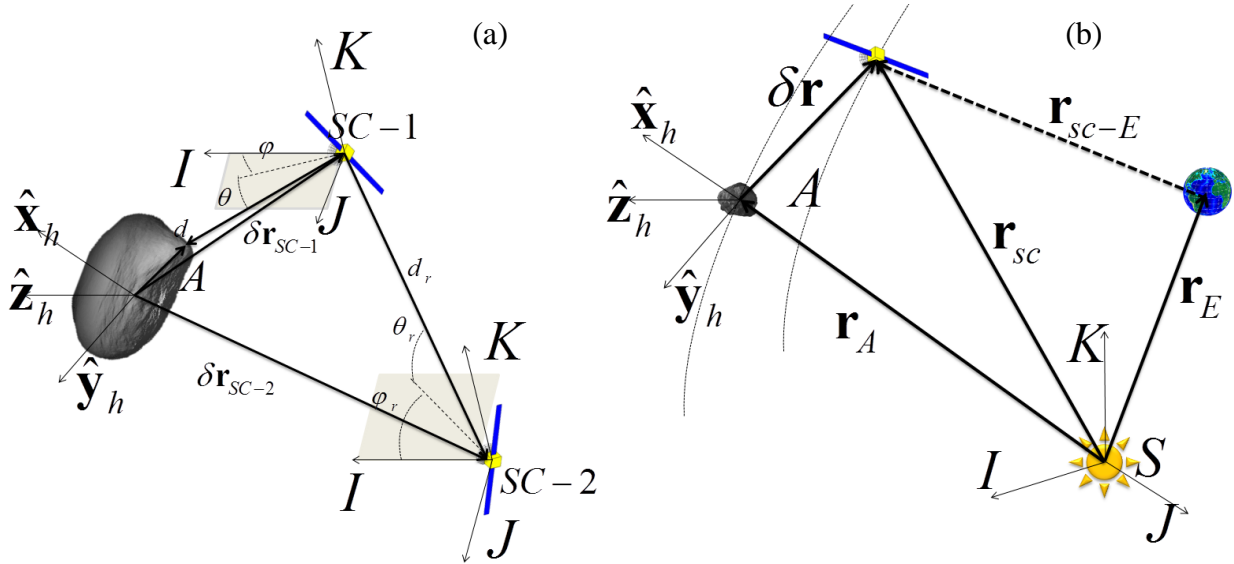


**Figure 37. Measurements models for (a) relative navigation geometry (b) absolute navigation geometry.**

When dealing with on-board sensors, these are affected by pointing errors. In theory, two intermediate reference frames should be required:

- 1) Spacecraft coordinates system  $SC\{\mathbf{x}_{sc}, \mathbf{y}_{sc}, \mathbf{z}_{sc}\}$  (Li et al., 2007): the origin of this frame lies in the spacecraft's mass centre; three body axes of symmetry are defined as three coordinate axes.
- 2) Camera coordinates system  $C\{\hat{\mathbf{x}}_c, \hat{\mathbf{y}}_c, \hat{\mathbf{z}}_c\}$ : the centre  $C$  is the perspective projection of the camera.  $\mathbf{z}_c$ -axis is parallel to the optical axis of the camera and directed to the centre of the asteroid. Image plane is defined as  $\mathbf{o}_c - \mathbf{x}_c \mathbf{y}_c$ . To simplify mathematics, it is assumed that the spacecraft and camera coordinate system are coincident.

Given that spacecraft attitude dynamics is not modelled, for sake of simplicity during the proximity phases the spacecraft coordinate system is assumed to be aligned with the Hill frame  $A$  (see Section 3.12.3). During the deep phase navigation the coordinate system is aligned with the inertial frame  $S$ . Thus, it is assumed that the attitude of each spacecraft is known with a level of precision corresponding to the one of the star tracker on two axes.

#### 4.2.1 Camera and LIDAR Model

We already have seen a camera and a LIDAR model in Section 3.5, in which a simple *pinhole* model was used. In this case we want to analyze in more detail, how the different sources of error affect the measurement. With reference to Figure 38, a generic point on the surface of the asteroid, with position  $\mathbf{r}_p = [x_c \quad y_c \quad z_c]^T$  in the reference frame of the camera, is defined on the image plane of the camera as:

$$\begin{bmatrix} u \\ v \end{bmatrix} = \frac{f}{x_c} \begin{bmatrix} y_c \\ z_c \end{bmatrix} \quad (139)$$

where  $x_c$  is the distance of the point from the image plane along the boresight direction and  $f$  is the focal length of the camera. The position in the camera reference frame is given by:

$$(140)$$

where  $\mathbf{R}$  is the rotation matrix from the Hill's reference frame to the camera frame  $\mathbf{r}_p$  is the vector position of the points with respect to the centre of the Hill's reference frame given in Eq.(125). The coordinates of the point on the image plane measured in pixels are given by Eq.(127).

The mean position of all the points on the image plane of the camera defines the coordinates of the centroid of the asteroid.

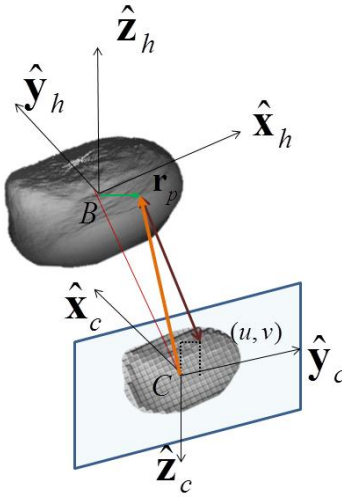


**Figure 38. Pin-Hole camera model.**

It is assumed that the centroid of the asteroid identifies the position of the centre of mass; therefore by measuring the angular position of the centroid one can estimate the angular position of the centre of mass in the reference frame of the camera. The azimuth and elevation angles of the centroid are given by Eq.(128).

The measurement from the camera is affected by both the spacecraft attitude pointing and pixelization errors. The latter error is due to the fact that the image of the asteroid is formed by a discrete number of pixels and this could lead to an incorrect position of a surface feature on the image plane.

By manipulating Eq.(128) and considering the pixelization error  $\zeta_p$ , one can write the observation equation:



$$\mathbf{z}_{camera} = \begin{bmatrix} \tan^{-1} \frac{{}^c u_c P_{width} + \zeta_p}{f} \\ \tan^{-1} \frac{{}^c v_c P_{width} + \zeta_p}{\sqrt{({}^c u_c P_{width} + \zeta_p)^2 + f^2}} \end{bmatrix} \quad (140)$$

By expanding Eq.(140) up to the first order in the noise component, one obtains:

$$\mathbf{z}_{camera} = \begin{bmatrix} \tan^{-1} \frac{{}^c u_c P_{width}}{f} \\ \tan^{-1} \frac{{}^c v_c P_{width}}{\sqrt{({}^c u_c P_{width})^2 + f^2}} \end{bmatrix} + \dots + \begin{bmatrix} \frac{1}{\sqrt{1 + \left(\frac{{}^c u_c P_{width}}{f}\right)^2}} \frac{\zeta_p}{f} \\ \frac{1}{\sqrt{1 + \left(\frac{{}^c v_c P_{width}}{\sqrt{({}^c u_c P_{width})^2 + f^2}}\right)^2}} \left( \frac{1}{\sqrt{\left(\frac{{}^c u_c P_{width}}{f}\right)^2 + 1}} - \frac{({}^c u_c P_{width})({}^c v_c P_{width})}{f^2 \sqrt{\left(\left(\frac{{}^c u_c P_{width}}{f}\right)^2 + 1\right)^3}} \right) \frac{\zeta_p}{f} \end{bmatrix} + O(\zeta_p^2) \quad (141)$$

From Eq.(141) one can see that the worst case error is achieved when the point is located at the centre of the screen. This means that in the worst case

$$\mathbf{z}_{camera} \leq \begin{bmatrix} \tan^{-1} \frac{{}^c u_c P_{width}}{f} \\ \tan^{-1} \frac{{}^c v_c P_{width}}{\sqrt{({}^c u_c P_{width})^2 + f^2}} \end{bmatrix} + \begin{bmatrix} \frac{\zeta_p}{f} \\ \frac{\zeta_p}{f} \end{bmatrix} \quad (142)$$

So the model for the observation equations used in the filter becomes:

$$\mathbf{z}_{camera} = h_{camera}(\delta\mathbf{r}, \mathbf{q}) + \boldsymbol{\varsigma}_{camera} = \begin{bmatrix} \tan^{-1} \frac{{}^c u_c \rho_{width}}{f} \\ \tan^{-1} \frac{{}^c v_c \rho_{width}}{\sqrt{({}^c u_c \rho_{width})^2 + f^2}} \end{bmatrix} + \begin{bmatrix} \frac{\varsigma_p}{f} \\ \frac{\varsigma_p}{f} \end{bmatrix} \quad (143)$$

Note that here the illumination conditions are not considered, so it is assumed that each spacecraft sees the whole visible surface from its position. This is sensible if one assumes that a complementary map could be built while starting the orbit acquisition, combining the pictures from the whole formation.

The ranging measurements are here reported for easing the reading of the document:

$$y_l = h_l(\delta\mathbf{r}_{sc}^h) + \varsigma_l = l + \varsigma_l \quad (144)$$

with  $\varsigma_l$  white measurement noise. The accuracy of this measurement depends on the characteristic error of the sensor, along with a bias defined by the mounting error of the instrument,  $\varsigma_l$  is the zero-mean Gauss white measurement noise.

Combining the LIDAR with the camera a relative position vector from the spacecraft to the surface point can be constructed as seen in Section 3.12.2:

$$\mathbf{z} = \begin{bmatrix} l \\ \varphi_c \\ \theta_c \end{bmatrix} = h(\delta\mathbf{r}_{sc}^h) + \boldsymbol{\varsigma} \quad (145)$$

where  $\mathbf{z}$  is the measurement vector obtained from the combination of camera and LIDAR,  $h(\mathbf{x})$  is the vector containing the model measurements,  $\boldsymbol{\zeta}$  is the Gauss white noise.

#### 4.2.2 Inter-spacecraft Measurements

The set of inter-spacecraft measurements is represented by the relative position vector between two spacecraft in the formation. Similarly to the model in Section 4.2.1 this is composed of the relative distance and the local azimuth and elevation (Oh et al., 2007). The measurements are given by the on-board camera and ranging instruments from one spacecraft to the other. For example, if the spacecraft 1 measures the relative position of spacecraft 2, the measurements are given as following

$$\begin{aligned} d_{rel} &= |\delta\mathbf{r}_{SC1} - \delta\mathbf{r}_{SC2}| \\ \varphi_{rel} &= \tan^{-1} \frac{y_{12}}{x_{12}} \\ \theta_{rel} &= \tan^{-1} \frac{f}{\sqrt{(x_{12})^2 + (y_{12})^2}} \end{aligned} \quad (146)$$

where  $d_{rel}$  is the relative distance between the two spacecrafts,  $\varphi_{rel}$  and  $\theta_{rel}$  are respectively the local azimuth and elevation angles measured from one spacecraft to the other,  $(x_{12}, y_{12})^T$  is the coordinates of spacecraft 2 on the screen of the camera on spacecraft 1. The observation equation is given as

$$\mathbf{z}_{rel} = h_{rel}(\delta\mathbf{r}_{SC1}^h, \delta\mathbf{r}_{SC2}^h) + \boldsymbol{\zeta}_{rel} = [d_{rel} \ \varphi_{rel} \ \theta_{rel}]^T + \boldsymbol{\zeta}_{rel} \quad (147)$$

where  $\boldsymbol{\varsigma}_{rel} = [\varsigma_d, \varsigma_{\theta_{rel}}, \varsigma_{\phi_{rel}}]^T$  is the zero-mean Gauss white measurement noise.

### 4.2.3 Ground Station Measurements

The set of measurements defined by range  $\rho$  and range rate  $\dot{\rho}$  with respect to the ground station is the typical set used to estimate spacecraft trajectory from Earth (Thornton et al., 2003), and is employed during deep space navigation. The observation equation were already given in Eq.(64), but the final set are here reported without the use of angles which is commonly excluded by the deep space orbit determination process (Thornton et al., 2003):

$$\mathbf{z}_g = h_g(\mathbf{r}_{SC}) + \boldsymbol{\varsigma}_g = [\rho \quad \dot{\rho}]^T + \boldsymbol{\varsigma}_g \quad (148)$$

with  $\boldsymbol{\varsigma}_g$  is assumed to be the zero-mean Gauss white measurement noise.

### 4.2.4 Sun Doppler Shift Sensor Model

The Doppler shift from sun-light can be measured by using a resonance-scattering spectrometer instrument which allows measuring the radial velocity of the spacecraft with respect to the Sun (Yim et al., 2000). This sensor is useful during the deep space navigation since the formation could be not visible from ground during some period. The measurement model of Doppler shift can be modelled by the following equation:

$$\dot{\rho}_{sc}^{Sun} = \frac{\mathbf{r}_{SC} \cdot \dot{\mathbf{r}}_{SC}}{r_{SC}} = \frac{\mathbf{r}_{SC} \cdot \mathbf{v}_{SC}}{r_{SC}} \quad (149)$$

The observation equation is given by

$$\mathbf{z}_{Sun} = h_{Sun}(\mathbf{r}_{SC}) + \mathbf{v}_{Sun} = \dot{\rho}_{sc}^{Sun} + \zeta_{Sun} \quad (150)$$

where  $\dot{\rho}_{sc}^{Sun} = \dot{\mathbf{r}}_{SC}^T \mathbf{r}_{SC} / r_{SC}$  is the relative radial velocity of spacecraft relative to the Sun.  $\zeta_{Sun}$  is the measurement noise which is assumed to be a white Gaussian noise process.

### 4.3 Navigation Strategy

A suitable filtering technique needs to be implemented in order to process the measurements defined in Section 4.2. Given the nonlinear dynamics of the problem in terms of both estimation and control, a natural choice is to use a nonlinear filtering technique. As seen in Section 3.12, the UKF is preferable to other nonlinear Kalman filter techniques, such as the particle filter and the high order expansions filters, because it can accurately handle with nonlinearities at low computational cost. Even though the Kalman filter has proved to work reasonably well when the Kalman filter hypotheses are not satisfied, another alternative filter, the  $H_\infty$  filter showed the best accuracy with a similar computational time. The  $H_\infty$  filter does not assume to precisely know the noise statistics, and it minimizes the worst-case estimation error. The choice of  $H_\infty$  filter is preferable when the Gaussian hypotheses are not fully satisfied as when biases in the instruments are not detected (Simons, 2006). Using the estimate theory formalism, the nonlinear discrete-time process in Eq.(134) and measurement equations in Section 4.2 are given by:

$$\begin{aligned} \mathbf{x}_{k+1} &= f(\mathbf{x}_k, \mathbf{u}_k, \mathbf{w}_k) \\ \mathbf{y}_k &= h(\mathbf{x}_k, \mathbf{v}_k) \end{aligned} \quad (151)$$

with  $w_k \sim N(0, \mathbf{Q}_k)$ ,  $v_k \sim N(0, \mathbf{R}_k)$ , which  $\mathbf{Q}_k$  is process noise covariance,  $\mathbf{R}_k$  is measurement noise covariance;  $\mathbf{u}_k$  represents the control input required to counteract the perturbations on the spacecraft (see Section 4.1.1). The control is based on the estimated state  $\tilde{\mathbf{x}}$ , represented by  $\delta\tilde{\mathbf{r}}$  and  $\delta\tilde{\mathbf{v}}$ , position and velocity of each spacecraft with respect to the asteroid. Thus the controller defined in Eq.(138) becomes:

$$\mathbf{u}_k(\tilde{\mathbf{x}}, t) = - \left( \mathbf{a}_{Sun}(\delta\tilde{\mathbf{r}}_k(t)) - \frac{\mu_A}{\delta r_{est}^3} \delta\tilde{\mathbf{r}}_k(t) \right) - \kappa (\delta\tilde{\mathbf{r}}_k(t) - \delta\mathbf{r}_{ref}) - c_d \delta\tilde{\mathbf{r}}_k(t) \quad (152)$$

We defined the control input as a function of time to stress that the control is a continuous function between  $t_k$  and  $t_{k+1}$  and it is based on the estimated current position and velocity of the spacecraft. The estimated motion  $\tilde{\mathbf{r}}_k(t)$  and  $\delta\tilde{\mathbf{r}}_k(t)$  between  $t_k$  and  $t_{k+1}$  in which the measurements are received and processed is simply given by the integration of Eq.(134) without the contribution of  $\mathbf{w}$ . The initial conditions are the estimated position and velocity from the filter at time  $t_k$ . We now show in Figure 39 an example of the combined filter and controller process for spacecraft 3 with different level of initial actual position error.

Being the closest spacecraft to the asteroid, spacecraft 3 experiences the highest level of perturbations from the gravity field of the asteroid. The controller gain  $\kappa$  is set again as  $10^{-6}/s^2$  while the steady dissipative coefficient  $c_d$  is as  $10^{-3}/s$ . The error for initial guess was equal to 10% in position and 1 mm/s on each components of the velocity. The whole process was simulated for 1 day. In this case the spacecraft could rely on relative and intersatellite measurements. The error on

range  $\zeta_l$  was 10 m, while the one on angles  $\zeta_{\theta,\varphi}$  was  $2.6 \cdot 10^{-3}$  degrees. The intersatellite error was  $\zeta_l = 2$  m, and  $\zeta_{\theta_{rel},\varphi_{rel}} = 10^{-3}$  degrees.

As one can see after an initial transient, the spacecraft is able to gain the nominal trajectory in less than 1 day even when the initial position error is 50% of the nominal trajectory, i.e. 300 m from the asteroid.

Eventually, for completeness, we want to show that the UHF has superior performance to the classical UKF, EKF and EHF. As an example, we considered the case of spacecraft 1 flying in the proximity for 2 day. We run 100 simulations to assess the statistical relevance of this comparison. Differently from the previous example, the spacecraft could rely only on relative measurements. In this case we use an error on range,  $\zeta_l$  of 50 m, biased of 10 m (1-sigma), and on angles  $\zeta_{\theta,\varphi}$  of  $2.6 \cdot 10^{-3}$  degrees, biased of  $10^{-3}$  degrees (1-sigma).

The error for initial guess was equal to 20% in position and 1 cm/s on each components of the velocity. The scaling parameter for UHF was  $\rho = 35$ . The initial spacecraft displacement was set to 10% of the nominal trajectory. Matrix  $\mathbf{R}_k$  was defined as a constant diagonal matrix with components equal to the ones of the previous case.

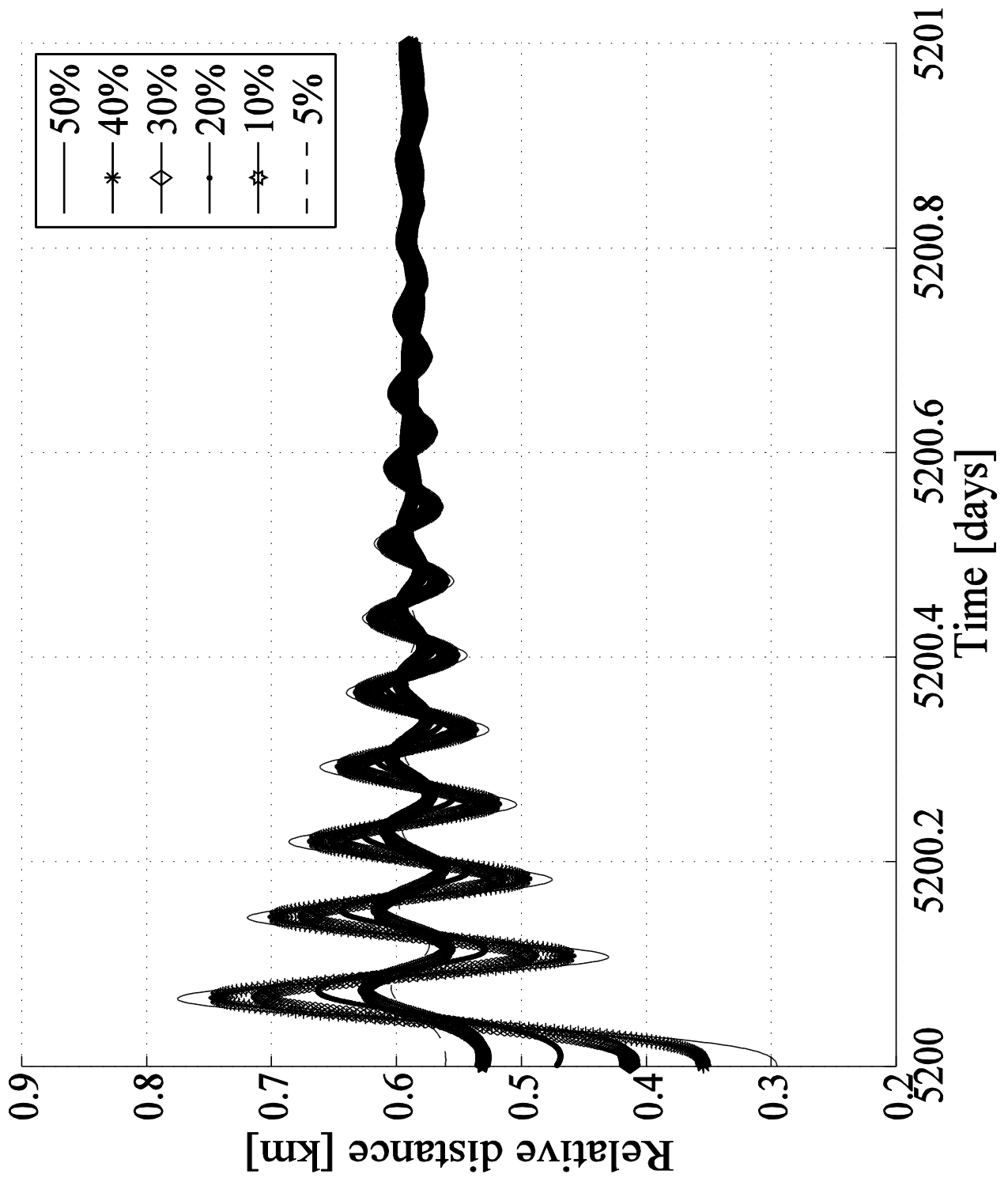


Figure 39. Relative distance for different level of initial position error for spacecraft 3.



Figure 40 shows the results of the orbit determination for the EKF and UKF while Figure 41 shows the ones for EHF and UHF. Both results are expressed in terms of root mean square error (RMSE) plus 1-sigma dispersion with respect to the mean value.

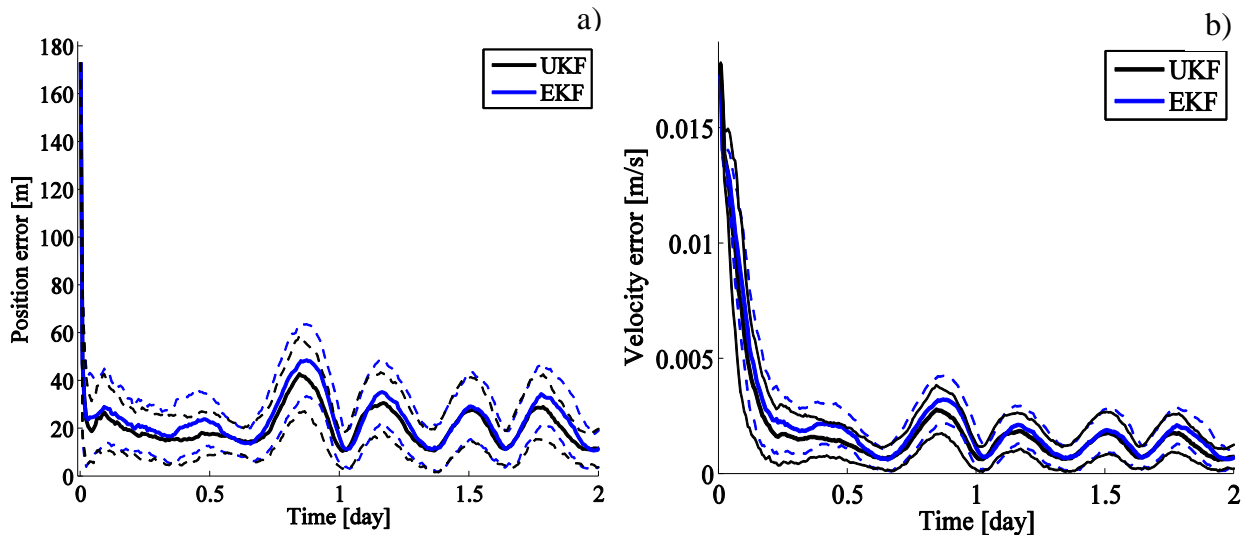


Figure 40. Estimated a) position and b) velocity (continuous line) and dispersion (1-sigma, dashed line) for UKF and EKF.

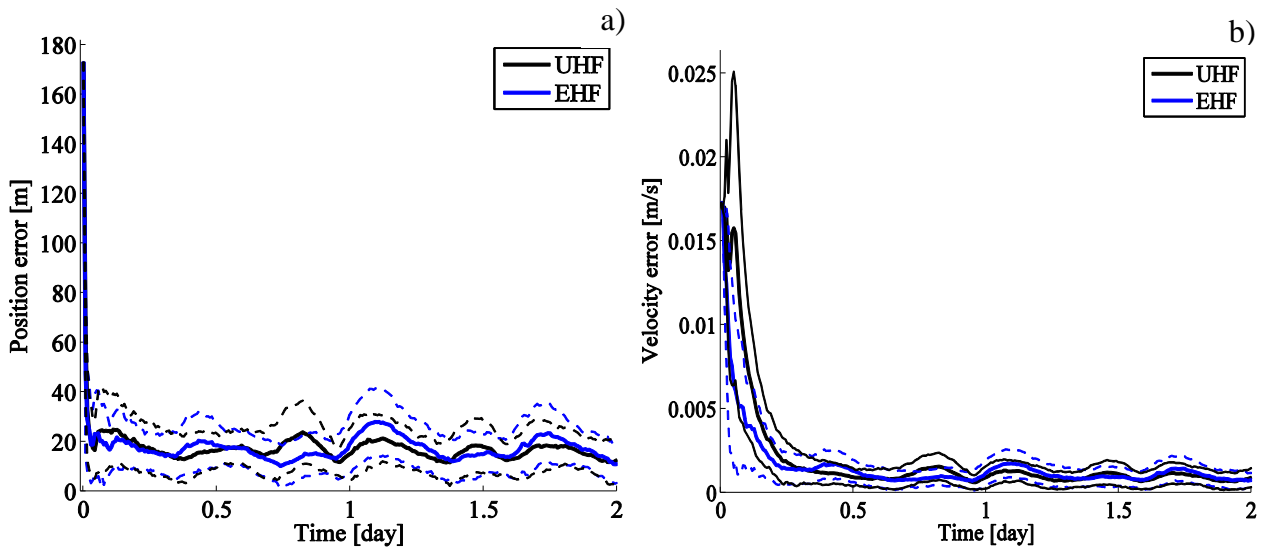
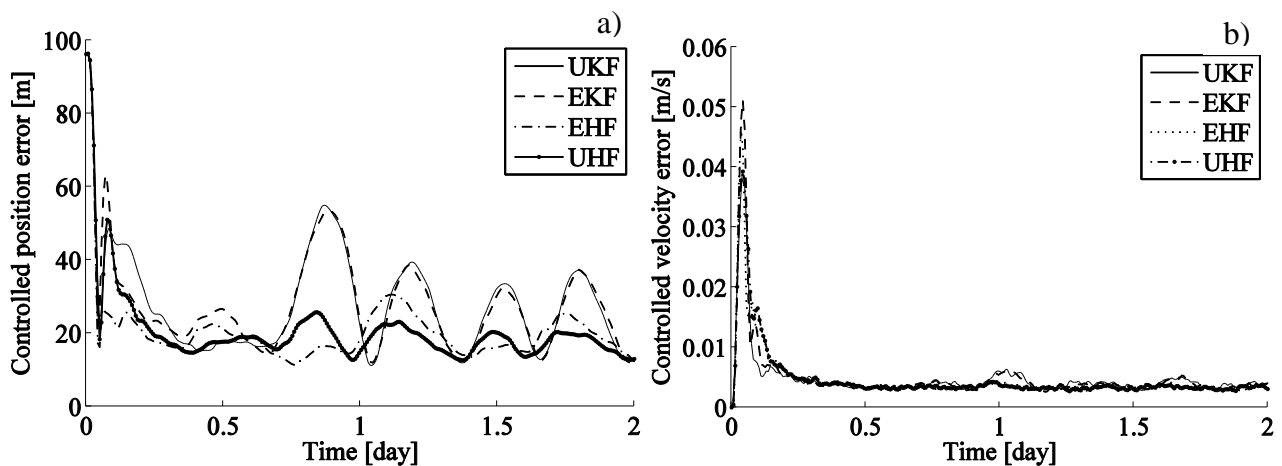


Figure 41. Estimated a) position and b) velocity RMSE (continuous line) and dispersion (1-sigma, dashed line) for UHF and EHF.

From the figures one can see that the estimated position and velocity errors differ significantly between the UKF and UHF and between the EKF and the EHF. The UHF appears better, although marginally, than the EHF, in particular in the controlled case. The reason can be found in the coupled interaction between state estimation and control process. In fact a small variation in the estimated state causes the controller to apply a higher or lower thrust level. This causes the nonlinear dynamics to produce quite diverse trajectories, see Figure 42. We based the selection of the filter technique on the average RMSE and on the maximum steady state expected error (1-sigma) after 1 day of operation, reported in Table 14.



**Figure 42. Controlled a) position and b) velocity average RMSE for UKF, EKF, UHF and EHF.**

A further confirmation comes from the Wilcoxon signed-rank test (Gibbons and Chakraborti, 2011) applied to the results of the different filters. When two sets of samples overlap completely the Wilcoxon signed-rank test reports 1, while 0 is obtained when the sets are completely independent. When we cross-checked the samples from the Kalman against the H-infinity filters, the results was below  $10^{-18}$ , while the cross-check between the UKF and EKF gave 0.643 and the one between

UHF and EHF was 0.538. This confirms that the realizations produce different results for the Kalman and H-infinity families on this particular problem. As one can see, the UHF presents superior performance compared to the other filters both in terms of estimated and controlled trajectory. The UHF is more accurate than the UKF with a RMSE that is 25% lower in position and about 30% in velocity. When one considers the maximum expected errors, the UHF also presents the best results.

**Table 14. Average RMSE comparison for different filters - SC1**

	Filter technique			
	UKF	EKF	UHF	EHF
RMSE position [m]	24.03	24.30	17.78	18.18
RMSE velocity [mm/s]	2.27	2.41	1.59	1.88
RMSE controlled position [m]	27.27	27.89	20.39	20.50
RMSE controlled velocity [mm/s]	4.67	4.90	4.63	4.67

One advantage of the UHF over the EHF is that it does not require the derivation and propagation of the Jacobian matrix, similarly to the UKF with the EKF (Crassidis and Junkins, 2004). Although the computational cost is 20% greater than for the EHF, nonetheless we considered the UHF as baseline filter because of its higher accuracy in the estimation of the fully controlled trajectory.

#### 4.4 Data Fusion Process

Having defined the filtering and control processes, each spacecraft needs to manage the on-board system and share information efficiently. This section describes the data fusion process implemented to address this issue.

Each spacecraft receives the whole set of measurements coming from all the members and builds the necessary matrices. It is assumed that the measurements are received at the same time. Otherwise, the measurements may be unavailable at a certain stage of the simulation. This would affect the forecasting and the updating stages, since it would introduce inconsistency between the forecast measurements and the measurements that the system actually receives. The data fusion management can be described as a small number of process steps:

At initial time  $t_0$ , an initial state vector and covariance matrix are assembled from the initial guess  $\tilde{\mathbf{x}}_0^i$  and covariance  $\mathbf{P}_0^i$  of each spacecraft ( $i = 1:N_{sc}$ ):

$$\begin{aligned} \mathbf{x}_0 &= [\tilde{\mathbf{x}}_0^1 \quad \cdots \quad \tilde{\mathbf{x}}_0^{N_{sc}}] \\ \mathbf{P}_0 &= \begin{bmatrix} \mathbf{P}_0^1 & & \emptyset \\ & \ddots & \\ \emptyset & & \mathbf{P}_0^{N_{sc}} \end{bmatrix} \end{aligned} \quad (153)$$

1. At each time  $t_k$  ( $k=1,2,\dots$ ) a set of measurements is received, a total array of measurements is assembled along with error covariance matrix using the available measurements  $\mathbf{z}_k^i$  and instruments covariance error  $\mathbf{R}_0^i$ :

$$\mathbf{z}_k = [\mathbf{z}_k^1 \quad \cdots \quad \mathbf{z}_k^{N_{sc}}]$$

$$\mathbf{R}_k = \begin{bmatrix} \mathbf{R}_k^1 & & \emptyset \\ & \ddots & \\ \emptyset & & \mathbf{R}_k^{N_{sc}} \end{bmatrix} \quad (154)$$

2. Based on the type of measurement the unperturbed set of equations  $\mathbf{h}_k(\mathbf{x}, t_k)$  is defined on the basis of the model introduced in Section 4.2.
3. The UHF is then employed between the two instants  $(t_k, t_{k+1})$ , obtaining the filter gain and the predicted state vector and measurements at time  $t_{k+1}$ .
4. At time  $t_{k+1}$  predicted and actual measurements are available. If the number of measurements is lower than the predicted number, only the consistent measurements between the two steps are considered in the update step. This is obtained either by removing the predicted measurements and the correspondent columns and rows in the filter gain or by giving a null value to the correspondent elements in the filter gain. If the number of actual measurements at time  $k+1$  is higher than the one at the previous instant, then  $\mathbf{R}_k$  and  $\mathbf{h}_k(\mathbf{x}, t_k)$  are consistently redefined and steps from 2 to 4 are repeated.

## 4.5 Results

Simulations focus on the condition that the spacecraft formation is flying in the proximity of Apophis. The final part of Section 4.1.1 showed that the spacecraft would fall on the asteroid in less than one day without control. The implemented controller of Section 4.1.3 requires a reliable and fast estimation in order to maintain the formation. The camera resolution is set as 2048x2048 pixels, the field of view is set as 30 degrees and the focal length is  $1.212 \times 10^{-3}$  m. Table 15 summarizes

conservative measurements errors used in the simulations. The LIDAR range error is set as 10 m according to Kubota et al. (2003), and a precision of 2 m is used for inter-spacecraft LIDAR range measurement error. Angular measurement and attitude error are from Yim et al. (2000).

**Table 15. Sensors error for close proximity navigation.**

Parameter variation (1-sigma)			
	Precision	Worst Case Precision	Bias
C-angles $\zeta_{\theta,\varphi}$ [deg]	$2.6 \cdot 10^{-3}$	/	$5 \cdot 10^{-4}$
LIDAR $\zeta_l$ [m]	10	50	1
I-distance $\zeta_d$ [m]	2	10	1
Local Angles $\zeta_{\theta_{rel},\varphi_{rel}}$ [deg]	$10^{-3}$	/	$5 \cdot 10^{-4}$
Attitude [deg]	$10^{-3}$	/	$5 \cdot 10^{-4}$

(C: camera, I: intersatellite)

For the asteroid refinement part, the measurements from Earth are taken from the ground station of Malindi (-2.9956° latitude and 40.1945° longitude). Typical errors considered in this Chapter are given in Table 16.

**Table 16. Measurements error for asteroid refinement (1-sigma).**

Characteristics	Unit	Value
Camera pointing angles	rad	$10^{-3}$
G-Range	m	20
G-Range rate	mm/s	0.5
Doppler shift	mm/s	0.1

(G: Ground station)

Range and range rate noise are from Thornton et al. (2003) while a Doppler shift sensor's accuracy is equal to the one used in Yim et al. (2000).

#### 4.5.1 Non-collaborative vs. Collaborative case

First we show that the collaboration among the members of the formation improves the accuracy of the estimates. The simulation spans 2 days with a time interval between measurements of 10 minutes. We repeated the test 100 times to assess the statistical relevance of the results. An initial uncertainty of max 20% in the position vector components and  $10^{-5}$  km/s on the velocity vector components, with respect to the reference trajectory, was considered for all the simulations.  $\mathbf{P}_0$  is a diagonal matrix with elements equal to the square of the initial state uncertainty for each spacecraft. The process noise covariance matrix  $\mathbf{Q}$  was set to  $10^{-24} \times \mathbf{I}_{6 \times 6}$  for the non-collaborative case and  $10^{-24} \times \mathbf{I}_{24 \times 24}$  for the collaborative one. The observation error covariance matrix  $\mathbf{R}$  is a square and diagonal matrix with the square of observation noise on its diagonal terms. In these two cases we considered that the sensors were working at nominal conditions as reported in Table 15. The process noise  $\mathbf{w}$  and the measurement noise  $\boldsymbol{\zeta}$  were assumed to be uncorrelated with each other and with their previous values over time.

Figure 43 and Figure 44 report the results for the non-collaborative and collaborative case respectively. Figure 43a), b) and Figure 44a), b) refers to the RMSE for the estimated position and velocity while Figure 43c), d) and Figure 44c), d) shows the RMSE for the controlled trajectory. In the non-collaborative case the error is higher than in the collaborative case.

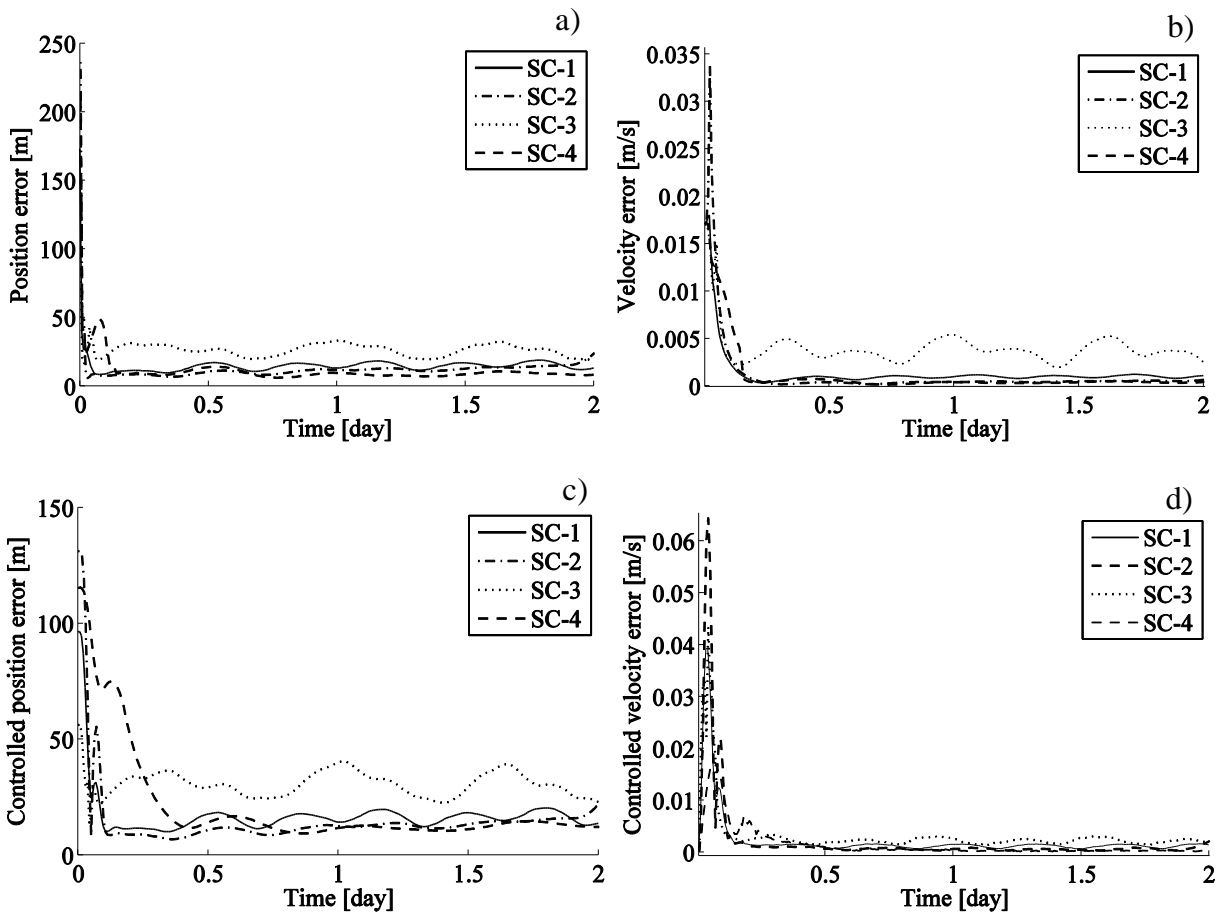


**Figure 43. Non-Collaborative case: RMSE for estimated a) position, b) velocity, c) controlled position and d) controlled velocity.**

In general the initial peaks in the controlled velocity are higher for SC-2 and SC-4 because the control exerts a thrust proportional to the position error. Given the initial conditions for the estimated and the actual trajectory, the control increases the velocity to cope with the actual trajectory deflection. SC-3 experiences the worst convergence in terms of accuracy in the estimated and controlled trajectory. When the intersatellite measurements are included, the convergence is improved both in terms of accuracy and time for all the spacecraft. In fact from Figure 44a), d) one can see how the error moves towards lower RMSE regions in about 0.1 day with respect to 0.5 day of Figure 43c), d).



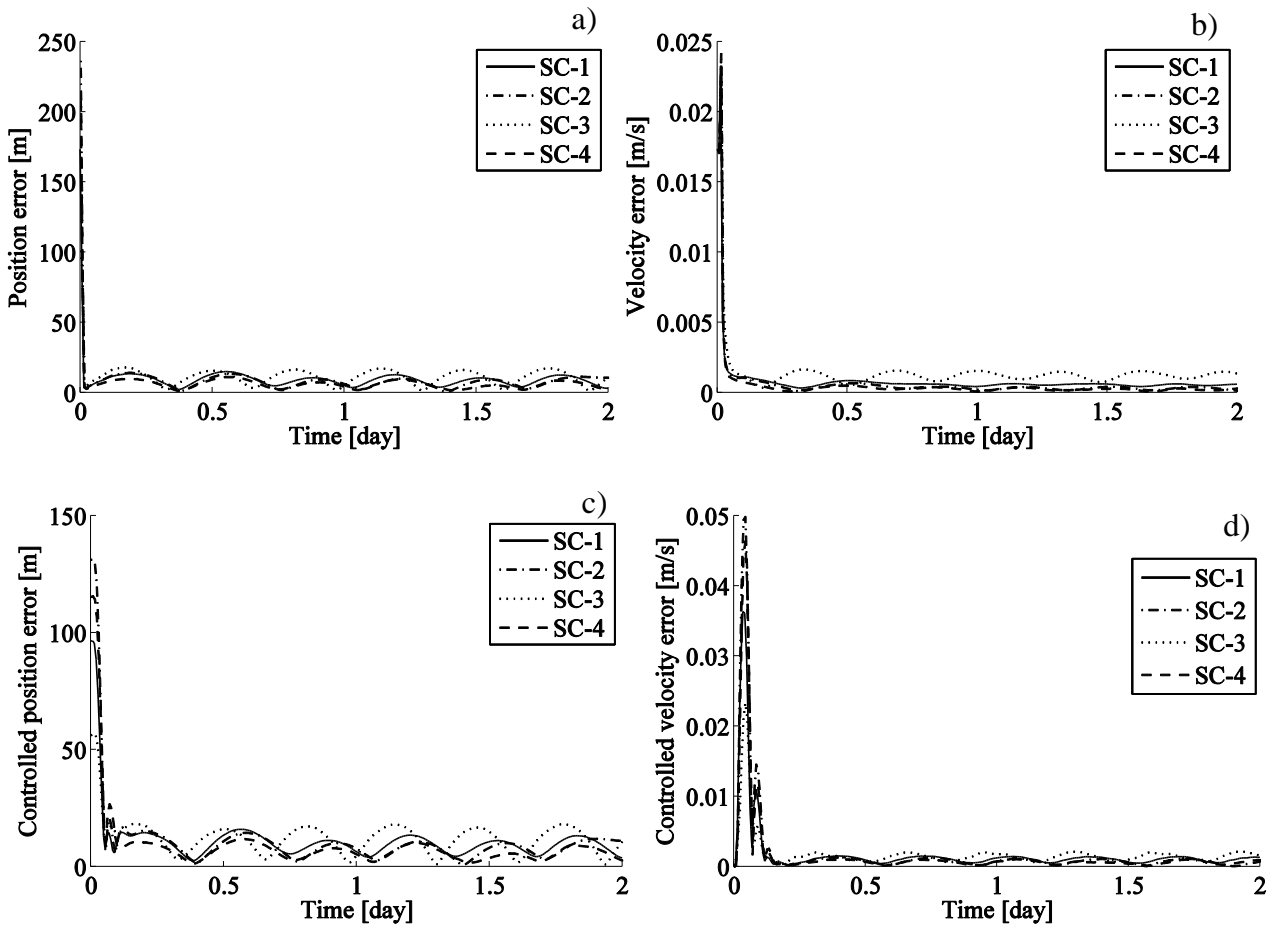


**Figure 44. Collaborative case: RMSE for estimated a) position, b) velocity, c) controlled position and d) controlled velocity.**

The magnitude of the oscillations is reduced, and the initial peaks in the estimated and controlled velocity results are lower than the non-collaborative case (see Figure 43b), d) and Figure 44b), d)). For the non-collaborative case the maximum error in the estimated velocity is about 3.5 cm/s (see Figure 44b) while this value reduces to circa 2.5 cm/s with collaboration (Figure 44b)). Similarly the collaboration reduces the maximum error in the controlled velocity to about 5 cm/s (Figure 44d)), compared to the 6.5 cm/s as in the non-collaborative case (Figure 43d).

Table 16 reports the average RMSE of each spacecraft. As one can see, the worst performance is achieved by SC-3, which experiences the higher level of perturbations, being the closest to the asteroid. When additional information from the intersatellite measurements is added, the improvement is quite considerable especially for SC-3, with the maximum RMSE in the controlled position equal to less than 50% than the non-collaborative case. For the non-collaborative case the maximum error in the estimated position is 37.70 m, while the collaboration reduces this value to 17.61 m. Similarly the maximum error in the controlled position is reduced to about 18.56 m from 45.57 m.

**Table 17. Average RMSE in estimated and controlled trajectory for the collaborative and un-collaborative case**

		No-collaboration	Collaboration
SC1	position/max 1- $\sigma$ [m]	14.77/20.72	9.35/12.62
	velocity/max 1- $\sigma$ [mm/s]	1.4/1.31	0.8/0.62
	controlled position/max 1- $\sigma$ [m]	16.94/22.32	11.05/13.46
	controlled velocity/max 1- $\sigma$ [mm/s]	2.1/1.94	1.7/1.45
SC2	position/max 1- $\sigma$ [m]	12.65/24.93	9.05/11.76
	velocity/max 1- $\sigma$ [mm/s]	1.2/0.70	0.6/0.45
	controlled position/max 1- $\sigma$ [m]	14.99/22.67	11.06/12.29
	controlled velocity/max 1- $\sigma$ [mm/s]	2.2/2.52	1.9/1.29
SC3	position/max 1- $\sigma$ [m]	26.73/37.70	11.60/17.61
	velocity/max 1- $\sigma$ [mm/s]	4.1/6.1	1.4/1.59
	controlled position/max 1- $\sigma$ [m]	30.81/45.57	12.45/18.56
	controlled velocity/max 1- $\sigma$ [mm/s]	3.2/4.3	1.8/2.31
SC4	position/max 1- $\sigma$ [m]	11.56/13.58	7.04/9.88
	velocity/max 1- $\sigma$ [mm/s]	1.2/0.67	0.5/0.40
	controlled position/max 1- $\sigma$ [m]	20.93/18.20	8.85/10.43
	controlled velocity/max 1- $\sigma$ [mm/s]	1.5/1.7	1.6/1.13

## 4.5.2 Failures

In order to assess the increased flexibility and robustness provided by intersatellite link, the following contingency scenarios were analysed:

1. LIDAR and camera fail on SC-1;
2. LIDAR and camera fail on SC-1 and SC-2;
3. LIDAR and camera fail on SC-1 and poor LIDAR on SC-4;
4. LIDAR and camera fail on SC-1 and SC-2 and poor LIDAR on SC-3 and SC-4;
5. LIDAR and camera fail on SC-1 and SC-2 with poor inter-satellite links on SC-1 and SC-2 and poor LIDAR on SC-3 and SC-4.

Table 18 reports the different test cases used to assess the improvement of the estimates even in case of absence of measurement or of failure by means of the decentralized navigation system.

**Table 18. Sensors set on spacecraft formation**

Case	SC-1	SC-2	SC-3	SC-4
1	I	C, L/R, I	C, L/R, I	C, L/R, I
2	I	I	C, L/R, I	C, L/R, I
3	I	C, L/R, I	C, L/R, I	C, L/R*, I
4	I	I	C, L/R*, I	C, L/R*, I
5	I*	I*	C, L/R*, I	C, L/R*, I

C-camera, L/R-LIDAR, I-inter-satellite, \*worst case condition

The initial conditions are the same for the collaborative case and the covariance matrix  $\mathbf{P}_0$ , similarly the process noise covariance  $\mathbf{Q}$  and  $\mathbf{R}$  are built as before. Figure 45 and Figure 46 report only the trend for SC-3 and SC-4 as they present the worst and best cases in terms of RMSE for all the cases. The results for SC-1 and SC-2 are pretty similar and are not reported for simplicity. The trend for

cases 1 to 4 is very similar to the collaborative case, demonstrating that the intersatellite link compensates for poor or incomplete direct measurements. In case 5, instead, spacecraft SC-3 experiences higher levels of error with oscillations due to the filter and control coupling and perturbations, see Figure 45a) and b). The controller is not able to converge as well as in the other case, shown in Figure 45c) and d).

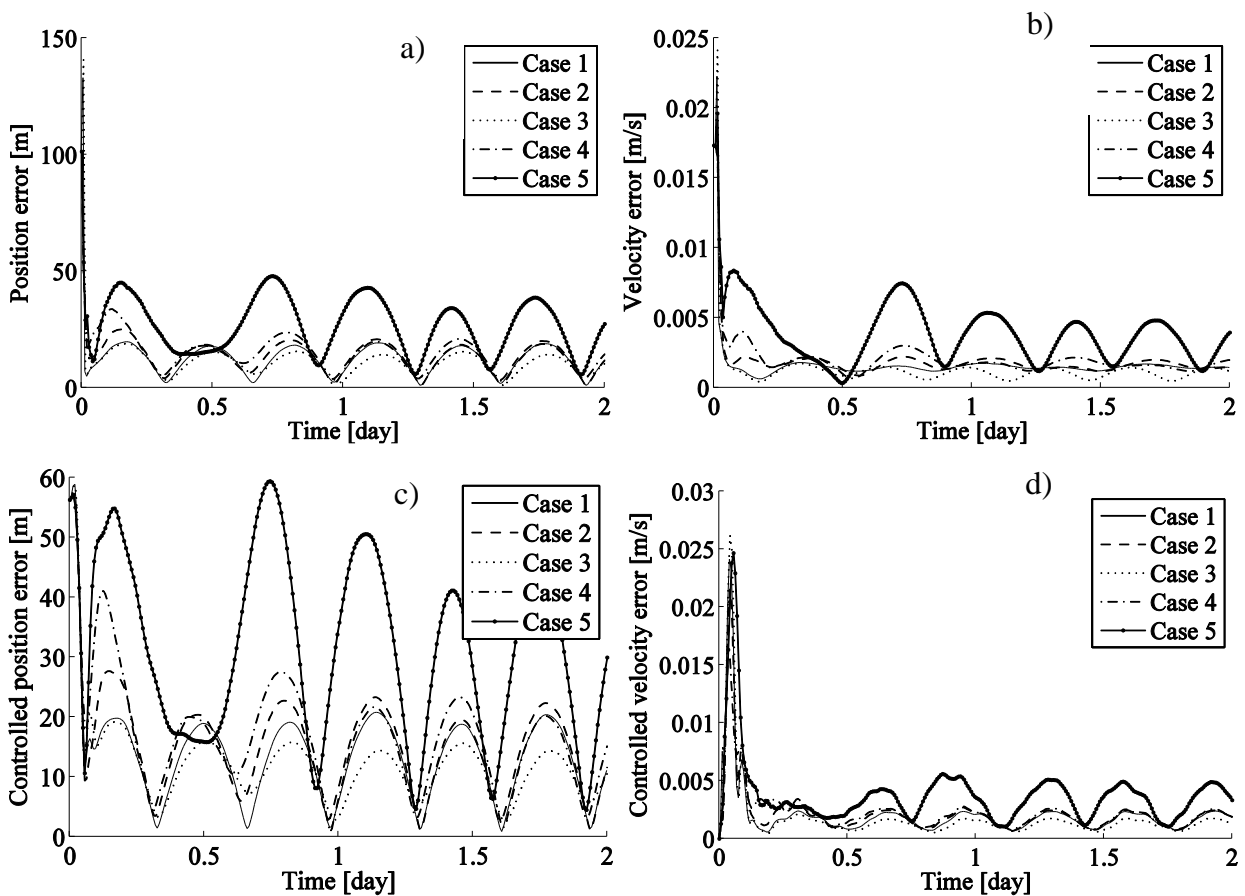


**Figure 45. SC-3 failures: RMSE for estimated a) position, b) velocity, c) controlled position and d) controlled velocity.**

Figure 46a) and b) show that for SC-4, the oscillatory behaviour due to the coupling between filter and controller is less pronounced in cases 1 to 4. While in case 5, SC-4 has behaviour comparable to the one of SC-3, with the maximum controlled position and velocity error respectively in the range 30-50 m and 3-6 mm/s (after the initial transient response), see c) and d).

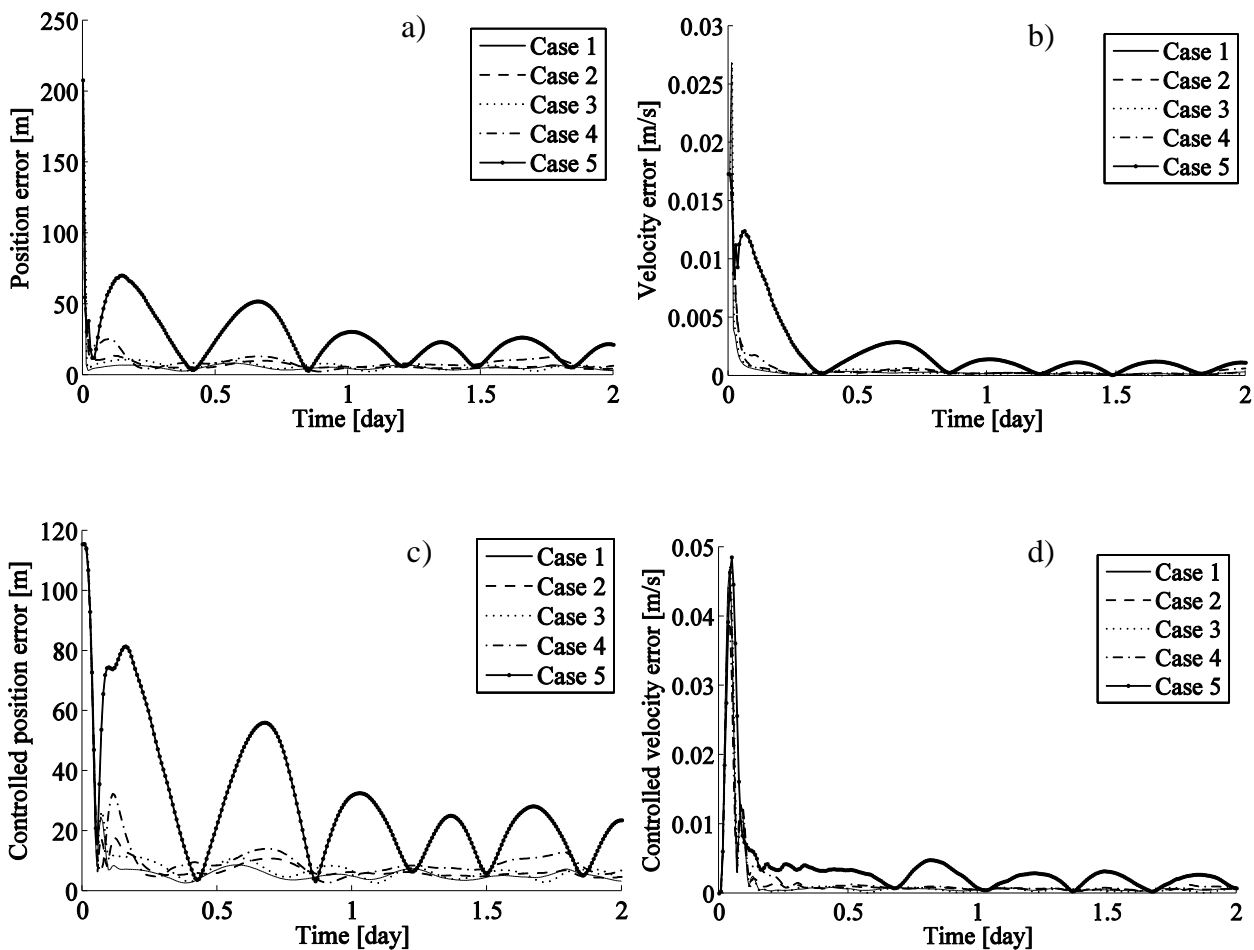


**Figure 46. SC-4 failures: RMSE for estimated a) position, b) velocity, c) controlled position and d) controlled velocity.**

The average RMSE of estimated and controlled trajectory of each spacecraft are summarized in Table 19. The results show that the overall performance of the formation is, in general, better than

for the non-collaborative case. One thing should be noted: in Cases 1 to 3, some of the spacecraft experience an improvement with respect to the collaborative case with all the instruments working.

**Table 19. Average RMSE of the estimated and controlled trajectory in case of failures.**

SC		Case 1	Case 2	Case 3	Case 4	Case 5
1	position/max 1- $\sigma$ [m]	7.79/9.67	9.22/11.95	9.50/12.84	10.75/11.79	17.96/19.02
	velocity/max 1- $\sigma$ [mm/s]	0.65/0.54	0.70/0.68	0.72/0.82	0.78/0.65	1.51/1.05
	controlled position/max 1- $\sigma$ [m]	9.13/10.33	10.51/12.86	10.79/14.01	12.10/12.41	19.99/20.63
	controlled velocity/max 1- $\sigma$ [mm/s]	1.51/1.11	1.65/1.13	1.79/1.30	1.86/1.15	2.65/2.14
2	position/max 1- $\sigma$ [m]	7.97/9.24	8.75/9.50	9.13/11.26	10.58/10.13	20.62/20.63
	velocity/max 1- $\sigma$ [mm/s]	0.56/0.35	0.60/0.38	0.62/0.48	0.65/0.36	1.48/2.14
	controlled position/max 1- $\sigma$ [m]	9.67/9.68	10.50/10.03	10.89/11.94	12.27/10.41	23.35/24.14
	controlled velocity/max 1- $\sigma$ [mm/s]	1.72/1.07	1.87/0.99	1.79/1.19	2.00/0.99	3.11/2.99
3	position/max 1- $\sigma$ [m]	12.57/19.39	14.11/21.37	11.40/15.66	15.49/21.51	26.89/43.97
	velocity/max 1- $\sigma$ [mm/s]	1.61/1.77	1.87/2.20	1.32/1.48	2.08/2.26	3.9/5.52
	controlled position/max 1- $\sigma$ [m]	13.63/21.19	15.60/23.93	12.20/15.79	17.13/23.95	31.78/51.93
	controlled velocity/max 1- $\sigma$ [mm/s]	1.99/2.53	2.17/2.71	1.75/1.81	2.28/2.82	3.79/5.56
4	position/max 1- $\sigma$ [m]	6.16/7.12	7.54/6.97	7.64/7.52	10.10/13.54	26.39/31.60
	velocity/max 1- $\sigma$ [mm/s]	0.47/0.31	0.56/0.35	0.53/0.36	0.65/0.66	2.09/1.48
	controlled position/max 1- $\sigma$ [m]	7.75/7.39	9.11/7.21	9.23/8.04	11.43/13.59	30.04/33.72
	controlled velocity/max 1- $\sigma$ [mm/s]	1.49/0.79	1.66/0.82	1.55/0.96	1.77/1.34	3.59/3.49

The explanation of this behaviour resides in the fact that the biases on the camera pointing towards the asteroid introduce a considerable error in the filtering process and the centroid identification is

not as precise as the intersatellite measurements. The result is that having less measurements relative to the asteroid has beneficial effects on the mean error. Cases 4-5 prove that the system is able to determine and maintain the trajectory without losing the proximity with the asteroid but the lack of inter-satellite links has a significant impact on the navigation and control capabilities of the formation. Even though the number of failures would not allow Spacecraft 1-2 alone to estimate their trajectories, the collaboration increases the reliability of the system and the robustness against sensors failures.

#### **4.6 Asteroid Ephemerides Refinement**

During the approach phase, the on-board measurements can be employed in combination with the absolute measurements from the ground station to refine the trajectory of the asteroid. Two different sets of measurements were considered for this analysis: the first set combines ground tracking with line of sight measurements taken from the spacecraft, while the second includes also a Sun Doppler shift sensor among the on-board measurements.

In the following, it is assumed that two spacecraft will approach the asteroid at the same time when the asteroid is at perihelion. In such a situation, if the spacecraft formation travels from the Sun direction, given its visual magnitude of 19.7, the asteroid could be detected from a distance of about 2,000,000 km (Vetrisano et al., 2013). We conservatively assumed that both spacecraft will concurrently start the acquisition of the target at 1,000,000 km from the asteroid.

The configuration of the approach and acquisition phase is depicted in Figure 47. The initial conditions are given with respect to the asteroid's Hill reference frame in terms of distance  $d_{ap}$ ,

azimuth  $\tau$  and elevation  $\lambda$ . Both spacecraft are placed at 1,000,000 km with an approach velocity  $v_{ap}$  of 100 m/s in magnitude directed along the spacecraft-to-asteroid vector. In the Hill reference frame the position and velocity vectors for the  $i$ -th spacecraft can be written as:

$$\begin{aligned}\delta\mathbf{r}_{sc-i}^h &= \mathbf{r}_A^h + d_{ap} [\cos \tau_i \cos \lambda_i \quad \cos \tau_i \sin \lambda_i \quad \sin \lambda_i] \\ \delta\dot{\mathbf{r}}_{sc-i}^h &= \mathbf{v}_A^h - v_{ap} [\cos \tau_i \cos \lambda_i \quad \cos \tau_i \sin \lambda_i \quad \sin \lambda_i]\end{aligned}\quad (155)$$

where the superscript  $h$  refers to the Hill reference frame.

From Figure 47 one can see that if the two spacecraft are separated by a small angle, the asteroid trajectory becomes poorly observable as it is not possible to accurately triangulate the position of the asteroid.

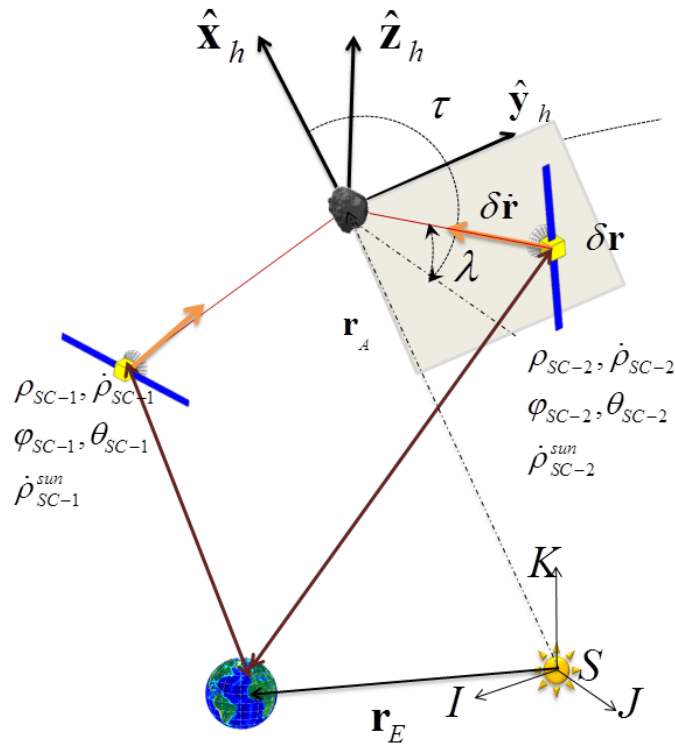


**Figure 47. Approach and acquisition phase configuration.**



Direct distance measurement from the asteroid to the spacecraft cannot be acquired using the LIDAR, neither can the distance be derived from a single camera unless complicated dogleg manoeuvres are adopted, because the shape of the asteroid might not be known in advance or the camera might not have a sufficiently high resolution. Therefore, the angular separation of the two spacecraft, seen from the asteroid, needs to be sufficiently high. As an example, Figure 48 reports the estimated error with respect to the actual trajectory of the asteroid when only a single spacecraft is used. The measurements are acquired over two weeks. The initial estimated position of the asteroid is randomly taken on a sphere with radius 10,000 km centred on the actual position, while for the estimated velocity a sphere of 2.5 m/s radius with respect to the actual velocity is considered. The 1-sigma dispersion in position is 50,000 km and 90 m/s in velocity. These error values are higher than the one used in Vetrivano et al. (2013) for a single spacecraft performing a dogleg approach to an asteroid whose trajectory is not precisely known.

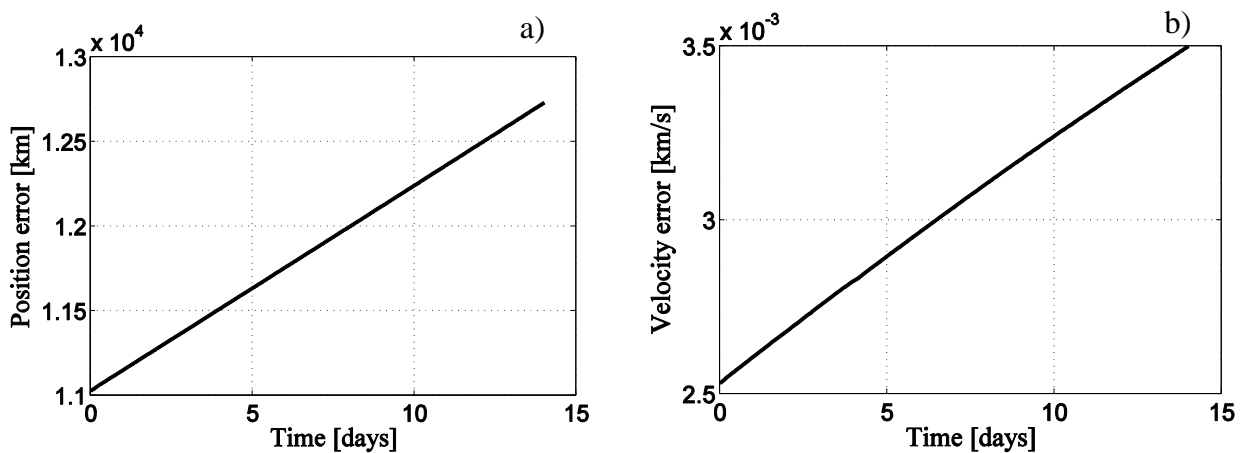


**Figure 48. Asteroid estimate a) position and b) velocity error in 14 days using only on-board optical observation from a single spacecraft with ground station tracking.**

It is clear that in this case the problem is not observable since the type of information is not sufficient to improve the estimate without a dogleg approach. In fact the error increases with time.

Consider two spacecraft where their positions are known with an initial accuracy of 1000 km and velocity with an accuracy of 0.1 m/s in magnitude. The sensors on-board the spacecraft and the ground station tracking system provide the navigation algorithm with 5 measurements for each spacecraft: line-of-sight angles and Doppler shift, range and range rate from Earth. In total there are up to 10 measurements acquired every 1 hour.

Table 20 reports the results for different configurations of  $\tau$  and  $\lambda$ , each one simulated 100 times. It is assumed that the measurement acquisition and state estimation processes run for 7 days.

**Table 20. Analysed configurations and final estimated error without and with Doppler shift.**

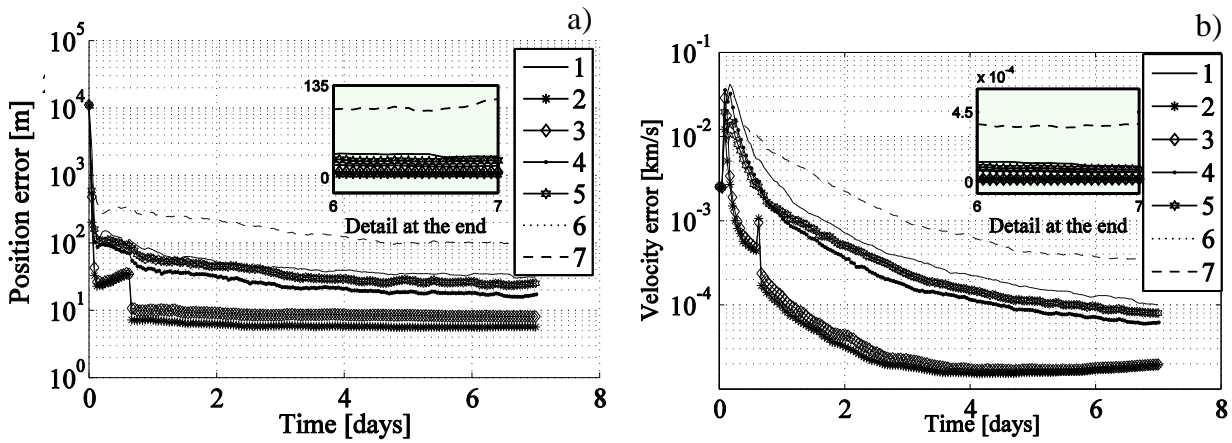
		Configuration						
		1	2	3	4	5	6	7
SC-1	$\tau$ [deg]	90	180	135	135	135	135	135
	$\lambda$ [deg]	0	0	0	0	0	0	0
SC-2	$\tau$ [deg]	270	270	270	139	136	135.5	135.5
	$\lambda$ [deg]	3	3	3	3	3	3	0.5
No Doppler	Position error [km]	31.38	5.657	8.04	17.50	25.14	26.25	115.25
	Velocity error [cm/s]	10.09	1.936	1.961	6.263	8.010	8.269	37.49
Doppler	Position error [km]	26.89	5.791	8.09	17.09	25.67	26.48	101.97
	Velocity error [cm/s]	9.087	1.905	1.915	6.288	8.227	8.405	35.81

The first spacecraft was placed on the nominal orbit plane of the asteroid while the second spacecraft was given a maximum out of plane component equal to the asteroid's initial dispersion in position that corresponds to a value of 3 degrees for  $\lambda$ . As expected, without the use of the Doppler measurement, when the two spacecraft are almost aligned along the same spacecraft-to-asteroid vector (see configurations 1-4-5-6-7), the estimated error, both in position and in velocity, is higher than when they are not (see cases 2 and 3).

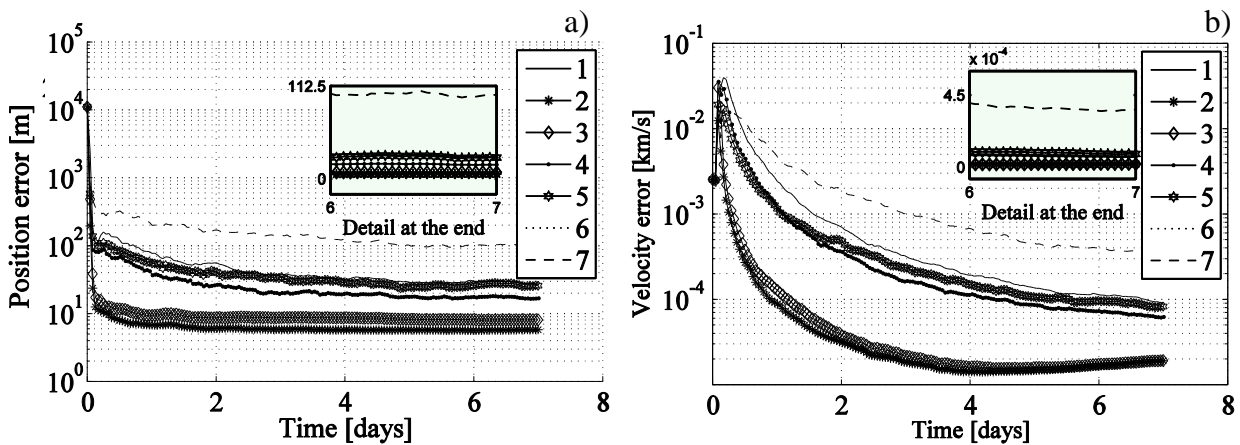
When the Doppler measurement is added, there is a general improvement of these estimates, especially for cases 1 and 7. However, for other configurations, the use of the Sun Doppler shift measurements does not lead to a noticeable improvement in the results.

Figure 49 and Figure 50 show the trend for the estimated position and velocity. As one can see from Figure 49a) and Figure 50a), the position error converges towards low values in less than one day as the first set of measurements is received.

Conversely from Figure 49b) and Figure 50b), the estimated velocity error needs between two and four days to converge. The peaks in the velocity error are due to the unavailability of ground station measurements when only on-board sensors are employed. When the Doppler shift is not considered the magnitude of these peaks is higher, with a maximum value of 42.3 m/s in case 1. When the Doppler shift is used, the maximum value slightly reduces to 39.6 m/s.



**Figure 49.** Asteroid estimate a) position and b) velocity error in 7 days combined on-board optical observation measurements with ground station tracking.



**Figure 50.** Asteroid estimate a) position and b) velocity error in 7 days combined on-board optical observation measurements with ground station observation and sun Doppler.

When the two spacecraft are very close as in configuration 7, the problem is not well conditioned because the measurements from the formation are almost coincident, and, thus, more affected by the measurement error. This can be seen in Figure 50a), where there are small peaks in position till day 4. With Doppler shift measurement, the peaks in position error disappear after 2 days, while the velocity error presents a slightly fastest convergence rate, as shown in Figure 50b).

It can be concluded that the combined use of on-board and ground station measurements improves the position estimate by approximately 3 orders of magnitude in 1 week. The use of Doppler instrument has beneficial effects since it helps the filter converge faster towards lower error regions when ground station tracking is not available. Nonetheless, the improvement is not equally significant for all the approach configurations.

#### **4.7 Summary**

This Chapter presents different navigation strategies for a 4-spacecraft formation in the proximity of the asteroid Apophis. Simulations base on UHF are implemented in order to data fuse the measurements from each spacecraft to estimate their relative states with respect to the asteroid. Different test cases are addressed to evaluate the improvement of navigation performance by adding the inter-spacecraft position measurements and the robustness against failures.

We showed that a disaggregated spacecraft formation where relative measurements are being shared and fused into the UHF is fault tolerant to multiple sources of instruments failures. The following conclusions can be drawn. The UHF-based navigation algorithm is used to estimate the relative state of each spacecraft with respect to the asteroid simultaneously. The navigation system achieves better localization performance by incorporating the inter-spacecraft range and angular measurements. The collaboration within the members of the formation increases the spacecraft navigation accuracy and improves the navigation and control performance on the aspects of stability and convergence property. The findings is not limited only to the explored scenario but can be also extended to any spacecraft formation where inter-satellite links are available.

In the considered scenario, the estimated error is decreased by more than 50% in position and 60% in velocity when the inter-spacecraft measurements are included. The results indicate that the inter-spacecraft measurements aiding navigation can better solve the problem of the orbit determination of spacecraft formation in the proximity of the asteroid. The disaggregate processing of the available measurements allows for higher flexibility as well for higher precision with respect to the single spacecraft data processing. This approach has proved to be robust against instruments failures and poor performance..

Furthermore, we have analysed the absolute orbit determination of the asteroid using on-board measurement combined with the ranging information from the ground station. We have shown that the combined use of on-board and ground station measurements can improve the asteroid's orbit estimate during the approach phases. There is a significant improvement in the estimated position accuracy, about 3 orders of the magnitude while the velocity is as precise as 1 cm/s. A better knowledge of the asteroid's orbit can be used for correction manoeuvres planning, thus approaching the asteroid could be accomplished with less propellant consumption. The method can be applied to the approach phases or during deep space missions to improve known and newly discovered asteroid's orbits.

## 5 Deflecting Small Asteroids

This Chapter investigates the use of the developed techniques for controlling the rotational motion of a small asteroid for a scientific demonstrator, while the spacecraft deflects the asteroid's trajectory through laser ablation. During the deflection, the proximity motion of the spacecraft is coupled with the orbital and rotational motion of the asteroid. In fact, a change in the angular velocity of the asteroid induces a variation of the sublimation rate that, in turns, affects both the orbital and rotational motion of the asteroid. At the same time a change in the sublimation rate, orbital and rotational motion affects the proximity motion of the spacecraft as it changes the perturbations due to the impingement with the plume of gas, the gravity of the asteroid and the relative acceleration between asteroid and spacecraft. Since the spot size of the laser beam needs to be kept below an acceptable limit to guarantee constant sublimation, the spacecraft needs to manoeuvre to maintain its relative distance under the effect of perturbations that are a function of the sublimation process. As shown in the works of Kahle et al. (2005) and Colombo et al. (2006) the lower is the angular velocity of the asteroid the higher is the imparted deflection acceleration. For this reason the simultaneous control of both the spacecraft relative position and asteroid's angular velocity is paramount.

The asteroid is modelled as a tumbling ellipsoid with a random initial angular velocity vector. The rotational motion of the asteroid is then controlled by off-setting the thrust vector, induced by the laser, with respect to the centre of mass. Analytic formulas for rotational control are developed in order to maximise the control torque along the instantaneous angular velocity.

The spacecraft proximity motion and the instantaneous rotational velocity of the asteroid are estimated through two filters: an augmented UKF that determines the spacecraft trajectory from optical and laser ranging measurements, and a batch filter which processes optical flow measurements from the camera to reconstruct the rotational velocity of the asteroid. It will be shown that, through the proposed control method, the time required to achieve a given variation of velocity can be substantially decreased and the displacement of the asteroid from its nominal unperturbed orbit maximised.

This Chapter is organised as follows. Section 5.1 briefly introduces the ablation model employed. Then, Section 5.2 describes the spacecraft dynamics and control during operations. Section 5.3 presents the asteroid rotational dynamics and the control to decrease the angular velocity. Section 5.4 focuses on the proximity and rotational motion reconstruction. Finally, Section 5.5 shows the results for the proposed mission scenario.

## 5.1 Ablation Model

This section outlines the ablation model used to predict the effect of the sublimation process on the asteroid and on the spacecraft. For further details, the interested reader can find an exhaustive description in (Vasile et al., 2013; Vasile et al., 2013b; Gibbings et al., 2013).

The force acting on the asteroid  $F_L$  is given by the product of the velocity of the ejected gas  $\bar{v}$  and the mass flow rate of the ablated material  $\dot{m}$ :

$$F_L = \lambda_s \bar{v} \dot{m} \quad (156)$$



where  $\lambda_s = 0.88$  is a constant scatter factor used to account for the non-unidirectional expansion of the ejecta. The mass flow rate is given by the integral, over the area illuminated by the laser, of the mass flow rate per unit area  $\dot{\mu}$  :

$$\dot{m} = 2V_{rot} \int_0^{y_{max}} \int_{t_{in}}^{t_{out}} \dot{\mu} dt dy \quad (157)$$

where  $V_{rot}$  is the speed at which the surface of the asteroid is moving under the spotlight,  $y_{max}$  is the maximum width of the spot and  $t_{in}$  and  $t_{out}$  are the entry and exist times from the spotlight of a point of the surface moving with velocity  $V_{rot}$  . The mass flow rate  $\dot{\mu}$  per unit area is expressed as:

$$E_v^* \dot{\mu} = P_{IN} - Q_{RAD} - Q_{COND} \quad (158)$$

where  $P_{IN}$  is the absorbed laser power per unit area,  $E_v^*$  is an augmented sublimation enthalpy,  $Q_{COND}$  the conduction and  $Q_{RAD}$  the radiation loss per unit area. The augmented enthalpy  $E_v^* = E_v^*(T_0, T_S, C_p, C_v, \bar{v})$  depends on the initial surface temperature  $T_0$  , the sublimation temperature  $T_S$  , the heat capacity of solid phase  $C_v$  , vapour phase  $C_p$  and the mean ejection velocity  $\bar{v}$  .

The input power  $P_{IN}$  in Eq.(158) is computed assuming that the beam is generated by an electrically pumped laser. The electric power is generated by a solar array with conversion efficiency  $\eta_s$  . The electric power is then converted into laser power with efficiency  $\eta_l$  . The surface of the asteroid is absorbing only the fraction  $\alpha_M = (1 - \alpha_s)$  of the incoming light, where  $\alpha_s$  is the albedo at the

frequency of the laser light. One can consider this as the worst case scenario. The absorbed power per square meter at the spot is therefore:

$$P_{IN} = \tau \tau_g \alpha_M \eta_F \eta_L \eta_S \frac{P_{1AU} A_{SA}}{A_{spot} r_{AU}^2} \quad (159)$$

where  $\tau$  is a degradation factor due to contamination,  $\eta_P$  is the efficiency of the power system,  $P_{1AU}$  is the solar constant at 1 Astronomical Unit (AU),  $A_{SA}$  is the area of the solar arrays,  $A_{spot}$  is the area of the spot and  $r_{AU}$  is the distance from the Sun measured in AU. The term  $\tau_g$  accounts for the fraction of laser light absorbed by the ejected gas. The degradation factor can be computed by following Kahle et al. (2006) and taking the plume density  $\rho_{plume}(r, \xi)$  at any given distance  $r$  from the spot location, and elevation angle  $\xi$  from the surface normal. The ejecta thickness on any exposed surface,  $h$ , grows linearly with the mean ejection velocity at the asteroid surface  $\bar{v}$  and the plume density  $\rho_{plume}(r, \xi)$ , which decreases as the distance from the asteroid increases (Vasile et al. 2013). The increasing thickness of the contaminants will ultimately reduce the power generated by the solar arrays and, therefore, the laser output power. The consequence is a reduction of the thrust imparted onto the asteroid until the sublimation ceases completely and the thrust with it. The reduction of the power generated by the solar arrays,  $\tau$  can be computed from the Beer-Lambert-Bouguer law:

$$\tau = e^{-\eta h} \quad (160)$$

where  $\eta$  is the absorbance per unit length of the accumulated ejecta.

### 5.1.1 Optimal distance from the asteroid and force due to the sublimation

The asteroid's orbital velocity variation given by the ablation process can be computed as:

$$\delta v_I = \int_{t_0}^{t_f} \frac{F_L(t)}{m_A(t)} dt \quad (161)$$

where  $m_A$  is the mass of the asteroid which is decreasing due to the sublimation process. From the ablation model presented in the previous section one can see that the thrust  $F_L$  is a function of both the power input to the laser and the distance from the spot, as the contamination of the solar arrays depends on the mass flow rate. Figure 51 represents the contour line of the thrusting time required to achieve a  $\delta v_I$  of 1 m/s with the laser positioned at a distance of 50 meters from an S-class asteroid with a mean radius of 2.18 m, a spinning rate of 19.47 rotations per hour and a mass of 130,000 kg. The thrusting time is plotted against the power input to the laser and the radius of the laser spot. Table 21 reports the parameters used for the calculation of Eq.(159) and (160).

**Table 21. Laser system coefficients.**

Parameter	Value
$\tau_g$	1
$\alpha_M$	0.84
$\eta_p$	0.85
$\eta_L$	0.55
$\eta_s$	0.3
$\eta$	$2 \cdot 10^{-4} \text{cm}^{-1}$
$c_A$	1361 J/(K·kg)
$\kappa_A$	4.51 W/(m·K)
$\rho_A$	3500 kg/m <sup>3</sup>
$T_s$	3800 K

Figure 51 shows that a variation of 20% in the radius of the spot corresponds to an increase in the deflection time that is between 40 to 50 days (about 22-24% of the maximum deflection time).

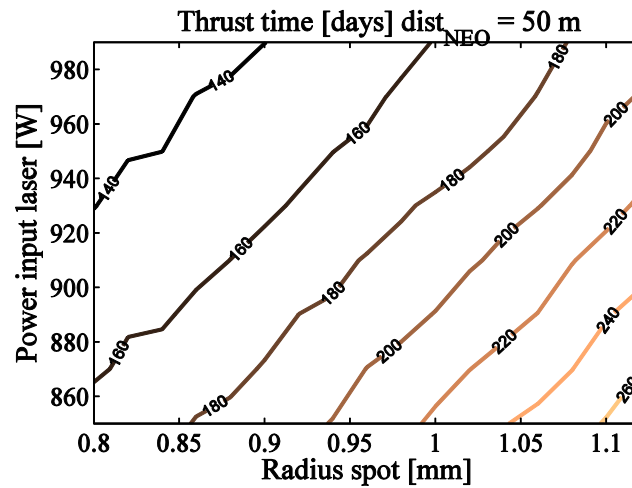


**Figure 51. Thrusting time required to achieve 1 m/s velocity change with a shooting distance of 50 m.**

A variation of the radius of the spot corresponds to the defocusing of the beam and is due to two reasons: the excavation of a groove along the surface of the asteroid and the variation of the relative position of the spot from the laser source due to the rotation of the asteroid and the relative motion of the spacecraft. The distance from the focal point, along the beam, at which the beam radius is  $w_0\sqrt{2}$  (known as Rayleigh length in Siegman, 1986), with  $w_0$  the radius at the focal point, is about 3 m, assuming a 50 mm in diameter focusing mirror, at a nominal distance of 50 m from the laser source to the spot. With reference to Figure 51, if the nominal radius is 0.8 mm at 3 m from the focal point the beam radius would be 1.13 mm. This means that at the rate of 19.47 rotations per hour a fluctuation of the distance within the Rayleigh length would yield a variation of about 24% of the deflection time. It follows that the Rayleigh length can be used to derive a requirement on the control of the distance between the spacecraft and the surface of the asteroid, which can be

converted in a requirement on the control of the distance between the spacecraft and the asteroid centre of mass as it will be illustrated in Section 5.3.

The variation of the deflection time with the defocusing of the beam is however a function of the rotation rate. In fact, if one assumes a constant input power of 860 W, a nominal spot size of 0.8 mm (Vasile et al., 2013), and an optics designed to focus the beam at a nominal distance of 50 m from the laser source, a variation of the distance will produce a bigger cross section  $A_{spot}$  of radius  $w$  on the surface of the asteroid consistently with the Rayleigh length, as shown in the following equation:

$$w(l) = w_0 \frac{\sqrt{2}(l - l_{focus \sin g})}{l_{Rayleigh}} \quad (162)$$

$$A_{spot} = \pi w^2 = 2\pi w_0^2 \frac{(l - l_{focus \sin g})^2}{l_{Rayleigh}^2}$$

where  $l$  is the distance from the spot,  $l_{focus \sin g}$  is the focusing length. This means that the light intensity at the spot decreases as the distance of the laser source from the surface departs from the focusing distance. Furthermore, Eq.(157) and (161) give a mass flow that decreases if the surface under the laser moves faster. Therefore, if one assumes a flat surface moving with velocity  $V_{rot}$  transversally to the incident light and positioned at a distance  $l$  from the laser source the resulting thrust is the one represented in Figure 52.

As one can see, the force increases as the velocity  $V_{rot}$  decreases and an absolute maximum is reached when  $V_{rot}$  is zero and the distance equals the focusing length. Moreover, for higher values of velocity, moving by 3 m with respect to the focusing length causes a reduction of about 75% of

the nominal value. With reference to Figure 52b), the trend is almost linear in the distance although a curvature can be seen. For lower velocities, the variation of the force with the distance is less pronounced, because the surface resides under the laser for longer time.

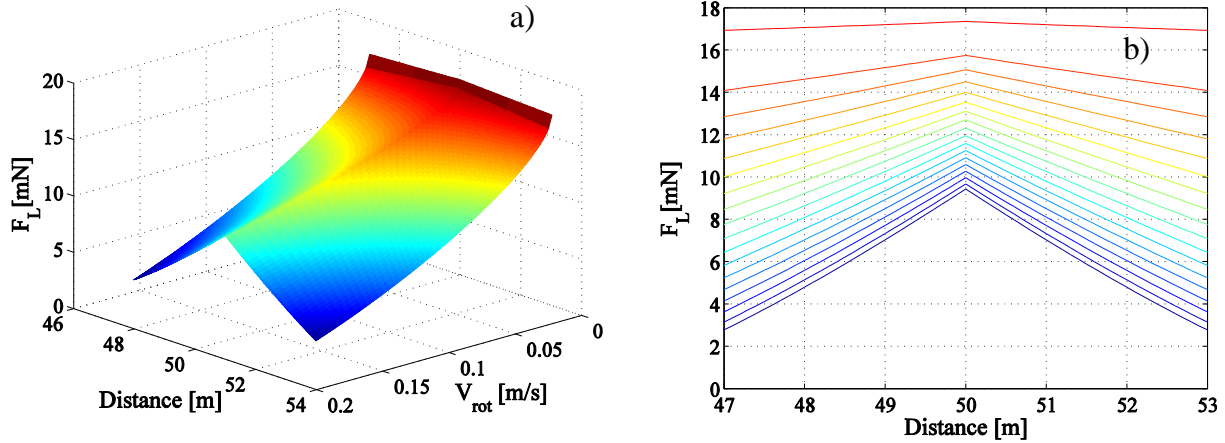


**Figure 52. a) Force due to the sublimation process with respect to the laser distance from the spot and the velocity of the surface under the spot light; b) cross section showing the force trend with respect to the distance at increasing tangential velocity.**

If the incident laser beam is not perpendicular to the surface the spot deforms from a circle to an ellipse and its area increases. The travel time of a point under the spot light  $t_{in} - t_{out}$  then changes depending on the direction of the velocity  $V_{rot}$  with respect to the local normal and Eq.(157) needs to be modified to account of the actual geometry. In this Chapter a simpler and more conservative approach is taken. Instead of calculating the exact travelling time the light intensity is simply reduced by modifying Eq.(162) as follows:

$$A_{spot} = 2\pi w_0^2 \frac{(l - l_{focus} \sin g)^2}{l_{Rayleigh}^2} \frac{1}{\cos \theta_{laser-normal}} \quad (163)$$

where  $\theta_{laser-normal}$  is the angle between the incident laser beam and local normal. The area given by Eq.(163) is then used in both Eq.(157) and (161). As one can see as the cross section increases with this angle, the power density decreases and progressively reduces to zero for nearly tangential configurations.

## 5.2 Proximity Motion Dynamics and Control

During the ablation process the spacecraft flies in close formation with the asteroid, thus it is convenient to describe the motion of the spacecraft in the rotating Hill reference frame. In the proximity of the asteroid, the spacecraft is subject to the force due to solar radiation pressure, the gravity of the asteroid, the gravity of the Sun, the centrifugal and Coriolis forces, the recoil of the laser, and the force induced by the impingement with the plume. Moreover, the asteroid is accelerating under the effect of laser ablation, and, thus, the spacecraft experiences the same acceleration in magnitude but in the opposite direction.

The asteroid's orbit around the Sun is defined with respect to the Sun-centred equatorial inertial reference frame  $\mathbf{I}-\mathbf{J}-\mathbf{K}$  as shown in Figure 53a). In this work, it is assumed that the asteroid is an ellipsoid with semi-axes  $a_I$ ,  $b_I$ , and  $c_I$  defined in the body fixed reference frame  $\bar{\mathbf{i}}-\bar{\mathbf{j}}-\bar{\mathbf{k}}$  (principal axes of inertia) as shown Figure 53b). With reference to Figure 53a),  $\delta\mathbf{r}$  is the position vector of the spacecraft with respect to the asteroid,  $\mathbf{r}_a$  and  $\mathbf{r}_{SC}$  are respectively the position of the asteroid and the spacecraft in the inertial frame. The spacecraft state vector relative to the asteroid is defined as  $[\delta\mathbf{r}^h, \delta\dot{\mathbf{r}}^h]^T = [x_h, y_h, z_h, v_{x_h}, v_{y_h}, v_{z_h}]^T$  in the Hill reference frame.

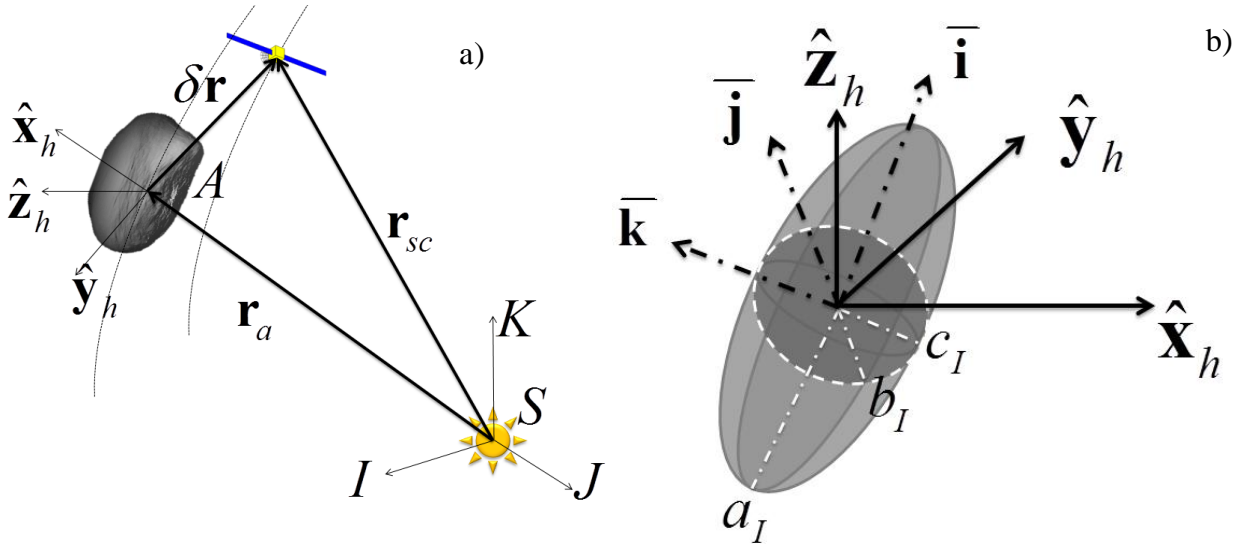


**Figure 53. (a) Definition of the inertial and Hill's reference frames; (b) definition of the asteroid's body fixed reference frame.**

The potential of the gravity field of the asteroid was expressed using the second order approximation given already in Eq.(120). When including the effects of the deflective action and considering the whole tri-dimensional dynamics, the set of equations of motion in Eq.(123) becomes:

$$\begin{aligned}
\delta \ddot{\mathbf{r}}^h &= -\ddot{\mathbf{r}}_a^h - 2\dot{\boldsymbol{\theta}}^h \times \delta \dot{\mathbf{r}}^h - \dot{\boldsymbol{\theta}}^h \times \delta \mathbf{r}^h - \dot{\boldsymbol{\theta}}^h \times (\dot{\boldsymbol{\theta}}^h \times \delta \mathbf{r}^h) - \frac{\mu_{sun}}{r_{Sc}^3} (\delta \mathbf{r}^h + \mathbf{r}_a^h) - \frac{\mu_a}{\delta r^3} \delta \mathbf{r}^h + \nabla U + \frac{\mathbf{F}_{sc}(\delta \mathbf{r}^h, \mathbf{r}_a^h)}{m_{sc}} = \\
&= -\ddot{\mathbf{r}}_{a-g}^h - 2\dot{\boldsymbol{\theta}}^h \times \delta \dot{\mathbf{r}}^h - \dot{\boldsymbol{\theta}}^h \times \delta \mathbf{r}^h - \dot{\boldsymbol{\theta}}^h \times (\dot{\boldsymbol{\theta}}^h \times \delta \mathbf{r}^h) - \frac{\mu_{sun}}{r_{Sc}^3} (\delta \mathbf{r}^h + \mathbf{r}_a^h) + \mathbf{a}_p
\end{aligned} \tag{164}$$

where the superscript  $h$  refers to the projection onto the Hill's local axes. The acceleration  $\ddot{\mathbf{r}}_a$ , which the asteroid is subjected to, in the inertial frame is defined as:

$$\ddot{\mathbf{r}}_a = -\frac{\mu_{sun}}{r_a^3} \mathbf{r}_a - \frac{\mu_{Sc}}{\delta r^3} \delta \mathbf{r} + \mathbf{a}_L = \ddot{\mathbf{r}}_{a-g} + \mathbf{a}_L \tag{165}$$



$\ddot{\mathbf{r}}_{a-g}$  represents the dynamics of the asteroid trajectory under gravitational effects only. The second component on the right hand side of Eq.(165) represents the tugging effect exerted by the spacecraft on the asteroid, and  $\mathbf{a}_L = \mathbf{F}_L/m_A$  is the acceleration due to the laser ablation process (see Section 5.1). The quantity  $\dot{\boldsymbol{\theta}}$  is the angular velocity with which the reference frame rotates. In the local reference frame the variation of  $\dot{\boldsymbol{\theta}}$  can be derived from:

$$\mathbf{r}_a^h \times (\ddot{\boldsymbol{\theta}}^h \times \mathbf{r}_a^h) + 2\mathbf{r}_a^h \times (\dot{\boldsymbol{\theta}}^h \times \mathbf{r}_a^h) = \mathbf{r}_a^h \times \mathbf{a}_L^h \quad (166)$$

being  $\mathbf{a}_L^h$  the projection of  $\mathbf{a}_L$  onto the Hill reference frame. Eq.(166) states that the instantaneous variation of the angular momentum with respect to time is proportional to the induced deflection acceleration  $\mathbf{a}_L$ . The acceleration  $\mathbf{a}_p = -\mathbf{a}_L^h + \mathbf{F}_{sc}(\delta\mathbf{r}^h, \mathbf{r}_a^h)/m_{sc} - \frac{\mu_a}{\delta r^3} \delta\mathbf{r}^h + \nabla U$  comprises all the perturbative accelerations acting on the spacecraft. The force vector  $\mathbf{F}_{sc}(\delta\mathbf{r}^h, \mathbf{r}_a^h)$  includes all the perturbations due to solar radiation pressure, the laser recoil and plume impingement (Vasile et al., 2013):

$$\begin{aligned} \mathbf{F}_{Solar}(\delta\mathbf{r}^h, \mathbf{r}_a^h) &= C_R S_{srp} \left( \frac{r_{AU}}{r_{sc}} \right)^2 A_M \frac{(\delta\mathbf{r}^h + \mathbf{r}_a^h)}{r_{sc}} \\ \mathbf{F}_{recoil}(\delta\mathbf{r}^h, \mathbf{r}_a^h) &= \eta_{sys} S_{srp} \left( \frac{r_{AU}}{r_{sc}} \right)^2 A_{SA} \frac{\delta\mathbf{r}^h}{\delta r} \\ \mathbf{F}_{plume}(\delta\mathbf{r}^h) &= \rho_{plume}(\delta r) \bar{v}_{plume}^2(\delta r) A_{eq} \frac{\delta\mathbf{r}^h}{\delta r} \end{aligned} \quad (167)$$

where  $S_R$  is the reflectivity coefficient and  $S_{srp}$  is the solar flux at 1 AU,  $\eta_{sys} = \tau\alpha_M\eta_p\eta_L\eta_S$  is the system efficiency,  $A_M$  is the area of the solar arrays plus the area of spacecraft bus,  $A_{eq}$  is the

spacecraft cross section area facing the incoming plume of gas,  $\rho_{plume}$  and  $\bar{v}_{plume}$  are respectively the plume's density and velocity.

### 5.3 Proximity Control Strategy

In section 5.1.1 it was suggested that the Rayleigh length could be used to derive a requirement on the relative distance between laser head and asteroid's surface. If one considers  $V_{rot}$  equal or lower than 19.47 rotations per hour (see Section 2.1), then a Rayleigh length of up to 3 m can be deemed to be acceptable without any control of the relative position. On the other hand, in order to control the rotational motion of the asteroid the laser needs to hit different points on its surface while the asteroid is rotating. It is therefore necessary to ensure that the difference between the focal distance and the distance between the laser head and the surface remains within the Rayleigh length at all times.

Let us consider the asteroid to be an ellipsoid with semi-axes  $a_l = 3$  m,  $b_l = 2.3$  m and  $c_l = 1.5$  m, with  $b_l$  the spinning axis, and the spacecraft located at a constant distance of 50 m from the asteroid's Centre of Mass (CoM) in the plane perpendicular to  $b_l$ . Furthermore, let us assume that the focal distance is 49.3 m from the laser head. With reference to Figure 54a), the difference between the focusing length and the distance between the laser head and the surface of the asteroid can now be calculated for each visible (i.e. reachable from the laser) point on the surface and for rotation angles.

If the modulus of this difference was greater than the Rayleigh distance, then the yield of the sublimation process would be compromised and might even cease. Figure 54b) shows the

maximum difference between the range to surface and the focusing length for different rotation angles first around  $\hat{x}_h$  and then  $\hat{z}_h$ . Given the symmetry of the problem, only rotation angles from -90 to 90 degrees were considered. The discontinuity at about  $\pm 25$  degrees and  $\pm 86$  degrees is due to the fact that the maximum variation goes from surface points closer to the spacecraft to points located farther from it. The maximum variation is reached at 0 degrees when the major axis is aligned with the asteroid-spacecraft direction and at  $\pm 35$  degrees when the range to surface is maximum. We can see that the maximum difference between the range to a surface point and the focusing length is about 2.3 m.

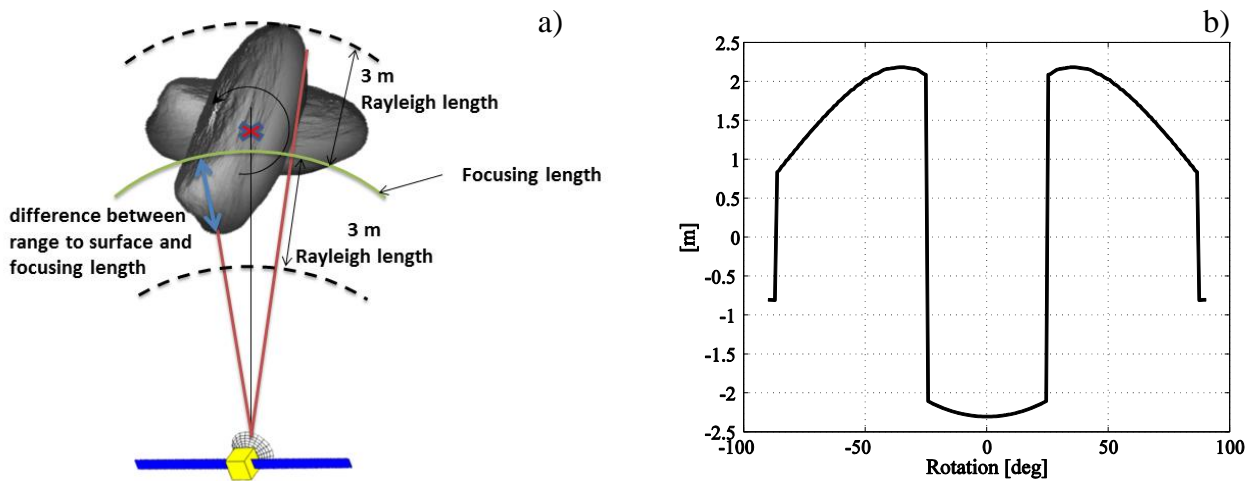


**Figure 54. a) Difference between range to a surface point and the focusing length with Rayleigh length b) Maximum difference as a function of the asteroid rotation around  $b_1$  (spacecraft positioned at 50 m from the asteroid's CoM and focusing length of 49.3 m).**

Given the maximum acceptable excursion of 3 m defined by the Rayleigh length, the spacecraft needs to be maintained within a 0.7 m radius control sphere around its nominal position with respect to the centre of mass of the asteroid. Nonetheless in order to compensate estimation errors and maintain the variations of the thrust due to the defocusing and  $\theta_{laser-normal}$  contained and

maintain the laser at optimal operative conditions, we decided to activate the control logics for a 0.4 m control sphere. In the following, it is assumed that the nominal position is placed at  $y_h = -50$  m with respect to the asteroid centre of mass.

If  $\mathbf{d} = [d_1, d_2, d_3]^T$  is the displacement from the nominal position in the Hill's reference frame, a correction manoeuvre  $\Delta \mathbf{v}$  is then implemented when  $\|\mathbf{d}\| = d^e / 2$ , where  $d^e$  is the diameter of the sphere.

In the derivation of the control, it is assumed that the acceleration  $\mathbf{a}_p$  acting on the spacecraft is constant within the control sphere. Under this assumption, the magnitude of each component  $\Delta v_i$  of the correction manoeuvre can be derived from the evolution of the displacement  $d_i$  in a time interval  $\Delta t$ . If  $d_i^s$  is the value of the displacement component when the spacecraft touches the limits of the control sphere and  $v_i^s$  the corresponding velocity component, then the displacement after an interval  $\Delta t$  from the implementation of the control manoeuvre is:

$$d_i = d_i^s + (v_i^s + \Delta v_i) \Delta t + a_{p,i} \frac{\Delta t^2}{2} \quad (168)$$

where  $a_{p,i}$  is the  $i$ -th component of the acceleration  $\mathbf{a}_p$  at the time the correction is performed. The control impulse bit  $\Delta v_i$  can now be allocated such that the spacecraft reaches a displacement  $d_i = -d_i^s$  with the corresponding velocity equal to zero. The time  $\Delta t_c$  to reach this condition is:

$$(v_i^s + \Delta v_i) + a_{p,i} \Delta t_c = 0 \Rightarrow \Delta t_c = -\frac{v_i^s + \Delta v_i}{a_{p,i}} \quad (169)$$

By substituting  $\Delta t_c$  into Eq.(168), one obtains the value of the  $i$ -th component of the correction manoeuvre:

$$\Delta v_i^2 + 2v_i^s \Delta v_i + (v_i^s)^2 + 2a_{p,i} d_i^s = 0 \quad (170)$$

Eq.(170) has two roots, one of which produces a positive value of  $\Delta t_c$ . Section 5 will present the navigation strategy to estimate the displacement  $d_i^s$ , velocity  $v_i^s$  and disturbing acceleration  $\mathbf{a}_p$ .

#### 5.4 Asteroid Rotational Dynamics and Control

From Figure 52 one can see that the ablation force is higher when the velocity  $V_{rot}$  is lower because the time interval  $[t_{in} \ t_{out}]$  to sublimate the surface tends to infinity. The velocity  $V_{rot}$  is given by the modulus of the cross product of the instantaneous angular velocity  $\boldsymbol{\omega}$  and  $\mathbf{s}$ , the position vector of the spot on the surface of the asteroid, with components  $\mathbf{s} = [s_x^b \ s_y^b \ s_z^b]^T$  in the body frame:

$$V_{rot} = \|\boldsymbol{\omega} \times \mathbf{s}\|$$

This means that decreasing the asteroid's angular velocity can increase the yield of the ablation process. The asteroid's rotational motion is governed by the following system of differential equations:

$$\begin{aligned} \dot{\mathbf{q}} &= \frac{1}{2} \boldsymbol{\Pi} \mathbf{q} \\ \mathbf{I} \dot{\boldsymbol{\omega}} + \boldsymbol{\omega} \times \mathbf{I}_a \boldsymbol{\omega} &= \mathbf{M}_c \end{aligned} \quad (171)$$

where  $\mathbf{q} = [q_1 \ q_2 \ q_3 \ q_4]^T$  is the quaternions vector,  $\boldsymbol{\omega} = [\omega_x \ \omega_y \ \omega_z]^T$  is the angular velocity vector in the body frame,  $\mathbf{I}_a$  is the matrix of inertia of the asteroid,  $\mathbf{M}_c$  is the control torque, and  $\boldsymbol{\Pi}$  is given by:

$$\boldsymbol{\Pi} = \begin{bmatrix} 0 & \omega_z & -\omega_y & \omega_x \\ -\omega_z & 0 & \omega_x & \omega_y \\ \omega_y & -\omega_x & 0 & \omega_z \\ -\omega_x & -\omega_y & -\omega_z & 0 \end{bmatrix} \quad (172)$$

Perturbative torques from the Sun light pressure and the YORP effect are neglected because their cumulative effect is negligible with respect to the torque induced by the laser. A strategy to reduce the spinning rate of the asteroid is to apply a control torque proportional to the opposite of the angular velocity vector:

$$\mathbf{M}_c \sim -\frac{\boldsymbol{\omega}}{\|\boldsymbol{\omega}\|} \quad (173)$$

The actual control torque  $\mathbf{M}_c$  that can be generated is given by the cross product of the thrust  $\mathbf{F}_L^b$  with the position vector  $\mathbf{s}$ :

$$\mathbf{M}_c = \mathbf{s} \times \mathbf{F}_L^b = \begin{cases} M_{c-x}^b = -F_z^b s_y^b + F_y^b s_z^b \\ M_{c-y}^b = F_z^b s_x^b - F_x^b s_z^b \\ M_{c-z}^b = -F_y^b s_x^b + F_x^b s_y^b \end{cases} \quad (174)$$

where thrust  $\mathbf{F}_L^b$  is the thrust vector, projected in body axes, produced by the ablation process at point  $\mathbf{s}$  on the surface of the asteroid (see Figure 55a)).

In the following it is assumed that the asteroid is an ellipsoid with a regular and smooth surface, and that  $\mathbf{F}_l^b$  is aligned with the vector normal to the surface and pointing inside the body of the asteroid.

The normal  $\mathbf{n}$  to the surface can be calculated as the gradient of the surface function as follows:

$$\mathbf{n} = \nabla(\mathbf{s}'\mathbf{A}(t)\mathbf{s}-1)/\|\nabla(\mathbf{s}'\mathbf{A}(t)\mathbf{s})\| = \left[ \frac{s_x^b}{a_l^2} \quad \frac{s_y^b}{b_l^2} \quad \frac{s_z^b}{c_l^2} \right] / \left\| \left[ \frac{s_x^b}{a_l^2} \quad \frac{s_y^b}{b_l^2} \quad \frac{s_z^b}{c_l^2} \right] \right\| \quad (175)$$

The achievable control torque then becomes:

$$\mathbf{M}_c = \mathbf{s} \times \mathbf{F}_L^b = F_L \left[ \frac{s_y^b s_z^b}{c_l^2} - \frac{s_y^b s_z^b}{b_l^2} \quad \frac{s_x^b s_z^b}{a_l^2} - \frac{s_x^b s_z^b}{c_l^2} \quad \frac{s_x^b s_y^b}{b_l^2} - \frac{s_x^b s_y^b}{a_l^2} \right] / \left\| \left[ \frac{s_x^b}{a_l^2} \quad \frac{s_y^b}{b_l^2} \quad \frac{s_z^b}{c_l^2} \right] \right\| \quad (176)$$

With reference to Figure 55b), it is convenient to parameterize the position of a point on the surface with the two angles  $\alpha$  and  $\beta$ :

$$\begin{aligned} s_x^b &= a_l \sin \alpha \cos \beta \\ s_y^b &= b_l \sin \alpha \sin \beta \\ s_z^b &= c_l \cos \alpha \end{aligned} \quad (177)$$

where  $\beta$  is the azimuth and  $\alpha$  is the polar angle taken from the minor semi-major axis (see Figure 55b)).

The achievable torque then can be rewritten as:

$$\mathbf{M}_c = \frac{1}{2} \frac{F_L}{\sqrt{\left( \frac{\sin \alpha \cos \beta}{a_l} \right)^2 + \left( \frac{\sin \alpha \sin \beta}{b_l} \right)^2 + \left( \frac{\cos \alpha}{c_l} \right)^2}} \begin{bmatrix} \sin \beta \sin 2\alpha \left( \frac{b_l^2 - c_l^2}{b_l c_l} \right) \\ \cos \beta \sin 2\alpha \left( \frac{c_l^2 - a_l^2}{a_l c_l} \right) \\ \sin 2\beta \sin^2 \alpha \left( \frac{a_l^2 - b_l^2}{a_l b_l} \right) \end{bmatrix} \quad (178)$$

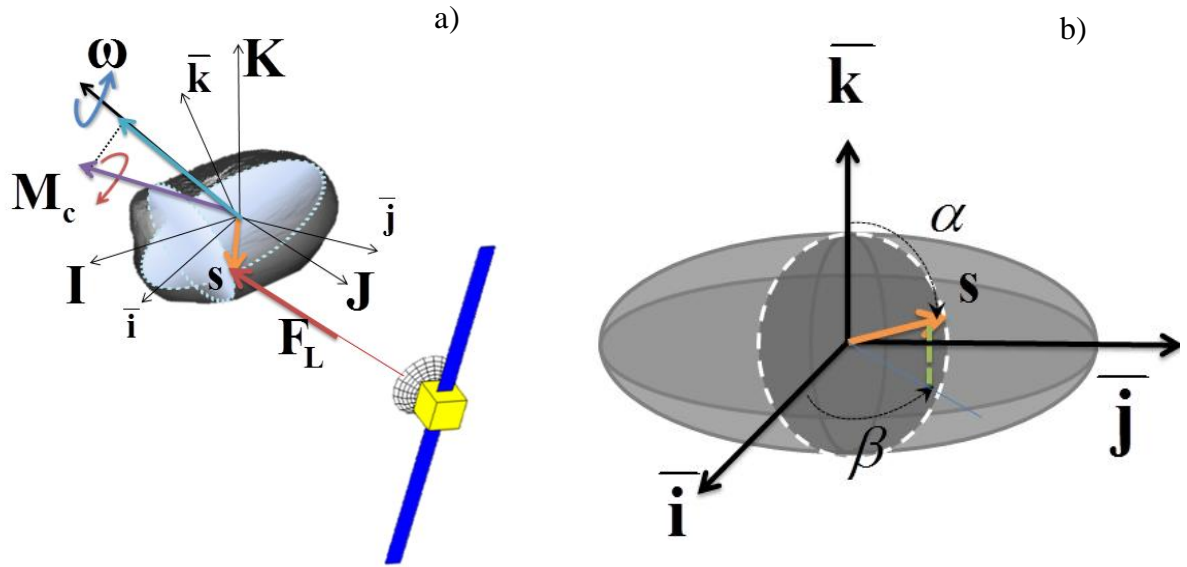


**Figure 55. Angular velocity control scheme (a); control arm representation in body frame (b).**

The required control torque is given by the projection of  $\mathbf{M}_c$  on the angular velocity vector:

$$\begin{aligned}
 M_\omega &= \mathbf{M}_c \cdot \boldsymbol{\omega} = \\
 &= \frac{F_L}{2} \frac{\sin \alpha \left( c_z \left( \frac{a_I^2 - b_I^2}{a_I b_I} \right) \sin \alpha \sin 2\beta + 2c_y \left( \frac{c_I^2 - a_I^2}{a_I c_I} \right) \cos \alpha \cos \beta + 2c_x \left( \frac{b_I^2 - c_I^2}{b_I c_I} \right) \cos \alpha \sin \beta \right)}{\sqrt{\left( \frac{\sin \alpha \cos \beta}{a_I} \right)^2 + \left( \frac{\sin \alpha \sin \beta}{b_I} \right)^2 + \left( \frac{\cos \alpha}{c_I} \right)^2}} = \\
 &= F_L r_{eq}
 \end{aligned} \tag{179}$$

where  $c_x$ ,  $c_y$ , and  $c_z$  are the cosine directors of the angular velocity in the body frame and

$r_{eq} = (\mathbf{s} \times \mathbf{n}) \cdot \boldsymbol{\omega}$  is here called equivalent control arm. A way to derive the point of application of the

laser, given by the two angles  $\alpha$  and  $\beta$  would be to solve the following maximization problem:



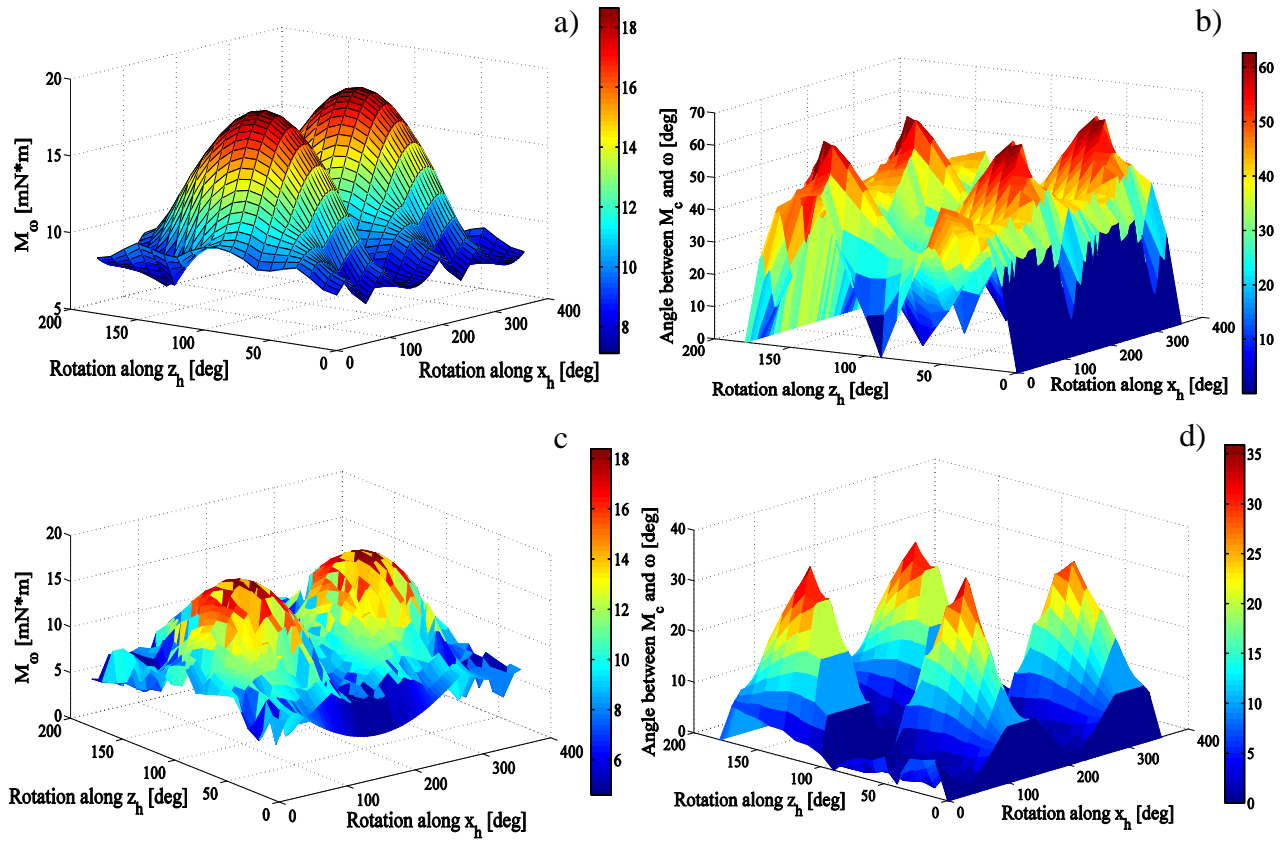
$$\begin{aligned}
& \max_{\alpha, \beta} M_{\omega}(\alpha, \beta) = \\
& = \max_{\alpha, \beta} \frac{F_L(\alpha, \beta)}{2} \frac{\sin \alpha \left( c_z \left( \frac{a_I^2 - b_I^2}{a_I b_I} \right) \sin \alpha \sin 2\beta + 2c_y \left( \frac{c_I^2 - a_I^2}{a_I c_I} \right) \cos \alpha \cos \beta + 2c_x \left( \frac{b_I^2 - c_I^2}{b_I c_I} \right) \cos \alpha \sin \beta \right)}{\sqrt{\left( \frac{\sin \alpha \cos \beta}{a_I} \right)^2 + \left( \frac{\sin \alpha \sin \beta}{b_I} \right)^2 + \left( \frac{\cos \beta}{c_I} \right)^2}}
\end{aligned} \tag{180}$$

Figure 56a) shows the maximum achievable projection of the control torque on the rotation velocity vector for different configurations of the ellipsoid. The different configurations are obtained by rotating the asteroid along the axes  $\hat{x}_h$  and  $\hat{z}_h$ . Figure 56b), instead, shows the misalignment between the applied torque and the angular velocity vector, for the same configurations. The solution of problem in Eq.(180) produces misalignment angles of up to 60 degrees, which would generate undesirable torque components along the directions orthogonal to the angular velocity. This effect is due to the direction of the thrust generated by the ablation process. Thus, a different strategy is to solve the following problem:

$$\begin{aligned}
& \max_{\alpha, \beta} r_{eq}(\alpha, \beta) = \\
& = \max_{\alpha, \beta} \frac{1}{2} \frac{\sin \alpha \left( c_z \left( \frac{a_I^2 - b_I^2}{a_I b_I} \right) \sin \alpha \sin 2\beta + 2c_y \left( \frac{c_I^2 - a_I^2}{a_I c_I} \right) \cos \alpha \cos \beta + 2c_x \left( \frac{b_I^2 - c_I^2}{b_I c_I} \right) \cos \alpha \sin \beta \right)}{\sqrt{\left( \frac{\sin \alpha \cos \beta}{a_I} \right)^2 + \left( \frac{\sin \alpha \sin \beta}{b_I} \right)^2 + \left( \frac{\cos \beta}{c_I} \right)^2}}
\end{aligned} \tag{181}$$

Figure 56c) and d) show that if one optimizes  $r_{eq}$ , the maximum achievable torque is lower but the maximum angle between the control torque and the angular velocity is about 35 degrees. Hence, even though optimizing  $r_{eq}$  yields a lower control torque with respect to the maximization of  $M_{\omega}$ ,

it has the beneficial effect of reducing the misalignment between  $\mathbf{M}_c$  and  $\boldsymbol{\omega}$  for each spacecraft-asteroid configuration.



**Figure 56. Maximum achievable torque: a) optimizing maximum torque  $M_\omega$ , c) optimizing  $r_{eq}$ . Angle between control torque and the angular velocity: b) optimizing maximum torque  $M_\omega$  d) optimizing  $r_{eq}$ .**

Figure 57 shows the modulus of  $r_{eq}$  and the point of application of the laser for a particular configuration of the asteroid at an instant of time in which the body axes are aligned with the Hill's axes and the angular velocity is aligned with  $\hat{\mathbf{z}}_h$ . The rainbow scale in Figure 57b) corresponds to the magnitude of  $r_{eq}$  for each location on the surface of the ellipsoid. Negative values refer to a

torques increasing the angular velocity. This is a trivial case for which no constraint given by the configuration and the visibility from the spacecraft is imposed. The maxima are localised along the equator of the ellipsoid with azimuth angles of 132 and 312 degrees, which depend on the value of the ratio between  $a_l$  and  $b_l$ .

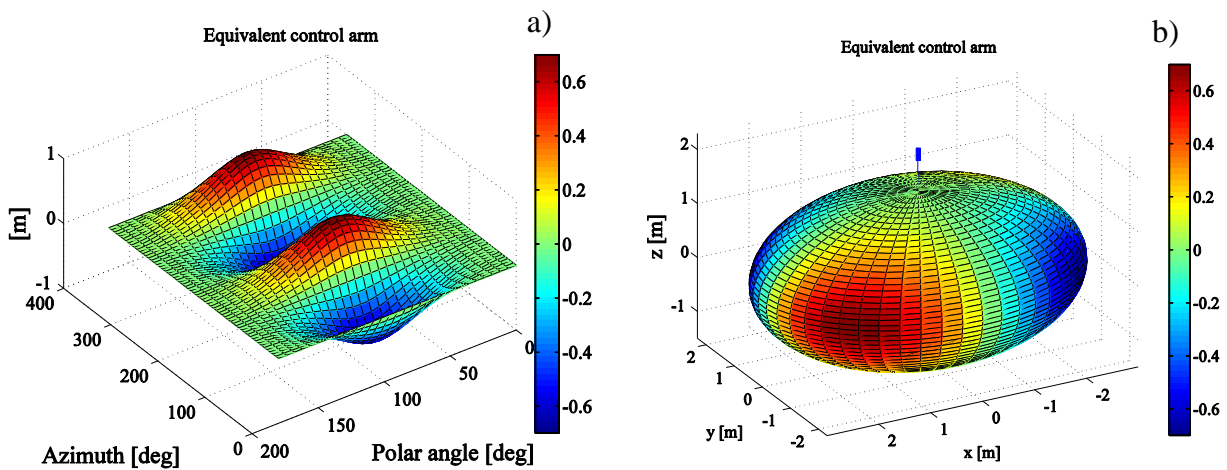


**Figure 57. Equivalent control arm a) with respect to azimuth and polar angles, b) on the ellipsoid surface.**

In the following, two constraints are imposed. One constraint is on the minimum angular velocity to be controlled. The asteroid angular velocity control is applied until the angular velocity reaches a value of  $10^{-3}$  rad/s. This value has been chosen after considering that the optical flow implemented as in Section 5.2 achieves an accuracy of comparable magnitude. The second constraint is on the relative asteroid-spacecraft configuration which will limit the region the laser could be pointed at and, subsequently, also the angle between laser beam direction and local normal. In this case a limit angle of 60 degrees between the local normal and the line of sight from the spacecraft to the spot was set to avoid nearly tangent conditions for the laser. The limit on the view angle partially account for the change in spot size due to the elevation of the beam over the surface of the asteroid.

Note that a non smooth surface could lead to a thrust that is not aligned with the local normal; however, since the surface that the laser can hit must be visible from the spacecraft, a torque opposite to the one expected assuming an expansion along the local normal is not possible. It is instead possible that the thrust vector and the vector connecting the spot with the barycentre form an angle that closer to 90 degrees producing a higher torque than expected. These effects due to the surface morphology can be the subject of a future work.

## **5.5 Proximity and Rotational Motion Reconstruction**

The motion of the spacecraft relative to the asteroid and the asteroid's rotational velocity are estimated by combining optical measurements from a camera with ranging information from a laser range finder and measurements from an impact sensor. The impact sensor, in particular, is used to measure the change in momentum due to the flow of ejecta impinging the spacecraft. The measurements then are processed through an UKF. Section 5.5.1 illustrates the measurement model. Then, Section 5.5.2 describes the proximity motion reconstruction while Section 5.5.3 shows the rotational motion reconstruction from optical flow measurements.

### **5.5.1 Measurement Model**

The model of the camera and the LIDAR are the same already used and expanded in Section 4.2. An impact sensor is used to measure the mass flow from the ablation process. These sensors provide information on the mean velocity and the mass flow per unit area of the ejecta plume. These can be used to estimate the force exerted by the ejecta plume as:

$$F_{plume} = \dot{m}_{laser} \bar{v}_s A_{S/C-attitude} = m_{SC} a_{plume} \quad (182)$$

where  $\dot{m}_{laser}$  is the mean mass flow per unit area,  $\bar{v}_s$  is the mean ejecta velocity at the spacecraft,  $A_{S/C-attitude}$  is the cross section of the spacecraft with respect to the ejection velocity (which depends on spacecraft attitude) and it is assumed to be equal to  $A_{eq}$  as in Eq.(167). The value of the term  $a_{plume}$  in Eq.(182) is estimated as part of the filtering process in Section 5.5.2. The observation equation is, thus, given as

$$y_{plume} = h_{rel}(a_{plume}) + \zeta_{plume} = m_{SC} a_{plume} + \zeta_{plume} \quad (183)$$

where  $\zeta_{plume}$  is the zero-mean Gauss white measurement noise.

The full set of observation equations is given by:

$$\mathbf{y} = h(\delta\mathbf{r}^h, \mathbf{q}, a_{plume}^h) + \boldsymbol{\zeta} = \begin{bmatrix} h_{camera}(\delta\mathbf{r}, \mathbf{q}) & h_l(\delta\mathbf{r}^h) & h_{plume}(a_{plume}^h) \end{bmatrix}^T + \begin{bmatrix} \boldsymbol{\zeta}_{camera} & \zeta_l & \zeta_{plume} \end{bmatrix}^T \quad (184)$$

where  $\boldsymbol{\zeta}$  comprises the measurement noises of all the sensors.

### 5.5.2 Proximity Motion Reconstruction

Given the non-linearities in the measurements and dynamics, it was decided to use an UKF to derive an estimate of the state and  $\mathbf{a}_p$ . It was found, in fact, that in order for the proposed proximity control to work, the state of the spacecraft needs to be known quite accurately while  $\mathbf{a}_p$  is required only when the correction manoeuvre is performed.

In order to maintain the desired distance from the surface of the asteroid, the control strategy requires the determination of the state vector  $[\delta\mathbf{r}^h, \delta\dot{\mathbf{r}}^h]^T = [x_h, y_h, z_h, v_{x_h}, v_{y_h}, v_{z_h}]^T$  and an estimation of the acceleration  $\mathbf{a}_p$  (see Eq.(170)).

The components of  $\mathbf{a}_p$  due to the laser recoil and solar radiation pressure are assumed to be well known because the acceleration due to solar pressure can be precisely estimated before the deflection operations begin and the laser recoil can be tested on ground. The component of  $\mathbf{a}_p$  that cannot be estimated only relying on models is the one due to the laser ablation itself, given the expected large degree of uncertainty in the outcome of the ablation process.

If the acceleration induced by the ablation  $a_L^h$  and the one due to the plume impingement  $a_{plume}$  were aligned, the camera and the LRF would suffice to determine the overall acceleration. Indeed, the acceleration induced by the plume impingement is directed along the asteroid-spacecraft direction, but the acceleration on the asteroid is directed along the local normal to the surface.

It would not be possible to estimate  $a_{plume}$  and  $a_L^h$  without any additional information. The impact sensor gives the necessary information.

The proposed method is the one used to estimate biases, commonly implemented to estimate solar radiation pressure (Maybeck, 1979). In this case, it consists of augmenting the state vector the UKF needs to determine by two variables  $[a_L^h, a_{plume}]^T$ . The augmented state vector then becomes

$\mathbf{x} = [\delta\mathbf{r}^h, \delta\dot{\mathbf{r}}^h, a_L^h, a_{plume}]^T = [x_h, y_h, z_h, v_{x_h}, v_{y_h}, v_{z_h}, a_L^h, a_{plume}]^T$  and the augmented dynamics reads as:

$$\begin{aligned}
\begin{bmatrix} \dot{x}_h \\ \dot{y}_h \\ \dot{z}_h \end{bmatrix} &= \begin{bmatrix} v_{x_h} \\ v_{y_h} \\ v_{z_h} \end{bmatrix} \\
\begin{bmatrix} \dot{v}_{x_h} \\ \dot{v}_{y_h} \\ \dot{v}_{z_h} \end{bmatrix} &= -\ddot{\mathbf{r}}_{a-g}^h - 2\dot{\boldsymbol{\theta}}^h \times \delta \dot{\mathbf{r}}^h - \dot{\boldsymbol{\theta}}^h \times \delta \mathbf{r}^h - \dot{\boldsymbol{\theta}}^h \times (\dot{\boldsymbol{\theta}}^h \times \delta \mathbf{r}^h) - \frac{\mu_{sun}}{r_{Sc}^3} (\delta \mathbf{r}^h + \mathbf{r}_a^h) + \mathbf{a}_p + \mathbf{w}_{sc} \\
a_L^h &= 0 + w_L \\
a_{plume} &= 0 + w_{plume}
\end{aligned} \tag{185}$$

where  $\mathbf{w}_{sc}$ ,  $w_L$  and  $w_{plume}$  are system noises. As shown in Section 5.1, the perturbative accelerations due to the laser ablation are dependent on the rotation velocity and on the distance. One needs to consider the thrust will be applied to produce the designed control torque in regions which presents similar geometry in terms of normal and control arm (i.e. tangential velocity). Then, taking into account also that the control torque will slowly decrease the angular velocity, the tangential velocity variation will be limited, and thus the magnitude of the exerted acceleration. This is especially true if the control acts such that spacecraft maintains its distance almost fixed. In this sense the variation in position due the perturbations will produce a variation to laser and plume accelerations which can be assimilated to noise processes, whose instantaneous dynamics is null in the short period. The dynamic equations associated to the acceleration from the laser ablation and plume impingement are thus time independent. It has been hereafter considered a level of system noise equal to the 10% of the actual value of the acceleration due to the laser and plume impingement at the beginning of each simulation. Treating these accelerations as biases is a strong assumption because it implies that their dynamics is slowly varying with time. In order to integrate

Eq.(185), one needs to update the instantaneous value of  $\mathbf{r}_a^h$ ,  $\dot{\boldsymbol{\theta}}^h$  in Eqs.(165) and (166) with the estimated current value of the acceleration exerted on the asteroid::

$$\mathbf{a}_L^h = a_L^h \mathbf{n} \quad (186)$$

The total perturbative acceleration acting on the spacecraft is then given by:

$$\mathbf{a}_p = -a_L^h \mathbf{n} + a_{plume} \frac{\delta \mathbf{r}^h}{\delta r} + \frac{\mathbf{F}_{Solar}(\delta \mathbf{r}^h, \mathbf{r}_a^h) + \mathbf{F}_{recoil}(\delta \mathbf{r}^h, \mathbf{r}_a^h)}{m_{SC}} - \frac{\mu_a}{\delta r^3} \delta \mathbf{r}^h + \nabla U(\delta \mathbf{r}, \mathbf{q}) \quad (187)$$

where the gravity gradient depends on the spacecraft position and attitude of the asteroid.

By using the estimate theory formalism the integration of the nonlinear discrete-time process in Eq.(185) and measurement equations in Section 5.5.1 can be expressed as:

$$\begin{aligned} \mathbf{x}_{k+1} &= g(\mathbf{x}_k, \mathbf{w}_k, \mathbf{q}_k) \\ \mathbf{y}_k &= h(\mathbf{x}_k, \mathbf{q}_k) + \boldsymbol{\zeta}_k \end{aligned} \quad (188)$$

with  $\mathbf{w}_k \sim N(0, \mathbf{Q}_k)$  the system noise in Eq.(185),  $\boldsymbol{\zeta}_k \sim N(0, \mathbf{R}_k)$  is the measurements noise in Eq.(184). The matrix  $\mathbf{Q}_k$  is the process noise covariance matrix and the matrix  $\mathbf{R}_k$  is the measurement noise covariance matrix.

In order to implement the UKF, we have to tailor the formulation for this kind of problem. The set of sigma points  $\Upsilon_i$  are transformed through the nonlinear function as:

$$\begin{aligned} \Upsilon_{i,k+1} &= g(\Upsilon_{i,k}, \tilde{\mathbf{q}}_k) \\ \gamma_i &= h(\Upsilon_{i,k}, \tilde{\mathbf{q}}_k) \end{aligned} \quad i=0, 1, \dots, 2n \quad (189)$$



where  $\tilde{\mathbf{q}}_k$  represents the estimated attitude of the asteroid at step  $k$ . In order to evaluate Eq.(189), one needs to have an estimate of the attitude of the asteroid between the time steps  $t_k$  and  $t_{k+1}$ . In this work this is given by integrating the first set of equations in Eq.(171), by using the estimated values of quaternions  $\tilde{\mathbf{q}}_k$  and asteroid angular velocity  $\tilde{\boldsymbol{\omega}}_k$  as follows:

$$\tilde{\mathbf{q}}_{k+1} = \tilde{\mathbf{q}}_k + \frac{1}{2} \mathbf{\Pi}(\tilde{\boldsymbol{\omega}}_k) \tilde{\mathbf{q}}_k (t_{k+1} - t_k) \quad (190)$$

The estimation process is hereafter specialized for the current problem. The mean value and covariance of  $\mathbf{z}$  are approximated using the weighted mean and covariance of the transformed vectors:

$$\begin{aligned} \tilde{\mathbf{y}} &= \sum_{i=0}^{2n} W_i^{(m)} \boldsymbol{\gamma}_i \\ \mathbf{P}_y &= \sum_{i=0}^{2n} W_i^{(c)} (\boldsymbol{\gamma}_i - \tilde{\mathbf{y}})(\boldsymbol{\gamma}_i - \tilde{\mathbf{y}})^T \end{aligned} \quad (191)$$

The predicted mean of the state vector  $\tilde{\mathbf{x}}_k^-$ , the covariance matrix  $\mathbf{P}_{x,k}^-$  and the mean observation  $\tilde{\mathbf{z}}_k^-$  can be approximated using the weighted mean and covariance of the transformed vectors:

$$\begin{aligned} \boldsymbol{\Upsilon}_{i,k|k-1} &= g(\boldsymbol{\Upsilon}_{i,k-1}, \tilde{\mathbf{q}}_{k-1}) \\ \tilde{\mathbf{x}}_k^- &= \sum_{i=0}^{2n} W_i^{(m)} \boldsymbol{\Upsilon}_{i,k|k-1} \\ \mathbf{P}_{x,k}^- &= \sum_{i=0}^{2n} W_i^{(c)} \left[ \boldsymbol{\Upsilon}_{i,k|k-1} - \tilde{\mathbf{x}}_k^- \right] \left[ \boldsymbol{\Upsilon}_{i,k|k-1} - \tilde{\mathbf{x}}_k^- \right]^T \\ \boldsymbol{\gamma}_{i,k|k-1} &= h(\boldsymbol{\Upsilon}_{i,k|k-1}, \tilde{\mathbf{q}}_k) \\ \tilde{\mathbf{y}}_k^- &= \sum_{i=0}^{2n} W_i^{(m)} \boldsymbol{\gamma}_{i,k|k-1} \end{aligned} \quad (192)$$

The updated covariance  $\mathbf{P}_{y,k}$  and the cross correlation matrix  $\mathbf{P}_{xy,k}$  are:

$$\begin{aligned}\mathbf{P}_{y,k} &= \sum_{i=0}^{2n} W_i^{(c)} \left[ \boldsymbol{\gamma}_{i,k|k-1} - \tilde{\mathbf{y}}_k^- \right] \left[ \boldsymbol{\gamma}_{i,k|k-1} - \tilde{\mathbf{y}}_k^- \right]^T \\ \mathbf{P}_{xy,k} &= \sum_{i=0}^{2n} W_i^{(c)} \left[ \boldsymbol{\Upsilon}_{k|k-1}^i - \tilde{\mathbf{x}}_k^- \right] \left[ \boldsymbol{\gamma}_{k|k-1}^i - \tilde{\mathbf{y}}_k^- \right]^T\end{aligned}\quad (193)$$

Finally, the filter state vector  $\tilde{\mathbf{x}}_k = [\tilde{x}_h, \tilde{y}_h, \tilde{z}_h, \tilde{v}_{x_h}, \tilde{v}_{y_h}, \tilde{v}_{z_h}, \tilde{a}_L^h, \tilde{a}_{plume}]^T$  and covariance updated matrix  $\mathbf{P}_{x,k}$  are calculated as in Eq.(46). Note that, the estimation process produces  $\mathbf{r}_a^h$  and  $\dot{\boldsymbol{\theta}}^h$  by integrating Eqs.(165) and (166), and using the value  $\tilde{a}_l$  estimated through the Kalman filter.

Once estimated values for the position and velocity of the spacecraft in the Hill's reference frame are available, one can calculate the displacement and velocity variation from the nominal position as:

$$\begin{aligned}\mathbf{d} &= [\tilde{x}_h - x_h^t \quad \tilde{y}_h - y_h^t \quad \tilde{z}_h - z_h^t] \\ \delta \tilde{\mathbf{r}}^h &= [\tilde{v}_{x_h} \quad \tilde{v}_{y_h} \quad \tilde{v}_{z_h}]\end{aligned}\quad (194)$$

where  $x_h^t = 0$  m,  $y_h^t = -50$  m,  $z_h^t = 0$  m are the components of the nominal position, while the nominal velocity is zero on all the components. The estimated perturbative acceleration is then:

$$\mathbf{a}_p = -\tilde{a}_l^h \mathbf{n} + \tilde{a}_{plume} \frac{\delta \tilde{\mathbf{r}}^h}{\delta \tilde{r}} + \frac{\mathbf{F}_{Solar}(\delta \tilde{\mathbf{r}}^h, \tilde{\mathbf{r}}_a^h) + \mathbf{F}_{recoil}(\delta \tilde{\mathbf{r}}^h, \tilde{\mathbf{r}}_a^h)}{m_{SC}} - \frac{\mu_a}{\delta r^3} \delta \tilde{\mathbf{r}}^h + \nabla U(\delta \tilde{\mathbf{r}}^h, \tilde{\mathbf{q}}) \quad (195)$$

### 5.5.3 Asteroid Rotational Motion Reconstruction

In order to control the rotational motion of the asteroid, it is necessary to estimate its instantaneous angular velocity. Moreover knowledge of the asteroid's angular velocity is required to compute an estimate  $\tilde{\mathbf{q}}_k$  of the asteroid attitude from the prediction step of the UKF. Tracking feature points on the asteroid's surface can be used to measure the asteroid's angular velocity.

By applying the time derivative to both sides of the pin-hole camera model in Eq.(139) (Longuet-Higgins et al., 1980), one can relate the optical flow with the angular and linear velocity of the asteroid:

$$\begin{bmatrix} \dot{u} \\ \dot{v} \end{bmatrix} = \frac{f}{x_c} \begin{bmatrix} \frac{dy_c}{dt} \\ \frac{dz_c}{dt} \end{bmatrix} - \frac{f}{x_c^2} \frac{dx_c}{dt} \begin{bmatrix} y_c \\ z_c \end{bmatrix} \quad (196)$$

with:

$$\begin{bmatrix} \frac{dx_c}{dt} \\ \frac{dy_c}{dt} \\ \frac{dz_c}{dt} \end{bmatrix} = -\boldsymbol{\omega}_{B/C} \times \mathbf{p}_c^a - \mathbf{V}_{B/C} \quad (197)$$

The vectors  $\mathbf{V}_{B/C}$  and  $\boldsymbol{\omega}_{B/C}$  are respectively the linear and angular velocities of the asteroid relative to the camera, assuming that the camera is static in the Hill's reference frame. The relative velocity vector is defined as:

$$\mathbf{V}_{B/C} = \mathbf{R}_{HC} \delta \dot{\mathbf{r}}^h \quad (198)$$

The vector  $\mathbf{p}_c^a = [x_c^a, y_c^a, z_c^a]^T$  gives the position of a point on the surface of the asteroid with respect to the centre of the Hill's reference frame, projected onto the reference frame of the camera:

$$\mathbf{p}_c^a = \mathbf{R}_{HC} \mathbf{x}_{surface} \quad (199)$$

For a single point on the surface of the asteroid Eq.(196) can now be written as:

$$\begin{bmatrix} \dot{u} \\ \dot{v} \end{bmatrix} = \mathbf{M}(f, \mathbf{r}_c, \mathbf{p}_c^a) \begin{bmatrix} \mathbf{V}_{B/C} \\ \boldsymbol{\omega}_{B/C} \end{bmatrix} \quad (200)$$

with:

$$\mathbf{M}(f, \mathbf{r}_c, \mathbf{p}_c^a) = \begin{bmatrix} \frac{u}{x_c} & -\frac{f}{x_c} & 0 & -v & -\frac{uv}{f} & \frac{u^2}{f} + f \frac{x_c^a}{x_c} \\ \frac{v}{x_c} & 0 & -\frac{f}{x_c} & u & -\frac{v^2}{f} - f \frac{x_c^a}{x_c} & \frac{uv}{f} \end{bmatrix} \quad (201)$$

The angular velocity can be obtained directly from Eq.(200) or by re-arranging the equation so that the angular velocity becomes a function of the linear velocity:

$$\begin{bmatrix} \dot{u} \\ \dot{v} \end{bmatrix} = \begin{bmatrix} \frac{u}{x_c} & -\frac{f}{x_c} & 0 \\ \frac{v}{x_c} & 0 & -\frac{f}{x_c} \end{bmatrix} \mathbf{V}_{B/C} + \begin{bmatrix} -v & -\frac{uv}{f} & \frac{u^2}{f} + f \frac{x_c^a}{x_c} \\ u & -\frac{v^2}{f} - f \frac{x_c^a}{x_c} & \frac{uv}{f} \end{bmatrix} \boldsymbol{\omega}_{B/C} = \mathbf{M}_{\tilde{\boldsymbol{\omega}}_{B/C}}(f, \mathbf{r}_c) \mathbf{V}_{B/C} + \mathbf{M}_{\tilde{\mathbf{V}}_{B/C}}(f, \mathbf{r}_c) \tilde{\mathbf{V}}_{B/C} \quad (202)$$

$\mathbf{M}_{\tilde{\boldsymbol{\omega}}_{B/C}}(f, \mathbf{r}_c)$  and  $\mathbf{M}_{\tilde{\mathbf{V}}_{B/C}}(f, \mathbf{r}_c)$  are the partitions of  $\mathbf{M}(f, \mathbf{r}_c)$  relatively to the angular and linear velocity of the asteroid. The algorithm requires knowing the relative position and relative attitude between the spacecraft and the asteroid to determine the relative position of each feature points. The relative position and velocity of the spacecraft with respect to the centre of mass of the asteroid can be extracted from the proximity motion reconstruction. It is here assumed that the centre of mass of the asteroid and the centre of the Hill's reference frame almost coincide except for an error  $\mathbf{x}_{CoM}^{bias}$ .

Furthermore, it is assumed that the attitude of the asteroid at time  $t_0$  and the position of each surface point with respect to the centre of mass are obtained from an observation campaign prior to the beginning of the ablation process. An estimation of the  $\mathbf{p}_c^a$  vector at any time during the ablation process can be obtained from:

$$\tilde{\mathbf{p}}_c^a = \begin{bmatrix} \tilde{x}_c^a & \tilde{y}_c^a & \tilde{z}_c^a \end{bmatrix} = \mathbf{R}_{SC-attitude} \mathbf{R}_{HC} \tilde{\mathbf{x}}_{surface} = \mathbf{R}_{SC-attitude} \mathbf{R}_{HC} \mathbf{R}(\tilde{\mathbf{q}}, \tilde{\mathbf{q}}_0) (\mathbf{x}_{surface}^0 + \mathbf{x}_{CoM}^{bias} + \boldsymbol{\varsigma}_{surface}) \quad (203)$$

where  $\mathbf{x}_{surface}^0$  is the actual position of a feature point at  $t_0$ ,  $\boldsymbol{\varsigma}_{surface}$  is an error which derives from the camera and LRF measurements required to build a three dimensional map of the asteroid,  $\mathbf{R}_{SC-attitude}$  is the attitude matrix of the spacecraft, which affects the pointing of the camera on two axes and  $\mathbf{R}(\tilde{\mathbf{q}}, \tilde{\mathbf{q}}_0)$  is the rotation matrix from the initial asteroid's attitude  $\tilde{\mathbf{q}}_0$  to the current attitude  $\tilde{\mathbf{q}}$ . The position of a feature point with respect to the camera then becomes:

$$\begin{aligned} \tilde{\mathbf{r}}_c &= \begin{bmatrix} \tilde{x}_c & \tilde{y}_c & \tilde{z}_c \end{bmatrix} = \mathbf{R}_{SC-attitude} \mathbf{R}_{HC} \mathbf{x}_{Surf-SC} = \mathbf{R}_{SC-attitude} \mathbf{R}_{HC} (\tilde{\mathbf{x}}_{surface} - \delta \tilde{\mathbf{r}}^h) = \\ &= \mathbf{R}_{SC-attitude} \mathbf{R}_{HC} \left( \mathbf{R}(\tilde{\mathbf{q}}, \tilde{\mathbf{q}}_0) (\mathbf{x}_{surface}^0 + \mathbf{x}_{CoM}^{bias} + \boldsymbol{\varsigma}_{surface}) - \delta \tilde{\mathbf{r}}^h \right) \end{aligned} \quad (204)$$

If one then introduces the pixelisation error, then the two matrices in Eq.(202) become:

$$\begin{aligned} \mathbf{M}_{\tilde{\boldsymbol{\omega}}_{B/C}}(f, \mathbf{r}_c) &= \begin{bmatrix} -\frac{(vp_{width} + \varsigma_p)}{p_{width}} & -\frac{(up_{width} + \varsigma_p)(vp_{width} + \varsigma_p)}{p_{width}^2 f} & \frac{(up_{width} + \varsigma_p)^2}{f} + f \frac{\tilde{x}_c^a}{\tilde{x}_c} \\ \frac{(up_{width} + \varsigma_p)}{p_{width}} & -\frac{(vp_{width} + \varsigma_p)^2}{p_{width}^2 f} - f \frac{\tilde{x}_c^a}{\tilde{x}_c} & \frac{(up_{width} + \varsigma_p)(vp_{width} + \varsigma_p)}{p_{width}^2 f} \end{bmatrix} \\ \mathbf{M}_{\tilde{\mathbf{v}}_{B/C}}(f, \mathbf{r}_c) &= \begin{bmatrix} \frac{(up_{width} + \varsigma_p)}{p_{width} \tilde{x}_c} & -\frac{f}{\tilde{x}_c} & 0 \\ \frac{(vp_{width} + \varsigma_p)}{p_{width} \tilde{x}_c} & 0 & -\frac{f}{\tilde{x}_c} \end{bmatrix} \end{aligned} \quad (205)$$

and  $\dot{u}$  and  $\dot{v}$  are approximated with  $\Delta \mathbf{u} / \Delta t$  at two consecutive instants of time  $k-1$  and  $k$ . The flow field then becomes:

$$\begin{bmatrix} \dot{u} \\ \dot{v} \end{bmatrix} = \begin{bmatrix} (u^k p_{width} + \zeta_p^k) - (u^{k-1} p_{width} + \zeta_p^{k-1}) \\ (v^k p_{width} + \zeta_p^k) - (v^{k-1} p_{width} + \zeta_p^{k-1}) \end{bmatrix} / (p_{width} \Delta t) \quad (206)$$

Introducing Eqs.(203), (204), (205) and (206) into Eq.(202) and solving for the angular velocity give:

$$\begin{aligned} \tilde{\boldsymbol{\omega}}_{B/C} &= \begin{bmatrix} -v & -\frac{uv}{f} & \frac{u^2}{f} + f \frac{\tilde{x}_c^a}{\tilde{x}_c} \\ u & -\frac{v^2}{f} - f \frac{\tilde{x}_c^a}{\tilde{x}_c} & \frac{uv}{f} \end{bmatrix} \begin{bmatrix} \left[ \begin{matrix} \dot{u} \\ \dot{v} \end{matrix} \right] - \begin{bmatrix} \frac{u}{\tilde{x}_c} & -\frac{f}{\tilde{x}_c} & 0 \\ \frac{v}{\tilde{x}_c} & 0 & -\frac{f}{\tilde{x}_c} \end{bmatrix} \tilde{\mathbf{V}}_{B/C} \end{bmatrix} \\ &= \mathbf{M}_{\tilde{\boldsymbol{\omega}}_{B/C}}^\diamond (f, \mathbf{r}_c) \left( \begin{bmatrix} \dot{u} \\ \dot{v} \end{bmatrix} - \mathbf{M}_{\tilde{\mathbf{V}}_{B/C}} (f, \mathbf{r}_c) \tilde{\mathbf{V}}_{B/C} \right) \end{aligned} \quad (207)$$

Finally, the estimated angular velocity  $\tilde{\boldsymbol{\omega}}_k$  to be used in Eq.(173) is obtained by rotating  $\tilde{\boldsymbol{\omega}}_k = \mathbf{R}(\tilde{\mathbf{q}}_k) \tilde{\boldsymbol{\omega}}_{B/C}$  from the camera frame to the asteroid frame. Including other points' measurements, to give additional information and filter the error,  $\boldsymbol{\omega}_{B/C}$  can be estimated using the batch least squares method:

$$\boldsymbol{\omega}_{B/C} = \begin{bmatrix} \mathbf{M}_{\boldsymbol{\omega}_{B/C}} (f, \mathbf{r}_{c,1}, \mathbf{p}_{c,1}^a) \\ \vdots \\ \mathbf{M}_{\boldsymbol{\omega}_{B/C}} (f, \mathbf{r}_{c,N}, \mathbf{p}_{c,N}^a) \end{bmatrix}^\diamond \begin{bmatrix} \dot{u}_1 \\ \dot{v}_1 \\ \vdots \\ \dot{u}_N \\ \dot{v}_N \end{bmatrix} - \begin{bmatrix} \mathbf{M}_{\mathbf{V}_{B/C}} (f, \mathbf{r}_{c,1}, \mathbf{p}_{c,1}^a) \\ \vdots \\ \mathbf{M}_{\mathbf{V}_{B/C}} (f, \mathbf{r}_{c,N}, \mathbf{p}_{c,N}^a) \end{bmatrix}^+ \mathbf{V}_{B/C} \quad (208)$$

where the + sign stands for pseudo-inverse, and all the points give equal contribution to the solution (i.e. the weight associated to their corresponding information is equal to 1). The algorithm

allows extracting velocity and attitude rates from at least three tracked feature points from two consecutive frames.

As an example, Figure 58 reports the error on the estimation of the angular velocity during 14 days operations time. A total of 10 features were considered at each time. The pixelization error  $\zeta_p$  is equal to the dimension of the pixel (78.5  $\mu\text{m}$  according to Table 24). The asteroid surface is known with an accuracy  $\zeta_{\text{surface}}$  of 15 cm (3- $\sigma$ ) and the bias  $\mathbf{x}_{\text{CoM}}^{\text{bias}}$  on the position of the barycentre is 20 cm (3- $\sigma$ ), which is equal to about 10% of the mean radius. The position and velocity of the spacecraft,  $\delta\tilde{\mathbf{r}}^h$  and  $\delta\tilde{\mathbf{v}}^h$ , are estimated with an accuracy of 20 cm and 0.1 mm/s (3- $\sigma$ ) respectively. An attitude determination error on 2 axes of  $10^{-3}$  degrees is also considered. The figure shows that with the assumed measurement errors, the system is able to determine the angular rate as precise as few milliradians per second.

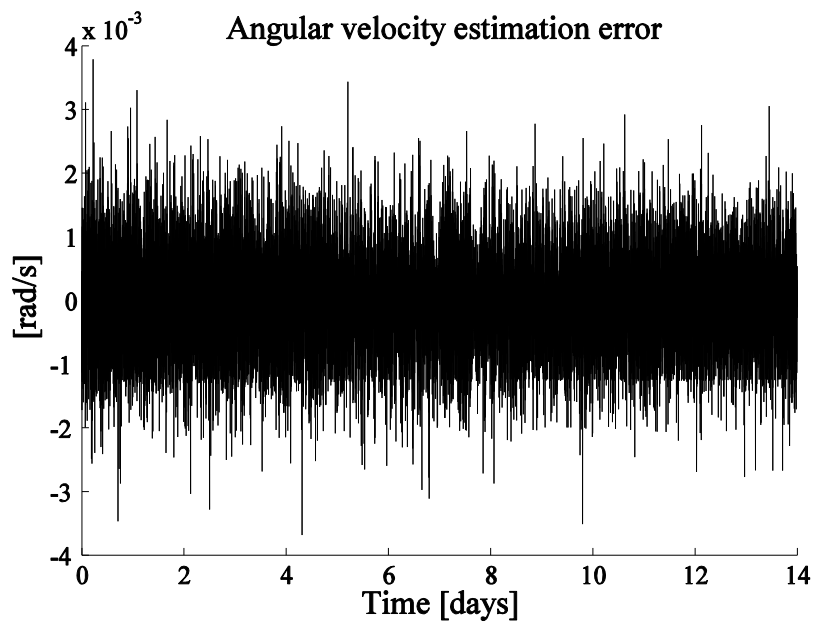


**Figure 58. Angular velocity estimation error.**

For sake of comparison if one derived the angular velocity from Eq.(200) instead of Eq.(207) the accuracy would be lower, as shown in Figure 59. In the case of Eq.(200), the error is higher with respect to the case of Eq.(207) because the optical flow method is not able to extract the linear velocity as accurately as the one obtained from the Kalman filter.

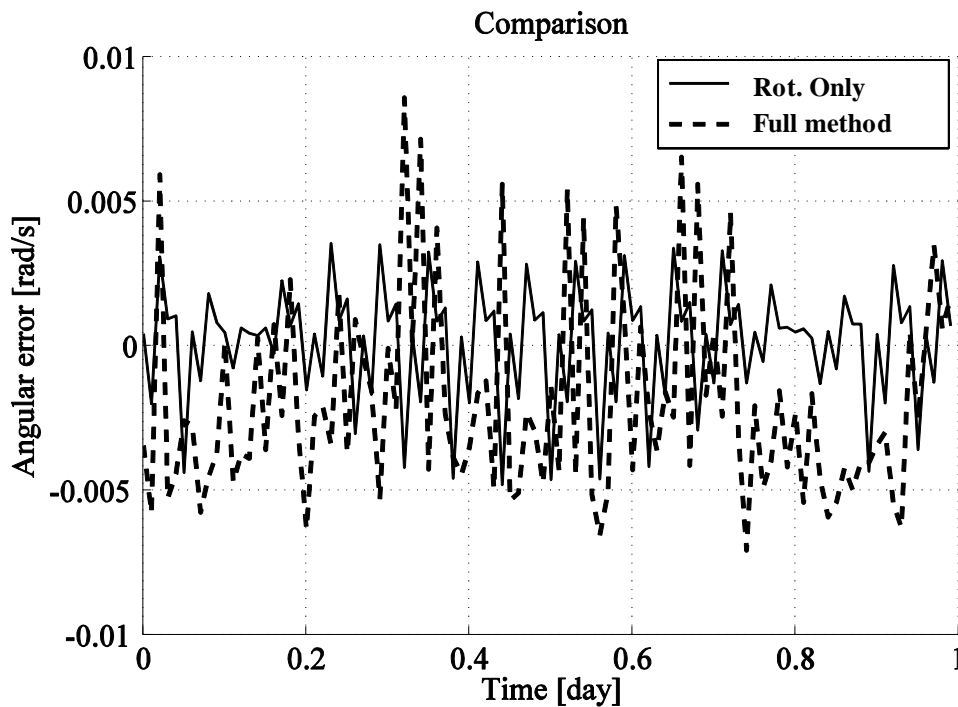


**Figure 59. Comparison between different methods of optical flow.**

## 5.6 Results

The selected candidate for the deflection mission is here assumed to be the Near Earth Object 2006 RH120 whose characteristics are listed in Table 22. The criteria for the candidate selection are explained in Vasile et al. (2013). Asteroid 2006 RH120 is a small rocky asteroid with an estimated mass of 130 tonnes.



**Table 22. Orbital elements of 2006 RH120 at Epoch MJD2000 2456200.5 (12 September 2012) (<http://ssd.jpl.nasa.gov/sbdb.cgi?sstr=2006%20RH120>).**

Orbital Element	Value
$a$	1.033252056035198 AU
$E$	0.02447403062284801
$q$	1.007964213574672 AU
$i$	0.5952660003048117 deg
$node$	51.14334927580387 deg
$M$	221.2498016727181 deg
$t_p$	2456348.356001016605 JD
period	383.6258326667335 days
$n$	0.9384143854377558 deg/d
$Q$	1.058539898495724 AU

It is assumed here that the ablation process starts when the asteroid is at perihelion. The initial angular velocity is  $\boldsymbol{\omega}_{B/C} = [0.0052, 0.0052, 0.0332]^T$  rad/s. As before, the asteroid is assumed to be an ellipsoid with  $a_l = 3$  m,  $b_l = 2.3$  m and  $c_l = 1.5$  m, and its principal axes of inertia are aligned with the Hill's frame axes at the beginning of operations.

Table 23 reports the spacecraft characteristics considered for the simulations. The spacecraft is assumed to be a cube with two symmetric deployable solar panels. The solar arrays are assumed to point towards the Sun for the whole simulation. In this way the cross section  $A_{eq}$  results to be less than 1/5 of the area  $A_M$  subjected to the solar radiation pressure. The initial state vector of the spacecraft is  $\mathbf{x}_0 = [0.1m \quad -50.1m \quad 0.1m \quad 10^{-4}m/s \quad 10^{-4}m/s \quad 10^{-4}m/s]^T$ .

In addition to the example presented in this section, the algorithm was run for different initial angular velocities and configurations. In particular it was tested on three worst case scenarios in which the largest component of  $\boldsymbol{\omega}$  was directed along one of the principal axis of inertia with

different spacecraft-asteroid relative configurations, and the matrix of inertia was dense with extra-diagonal terms with a magnitude up to 30% of the minimum inertia value.

**Table 23. Spacecraft characteristics.**

Element	Value
Mass	500 kg
$C_R$	0.18
$A_M$	8.4 m <sup>2</sup>
$A_{eq}$	1.6 m <sup>2</sup>

The camera is assumed to have a 30 degrees field of view, 2048 pixels resolution, and a 30 cm focal length. The focal length and resolution are such that at 50 m distance an object of approximately 4 m diameter occupies about 10 degrees of the field of view. In this way, it is assured that the asteroid remains completely within the camera's field of view during ablation.

Table 24 reports the magnitude of the errors considered during the simulation and estimation process.

**Table 24. Errors in the measurements model.**

Error	Value
$\zeta_p$	78.5 $\mu$ m
$\zeta_l$	10 cm (1 $\sigma$ )
$\zeta_{camera}$	2.6·10 <sup>-3</sup> deg/s (1 $\sigma$ )
$\zeta_{plume}$	5% measured value (1 $\sigma$ )
S/C Attitude determination	10 <sup>-3</sup> deg/s on two axes (1 $\sigma$ )
$\mathbf{x}_{CoM}^{bias}$	20 cm (3 $\sigma$ )
$\zeta_{surface}$	15 cm (3 $\sigma$ )

The accuracy of the LRF  $\zeta_l$  is consistent with the current state of the art for this kind of technology (Hashimoto et al., 2003). A 5% random variation in the measured mass flow rate was added to take

into account a possible fluctuation in the yield of the ablation process. The attitude determination error on 2 axes corresponds to the accuracy of a star-tracker (Yim et al., 2000).

### 5.6.1 Spacecraft Proximity Control

Figure 60 shows the error in the filter estimates for both position and velocity. It is assumed that the spacecraft starts ablating with an initial state estimation  $\tilde{\mathbf{x}}_0 = [0.2m \quad -50.2m \quad 0.2m \quad 2 \cdot 10^{-4}m/s \quad 2 \cdot 10^{-4}m/s \quad 2 \cdot 10^{-4}m/s]^T$ . From Figure 60a), the estimate is as precise as 20 cm in position, while in Figure 60b) the velocity error is less than 0.1 mm/s. The higher error is along the y-component, which is almost coincident with the pointing direction of the LRF.

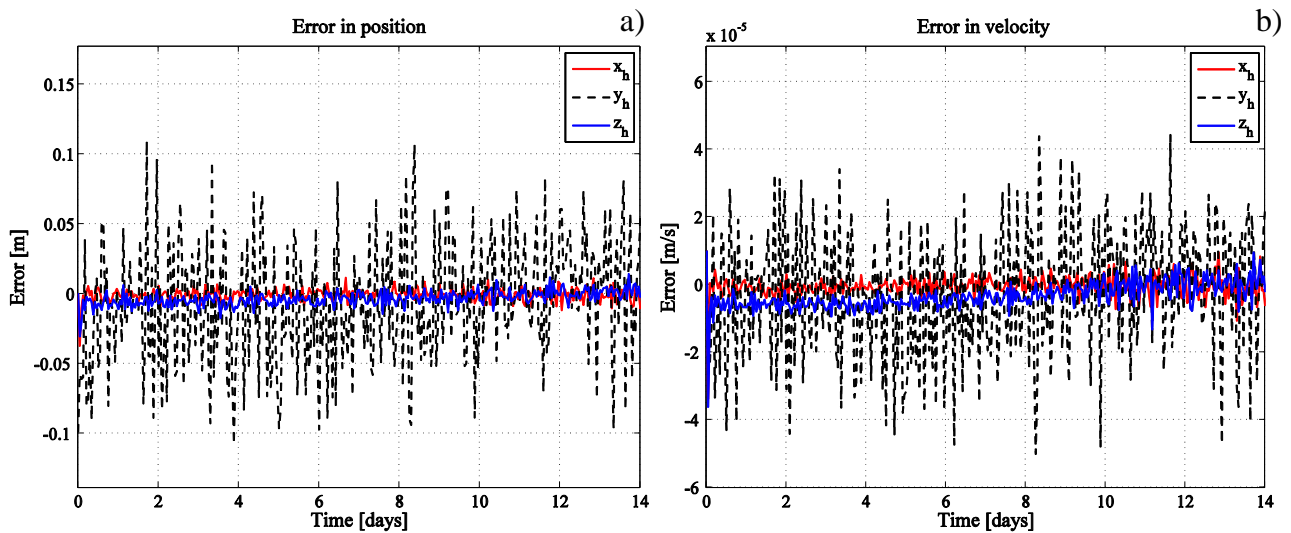


**Figure 60. Spacecraft Control: estimated position (a) and velocity error (b).**

Conversely, when one considers the actual error with respect to the desired position (i.e. spacecraft placed with zero velocity at 50 m along track), the discrete control sometimes fails to maintain the spacecraft within 0.4 m as shown in Figure 61a). For clarity we report also the norm of the

controlled position error. The maximum error in velocity in b is around 1 mm/s which is obtained at the boundaries of the control box.

The change in sign of the velocity components is due to the actuation. Figure 61b) shows that the main perturbations are confined in the x-y plane of the Hill's frame. This is consistent with the fact that the solar radiation pressure is directed along x-axis and that the force has to be contained in the x-y plane in order to apply a control torque mainly directed as z-axis.

Nonetheless, the peaks outside the control boundaries are not detrimental to the overall process itself because their frequency and the magnitude are low, also considering the actual point the laser impinges. In fact Figure 62 reports the actual defocusing due to spacecraft and asteroid rotation control, which results contained within the Rayleigh length of 3 m.

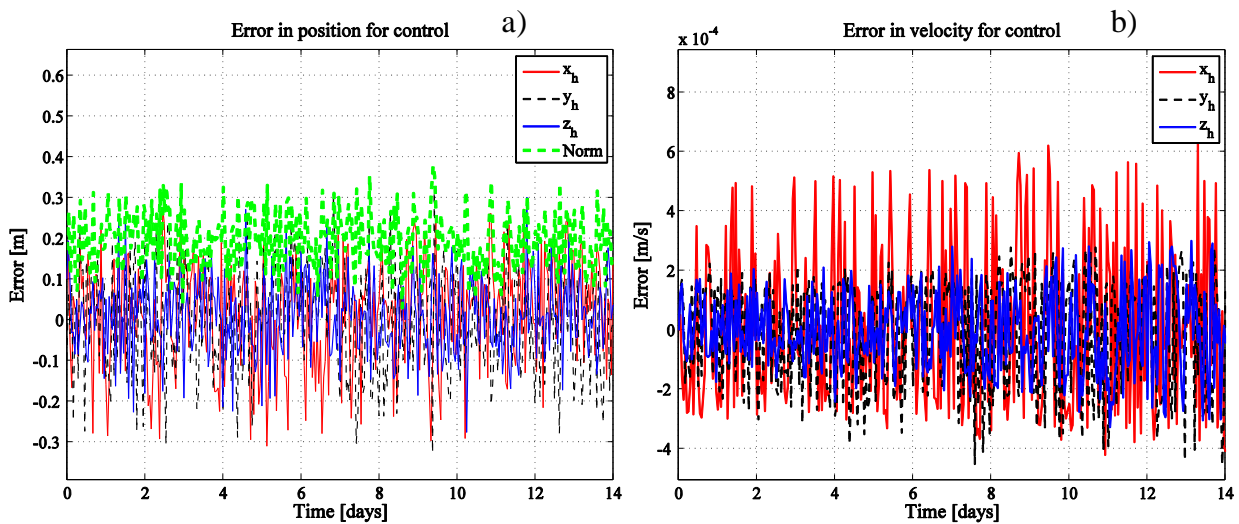


**Figure 61. Discrete Control: actual controlled position (a) and velocity error (b).**

Note that the combination of the visibility, rotation of the asteroid and constraint on the angle between the laser and the normal vector directions lead to impinge mainly on surface spots closer to the spacecraft (i.e. below the focussing length).

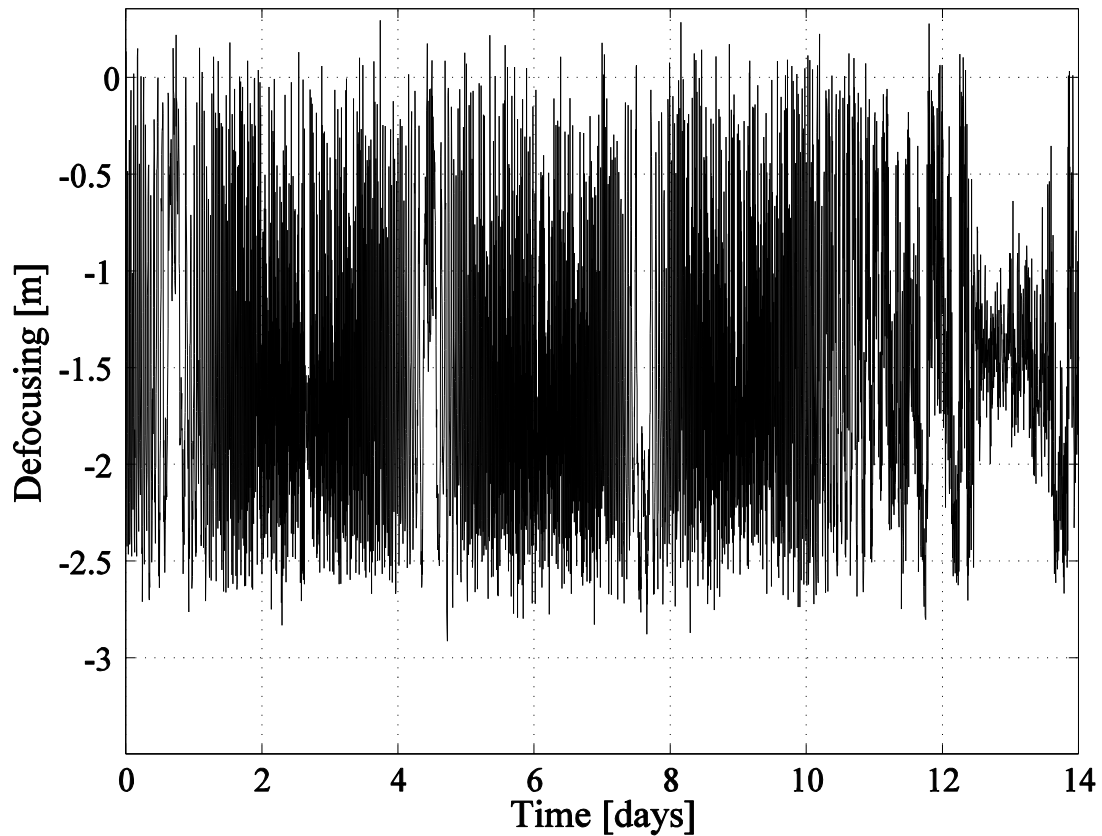


**Figure 62. Discrete Control: actual defocusing due to spacecraft and asteroid rotation control.**

### 5.6.2 Estimated Perturbations during Proximity Operations

Estimating the perturbations acting on the spacecraft in real time is required to implement the control strategy defined in Section 5.2. Figure 63 shows the trend of the estimated perturbations due to laser ablation with respect to the actual values.

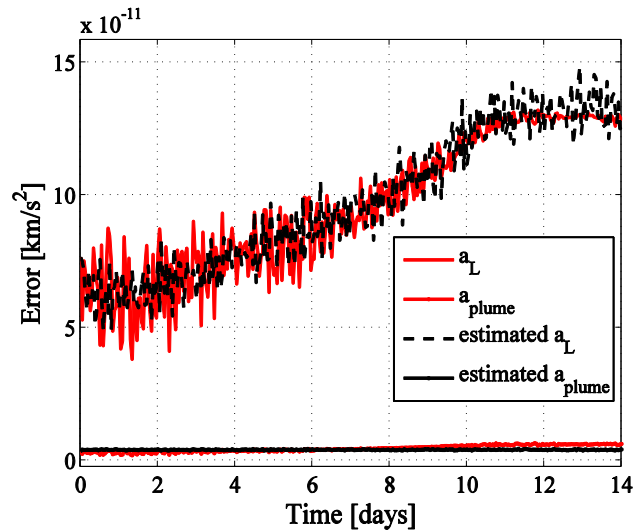


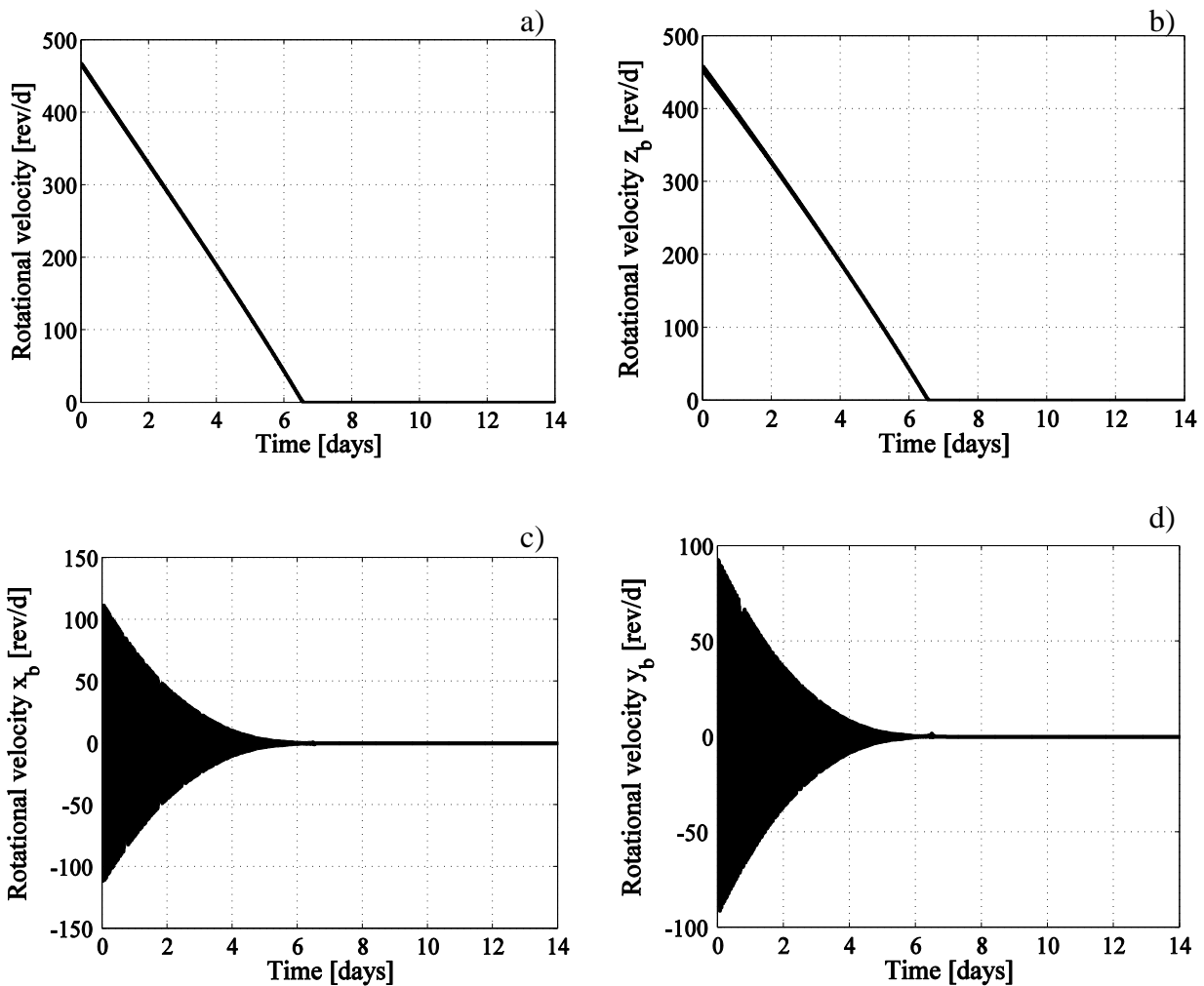
**Figure 63. Estimated acceleration from the laser and plume force vs. the actual acceleration.**

The perturbative force due to the ablative process increases with time as one can see from the figure. This is due to the fact that the angular velocity diminishes and the efficiency of the ablative process increases. After about 12 days it converges to a nearly constant value, which corresponds to a rotational velocity of about  $10^{-3}$  rad/s. When the asteroid reaches this rotational velocity the rotational control is terminated. The figure shows that there is a good agreement between the actual and the estimated perturbative accelerations, although the level of measurements noise affects the steady state estimate.

### 5.6.3 Asteroid Rotational Velocity Control

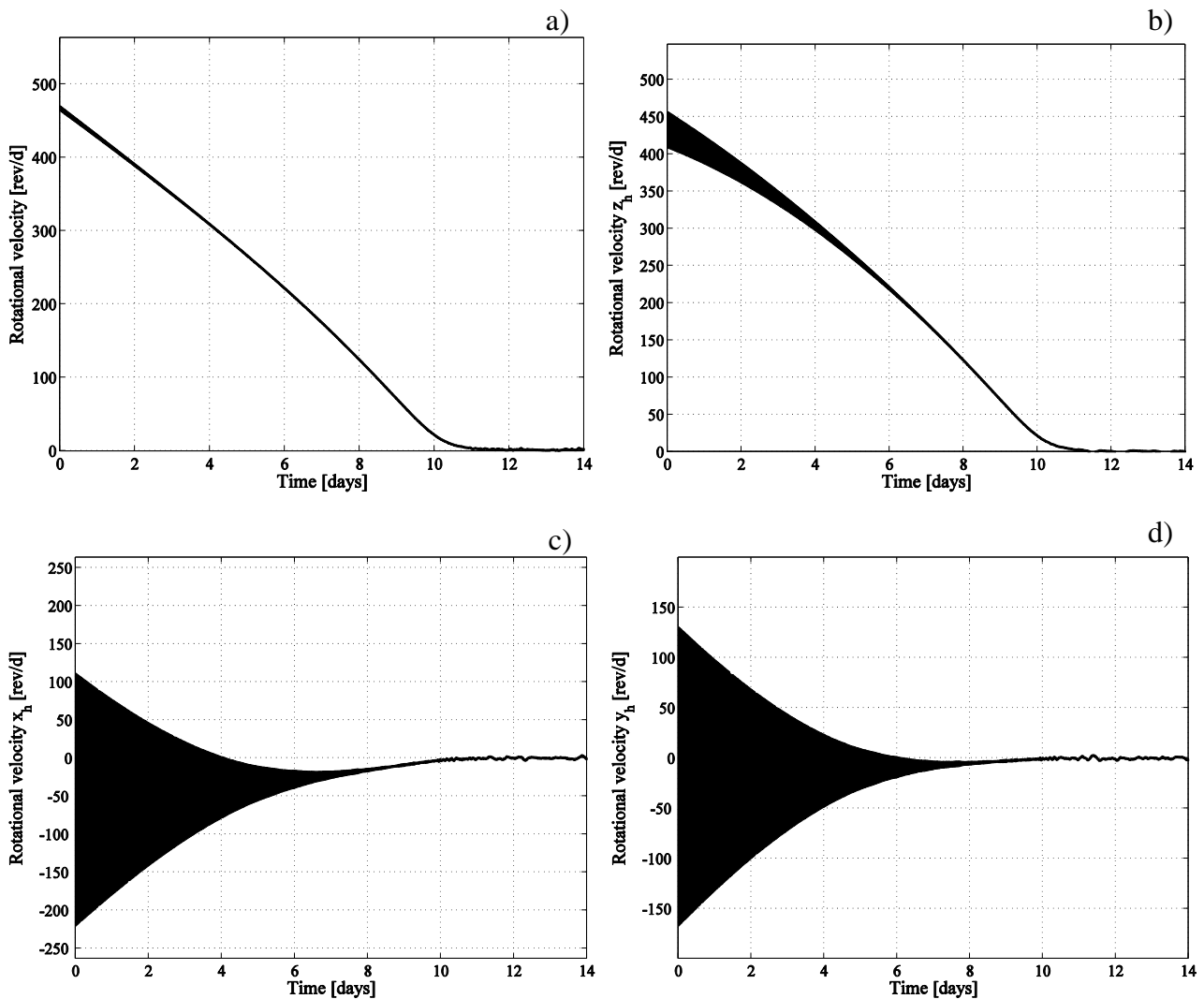
In the absence of any perturbation acting on the spacecraft, the implemented rotation control strategy would produce an effective reduction of the asteroid angular velocity in about 6.2 days as shown in Figure 64, where the components of the angular velocity in the body fixed frame are represented. As one can see the control torque acts efficiently along the three directions. The angular velocity, as well as the third component, decreases almost monotonically as shown in

Figure 64a,b). The other two components converge towards the zero velocity condition with progressively decreasing oscillations (Figure 64c,d)). When the spacecraft proximity control and all the perturbation effects, as well as the angle between the laser beam and the normal to surface, are included in the model, a similar trend in a different time is obtained as shown in Figure 65.



**Figure 64. Asteroid rotation control with spacecraft fixed at 50 m. a) Absolute magnitude and b) z, c) x and d) y axes of the body fixed frame.**

Also in this case the components of the angular velocity refer to the body fixed frame. The inertia matrix of the asteroid is almost diagonal with the extra-diagonal terms equal to 1/100 of the maximum inertia.



**Figure 65. Rotational velocity of the asteroid considering the actual incidence of the laser. a) Absolute magnitude and b) z, c) x and d) y axes of the body fixed frame.**

Also in this case, Figure 65a) and c) show a similar trend for the angular velocity and the  $z_b$  component with oscillations in the final part of the simulations. The time required to almost halt the



asteroid rotation is about 12 days. It takes about 5 days more than the case where the spacecraft is fictitiously maintained fixed at 50 m from the asteroid and the laser beam cross section varies only because of the rotation of the asteroid. From Figure 65c) and d) one can see that the other two components converge towards zero as the previous case after 12 days, then all the components present oscillations. These are due to the fact that the main component of the angular velocity moves continuously among the components. The oscillations in the position of the spacecraft, as shown in Section 5.6.1, cause also the laser beam to periodically defocus. Moreover, the whole control procedure is affected by the accuracy level provided by the optical flow method and the estimated position of the spacecraft with errors in the exerted control torque.

Regarding the other tests mentioned in Section 5.6, we found that the worst case was the one with all the angular velocity directed along the tangential direction and coincident with the maximum axis of inertia (at initial time), which we show in Figure 66. It required about 28 days converging to  $10^{-3}$  rad/s. The reason for the extended duration is of course due to the relative spacecraft-asteroid configuration where the laser can be pointed where the control arms are less effective. To speed up the deceleration the spacecraft will be required to hover at fixed position in an out of plane configuration. In this way the control time will go down to about 12 days as in the case we are analysing. So once the rotation is almost halt the spacecraft can be position along the tangential direction to maximise the deflection.

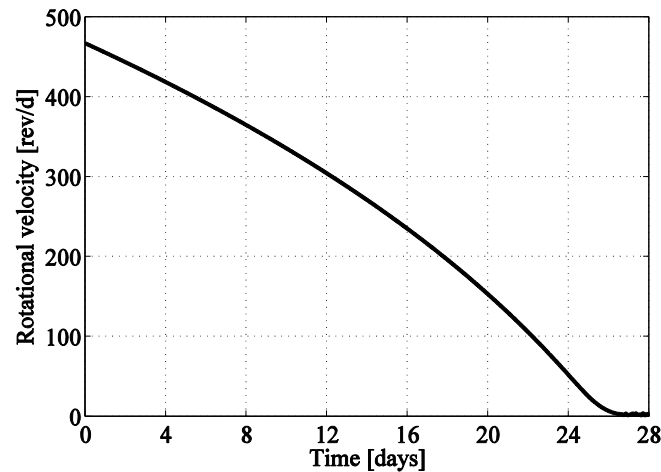


**Figure 66. Rotational velocity of the asteroid with angular velocity directed as the orbit tangent and aligned to the maximum axis of inertia. Spacecraft is also placed along the tangent.**

#### 5.6.4 Effect of the Asteroid's Rotation on its Deflection

The sublimation thrust in Eq.(156) induces a slow and constant variation of the orbit of the asteroid. As explained in Section 5.4, the asteroid angular velocity control is performed until the angular velocity reaches a value of  $10^{-3}$  rad/s. It is assumed that the deflection action on the asteroid starts at asteroid's perihelion and the rotation control is active for up to 14 days, as shown in Section 5.6.3. It is assumed that, once the desired rotational velocity is reached at time  $t_i$ , the laser beam is pointed in such a way that the resulting thrust vector goes through the centre of mass of the asteroid. In reality a misalignment of the thrust is expected but can be easily corrected by monitoring the rate of change of  $\omega$  so that the average thrust vector is as desired. From Figure 67a) it can be seen that the thrusting time to achieve a target  $\delta v_i$  of 1 m/s can be decreased from 220 days up to 110 days with only 7 days of control of the rotation of the asteroid.

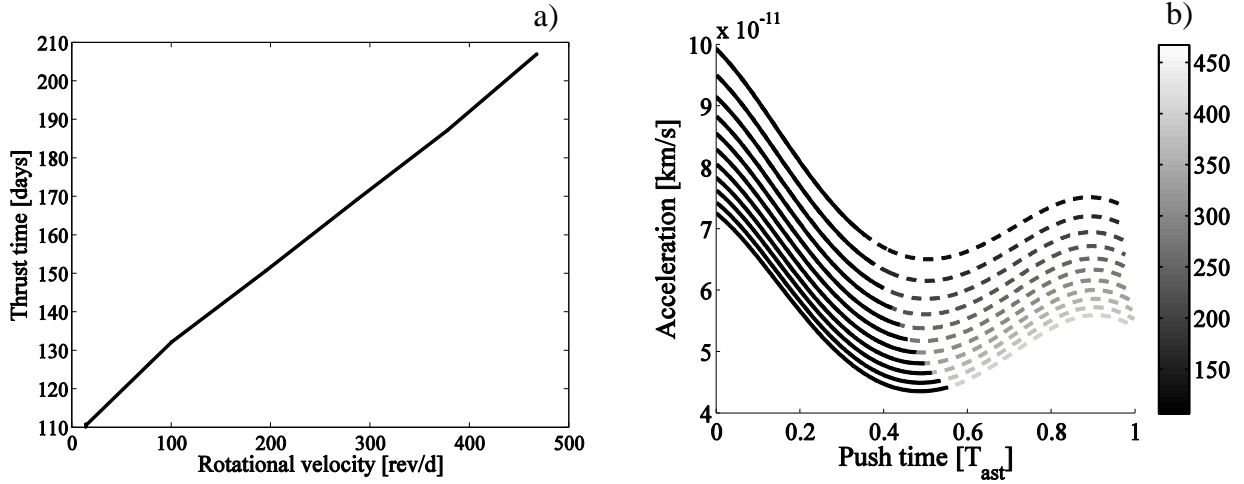


**Figure 67. a) Thrust time to achieve the target delta-velocity change as function of the initial rotational velocity of the asteroid. b) Actual acceleration onto the asteroid as function of time with different initial rotational velocities of the asteroid (colour bar). The black portion of the lines represents the time needed to achieve the target change in velocity of 1 m/s.**

While the target delta-velocity is independent of the direction of thrust, the effect on the displacement from its nominal position at a given point along the orbit (called check-point in the following) depends on the direction of the thrust. Let  $a$ ,  $e$ ,  $i$ ,  $\Omega$ ,  $\omega_p$  and  $M$  be respectively the semi-major axis, eccentricity, inclination, anomaly of the ascending node, anomaly of the pericentre and mean anomaly of the nominal orbit of the asteroid. The effect of the deflection is calculated at predefined check-points. Let  $t_{check}$  be the instant of time corresponding to a generic check point. If  $\theta_{check}$  is the true anomaly of the asteroid, and  $\theta_{check}^* = \theta_{check} + \omega$  the corresponding argument of latitude, one can write the variation of the position of the asteroid after deviation, with respect to its unperturbed position, by using the proximal motion equations as in (Vasile and Colombo, 2008) and (Colombo et al., 2009):

$$\delta \mathbf{r}_a(t_{check}) = \mathbf{A}_{check} \delta \mathbf{a}_p(t_{check}) \quad (209)$$

where  $\delta \mathbf{r}_a = [\delta x_{h-a} \quad \delta y_{h-a} \quad \delta z_{h-a}]^T$  with  $\delta x_{h-a}$ ,  $\delta y_{h-a}$  and  $\delta z_{h-a}$  the displacements in the radial, transversal and out-of-plane directions in the Hill's reference frame centred at the unperturbed position of the asteroid at the check point (see Figure 68). The vector  $\delta \boldsymbol{\alpha}_p(t_{\text{check}}) = [\delta a \quad \delta e \quad \delta i \quad \delta \Omega \quad \delta \omega_p \quad \delta M]^T$  is the variation of the orbital parameters at the check-point and the matrix  $\mathbf{A}_{\text{check}}$  transforms the variation of the orbital parameters in trajectory displacements.

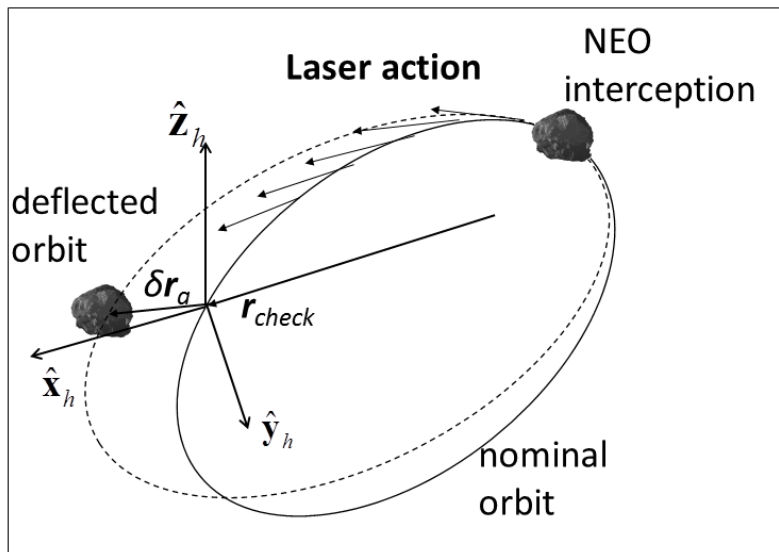


**Figure 68. Asteroid's proximal motion.**

The assumption used to compute Eq.(209) is that the variation of the relative position  $\delta r_a = \|\delta \mathbf{r}_a\|$  is small compared to the unperturbed orbit radius  $r_{\text{check}}$ , that is  $\delta r_a \ll r_{\text{check}}$ .

When a low-thrust deviation action such as the one in Eq.(156) is applied over the interval  $[t_i \quad t_e]$ , where  $t_e \leq t_{\text{check}}$  is the time when the manoeuvre ends, the total variation of the orbital parameters

$\delta \mathbf{a}_p(t_{check})$  can be computed by integrating Gauss' planetary equations over the thrusting arc. Note that the derivative of  $M$  in Gauss' planetary equations

$$\frac{dM}{dt} = n - \frac{b}{eav} \left[ 2 \left( 1 + \frac{e^2 r_a}{p} \right) \sin \theta a_t + \frac{r_a}{a} \cos \theta a_n \right]$$

takes into account the instantaneous change of the orbit geometry at each instant of time  $t \in [t_i \ t_e]$  and the variation of the mean motion  $n$  due to the change in the semi-major axis along the thrust arc. The total variation  $\delta M$  in the mean anomaly between the proximal and the unperturbed orbit was found to be (Colombo et al., 2009):

$$\delta M = \tilde{M}_{check} - M_{check} = (n_e - n_i) t_{check} + n_i t_i - n_e t_e + \Delta M \quad (210)$$

where  $n_i$  is the nominal angular velocity,

$$n_e = \sqrt{\frac{\mu_{Sun}}{(a + \Delta a)^3}}$$

is the varied angular velocity and  $\Delta M = - \int_{t_i}^{t_e} \frac{b}{eav} \left[ 2 \left( 1 + \frac{e^2 r_a}{p} \right) \sin \theta a_t + \frac{r_a}{a} \cos \theta a_n \right] dt$ .

From Eq.(209) one can compute the effect of the deflection action at the check-points  $t_{check} = t_e$ . The deflection depends on the direction of the thrust (see Vasile and Colombo, 2008) as visible in Figure 69. The figure represents the deviation in Eq.(209) achieved in the thrusting time  $[t_i \ t_e]$  as a function of the initial rotational velocity of the asteroid at time  $t_i$ . The figure reports also the ideal cases in which the thrust is applied along the tangent (black continuous line), normal (dash-dotted

line) and out-of-plane (dotted line) direction. The bold black line corresponds to the deviation achieved with the actual mean thrust vector. As expected, the deflection is contained between the two extremes of pure tangential and pure out-of-plane deflections.

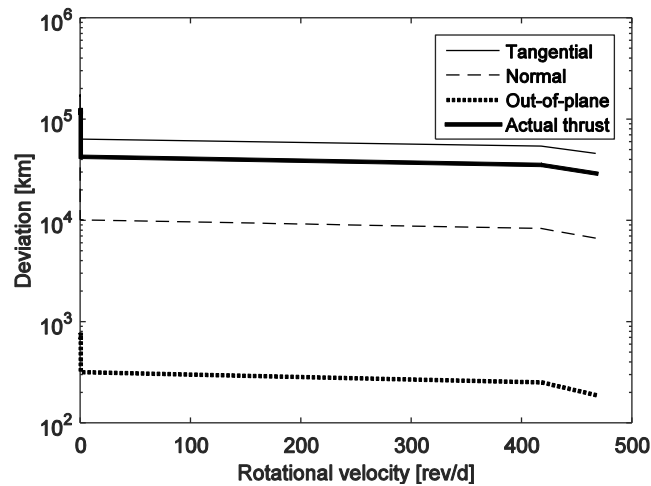


**Figure 69. Deviation of the asteroid at the check point as function of the initial rotational velocity of the asteroid.**

The reason why the bold black line does not decrease monotonically with the number of revolutions is that the mean thrust direction depends on the angular velocity of the asteroid at the end of the rotational control phase. Since the control only reduces the angular rate but does not control the direction of the angular velocity the resulting direction of the thrust is not purely tangential but can have components along all the three directions.

## 5.7 Summary

This Chapter has dealt with the problem of simultaneous spacecraft navigation and asteroid's orbit and attitude control using a laser ablation system for the problem of asteroid's threat mitigation. In order to keep the efficiency of the deflective action at the highest, we have presented a strategy to

reduce the asteroid's rotational velocity, while maintaining the optimal focussing of the laser. For this reason a precise guidance, navigation and control system has been implemented to control the position of the spacecraft within a limit sphere at a given distance from the asteroid.

The navigation problem is tackled by considering the use of on-board instruments and combining a UKF with an optic flow filter to estimate of the asteroid's rotational rate, spacecraft trajectory and the ablative force. Camera and ranging instruments are used to estimate the spacecraft relative motion, while additional information from an impact sensor is used to separate the plume impingement contribution from the actual acceleration due to the laser ablation. In this way, it is possible to accurately estimate the deflection action on the asteroid without relying on any interaction model between the laser and the asteroid. We have showed that laser ablation can be employed to reduce the angular velocity of the asteroid by pointing the laser off-barycentre.

In the considered example it is shown that, if an initial map of the asteroid and estimation of its attitude and centre of mass are available, it is possible to decrease the asteroid's angular velocity in less than two weeks of operations with a moderate size laser. It is also demonstrated that the control of the rotation can significantly improve the deflection action for the same power at the laser.

The methodology developed in this Chapter can be extended to de-orbiting space debris around the Earth. In fact, also in that case there will be an uncooperative target (the debris) possibly tumbling, chased by the laser carrying spacecraft which will have to point the laser beam onto suitable points of the surface. By knowing the geometry of the debris, the concept of control arm can be exploited to control the rotational velocity of the debris while assuring that the overall effect will drive the debris to re-enter the atmosphere.

## 6 Conclusions

The main contributions of this thesis is the identification and the development of methodologies for uncertainty propagation for spacecraft orbit and the application to orbit determination, particularly to asteroid's close proximity operations.

In this Chapter we will provide an overview of the work done. The main results of this thesis are summarised and commented. On the base of the findings of this study, an outline of future works and some recommendations are given.

### 6.1 Summary and Conclusions

In order to perform uncertainty analysis and state estimation suitable for complex nonlinear problem for spaceflight, we first analysed which techniques can be suitable for uncertainty propagation in the orbital dynamics for the practical and nonlinear problem of end-of-life disposal in the perturbed Sun-Earth-Moon four-body problem. In general if one wants to achieve higher accuracy in the propagation of the mean and covariance matrix, more computational power is needed and this will not be cost effective compared to a full MC. The higher order Taylor expansions could be a solution because the STTs can be calculated once and then used with simple algebraic formulas. Nonetheless if the spacecraft is not close to the nominal trajectory with a small deviation, the STTs have to include high terms and the integration time will be more demanding than a full MC. The PCE is an interesting tool to study the propagation of the initial dispersion around the nominal trajectory and draw statistical information. We saw that the use of Genz-Keister sparse grid permits to decrease the number of samples, obtaining results which are very



close to the Monte Carlo simulations but at lower computational cost. The accuracy in the model is such that not only the statistical parameters (mean, covariance and impact probability) were very precise but also the overall reconstructed distributions were described precisely.

Then we used these techniques to evaluate the propagation of the mean and covariance matrix within the estimation process. This propagation step is in fact fundamental to obtain an accurate estimate of the uncertain trajectory. We investigated two main families of filters, i.e. Kalman filters and the  $H_\infty$  filters also called minmax filters. Having a common structure the comparison is straightforward. The measurements are included via a suitable gain to obtain a state estimate update. The analysis of the Sun-Earth-Moon four-body problem and the Sun-asteroid three-body problem provided the test cases to identify the right balance between precision and computational cost.

The unscented H-infinity filter showed the best compromise thanks to the hybrid characteristics between the Kalman and the H-infinity filter, and the use of a tuning parameter with the UT providing a satisfactory propagation of mean and the covariance. But also the more classical UKF, EKF and EHF provided good results with low CPU burden. Particle filters such as the UPF and EnKF based on polynomial chaos expansions are very accurate as well but they are very demanding for the required computational time.

Although in general not very much attractive when the nonlinear effects are strong, we saw that the propagation step via STTs offers a precious tool to include the effects of uncertainty in designing suitable correction manoeuvres which statistically drive the trajectory onto the nominal one. Such an approach represents a valid alternative to the classical design based on Monte Carlo simulations.

Having identified a suitable filter technique we applied it to the case of a formation flying around asteroid 99942 Apophis. We saw that by complementing the spacecraft to asteroid information from camera and ranging instrument with inter-spacecraft measurements the system can achieve better estimations and higher accuracy in trajectory control. In particular the navigation accuracy is improved by sharing the information within the members of the formation. Moreover the system proved to be failure tolerant when several instruments fail or provide very poor information.

Exploiting the optical information from the formation, the possibility to refine the asteroid's trajectory estimate prior to starting the orbit acquisition was also considered. It was shown for different approach configurations that the combined use of on-board and ground station measurements can enhance the asteroid's orbit estimate during the approach phases. There is a significant improvement in the estimated position accuracy, about 3 orders of the magnitude while the velocity is as precise as 1 cm/s. A better knowledge of the asteroid's orbit can be used for planning correction manoeuvres, thus approaching the asteroid could be accomplished with less propellant consumption. Besides, this technique can also be used to refine the trajectories of other potentially hazardous asteroids which the spacecraft formation might encounter during deep space navigation phases.

Finally we investigated an approach to control the rotational motion of a small asteroid for a scientific demonstrator, while the spacecraft deflects the asteroid's trajectory through laser ablation. This task required the simultaneous control of both the spacecraft relative position and asteroid's angular velocity. Analytic formulas for rotational control were developed in order to maximise the control torque along the instantaneous angular velocity. For this purpose the spacecraft proximity motion and the instantaneous rotational velocity of the asteroid were estimated through a camera

and ranging instruments. A precise guidance, navigation and control system was implemented to control the position of the spacecraft within a limit sphere at a given distance from the asteroid. Eventually we estimated the perturbations due the laser ablation using a procedure employed for biases, by including the additional information coming from an impact sensor without relying on ablation model (except for the asteroid geometry). It was shown that laser ablation can be employed to reduce the angular velocity of the asteroid by pointing the laser off-barycentre. If an initial map of the asteroid and estimation of its attitude and centre of mass are available, it is possible to decrease the asteroid's spin rate in few days of operations with a moderate size laser. The control of the rotation can significantly improve the deflection action for the same total mass into space.

### **6.1.1 Key Contributions**

The key contributions presented with this thesis can be summarized as follows:

- It is for the first time considered the use of Polynomial Chaos Expansions to study a spacecraft trajectory evolution under uncertain initial conditions for the case of disposal strategy. Compared to a full MC simulation, the use of PCE results in being the most computationally effective methods, in terms of CPU time and accuracy of results, when compared to other methods such as the high order expansions tensors, for their capability to include the effects of non-linearities over long propagation intervals.
- It is demonstrated through several examples and applications that the spacecraft trajectory estimation through the Unscented Kalman Filter outperforms other Kalman filters, mainly in terms of balance between accuracy and computational cost. UKF is the best choice for on-board application, especially when the system and measurements noises are (quasi)

Gaussian. When no precise a-priori information relatively to these noises is available, the minmax variant of the UKF, that is the Unscented H-infinity, has to be preferred for its capability to minimize the expected error when the system and measurements noises are maxima.

- We showed that a disaggregated spacecraft formation where relative measurements are being shared and fused into the UHF is fault tolerant to multiple sources of instruments failures. The findings is not limited to the explored scenario but can be extended to any spacecraft formation where inter-satellite links are available.
- It is proposed and analysed the combined use of ranging and optical measurements from a two-spacecraft formation to refine asteroid's trajectory knowledge during deep space flight to avoid implementing complex approach strategies (i.e. dog-legs manoeuvres). The method can be applied to the approach phases or during deep space missions to improve known and newly discovered asteroid's orbits. It is shown that depending on the relative configuration this technique can accurately determine the trajectory of the asteroid.
- It is for the first time treated the problem of simultaneous spacecraft navigation and asteroid's orbit and attitude control using a laser ablation system for the problem of asteroid's threat mitigation. This navigation problem is tackled by considering the use of on-board instruments (camera, altimeter and impact sensors) and combining a UKF with an optic flow filter to estimate of the asteroid's rotational rate, spacecraft trajectory and the ablative force. The asteroid's control is solved with the developed concept of control arm which allows reducing the overall angular velocity by identifying the points where resulting control torque acts mainly in the opposite direction of the rotational velocity vector.

## 6.2 Limitations of This Work

During the final phases of the impacting trajectory in Section 2.3.2 we had to use a simplified approach to evaluate the distribution on the surface. This was due to the strong deformations and stretch distribution can incur because of gravity field of the Moon, which leads the particles to impact at different times. If one tried to represent the final phase using the PCE approach, a very high order multivariate, and thus a very dense sparse grid, would be required. As a consequence one would lose the computational convenience of the PCE technique over a full MC analysis. This difficulty in dealing the last and closest phases with PCE suggests that additional study is required to handle the strong deformation.

For the formation analysis of Chapter 4, we considered a minimum set of instruments to perform the mission with the possibility to share the necessary information from the other spacecraft in the case of failure. Nonetheless having used a fixed configuration we did not take into account the fact that some spacecraft could have their intersatellite link obstructed by the asteroid as well as no possibility to use the camera for optical navigation. Moreover we do not address the technological requirements for the intersatellite link to point towards the other member of the formation, although expensive low power flash-LIDAR camera could be used.

During the asteroid deflection scenario of Chapter 5, we used a simplified shape model for the asteroid, where the composition and geometry characteristics were basically well defined (despite the position of the centre of mass). This was in line with the way the NEOs missions have been carried out, where a global mapping campaign of the asteroid is performed by ground using the information taken from the spacecraft. Nonetheless, accurately knowing the geometry (i.e. the mesh

of the asteroid and local normal) could be too expensive for the on-board computer. In order to be compliant with reduced computational resources a low fidelity mesh could be stored and used. This of course could impact the overall performance of the deflective action and might produce a change in the deflection strategy itself. Moreover we assumed that there is an actuation system (either the laser optics or the attitude control) able to point the laser on the selected points on the surface. The simulation of the whole GNC system, comprising the attitude dynamics and control, could be an additional factor which could affect the efficiency of the deflective action.

### **6.3 Remarks for Future Work**

In addition to the research studied in this thesis, some analyses and hints for future research which could complement or improve the results are presented. These considerations are given hereafter.

An important area of research is the application of PCE to the propagation and control of asteroid's trajectory deflection under uncertainty. In fact for some asteroids the deflection could push the object through key-holes which would increase the impact risk rather than reducing it. This event is something which needs to be thoroughly assessed. Future works will see the application of PCE to the study of uncertainty effects on other trajectories which can involve multi-revolutions and fly-bys. Given the difficulties to handle highly perturbed sections of the propagations during close encounters where region of the uncertain space will impact the surface of the body, a smart approach could be required. For instance one could first perform an analysis similar to the one of Chapter 2 to filter out impacting particles generated through the sampling of the reconstructed PCE distribution. Then the surviving particles can be used to reconstruct the post encounter distribution when these are sufficiently far from the body. Eventually the same techniques, based on sparse

grids, could be used on the post-encounter reconstruction. Alternatively to this discrete procedure, one could think of adaptively dividing the uncertain region in a suitable number of sub-domains, where the degree of the polynomials can be maintained relatively low. For the sub-domains creation the solution of Wittig et al. (2014) developed for differential algebra techniques can be a starting point of investigation. Moreover one could include other uncertain variables such as the attitude and solar radiation pressure to analyse the evolution of the trajectory with PCE.

In recent years there have been developed a great number of filtering techniques based on the Kalman and H-infinity filter. An interesting area that could be applied to the spacecraft navigation for mission to minor celestial objects is represented by the adaptive filtering and control which have been applied to several fields, most notably aeronautics (Vrabie et al., 2013) with few application to spacecraft orbit determination (for example relative navigation in Li et al., 2015). These methods are particularly appealing for their capability to deal with complex systems that have unpredictable parameter deviations and uncertainties such as the imprecise knowledge of the gravity field of a minor body. Autonomous adaptive techniques can be used to characterise unknown systems in time-variant environments. The advantage of such an approach will be to dramatically decrease the number of ground operations which are required to characterize the asteroid's environment before spacecraft final approach. In this way the navigation system would be adaptable to any size of asteroid with little support from Earth. Of course this capability needs concurrent improvement in the hardware and artificial intelligence since the system has to be smart and computationally powerful enough in order to auto-tune itself and make decisions.

In the case of formation flying scenario, an improvement in the dynamic model could include more gravitational harmonics as well as the perturbations due to the asteroid tugging and surface ablation.

The interaction will produce deviations from the nominal asteroid trajectory, which implies that it will be necessary to estimate the asteroid's trajectory during the formation proximal motion and operations. Future research could analyse the influence of the number of the spacecrafts in the formation on navigation performance. Moreover it could consider a redundant set of sensors, and then study suitable spacecraft failure detection, identification and compensation systems for different phases. In the case the ranging instruments failure, for instance, a camera could supply enough information to the spacecraft to navigate if the physical size of the asteroid had been identified before the failure. When the spacecraft is in shadow and if the camera is able to identify the border of the body, this could provide some information to obtain a rough estimation to navigate relatively safe at least for short period. Alternatively a suitable technique based on differential correction guidance might be necessary to estimate the size and then navigate safely without the intervention from ground.

For the deep space approach of the two spacecraft, one could pursue two possible investigations. The first one is to process the on-board angular measurements and ground tracking in conjunction with dogleg manoeuvres to improve the asteroid trajectory estimate. The second is to implement a fully autonomous on-board system on the two spacecraft, similarly to the AutoNav system used by Deep Space 1 (Bhaskaran, 2012), with the possibility for them to communicate through a low gain antenna which can be used also as a range measurements (given the needs of a precise on-board clock).

For what concerns the deflection of asteroids, future research could foresee a trade-off between the attitude pointing and a mechanism pointing for the laser through a complete GNC simulator where the attitude of the spacecraft is simulated. This could also drive the selection of different control



pointing strategy, taking into account that millions of laser focusing cycles can be envisaged for a mission lasting several years. Moreover a practical study of the navigation strategy, taking into account the control complexity of the system, can be performed over other contactless solution to assess the impact on the total deflection during the same operative interval. In all the case non-uniform shapes could be considered extending the results to bigger asteroids, to evaluate the robustness of the whole strategy against unknown geometrical and material characteristics.

## Bibliography

- [1] Alonso, R., Du, J. and Hughes, Y.: ‘Relative Navigation for Formation Flying of Spacecraft’. Proceedings of the Flight Mechanics Symposium, NASA-Goddard Space Flight Center, Greenbelt, MD, 2001, pp. 115-129.
- [2] Agarwal, N., Aluru, N. R.: ‘Weighted Smolyak algorithm for solution of stochastic differential equations on non-uniform probability measures’. International Journal for Numerical Methods in Engineering, Int. J. Numer. Meth. Engng 2011, Vol. 85, pp. 1365-1389.
- [3] Armellin R., Di Lizia P., Rasotto M., Di Mauro G., Landgraf, M.: ‘Disposal Strategies for Spacecraft in Lagrangian Point Orbits’. The 24th AAS/AIAA Space Flight Mechanics Meeting, Jan. 26-30, 2014, Santa Fe, New Mexico.
- [4] Babuska I, Nobile F, Tempone R.: ‘A stochastic collocation method for elliptic partial differential equations with random input data’. SIAM Journal on Numerical Analysis 2007; 45(3):1005–1034.
- [5] Bhaskaran, S.: ‘Autonomous Navigation for Deep Space Missions’. Proceedings of SpaceOps 2012, 11-15 June in Stockholm, Sweden
- [6] Bate, R., Mueller, D. and White, J.: ‘Fundamentals of Astrodynamics’. Dover. 1971.
- [7] Battin, R.H., Levine, G. M., 1970: ‘Application of Kalman Filtering Techniques to the Apollo Program’. Theory and Applications of Kalman Filtering, edited by C.T. Leondes, AGARD-ograph 139, 1970, 335-361.
- [8] Belbruno, E.A., 1987: ‘Lunar Capture Orbits, a method for constructing Earth-Moon Trajectories and the lunar GAS mission’. Proceedings of AIAA/DGLR/JSASS Inter. Propl. Conf. AIAA Chapter No 87-1054 (1987).
- [9] Bellei, G., Cano, J.L., Sanchez, M.: ‘Operational Orbiting Strategies about Minor Bodies’. International Symposium on Space Flight Dynamics, September 28-October 2, Toulouse, France, 2009.
- [10] Blanchard, E. D., Sandu, A., and Sandu, C.: ‘A Polynomial Chaos-Based Kalman Filter Approach for Parameter Estimation of Mechanical Systems’. Journal of Dynamic Systems, Measurement, and Control, Vol. 132, No. 6, November 2010, pp. 061404.

- [11] Bombardelli, C. and Peláez, J.: ‘Ion Beam Shepherd for Asteroid Deflection’. *Journal of Guidance, Control, and Dynamics*, Vol. 34, No. 4, July–August 2011, pp. 1270–1272, 2011.
- [12] Brandon A.J., and Alireza, D.: ‘Satellite Collision Probability Estimation Using Polynomial Chaos’. *Advances in Space Research* Volume 52, Issue 11, 1 December 2013, Pages 1860–1875.
- [13] Canalias E., Gomez G., Marcote M., Masdemont J. J.: ‘Assessment of mission design including utilisation of libration points and weak stability boundaries’. European Space Agency, the Advanced Concepts Team, Ariadna Final Report (03-4103a), 2004.
- [14] Chapman C. R. and Morrison D.: ‘Impacts on the Earth by Asteroids and Comets: Assessing the Hazard’. *Nature*, Vol. 367, No. 6458, Jan. 1994, pp. 33–40, doi: 10.1038/367033a0
- [15] Cheng, Y., Jia, B. and Xin, M.: ‘Sparse Grid Approach to Orbit Uncertainty Propagation’. In *ICCES: International Conference on Computational & Experimental Engineering and Sciences*, vol. 16, no. 2, pp. 33-34, 2011.
- [16] Chung, L. R.: ‘Orbit determination methods for deep space drag-free controlled laser interferometry missions’. Master thesis. University of Maryland, 2006.
- [17] Colombo, C., Sanchez Cuartielles, J. P., Vasile, M., Radice, G.: ‘A comparative assessment of different deviation strategies for dangerous NEO’. In: *International Astronautical Congress*. Valencia, Spain, 2006.
- [18] Colombo, C. Sanchez Cuartielles, J. P., Vasile, M. et al.: ‘Comparison of single and multi-spacecraft configurations for NEA deflection by solar sublimation’. In: Belbruno, E. (Ed.), *New Trends in Astrodynamics and Applications III*. Vol. 886. American Institute of Physics, 2007, pp. 303–316.
- [19] Colombo C., Vasile M. and Radice G.: 2009, ‘Semi-Analytical Solution for the Optimal Low-Thrust Deflection of Near Earth Objects’. *Journal of Guidance, Control and Dynamics*, Vol. 32, No. 3, May–June 2009, pp. 796–809, doi: 10.2514/1.40363.
- [20] Colombo, C., Letizia, F., Soldini, S., Vasile, M., Vetrignano, M., van der Weg, W., Alessi, E. M., Rossi A.: *End-Of-Life Disposal Concepts for Lagrange-Point and Highly Elliptical Orbit Missions*. Final Report, 2014, ESA/ESOC contract No. 4000107624/13/F/MOS
- [21] Colombo, C., Alessi, E.M., van der Weg, W., Soldini, S., Letizia, F., Vetrignano, M., Vasile, M. Rossi, A., and Landgraf, M.: ‘End-of-life disposal concepts for Libration Point Orbit and Highly

- Elliptical Orbit missions'. *Acta Astronautica*, Volume 110, May–June 2015, Pages 298–312, Dynamics and Control of Space Systems.
- [22] Crassidis, J.L. and Junkins, J.L.: 'Optimal estimation of Dynamic Systems'. S.Haykin, 2001.
- [23] Croisard, N. et al.: 'European Student Moon Orbiter Mission Analysis Phase A1 Report'. Glasgow: Glasgow University. 2009.
- [24] Cui, P.Y., Chang, X.H., Cui, H.T., 2010: 'Autonomous orbit determination of deep space probe based on the Sun line-of-sight vector'. *IEEE*, 2010, 540-544.
- [25] Cunningham, L.E.: 'On the computation of the spherical harmonics needed during the numerical integration of the orbit motion of an artificial satellite'. *Celestial Mechanics* 2, 2007-2016 (1970).
- [26] Dhome, M., Richetin, M., Lapreste, J.T., Rives, G.: 'Determination of the Attitude of 3-D Objects from a Single Perspective View'. *IEEE Transactions on pattern analysis and machine intelligence*. Vol II. No. 12. December 1989.
- [27] Dionne K.: 'Improving Autonomous Optical Navigation for Small Body Exploration Using Range Measurements'. AIAA 2009-6106. AIAA Guidance, Navigation, and Control Conference, 10 - 13 August 2009, Chicago, Illinois.
- [28] Eismont N. A., Ditrikh A. V., Janin G., Karrask V. K., Clausen K., Medvedchikov A. I., Kulik S. V., Vtorushin N. A., Yakushin N. I.: 'Orbit design for launching INTEGRAL on the Proton/Block-DM launcher', *Astronomy and Astrophysics*, Vol. 411, N. 1, pp. L37–L41, Nov. 2003, doi: 10.1051/0004-6361:20031452
- [29] Eldred M. S., Swiler L.P., and Tang, G.: 'Mixed aleatory-epistemic Uncertainty quantification with stochastic expansions and optimization-based interval estimation'. *Reliability Engineering and System Safety*, Vol. 96, 2011, pp. 1092-1113.
- [30] Ganapathysubramanian B, Zabarar N.: 'Sparse grid collocation schemes for stochastic natural convection problems'. *Journal of Computational Physics* 2007; 225:652–685.
- [31] Garmier, R., Ceolin, T., Martin, T. et al.: 'Philae Landing on Comet Churyumov-Gerasimenko: Understanding of Its Descent Trajectory, Attitude, Rebound and Final Landing Site'. In 25th International Symposium on Space Flight Dynamics ISSFD, October 19 – 23, 2015, Munich, Germany.

- [32] Genz, A.: 'Fully Symmetric Interpolatory Rules for Multiple Integrals'. *SIAM J. Numer. Anal.* 23 (1986), pp. 1273-1283.
- [33] Genz, A. and Keister, B.: 'Fully Symmetric Interpolatory Rules for Multiple Integrals over Infinite Regions with Gaussian Weight'. *J. Comp. Appl. Math.* 71 (1996), pp. 299-309.
- [34] Ghanem R.G. and Spanos P.: 'Stochastic Finite Elements: A Spectral Approach'. Springer: Berlin, 1991.
- [35] Ghanem, R. and Dham, S.: 'Stochastic finite element analysis for multiphase flow in heterogeneous porous media'. *Transporting Porous Media*, Vol. 32, No. 3, pp. 239-262, 1998.
- [36] Ghanem R., Doostan A.: 'On the construction and analysis of stochastic models: characterization and propagation of the errors associated with limited data'. *Journal of Computational Physics* 2006; 217:63–81.
- [37] Gibbings A., Vasile M., Hopkins J.-M., Burns D., Watson I.: 'Experimental Characterization of the Thrust Induced by Laser Ablation on an Asteroid', *Planetary Defense Conference 2013*, Flagstaff, USA, AA-PDC2013-04-21.
- [38] Gibbons, J. D. and Chakraborti, S.: 'Nonparametric Statistical Inference'. 5th Ed., Boca Raton, FL: Chapman & Hall/CRC Press, Taylor & Francis Group, 2011.
- [39] Gilli, L., Lathouwers, D., Kloosterman, J.L., and van der Hagen, T.H.J.J.: 'Performing uncertainty analysis of a nonlinear Point-Kinetics/Lumped Parameters problem using Polynomial Chaos techniques'. *Annals of Nuclear Energy* 40 (2012) 35–44.
- [40] Gil-Fernandez, J.: 'Autonomous GNC System to enhance science of asteroid'. *63rd International Astronautical Congress*, Naples, Italy, 2012.
- [41] Godard, B., Croon, M., Budnik, F. and Morley, T.: 'Orbit determination of the Plank Satellite'. *The 21st International Symposium on Space Flight Dynamics*. Toulouse, France, 2009.
- [42] Gibbings A., Vasile M., Hopkins J.-M., Burns D., Watson I.: 'Experimental Characterization of the Thrust Induced by Laser Ablation on an Asteroid', *Planetary Defense Conference 2013*, Flagstaff, USA, AA-PDC2013-04-21.
- [43] Gordon, N. J., Salmond, D. J. and Smith, A. F. M.: 'Novel approach to nonlinear/non-Gaussian Bayesian state estimation'. *IEEE Proceedings F, Radar and Signal Processing*, Vol. 140, Nr. 2 IET (1993), p. 107-113.

- [44] Hashimoto, T., Kubota, T., Mizuno, T.: ‘Light weight sensors for the autonomous asteroid landing of MUSES-C mission’. *Acta Astronautica*, Volume 52, Issues 2–6, January–March 2003, Pages 381–388.
- [45] Hu, W. and Scheeres, D. J.: ‘Spacecraft motion about slowly rotating asteroids’. *Journal of Guidance, Control and Dynamics* 25 (4), 765–775.
- [46] Heiss F. and Winschel V.: ‘Likelihood approximation by numerical integration on sparse grids’. *Journal of Econometrics* (2008), doi:10.1016/j.jeconom.2007.12.004
- [47] Hirai, H., Masutani, Y., Miyazaki, F.: ‘Motion Estimation of an Unknown Rigid Body Rotating Freely in Zero Gravity Based on Complex Spectrum of Position of a Point on the Body’. *IEEE International Conference on Robotics & Automation Leuven, Belgium, May 1998*.
- [48] Hu, W. and Scheeres, D. J.: ‘Spacecraft motion about slowly rotating asteroids’. *Journal of Guidance, Control and Dynamics* 25 (4), 765–775, 2002.
- [49] Hu, W. and Scheeres, D. J.: ‘Numerical Determination of Stability Regions for Orbital Motion in Uniformly Rotating Second Degree and Order Gravity Fields’. *Planetary and Space Science* 52. 685-692, 2004.
- [50] Hosder, S., Walters, R. W., and Perez, R.: ‘A Non-Intrusive Polynomial Chaos Method for Uncertainty Propagation in CFD Simulations’. *44th AIAA Aerospace Sciences Meeting and Exhibit, Reno, Nevada, January 9 - 12 2006*.
- [51] Jia, Y. and Xiu, W., 2009: ‘A generalized polynomial chaos based ensemble Kalman filter with high accuracy’. *Journal of Computational Physics* 228 (2009) 5454–5469.
- [52] Johnson, A.E. and Matthies, L. H.: ‘Precise Image-Based Motion Estimation for Autonomous Small Body Exploration’. *Appearing in the 5th International Symposium on Artificial Intelligence, Robotics and Automation in Space (iSAIRAS’1999)*, pp. 627-634.
- [53] Julier, J. K. Uhlmann and Durrant-Whyte, H.F.: ‘A new approach for filtering nonlinear systems’. *Proceedings of the American Control conference, Seattle, Washington, 1995*.
- [54] Kahle, R., Kuhrt, E., Hahn, G., Knollenberg, J.: 2006, ‘Physical limits of solar collectors in deflecting Earth-threatening asteroids’. *Aerospace Science and Technology* Vol. 10, pp. 253–263.
- [55] Kelbel, D., Lee, T. et al.: ‘Evaluation of Relative Navigation Algorithms for Formation-Flying Satellites’, *Nasa Archive, 2001*.

- [56] Knio, O. M. and Le Maître, O. P. L.: ‘Uncertainty Propagation in CFD Using Polynomial Chaos Decomposition. *Fluid Dynamics Research*, Vol. 38, No. 9, September 2006, pp. 616–640.
- [57] Konimoto, M., Matsuoka, M., Uo, M., Hashimoto, T. and Kawaguchi, J.: ‘Optical Hybrid Navigation in Hayabusa – Approach, Station Keeping & Hovering’. NEC Aerospace Systems, NEC Toshiba Space Systems, ISAS, JAXA, 2006.
- [58] Kubota, T., Hashimoto, T. et al.: ‘An autonomous navigation and guidance system for MUSES-C asteroid landing’. *Acta Astronautica*, 2003, 52(2-6): 125-131.
- [59] Kubo-oka, T. and Sengoku, A.: ‘Solar radiation pressure model for the relay satellite of Selene’. *Earth Planets Space*, 51:979{986, 1999}.
- [60] Lagarias, J.C., Reeds, J. A., Wright, M. H. and Wright, P. E.: ‘Convergence Properties of the Nelder-Mead Simplex Method in Low Dimensions’. *SIAM Journal of Optimization*, Vol. 9 Number 1, pp. 112-147, 1998.
- [61] Li, S., Cui, P.Y. et al.: ‘Autonomous navigation and guidance for landing on asteroids’. *Aerospace science and technology*, 2006, 10(3): 239-247.
- [62] Li, S., Cui, P.Y., Cui, H.T.: ‘Vision-aided inertial navigation for pinpoint planetary landing’. *Aerospace Science and Technology*, 2007, 11(6):499-506.
- [63] Le Maître O.P., Ghanem R.G., Knio, O.M., Najm H.N.: ‘Uncertainty propagation using Wiener–Haar expansions’. *Journal of Computational Physics* 2004; 197:28–57.
- [64] Li, W. and Jia, Y., 2010: ‘H-infinity filtering for a class of nonlinear discrete-time systems based on unscented transform’. *Signal Processing* 90 (2010) 3301–3307
- [65] Li, W., Jia, Y. and Du, J.: Windowing-based Adaptive Unscented Kalman Filter for Spacecraft Relative Navigation. *Proceedings of the 34th Chinese Control Conference July 28-30, 2015, Hangzhou, China.*
- [66] Longuet-Higgins, H.C. and Prazdny, K.: ‘The interpretation of a moving retinal image’. *Proceedings of the Royal Society of London B* 208, 385-397, 1980.
- [67] Najm, H. N.: ‘Uncertainty Quantification and Polynomial Chaos Techniques in Computational Fluid Dynamics’. *Annual Reviews of Fluid Mechanics*, Vol. 41, 2009, pp. 35–52.
- [68] Mardia, K. V., Kent, J. T. and Bibby, J. M.: ‘Multivariate Analysis’. Academic Press, London, 1979.

- [69] Maybeck, P.S.: 'Stochastic Models, Estimation, and Control'. Mathematics in Science and Engineering. 141-1. Academic Press, Inc., New York, 1979, pp. 423. ISBN 0-12-480701-1.
- [70] Maybeck, P.S.: 'Stochastic Models, Estimation and Control. Vol 2'. Academic Press, Inc., New York, 1982. Chapter 12.
- [71] Melosh, H. J., Nemchinov, I. V. and Zetzer, Y. I.: 'Non-nuclear strategies for deflecting comets and asteroids. In: Gehrels, T. (Ed.), Hazard due to comets and asteroids'. University of Arizona Press, 1994, pp. 1111–1132.
- [72] Morley, T., Budnik, F.: 'Rosetta Navigation for the fly-by of the asteroid 2867 Steins'. Proceedings of the 21st International Symposium on Space Flight Dynamics. Toulouse, France, 2009.
- [73] Montenbruck, O. and Gill, E.: 'Satellite orbits: models, methods and applications'. Springer-Verlag, Berlin, 2000.
- [74] Nister, D.: 'An Efficient Solution to the Five-Point Relative Pose Problem'. IEEE Transactions on pattern analysis and machine intelligence. Vol 26. No. 6. June 2006.
- [75] Oh, S.M and Johnson, E. N.: 'Relative Motion Estimation for Vision-based Formation Flight using Unscented Kalman Filter'. AIAA Guidance, Navigation and Control Conference and Exhibit, Hilton Head, South Carolina, 2007.
- [76] Park, R. and Scheeres, D.: 'Nonlinear Semi-Analytic Method for Spacecraft Navigation'. AIAA/AAS Astrodynamics Specialist Conference and Exhibit, Keystone, Colorado, 21-24 August 2006(a).
- [77] Park, R. and Scheeres, D.: 'Nonlinear Mapping of Gaussian Statistics: Theory and Applications to Spacecraft Trajectory Design'. Journal of Guidance, Control and Dynamics, Danvers, Maryland, Vol 29, No 6, pp. 1367-1375, 2006(b).
- [78] Park, S.: 'Nonlinear Trajectory Navigation'. PhD Dissertation, University of Michigan, Ann Arbor, Michigan, 2007.
- [79] Park, R. and Scheeres, D.: 'Nonlinear Semi-Analytic Method for Spacecraft Navigation'. AIAA/AAS Astrodynamics Specialist Conference and Exhibit, Keystone, Colorado, 21-24 August 2006.



- [80] Perozzi E., Ferraz-Mello S. editors: *Space manifold Dynamics: Novel Spaceways for Science and Exploration*. Springer New York Dordrecht Heidelberg London, 2010. DOI 10.1007/978-1-4419-0348-8\_1.
- [81] Sanchez J. P., Colombo C., Vasile M. and Radice G.: 'Multi-Criteria Comparison among Several Mitigation Strategies for Dangerous Near Earth Objects', *Journal of Guidance, Control and Dynamics*, Vol. 32, No. 1, Jan.-Feb. 2009, pp. 121-142, doi: 10.2514/1.36774.
- [82] Schaub, H., Junkins, J. L.: 'Analytical mechanics of space systems'. 1st Edition. AIAA Education Series. AIAA, Virginia, U.S.A., 2003.
- [83] Scheeres, D.J., Broschart, S., Ostro, S.J. and Benner, L.A.: 'The Dynamical Environment About Asteroid 25143 Itokawa: Target of the Hayabusa Mission'. AIAA/AAS Astrodynamics Specialist Conference and Exhibit. 16 - 19 August 2004(b), Providence, Rhode Island.
- [84] Scheeres, D.J.: 'Interactions between ground-based and autonomous navigation for precision landing at small solar-system bodies'. The Telecommunications and Data Acquisition Progress Report 42-132, October–December 1998, pp: 1-12.
- [85] Scheeres, D.J., Gaskell, R., Abe, S., Barnouin-Jha, O., Hashimoto, T., Kawaguchi, J., Kubota, T., Saito, J., Yoshikawa, M., Hirata, N., Mukaik, T., Ishiguro, M., Kominato, T., Shirakawa, K., Uo, M.: 'The Actual Dynamical Environment About Itokawa'. AIAA/AAS Astrodynamics Specialist Conference and Exhibit. 16 - 19 August 2004(a), Keystone, Colorado.
- [86] Scheeres, D.J.: 'Orbit Mechanics about Asteroids and Comets. *Journal of Guidance, Control and Dynamics*, 2012, 35(3): 987-997.
- [87] Sebaldt W., Reichert M., Hanowski N. and Novara M.: 'A Review of the Long-Term Options for Space Exploration and Utilisation', *ESA Bulletin*, Vol. 101, Feb. 2000.
- [88] Seidelmann, P.K., Archinal, B.A., A'hearn, M.F., Conrad, A., Consolmagno, G.J., Hestroffer, D., Hilton, J.L., Krasinsky, G.A., Neumann, G., Oberst, J., Stooke, P., Tedesco, E.F., Tholen, D.J., Thomas, P.C., Williams, I.P.: 'Report of the IAU/IAG Working group on cartographic coordinates and rotational elements: 2006'. *Celestial Mech Dyn Astr*(2007) 98:155-180. DOI 10.1007/s10569-007-9072-y.
- [89] Shim, S., Park, S. Y. et al.: 'Autonomous Real-time Relative Navigation for Formation Flying Satellites'. *Journal of Astronomy and Space Sciences*, 2009, 26: 59-74.

- [90] Shi, J. and Ghanem, R. G.: ‘Nonlocal, Stochastic Modeling of Materials with Multiscale Structures’. Proceedings of the 6th World Congress on Computational Mechanics, Beijing, China, September 5-10 2004.
- [91] Siegman, A. E.: ‘Lasers’. University Science Books. pp. 664–669. ISBN 0-935702-11-3. 1986.
- [92] Simon, D. A.: ‘Optimal State Estimation Kalman,  $H_\infty$ , and Nonlinear Approaches’. A John Wiley & Sons, Inc., Publication. 2006.
- [93] Smolyak S.: ‘Quadrature and interpolation formulas for tensor products of certain classes of functions’. Soviet Mathematics - Doklady 1963; 4:240–243.
- [94] Smoliak, N. A., Aluru, N. R.: ‘Weighted Smolyak algorithm for solution of stochastic differential equations on non-uniform probability measures’. International Journal for Numerical Methods in Engineering, Int. J. Numer. Meth. Engng 2011, Vol. 85, pp. 1365-1389.
- [95] Valli, M., Armellin, R. Di Lizia, P. and Lavagna M. R.: ‘Nonlinear Mapping of Uncertainties in Celestial Mechanics’. Journal of Guidance, Control, and Dynamics, Vol. 36, No. 1 (2013), pp. 48-63. doi: 10.2514/1.58068
- [96] Thornton, C. L. and Border, J.S.: ‘Radiometric Tracking Techniques for Deep-Space Navigation’. JPL Deep Space Communications and Navigation Series, John Wiley & Sons Inc., Hoboken, New Jersey, 2003.
- [97] Vallado. D.A. and McCain, W.D: ‘Fundamentals of Astrodynamics and Applications’. David Anthony Vallado, Volume 12 of Space technology library, ISSN 0924-4263, 2001.
- [98] Vasile M., Maddock C.: ‘Design of a Formation of Solar Pumped Lasers for Asteroid Deflection’. Advances in Space Research, 2012.
- [99] Vasile M., Vetrivano M., Gibbings A., Garcia Yarnoz D., Sanchez Cuartielles J-P., Burns D., Hopkins J-M., Colombo C., Branco J., Wayman A., Eckersley S. 2013: ‘Light Touch2, Effective Solutions to Asteroid Manipulation’, ESA Final report, SysNova Study, ESA Reference Nos.: 12/X02, 12/X03, February 2013.
- [100] Vasile M., Vetrivano M., Gibbings A., Garcia Yarnoz D., Sanchez Cuartielles J-P., Hopkins J-M., Burns D., McInnes C., Colombo C., Branco C., Wayman A., Eckersley S.: ‘Light-Touch2: 2013, A Laser-Based Solution for the Deflection, Manipulation and Exploitation of Small Asteroids’, Planetary Defense Conference 2013(b), Flagstaff, USA, IAA-PDC13-04-22.

- [101] Vasile M. and Colombo C.: ‘Optimal Impact Strategies for Asteroid Deflection’. *Journal of Guidance, Control, and Dynamics*, Vol. 31, No. 4, July–August 2008, pp. 858–872, doi: 10.2514/1.33432.
- [102] Vetrisano, M. and Vasile, M.: ‘Navigating to the Moon along low-energy transfers’. *Celestial Mechanics and Dynamical Astronomy* 2012, in press DOI 10.1007/s10569-012-9436-9, 2012.
- [103] Vetrisano, M. and Vasile, M.: ‘Collaborative guidance navigation and control of disaggregated spacecraft in the proximity of minor bodies’. In: 63rd International Astronautical Congress, Naples, Italy, 2012.
- [104] Vetrisano, M., Branco, J. and Garcia-Yarnoz, D.: ‘Effective approach navigation prior to small body deflection’. 64th International Astronautical Congress, Beijing, China, 2013.
- [105] Xiu D. and Karniadakis G.E.: ‘The Wiener–Askey polynomial chaos for stochastic differential equations’. *SIAM Journal on Scientific Computing* 2002; 24(2):619–644.
- [106] Van der Merwe, R., Doucet, A., de Freitasz, N. and Wan, E.: ‘The Unscented Particle Filter, Technical Report CUED/F-INFENG/TR 380’, Cambridge University Engineering Department, 2000.
- [107] Vrabie D., Vamvoudakis, K.G. and Lewis, F.: ‘Optimal Adaptive Control and Differential Games by Reinforcement Learning Principles’. Published by The Institution of Engineering and Technology, London, United Kingdom, 2013.
- [108] Wie, B.: ‘Dynamics and control of gravity tractor spacecraft for asteroid deflection’. *Journal of Guidance, Control, and Dynamics*, 2008, 31(5): 1413-1423.
- [109] Wiener N.: ‘The homogeneous chaos’. *American Journal of Mathematics* 1938; 60:897–936.
- [110] Wittig, A., Di Lizia, P., Armellini, R., Bernelli, F., Makino, K. And Berz, M.: ‘An Automatic Domain Splitting Technique to Propagate Uncertainties in Highly Nonlinear Orbital Dynamics’. *Advances in the Astronautical Sciences*, Vol. 152, Univelt Inc., USA, 2014. pp. 1923-1941.
- [111] Xiu D.: Hesthaven J.S.: ‘High-order collocation methods for differential equations with random inputs’. *SIAM Journal on Scientific Computing* 2005; 27(3):1118–1139.
- [112] Yim, J. R., Crassidis, J. L., Junkins, J. L.: ‘Autonomous Orbit Navigation of Interplanetary Spacecraft’. *AIAA Guidance, Navigation, and Control Conference*, Denver, CO, Aug. 2000, AIAA Chapter 2000-3936.